Title

Superparamagnetic Core/Shell Silica Nanoparticles for Stimuli-Responsive Drug Delivery, Therapeutics, and Diagnostics

Author

lin, fang-chu

Publication Date

2021

UNIVERSITY OF CALIFORNIA

Los Angeles

Superparamagnetic Core/Shell Silica Nanoparticles for Stimuli-Responsive Drug Delivery, Therapeutics, and Diagnostics

A dissertation submitted in partial satisfaction of the
requirements for the degree Doctor of Philosophy
in Chemistry

by

Fang-Chu Lin

2021

ABSTRACT OF THE DISSERTATION

Superparamagnetic Core/Shell Silica Nanoparticles for Stimuli-Responsive Drug Delivery, Therapeutics, and Diagnostics

by

Fang-Chu Lin
Doctor of Philosophy in Chemistry
University of California, Los Angeles, 2021
Professor Jeffrey I. Zink, Chair

There is currently a high unmet medical need for chemotherapy and early diagnostics for cancer. Conventional direct administration of chemotherapeutic agents shows several major drawbacks, including restricted cellular penetration, low therapeutic indices, and low specificity to tumor cells thus consequently off-target toxicity in healthy cells. Nanoparticles with an enhanced permeability and retention (EPR) effect provide both delivery and diagnostic modalities and show promise for addressing these challenges in cancer therapy. Superparamagnetic iron oxide nanoparticles (SPIONs) that respond to external magnetic fields can generate heat in the presence of an alternating magnetic field (AMF). Owing to this unique property, SPIONs are being used in clinics as magnetic resonance imaging T_2 contrast agents and as AMF-induced therapeutic agents to treat cancers. Mesoporous silica nanoparticles embedded with SPIONs (SPION@MSNs) possess the advantageous features of both the SPION core and the shell, i.e., localized magnetic heating and a high payload of various cargo molecules such as anticancer drugs. A part of this dissertation focuses on the development of SPION@MSNs as a heat-activated drug delivery platform in which the precise drug release can be directly controlled by using AMF. To expand our knowledge base in this application, we first studied the local heating mechanism of SPIONs in suspension and in MSNs. We carried out this investigation by using fluorescence depolarization based on detecting the mobility-dependent polarization anisotropy of two luminescence emission bands corresponding to the luminescent SPION core and the shell of the SPION@MSNs. Utilizing magnetic heating, we designed magnetically-activated and enzyme-responsive SPION@MSNs with extra-large pores for *in vivo* delivery and release of anticancer peptides on-demand. In addition, we introduced the design of MSNs-based delivery vehicles with a supramolecular capping system that traps the cargos in the pores of nanoparticles and only releases the cargos in response to ultrasound. Finally, by employing surface functionalization of silica, we developed new fluorinated ferrofluids that can be encapsulated in a microdroplet for measuring microenvironment stiffness, which has been shown to relate to tumor progression. Altogether, these works show the full potential of SPION core/shell nanoparticles for advancing cancer therapy and diagnostic.

The dissertation of Fang-Chu Lin is approved.

William M. Gelbart

Charles M. Knobler

Holden H. Wu

Jeffrey I. Zink, Committee Chair

University of California, Los Angeles

2021

This dissertation is dedicated to my dearest family

TABLE OF CONTENTS

Abstract of this Dissertation ii

Committee Page. iv

List of Figures xi

List of Supporting Information Figures xvi

List of Schemes xviii

List of Tables xix

Acknowledgements xx

VITA xxiv

Selected Publications xxv

Chapter 1 Introduction 1

- 1.1 Biomedical Applications of Superparamagnetic Iron Oxide Nanoparticles (SPIONs) Core/Shell Mesoporous Silica Nanoparticles 1
- 1.2 Abstracts of the Dissertation Chapters 4
- 1.2.1 Magnetism, Ultrasound, and Light-Stimulated Mesoporous Silica Nanocarriers for Theranostics and Beyond 4
- 1.2.2 Probing the Local Nanoscale Heating Mechanism of a Magnetic Core in Mesoporous Silica Drug-Delivery Nanoparticles Using Fluorescence Depolarization 5
- 1.2.3 Self-Contained Nanocapsules Carrying Anticancer Peptides for Magnetically Activated and Enzyme-Cleaved Drug Delivery 5
- 1.2.4 A Facile Method to Synthesize Fluorinated Ferrofluids for Measuring Mechanics in Living Systems 6
- 1.2.5 Drug Delivery by Ultrasound-Induced Binding Affinity Change 7
- 1.2.6 Nano-Therapeutic Cancer Immunotherapy Using Hyperthermia-Induced Heat Shock Proteins: Insights from Mathematical Modeling. 7
- 1.3 References 8

Chapter 2 Magnetism, Ultrasound, and Light-Stimulated Mesoporous Silica Nanocarriers for Theranostics and Beyond 10
2.1 Introduction 10
2.2 Alternating Magnetic Field Control of Nanocaps 12
2.2.1 AMF-Stimulated Supramolecule-Based Nanocaps 13
2.2.2 AMF-Stimulated Polymer-Based Nanocaps 14
2.2.3 AMF-Stimulated Biomolecule-Based Nanocaps 16
2.3 Ultrasound Control of Nanocaps 17
2.3.1 Ultrasound-Stimulated Supramolecular-Based Nanocaps 18
2.3.2 Ultrasound-Stimulated Polymer-Based Nanocaps 20
2.4 Light Control of Nanocaps 21
2.4.1 NIR Light-Responsive Nanocaps 22
2.5 Outlook and Perspectives 25
2.5.1 Research Opportunities Taking Advantage of Modern Clinically Available Medical Devices 25
2.5.2 Research Directions Based on Surface Engineering for Enhancing Targeting Efficacy 26
2.5.3 Research Opportunities Using Core-Shell, Large-Pore and Hollow MSNs 28
2.6 General Considerations 30
2.7 Figures 32
2.8 References 36
Chapter 3 Probing the Local Nanoscale Heating Mechanism of a Magnetic Core in Mesoporous Silica Drug-Delivery Nanoparticles Using Fluorescence Depolarization 45
3.1 Introduction 45
3.2 Theory of Magnetic Heating by SPIONs 48
3.3 Synthesis of Lanthanide Ions (Ln)-Doped Luminescent SPIONs 49
3.4 Results and Discussion 50
3.4.1 Possible Motions of the Core and the Shell caused by AMF 50
3.4.2 Steady-State Degree of Polarization Measurements for AMF-Induced Motions. 51
3.4.3 Synthesis and Properties of the Luminescent EuSPION 52

3.4.4 Magnetic Properties of Superparamagnetic Luminescent EuSPION 53
3.4.5 Fluorescence Anisotropy Measurements of Free EuSPION................................ 55
3.4.6 Luminescence of the MSN shell 56
3.4.7 Fluorescence Anisotropy Measurements of Core Shell EuSPION@MSN 56
3.4.8 Fluorescence Anisotropy Measurements of Dye-Doped SPION@MSN-RITC... 57
3.4.9 Fluorescence Anisotropy Measurements of Silica Nanoparticles without a Core 58
3.5 Conclusions.. 59
3.6 Experimental Section 60
3.6.1 Materials and Chemicals.. 60
3.6.2 Nanoparticles Synthesis 60
3.6.3 Optical Measurements 62
3.6.4 AMF-Induced Superparamagnetic Heating 64
3.6.5 Characterization 64
3.7 Acknowledgment 65
3.8 Schemes and Figures.. 65
3.9 Supporting Information.. 70
3.10 References.. 77

Chapter 4 Self-Contained Nanocapsules Carrying Anticancer Peptides for Magnetically Activated and Enzyme-Cleaved Drug Delivery 82
4.1 Introduction.. 82
4.2 Results and Discussion 85
4.2.1 Synthesis and Magnetic Properties of SPIONs and SPION@EXpMSNs 85
4.2.2 Synthesis and Characterization of Peptide Drug-Loaded SPION@EXpMSNs ... 87
4.2.3 Synthesis and Characterization of the Thermoresponsive Separating Barrier...... 88
4.2.4 PEG on Particle Exterior Surfaces for Enzyme Trapping in Particle Pores 89
4.2.5 AMF-Triggered Enzyme Activation for Release of Drugs................................. 90
4.2.6 Cancer Cell Death by Induced AMF-Triggered Drug Release............................ 92
4.2.7 *In vivo* Antitumor Efficiency of the Nanocapsules under AMF Stimulus............ 94
4.3 Conclusion 95
4.4 Experimental Section 96
4.4.1 Materials and Chemicals.. 96

4.4.2 Characterization ... 97

4.4.3 Nanoparticles Synthesis ... 100

4.5 Schemes and Figures ... 104

4.6 References ... 117

Chapter 5 A Facile Method to Synthesize Non-Ionic Fluorinated Ferrofluids for Measuring Mechanics in Living Systems ... 122

5.1 Introduction ... 122

5.2 Results and Discussion ... 124

5.2.1 Synthesis of SPION@SiO_2-1 Using Biphasic Approach ... 125

5.2.2 Attaching of Silane 2 via Direct-Coating Approach ... 125

5.2.3 Synthesis of SPION@SiO_2-1-2 Using a Combination of Biphasic and Direct-Coating Approach ... 126

5.2.4 Synthesis of SPION@SiO_2-[1+2] with 70% Total Silane Attachment Using Biphasic Approach ... 127

5.3 Conclusion ... 129

5.4 Experimental Section ... 130

5.4.1 Materials and Chemicals ... 130

5.4.2 Characterization ... 130

5.4.3 Nanoparticles Synthesis ... 131

5.5 Acknowledgements ... 133

5.6 Figures, Scheme, and Table ... 134

5.7 References ... 139

Chapter 6 Drug Delivery by Ultrasound-Induced Binding Affinity Change ... 141

6.1 Introduction ... 141

6.2 Results and Discussion ... 142

6.2.1 US-Induced Lowering of Binding Affinity between Host and Guest ... 142

6.2.2 US-Induced Contrast Change Due to Bubble Generation and Phase Change of SPIONs’ Surrounding Environment ... 144

6.3 Conclusion ... 146

6.4 Experimental Section ... 146

6.4.1 Materials and Chemicals ... 146

6.4.2 Characterization 146
6.4.3 Nanoparticles Synthesis 147
6.5 Figures and Tables 151
6.6 References 153
Chapter 7 Nano-Therapeutic Cancer Immunotherapy Using Hyperthermia-Induced Heat Shock Proteins: Insights from Mathematical Modeling 155
7.1 Introduction 155
7.2 Materials and Methods 159
7.2.1 Induction and Generation of HSPs 159
7.2.2 HSP Synthesis and Cell Death Model Integration 160
7.3 Results and Discussion 162
7.3.1 Analysis of Rate Constants 162
7.3.2 Analysis of Optimal HSP Synthesis 164
7.3.3 Effect of Heating Duration Time on HSP Synthesis 165
7.4 Conclusion 167
7.5 Figures and Tables 169
7.6 References 172

LIST OF FIGURES

Figure 2.1 TEM images of the most common spherical mesoporous silica nanoparticles (MSNs) used for biomedical drug delivery. (a) Tubular pores ~2.5 nm in diameter in a two-dimensional hexagonal array. The pores are commonly templated with cetyltriammoniumammonium bromide (CTAB) surfactant. (b) "Large pore" MSNs with dendritic center-radial oriented pores ~ 4 nm in diameter. The pore size can be changed using "swelling" agents, larger molecular weight templating surfactants, or a hydrophilic and hydrophobic solvent mixture. (c) Hollow MSNs. The hollow center is frequently formed by condensing mesoporous silica around a spherical nanoparticle that is then dissolved and leaves behind a spherical void. (d) Core-shell MSNs with radial pores. This important example contains a superparamagnetic iron oxide (SPION) core. Scale bar: 100 nm 32

Figure 2.2 Schematic representations of capping systems over pores and their responses to external magnetic field, ultrasound, or light stimuli that cause cargo molecules trapped in the capped pores to be released. Top: the phase change of polymer caps on a SPION@MSN that is stimulated by heat from a superparamagnetic core in an alternating magnetic field (AMF). Middle: bond cleavage of linker-based caps that are triggered by ultrasound. Bottom: the dissembling of supramolecular caps that are activated by light. In all cases the trapped cargo molecules (orange spheres) diffuse out of the pores after the stimulation opens the cap. Note that the pores are not drawn to scale and that each illustration only shows a few of many pores in a nanoparticle. 33

Figure 2.3 AMF activation of a nanovalve. The bulky cucurbit(6)uril caps trap cargo molecules in the pores of a SPION@MSN. Upon heating of the core by the AMF, the temperature-dependent binding constant of the cucurbit(6)uril to the diamine thread decreases, resulting in the disassembly of the nanovalve and subsequent release of cargo. Image adopted with permission from ref [29]. Copyright 2010 American Chemical Society. 33

Figure 2.4 AMF-responsive bulky molecular caps are attached to pore openings by thermally reversible Diels-Alder reactions and trap the cargo inside the pores. When the temperature is raised by AMF heating of the core, a cyclo-reversion reaction is triggered, leading to dissociation of the bulky caps and allowing cargo molecules to diffuse out of the mesopores. Image adopted from ref [31] with permission from The Royal Society of Chemistry. 34

Figure 2.5 Capping system stimulated by high-intensity focused ultrasound (HIFU) to control drug release from MSNs. The release is imaged by magnetic resonance imaging (MRgHIFU). (a) On the left, doxorubicin (DOX) is trapped in the mesopores by β-CD caps that are held in place by thermo-sensitive azo bonds. On the right, after the HIFU stimulation is turned on, the thermo-sensitive bonds are cleaved by HIFU, the cap is opened and DOX is released. The increased water access to the superparamagnetic iron oxide core causes the T_2 MRI contrast to change. (b) TEM images of core-shell MSNs, and (c) the bond cleavage reaction stimulated by HIFU. Image adopted from ref [50] with permission from The Royal Society of Chemistry. 34

Figure 2.6 An ultrasound-responsive copolymer grafted on the surface of MSNs changes conformation in response to ultrasound irradiation. The cargo is retained in the pores when the polymer is coiled. Ultrasound irradiation induces the change in polymer conformation to extended coil-like, unblocking the pore openings and allowing the trapped cargo to be released. The image adopted from ref. [53] Copyright 2015 American Chemical Society. 35

Figure 2.7 The mechanism of a two-photon infrared light-activated transducer for cargo release. (a) An azobenzene “nano-impeller” is in its trans configuration in its ground electronic state. (b) When excited with 760 nm two-photon energy, the fluorophore with a large two photon absorption cross-section transfers the energy to azobenzene via fluorescence resonance energy transfer (FRET). (c) The excited azobenzenes in the pores undergo reversible trans-cis isomerizations and act as nano-impellers; the large amplitude motions allow the cargo molecules to escape from the pores. Image adopted from ref [68] with permission from John Wiley and Sons. 35

Figure 3.1 Emission spectra of Ln-doped SPIONs (Ex. 377 nm) in hexane, including U-SPIONs, Eu-SPIONs, and Tb-SPIONs. 66

Figure 3.2 Field-dependent magnetization curves (M-H loop) at 300K, ZFC/FC modes of Temperature-dependent magnetization curves (M-T loop) under an applied magnetic field of 50 Oe, and TEM images of EuSPIONs synthesized under different experimental conditions. 67

Figure 3.3 Experimental arrangement combining AMF with fluorescence spectroscopy. Components are as follows: (A) sample, (B) five-turn AMF coil, (C) collecting lens, (D) focusing lens, (E) polarizer, (F) depolarizer, (G) monochromator, (H) CCD detector. The sample was excited by a vertically polarized laser pulse with an excitation wavelength of 377 nm. 67

Figure 3.4 (a) TEM image of EuSPIONs. (Black bar scales 50 nm) (b) Field-dependent magnetization curves (M-H loop) of EuSPIONs at 300K and 5K (inset: magnification of M-H curves from -2000 to 2000 Oe at 300K and 5K). (c) ZFC/FC modes of Temperature-dependent magnetization curves (M-T loop) of EuSPIONs under an applied magnetic field of 50 Oe. Blocking temperature of EuSPIONs was determined to be 98K. (d) TEM image of EuSPION@MSNs.. 67

Figure 3.5 (a) Polarized emission spectra of EuSPIONs (Ex. 377 nm) in hexane, cyclohexane, and in solid form. (b) Corresponding r collected at 550±5 nm in different AMF strengths. 68

Figure 3.6 The normalized emission spectra for (a) EuSPIONs, (b) MSNs, and (c) EuSPION@MSNs (Solid line: I ǁ dots: I ⊥). (d) Fitting of EuSPIONs and MSNs emission peaks in emission spectra of EuSPION@MSNs. Silica shell and EuSPIONs contribute approximately 75% intensity to the emission of EuSPION@MSNs at 450nm and 550nm, respectively. 68

Figure 3.7 (a) Polarized (I ǁ and I ⊥) emission spectra of EuSPION@MSNs (Ex. 377 nm) in ethanol. (b) r of luminescent magnetic core and silica shell of EuSPION@MSNs in different AMF strength. (Luminescence of shell collected at 450±5 nm and core at 550±5 nm)....... 69

Figure 3.8 (a) Polarized emission spectra of SPION@MSNs-RITC and free RITC dye in ethanol (at the 570 nm emission maximum). The blue band that corresponds to the silica shell only appeared when SPION@MSNs-RITC was measured. (b) r of the silica shell and the doped RITC dye in different AMF strengths collected at 465±5 nm and 570±5 nm, respectively. (Ex: 377 nm) 69

Figure 3.9 (a) Polarized emission spectra of MSNs and PEI-MSNs in ethanol (Ex. 377 nm). (b) r of various MSNs in different AMF strengths. The wavelength with maximum emission peak intensity (MSN=465±5 nm and PEI-MSN=500±5 nm) was used to calculate each r. For each experimental condition, the measurement was repeated five times. 70

Figure 4.1 TEM images of (a) SPIONs and (b) SPION@EXpMSNs (inset: the enlarged SPION@EXpMSNs and a pore size of approximately 30 nm distributed over the particle). Field-dependent magnetization curves (M-H loops) of (c) SPIONs and (d) SPION@EXpMSNs at 300 K and 5 K (inset: magnification of M-H curves from −2500 to 2500 Oe). ZFC/FC modes of temperature-dependent magnetization curves (M-T loops) of (e) SPIONs and (f) SPION@EXpMSNs under an applied magnetic field of 50 Oe. Results from M-H and M-T loops showed that both the core and core@shell nanoparticles possess superparamagnetic characteristics. 105

Figure 4.2 (a) Scheme of the step-by-step conjugation of the β-CD, succinic acid (Suc), and peptide drug melittin (MEL) on the pore wall of SPION@EXpMSNs to obtain SPION@EXpMSN-MEL. (b) TEM images of SPION@EXpMSN-MEL. (c) FT-IR spectra, (d) DLS size distribution, (e) ζ-potential values of SPION@EXpMSNs, SPION@EXpMSN-CD, SPION@EXpMSN-Suc, and SPION@EXpMSN-MEL, respectively. 106

Figure 4.3 (a) Release profile of FITC-MEL from SPION@EXpMSN-MEL+CosA+PLE+PEGAda. (With or without PLE) and bulk temperature rise under different AMF exposure time (AMF was off at 0 min; AMF induction power = 5 kW). (b) Release of FITC-MEL from SPION@EXpMSN-MEL+CosA+PLE+PEGAda under AMF for 30 minutes with different induction power (0 ~5 kW) at an AMF frequency of 375 kHz. The samples were well-insulated from the coil to minimize the heat transfer from the coil. Asterisks (*) indicate significant difference between the SPION@EXpMSN-MEL+CosA+PLE group and other groups (*P*<0.05). (c) Confocal images of the PANC-1 tumor cells treated by the SPION@EXpMSN-MEL+CosA+PLE with no AMF stimulation (**- AMF**) or with AMF stimulation for 30 minutes (**+ AMF)**. The blue-emitting nuclei and red-emitting lysosomes of PANC-1 cells were stained by Hoechst 33342 and LysoTraker Red, respectively. The white arrows show the internalization of FITC- MEL to the lysosomes, indicating that MEL can be triggered and released by an external AMF. 107

Figure 4.4 Cell death induced by SPION@EXpMSN-MEL, SPION@EXpMSN-MEL+CosA, or SPION@EXpMSN-MEL+CosA+PLE with no AMF stimulation (**- AMF** (a) and (b)) or with AMF stimulation for 30 minutes (**+ AMF**, (c) and (d)). (a,c) Fluorescence images of the treated PANC-1 cells with the blue-emitting nucleus and red-emitting dead cells stained by Hoechst 33342 and PI, respectively. (b,d) Statistical analysis of dead tumor cells. FITC indicates the distribution of FITC-MEL. The merged image shows that AMF heating initiated the triggered release of FITC-MEL, which then diffused into the cancer cells and caused significant killing of cancer cells. Asterisk (*) indicates significant difference between the

SPION@EXpMSN-MEL+CosA+PLE group and other groups (*P*<0.05). The control group is cells without nanoparticle treatment. 108

Figure 4.5 CCK-8 assays of PANC-1 cells treated by SPION@EXpMSN-MEL, SPION@EXpMSN-MEL+CosA, SPION@EXpMSN-MEL+CosA+PLE+PEGAda, and free MEL with the same initial concentration (6 μM). Cell viability treated with different MEL-contained core@shell nanoparticles under (a) no AMF treatment and (b) under AMF treatment. Asterisk (*) indicates significant difference between the SPION@EXpMSN-MEL+CosA+PLE+PEGAda group and other groups (*P*<0.05). The control group is cells without nanoparticle treatment. 109

Figure 4.6 *In vivo* antitumor efficiency of the nanocapsules under AMF treatment. (a) Hemolysis assays of free MEL and the nanocapsules (three different groups: SPION@EXpMSN-MEL, SPION@EXpMSN-MEL+CosA, and the SPION@EXpMSN-MEL+CosA+PLE+PEGAda). The nanocapsules (100 mg/L) or free MEL (6 μM) were added into red cell suspension in PBS. The mixtures were incubated at 37 °C and photographed. The control group is cells without nanocapsules treatment. (b) Distribution of the SPION@EXpMSN-MEL+CosA+PLE+PEGAda nanoparticles in the PANC-1 tumor-burden mouse after 6 h of injection (50 mg/kg). The black arrow indicates the tumor site. Note that the nanocapsules accumulated mainly in the tumor tissues. (c) Tumor weights, (d) tumor volumes, (e) histopathological images of the tumor tissues, and (f) histopathological images of the organ tissues of the three different groups after 14 days of intravenous injection of nanocapsules and AMF treatment (30 min, 375 kHz, 5 Kw). Asterisks (*) indicate significant difference between the groups (*P*<0.05). 110

Figure 5.1 (a) Schematic illustration of fluorinated ferrofluids. SPIONs were first coated with a thin layer of silica for attachment of fluoroalkyl silanes. TEM images of (b) SPIONs and (c) SPION@SiO_2, and photo of (c) fluorinated ferrofluids under an application of external magnetic field. Organic solvent = hexane, aqueous solvent = ethanol, and fluorous solvent = HFE7700. 134

Figure 5.2 (a) Photos of the results of using the biphasic approach for attachment of **1** only, **2** only, or **1+2**. Co-addition of **1** and **2** accelerates the phase transfer of SPION@SiO_2 nanoparticles whereas no phase transfer was observed in the absence of **1**. (b) TGA results of silane attachments by using biphasic approach, biphasic + direct coating approach, and biphasic co-addition approach. (c) Schematic illustration of the enhanced total silane attachment via both the silanization between **2** and silanol sites on exposed SPION@SiO_2 nanoparticles surface and the polymerization between silanols of **1** and **2**. 135

Figure 5.3 (a) DLS and (b) FTIR of comparison between the unfunctionalized SPION@SiO_2 nanoparticles (pre) with fluoroalkyl silanes-functionalized by using biphasic approach, biphasic + direct coating approach, and biphasic co-addition approach. 135

Figure 6.1 Synthesis of naphthyl (Nap) group-functionalized MSNs. (a) Thiourea formed by the coupling between the amine and isothiocyanate group. (b) TEM image of MSN-Nap. (c) FTIR characterization of MSN-Nap. (d) UV-Vis spectrum of MSN-Nap. 152

Figure 6.2 (a) DOX release by US-induced change of binding affinity. Probe sonication with a 40% amplitude was used. (b) DOX can be released at a physiological pH (pH 6 and pH 7) by US triggering... 152

Figure 6.3 (a) Characterization by DLS size and Zeta potential showed the successful encapsulation of perfluorohexane (PFH) and attachment of PEG. (b) T_2 measurements by 14T NMR. T_2-%-change of SPION@EXpMSN-PHF-PEG (calculated with respect to the T_2 measured at 37 °C) shows that the gasification of the encapsulated PFH at a temperature of 65 °C generates the two-stage T_2 contrast change.. 153

Figure 7.1 Total HSP generated at each temperature, in a.s.M (arbitrary scale molarity). (A) When kf values are adjusted to 0.10, 0.16, 0.20, and 0.30 min^{-1}, respectively. (B) When kb values are adjusted to 0.12, 0.23, 0.47, and 0.61 min^{-1}, respectively. A higher heating temperature, a larger kf, or a smaller kb do not necessarily give the maximum HSP synthesis, indicating both heating temperature, T, and heating duration time, τ, are crucial parameters to achieve optimal immune activation... 169

Figure 7.2 Total HSP generated at each temperature. Comparison between the chosen kf and kb values. After each rate constant adjustment, a maximum HSP synthesis at 43℃ can be achieved and HSP amount decreases, if the temperature is further raised. kf = 0.15 and kb = 0.62 min^{-1}. a.s.M (arbitrary scale molarity). 169

Figure 7.3 Maximum HSP synthesis is achieved at 43℃ by using either the optimized kf or kb. Results for cytotoxic temperatures (≥43℃) are significantly different from those that are around the body temperature. (A) HSP generation rate, $S\tau, T$, for different heating temperatures using the optimized kb value. a.s.M/min. (B) Heating duration time and the accumulated HSP at different temperatures using the optimized kb value 170

Figure 7.4 Dead cell fraction rate, $dD\tau, Td\tau$, generated by cell death model using the optimized kf value. Even though maximum HSP was obtained at 43℃, when heating temperature is raised, cells still die at a faster rate and the final dead cell fraction increases along with the applied temperatures.. 170

Figure 7.5 Heating duration time, τ, and the accumulated HSP at different temperatures, T, using the optimized kf value. A maximum final accumulated HSP was achieved at 43℃ despite an enhanced HSP generation at higher temperatures when heat is applied initially. a.s.M (arbitrary scale molarity). The dashed line is for the result obtained at body temperature 37℃, as a reference.. 171

Figure 7.6 Maximum HSP synthesis with respect to heating temperature, T, and duration time, τ, using the optimized kf value. Duration time is approximately 100 mins to achieve maximum HSP synthesis at 43℃. Maximum amount of HSP generated at the other temperatures is smaller than the amount achieved at 43℃, even a longer heating time is applied. 171

LIST OF SUPPORTING INFORMATION FIGURES

Figure S 3.1 (a) Polarized and depolarized emission spectra of EuSPIONs with an excitation wavelength of 377 nm. (b) Fluorescence excitation spectra of EuSPIONs monitored at 550 and 600 nm. EuSPIONs were dispersed in hexane for the optical measurements. (c) High-resolution XPS spectra of EuSPIONs and the enlarged Eu and Fe regions of EuSPIONs XPS spectra. 70

Figure S 3.2 (a) Field-dependent magnetization curves (M-H loop) of SPIONs and EuSPIONs at 300K. (b) Temperature-time profile of a cyclohexane solution (4mg/ml) containing EuSPIONs in AMF. (Image: EuSPIONs respond to an external magnetic field.) 71

Figure S 3.3 (a) Field-dependent magnetization curves (M-H loop) of SPION@MSNs and EuSPION@MSNs at 300K. Both M_s values of SPION@MSNs (~46.5 emu/g) and EuSPION@MSNs (~24.4 emu/g) decreased when compared with the M_s value of the respective magnetic core. (b) ZFC/FC modes of Temperature-dependent magnetization curves (M-T loop) of SPION@MSNs and EuSPION@MSNs under an applied magnetic field of 50 Oe (Solid: ZFC, Dots: FC). Blocking temperatures were determined to be 143K and 90K for SPION@MSNs and EuSPION@MSNs, respectively. 71

Figure S 3.4 (a) Characterization of the nanoparticles'sizes using DLS. (b) The positive zeta potential value shows the successful attachment of PEI-MSNs. The nanoparticles were dispersed in deionized water (pH=7). 72

Figure S 3.5 Polarized emission spectra, r, and TEM images of (a) PEI-MSNs, (b) MSNs, (c) SPION@MSNs, and (d) EuSPION@MSNs in ethanol. (Scale bar: 50 nm) (e) r calculated from the silica shell photoluminescence of particles under different induction powers of AMF. (500±5 nm for PEI-MSNs and 450±5 nm for the others) (f) TEM images of SPIONs (Scale bar: 50 nm). Each bar is the average of five measurements. The induction power was set at 5 kW for the "high power" measurements and 2.5 kW for the "low power" measurements. . 73

Figure S 3.6 Comparison of r calculated from the emission spectra of PEI-MSNs (500±5 nm), EuSPION@MSNs (shell: 450±5 nm blue band, core: 550±5 nm green band), SPION@MSNs-RITC (shell: 465±5 nm blue band, doped RITC on shell: 570±5 nm), EuSPIONs in cyclohexane, EuSPIONs in hexane, and dry EuSPION powder (550±5 nm) with different AMF induction powers (5 kW for the "high power" measurements and 2.5 kW for the "low power" measurements). 74

Figure S 3.7 (a) Polarized emission spectra and the r of PEI@MSNs in ethanol measured at temperatures of 25, 35, 50, 60, and 70°C. (b) r started to decrease after reaching a threshold temperature (~ 60°C). The decrease of emission intensity shown on the polarized emission spectra is due to the temperature-dependent quantum yield of luminescence. 74

Figure S 3.8 (a) Polarized emission spectra and the r of EuSPION@MSNs in ethanol measured at ~25°C in the absence of AMF (AMF 0), in the presence of AMF (AMF low and AMF high), and at ~50°C of the pre-heated sample followed by AMF exposure using the high induction power. The difference of r values at different experimental conditions is minimal, indicating Néel relaxation is the only heating mechanism presents at a temperature range of 25°C-50°C.

The induction power was set at 5 kW for the "high power" measurements and 2.5 kW for the "low power" measurements. 75

Figure S 4.1 Temperature-time profile of a cyclohexane solution (3 mg/mL) containing SPION in AMF with a power of 5, 3.75, 2.5, and 1.25 kW. The initial slope (dT/dt) of the profile was used to calculate the specific loss power (SLP) of SPION by equation 1, as shown: 111

Figure S 4.2 Characterizations of CosA. (a) FTIR analysis, and (b) ^{1}H-NMR of CosA. The integrated ^{1}H-NMR spectrum was used to calculate the ACVA attachment on Cos. 111

Figure S 4.3 (a) DLS size distribution and (b) Zeta potential of SPION@EXpMSN-MEL (before PEGAda addition) and SPION@EXpMSN-MEL+PEGAda (after PEGAda addition). 112

Figure S 4.4 Release of PLE from the SPION@EXpMSN-MEL+CosA+PLE+PEGAda nanoparticles, which are capped by PEGAda. The percent of PLE release was calculated by PLE activity in the nanoparticle-suspending solution divided by PLE activity in the nanoparticles ×100%. PLE activity was evaluated by DCFDA hydrolysis assays. 112

Figure S 4.5 Time-dependent release profile of FITC-MEL from SPION@EXpMSN-MEL triggered by free PLE via the catalytic effect. % Release = release efficiency of cleavable MEL. 113

Figure S 4.6 Time-dependent release profile of MEL from SPION@EXpMSN-MEL+CosA+PLE+PEGAda with no AMF stimulation. CosA has a strong inhibitory effect on the toxicity of PLE-contained nanoparticles, leading to the minimized nonspecific cytotoxicity of the SPION@EXpMSN-MEL+CosA+PLE+PEGAda. 113

Figure S 4.7 Cell death of PANC-1 cells treated by SPION@EXpMSN-MEL+PLE (no PEGAda). (a) Fluorescence microscopy images of the cells. (b) Statistical analysis of dead cells. Panels from left to right: PANC-A cells with the blue-emitting nucleus stained by Hoechst 33342, green emission from FITC-MEL, red-emitting dead cells stained by PI, and the merged images. * indicates significant difference between the groups ($P<0.05$). The control group is cells without nanoparticle treatment. 114

Figure S 4.8 Impact of native MEL doses on viability of tumor cell viability. * indicates significant difference between the groups ($P<0.05$). Note that the remaining cell viability at high MEL concentration (6 μM and 12 μM) is due to the limitation of the assay (resulting from background luminescence), which was based on detecting fluorescence. PI staining results showed the complete cell killing at an equivalent MEL concentration (6 μM).......... 114

Figure S 4.9 Viability of the PANC-1 tumor cells treated by released MEL from the nanocapsules (100 mg/L) triggered by AMF (30 min) and native MEL (6 μM, same as the concentration of released MEL from the nanocapsules). Both the nanocapsule-released MEL and the native MEL caused comparable decrease in cell viability, indicating that the remaining succinate group at MEL has no impact on the cell-killing efficiency of MEL. Note that there is no significant difference between the released MEL group and the initial MEL group ($P < 0.05$). 115

Figure S 4.10 Body and organ weights in the mice treated by the nanocapsules. Note that the nanocapsules have no obvious impact on the weights of both the bodies and the tested organs, including the liver, the lung, the heart, the kidney, and the spleen ($P<0.05$). 115

Figure S 5.1 TEM images of SPION@SiO$_2$ nanoparticles with (a) 15 nm silica shell thickness, (b) rough silica surface when only TEOS was reduced, and (c) 5 nm and (d) 3 nm silica shell thickness when both TEOS and ammonia were adjusted. 136

Figure S 5.2 Photos of the ferrofluid attraction to a magnet. SPION@SiO$_2$-**1** fluorinated ferrofluids were synthesized by using the biphasic approach. 136

Figure S 5.3 TGA results of silane attachment via direct coating approach. 137

Figure S 5.4 TEM images of (a) unfunctionalized SPION@SiO$_2$ nanoparticles and (b) fluoroalkyl silanes-functionalized SPION@SiO$_2$ nanoparticles (SPION@SiO$_2$-**[1+2]**) via biphasic approach. 137

Figure S 5.5 (a) SPION@SiO$_2$-**3** in PFCs phase returned to the ethanol phase after 5 min of ultrasonication, indicating the loosely absorbed silanes. SPION@SiO$_2$-**[1+3]** remained in PFCs phase after sonication, suggesting the improved stability of attached **3** on nanoparticles with the assistance of **1**. (b) TGA of comparison between non-chemically bonded/absorbed silanes (negative control) with chemically bonded silane. The unstable silane layer generates a degradation peak at a temperature of 150°C. 138

LIST OF SCHEMES

Scheme 3.1 Two possible scenarios of the nanoparticle rotational motion under AMF exposure. Scenario (a) shows that only the internal magnetization vector moves (Néel relaxation) whereas scenario (b) shows that the entire particle moves (Brownian relaxation). 66

Scheme 4.1 (a) Schematic illustration of the encapsulation of peptide drugs and the AMF-triggered release of the peptide drugs from the pore of a core@shell large pore mesoporous silica nanoparticle (side view and top view). (b) Chemical synthesis steps of the ester linker-peptide drugs, the thermal-sensitive chitosan oligosaccharide barrier, and the PEG porous screen. The large pore in the nanoparticles provides ample space for containing the ester linker (red)-peptide drugs (orange), the thermal-sensitive separating barrier (green), and the enzymes (yellow). The enzymes were trapped by the PEG porous screen (black). The thermal-sensitive barrier is broken by AMF heating and pieces of it escape through the porous screen, allowing the enzymes to catalyze the cleavage of the ester bonds holding the drugs. The drugs are released and diffuse through the porous screen. (b) Systematic order of attachment of the components: red and orange → green → yellow → black. 104

Scheme 5.1 Proposed mechanism of fluoroalkyl silane attachment and phase transfer of SPION@SiO$_2$ nanoparticles. 134

Scheme 6.1 Design of capping systems based on a host-guest inclusion complex with different association constant (K_a). 151

LIST OF TABLES

Table 3.1 r of all measurements in the absence/presence of the AMF. The τ_c of each nanoparticle in the absence of the AMF was calculated. The τ_c of each nanoparticle correlated well with the obtained r. Larger τ_c gives rise to larger r and vice versa. The magnetic vector of a AMF with an oscillation frequency of 375 kHz takes 4.24×10^{-7}s to rotate one radian............... 77

Table 5.1 Different biphasic conditions tested to graft **2** on SPION@SiO_2 nanoparticles. Upper phase contains 1 mL of solvent. Solvent mixture of 3:1: 1: 0.1 Ethanol/ HFE7100/PFH/H_2O or 3:1: 1: 0.1 Ethanol/ HFE7100/H_2O was also tested. The reactions were allowed to be rotated for 1 week. The silanization of **2** with SPION@SiO_2 nanoparticles was monitored by the phase transfer of SPION@SiO_2 nanoparticles, where SPION@SiO_2 nanoparticles remained in the upper phase even with prolonged reaction time (>1week). 138

Table 7.1 List of [HSP]-cell death parameters and values for optimized results...................... 171

ACKNOWLEDGEMENTS

My Ph.D. journey involves many people with whom I would like to share my excitement and feeling of completion of this stage. I am fortunate to be blessed with so many great minds along the journey. I would never have been able to complete this dissertation without their continued support and encouragement.

My deep gratitude goes first to my greatest research advisor Professor Zink, who believed in me and expertly guided me through my graduate education and who shared new research ideas and excitement of discoveries for the past four years. His patience, immense knowledge, and unwavering enthusiasm for science kept me constantly engaged with my research, and his continuous support and personal generosity made my time at UCLA enjoyable and memorable. I will never forget what he has once told me, “You are better than you think you are”. His encouragement and kindness keep me stay motivated and focused to achieve my goals and will always remind me to pay it forward. Special thanks also go to Mrs. Zink, who kindly added “sweetness” to my Ph.D. life with her warm support and homemade desserts.

I would also like to thank my committee members, Professor William Gelbart, Professor Charles Knobler, and Professor Holden Wu for their insightful advice during my Ph.D. study and Professor Yung-Ya Lin for introducing me to the interdisciplinary journey of chemistry.

My sincere thanks also go to Professor Karl Haushalter, who opened my first window into the world of scientific research and who was the best undergraduate research mentor I could ever ask for. I would also like to thank Dr. Johnny Pang who plays an important role in my teaching experience at UCLA and constantly support me on becoming a better educator.

My appreciation also extends to my laboratory colleagues. I would especially like to thank Dr. Chao-Hsiung Hsu, my mentor and long-time friend, for his continuous and selfless help throughout my Ph.D. study. He always reminds me of Albert Einstein's best saying - "Try not to become a man of success, but rather try to become a man of value." He is truly a man of value and a role model of mine. I also like to thank my laboratory friends Dr. Navnita Kumar, Dr. Chia-Jung Yu, Dr. Sayoni Ray, Dr. Jingwen Yao, and Dr. Huimin Yang for their caring and help. My Ph.D. life would have been less colorful without them. I would also like to thank Dr. Bastian Ruehle for his advice and help. All of that remote assistance came all the way from Germany is one of the things that kept me going when I first moved into a new field of research study. I also want to thank all the past and present lab mates: Professor Qilin Yu, Professor Kun Nei, Dr. Wei Chen, Dr. Chi-An Chang, Dr. Ruining Wang, Dr. Chencai Wang, Dr. Sheba Plamthottam, Dr. Yao Cai, Dr. Zhao Li, Tian Deng, Chiao-Yueh Lo, and Jamie Fidel Ruiz-Robles.

In addition, I would like to express my thanks to our research collaborators. For perfluoro-based ferrofluids and polymer-based microdroplet collaborative study, I would like to thank Professor Ellen Sletten and Professor Otger Campàs (UCSB) and their postdoctoral researcher Dr. Heidi L. van de Wouw and Dr. Antoine Vian (UCSB), Ph.D. students Daniel Estabrook and Carlos Gomez (UCSB), and lab technician Yucen Liu (UCSB). For ultrasound-responsive drug delivery collaborative study, I would like to thank Professor Holden Wu and his postdoctoral researcher Dr. Le Zhang and Ph.D. student Xinzhou Li and Qing Dai for their guidance and advice on high-intensity focused ultrasound and magnetic resonance imaging experiments. I would also like to acknowledge Professor Huan-Cheng Chang, Professor Tsyr-Yan Yu, and Dr. Be-Ming Chang for all the works on the study of multiscale cancer molecular imaging for glioblastoma detection and characterization.

I would also like to thank friends I have known during the Ph.D. study. My badminton buddies Dr. Yu-Lin Chang, Jonathan Chun-Hau Chang, Dr. Yu-Jui Chang, Yi-Chi Chan, Bryan Chang, Dr.

Eugene Yu-Chun Kung, Dr. Chih-Ping Charles Wang, Dr. Jack Chih-Chun Wei, Dr. Esther Chun-Pin Chang, Dr. Yu-Yu Lin, Albert Lee, and Alvin Chen. I feel so grateful to have so many good friends to share ups and downs over the past six years. I would also like to thank Dr. Chengzhang Wan, Dr. Lun Liu, Arkaprabha Nishachor Basu, and Hannah Rodriguez. I am glad that we were able to share the journey of our Ph.D. studies and memories together.

Finally, I am deeply indebted to my father, mother, older sister, twin sister, and younger brother for their encouragement and unconditional support. They are my sources of motivation and my "life chargers", who blessed me with a life of joy. I am who I am today because of them.

Chapter 2 is adapted and reprinted with permission from a Perspective paper (*J. Am. Chem. Soc.* 2021, 143, 16, 6025–6036). Copyright 2021 American Chemical Society. Co-author contributions: Lin, F. C., Xie, Y., Deng, T. and Zink, J. I. reviewed the literature and drafted the manuscript. Jeffrey I. Zink was the P.I.

Chapter 3 of the dissertation was adapted and reprinted with permission from Fang-Chu Lin and Jeffrey I. Zink *J. Am. Chem. Soc.* 2020, 142, 5212−5220. Copyright 2020 American Chemical Society. Lin F.-C. designed and performed all the experiments. Jeffrey I. Zink was the P.I.

Chapter 4 of the dissertation is based on the collaborative work with Professor Qilin Yu at Nankai University when he was a visiting scholar at Zink lab. Co-author contributions: Lin, F. C. and Yu, Q. designed and performed experiments and drafted and reviewed the manuscript. Yu, Q. conducted the cell and animal experiments. Jeffrey I. Zink was the P.I.

Chapter 5 is based on collaborative work with Professor Ellen Sletten's group at UCLA and Professor Otger Campàs's group at UCSB. The study aims to optimize *in vivo* mechanical force measurements (*in vivo* mechanosensing) based on microdroplet deformation by the fluorinated ferrofluids that are encapsulated in the microdroplet under the application of an external field. Lin, F. C. designed and performed all the experiments and synthesized new fluorinated ferrofluids. Jeffrey I. Zink was the P.I.

Chapter 6 of the dissertation is based on the collaborative work with Professor Holden Wu's group at UCLA Radiology. The long-term goal of this study is to design and develop a core/shell drug delivery platform where the drug release can be triggered by a high-intensity focused ultrasound (HIFU) and the release process can be monitored by magnetic resonance imaging (MRI) that is coupled with the HIFU. Lin, F. C. designed and performed all the experiments reported in this dissertation. Jeffrey I. Zink was the P.I.

Chapter 7 of the dissertation was adapted and reprinted with permission from Fang-Chu Lin, Chao-Hsiung Hsu, and Yung-Ya Lin. *Int J Nanomedicine*. 2018, 13, 3529-3539. This work is published and licensed by Dove Medical Press Limited. Lin, F.C. proposed and designed the study. Lin, F.C. and Hsu, Chao-Hsiung designed and generated the mathematical model. Jeffrey I. Zink and Yung-Ya Lin were co-P.I.s.

VITA

2021	Inorganic Chemistry Dissertation Award, sponsored by the Charles J. Pederson/E.I. Dupont Graduate Fellowships
2020	Excellence in Research Award, sponsored by Maria Rebecca and Maureen Bellettini
2019 – 2020	Outstanding Graduate Student, sponsored by the George Gregory Fellowship
2017 – 2021	Graduate Student with Professor Jeffrey I. Zink Department of Chemistry and Biochemistry, University of California, Los Angeles
2018 – 2019	Taiwanese Government Scholarship to Study Abroad
2018	ISMRM Magna Cum Laude Merit Award
2016	Hanson-Dow Excellence in Teaching Award
2015 – 2019	Teaching Fellow Department of Chemistry and Biochemistry, University of California, Los Angeles
2015 – 2017	Master Student with Professor Yung-Ya Lin Department of Chemistry and Biochemistry, University of California, Los Angeles
2014 – 2015	Research Technician with Professor Lian-Pin Hwang Department of Chemistry, National Taiwan University Taipei, Taiwan
2013 – 2014	NIH/NSF CARE Fellowship
2012 – 2014	Bachelor of Science Department of Chemistry and Biochemistry, University of California, Los Angeles
2012	NSF STEM Research Scholarship

SELECTED PUBLICATIONS

6. Lin, F.-C., Xie, Y., Deng, T., Zink, J. Magnetism, Ultrasound, and Light-Stimulated Mesoporous Silica Nanocarriers for Theranostics and Beyond. *JACS*, 143, 16, 6025-6036, (2021)

5. Lin, F.-C. and Zink, J. Probing the Interior Nanoscale Heating Mechanism of a Magnetic Core in Mesoporous Silica Drug-Delivery Nanoparticles Using Fluorescence Depolarization. *JACS*, 142, 11, 5212-5220, (2020)

4. Yu, Q., Deng, T., Lin, F.-C., Zink, J. Supramolecular Assemblies of Heterogeneous Mesoporous Silica Nanoparticles to Co-Deliver Antimicrobial Peptides and Antibiotics for Synergistic Eradication of Pathogenic Biofilms. *ACS Nano*, 14, 5, 5926-5937, (2020)

3. Cheng, C.-A., Deng, T., Lin, F.-C., Cai, Y., Zink, J. Supramolecular Nanomachines as Stimuli Responsive Gatekeepers on Mesoporous Silica Nanoparticles for Antibiotic and Cancer Drug Delivery. *Theranostics* 9(11):3341-3364, (2019)

2. Lin, F.-C., Hsu, C.-H., Lin, Y.-Y. Nano-Therapeutic Cancer Immunotherapy Using Hyperthermia Induced Heat Shock Proteins: Insights from Mathematical Modeling. *Int J Nanomedicine*.13, (2018)

1. May, M., Lin, F.-C., Haushalter, K. The Effect of Cassette Order on Gene Expression Knockdown by Triple tRNA-shRNA constructs designed for anti-HIV Gene Therapy (749.6). *FASEB J.* 28, (2014)

Chapter 1 Introduction

In the first part of Chapter 1, I provide a background of the field and an overview of the research work of my dissertation. In the second part of Chapter 1, I provide abstracts of Chapters 2 to 7 in my dissertation.

1.1 Biomedical Applications of Superparamagnetic Iron Oxide Nanoparticles (SPIONs) Core/Shell Mesoporous Silica Nanoparticles

Superparamagnetic iron oxide nanoparticles (SPIONs), with a particle size below the superparamagnetic diameter (~25 nm) and are a single domain, attain a unique property called superparamagnetism.[1] SPIONs generate heating in the presence of an alternating magnetic field (AMF). Owing to their low cost, low toxicity, and unique magnetic properties, SPIONs, in particular Fe_3O_4, have been intensely studied and used in biomedical applications.[2] Magnetic hyperthermia utilizing SPIONs for cancer treatment has been shown to play an effective therapeutic role due to the ability to selectively target cells of interest and induce local heat upon application of AMF while minimizing secondary effects in surrounding healthy tissues.[3] Studies have shown that the localized hyperthermia utilizing SPIONs increases the efficacy of radiation, surgery, and chemotherapeutics.[2,4] In addition, the quick response of SPIONs to the applied magnetic field allows the immediate withdrawal of magnetization by removing the external field and therefore was used to prevent the possible agglomeration after the particles are introduced into biological systems.[5] The inherent magnetic resonance imaging (MRI) contrast of SPIONs was also used to monitor the particle localization and concentration for diagnostic applications.[2]

The mesoporous silica nanoparticles (MSNs) discussed in this dissertation are made by the sol-gel synthesis of silica and the self-assembling surfactant templating of the pores. The original materials were multi-sized aggregates, but further research led to the controllable synthesis of spherical particles with primary sizes of less than 100 nm with mesopores between 2 – 10 nm.[6–8] The ubiquitous MSNs utilized in biomedical studies reported in the literature are spheres containing pores templated by surfactants such as cetyltrimethylammonium bromide or chloride (CTAB or CTAC) with two-dimensional hexagonal (or less commonly radial) pore morphology. The tubular pores are about 2.5 nm in diameter, and one gram of particles has a surface area of about 1000 m^2 and a pore volume of about 1 cm^3. Because typical anticancer drugs have a density of about 1g/cm^3, the carrying capacity can be 100 wt%. However, because of imperfect molecular packing, this upper limit is rarely achieved, and therefore the development of high drug load formulations through optimizing the nanocarriers is necessary. The pore dimensions of MSNs can be readily expanded or contracted. By using organic “pore swelling agents” such as 1,3,5 trimethyl benzene or other organic additives/solvents the pore diameters can be increased by several nm, and by using smaller or larger surfactants the pore diameter can be decreased by a nanometer or increased up to 10 nm or larger. These remarkable properties of MSNs have made them excellent candidates for different biomedical applications.

MSNs that are formed around SPIONs are called SPION core/shell mesoporous silica nanoparticles (SPION@MSNs). They offer unparalleled opportunities for nanotheranostics of cancer. SPION@MSNs exploit their unique features such as surface functionalization and high pore volumes for controlled and targeted drug delivery. The incorporation of an iron oxide nanoparticle core that responses to the AMF further facilitates the on-demand release of drugs on the targeted sites which helps avoid premature drug release that may result in undesired effects on the normal cells. SPIONs can also be coated with a layer of dense silica shell to generate

SPION@SiO_2 nanoparticles, where such dense silica shell not only allows easiness of surface functionalization but also tuning of silica shells with a thickness of 5 – 250 nm.[9]

In light of the importance of SPION@MSNs in the field of cancer therapeutics, many studies in the field have focused on improving on-demand drug delivery and release systems by employing stimuli-responsive nanocaps such as thermosensitive or thermally degradable pore blockers. In Chapter 2 of my dissertation, the advanced works in the field which focus on the design of stimuli-responsive mesopore capping systems will be discussed. As I am compelled by the mechanisms, properties, and applications of core/shell nanoparticles, my dissertation work is largely involved with core/shell systems and can be grouped into five chapters (Chapter 3-7), including (a) analysis of AMF-induced local heating mechanism of SPIONs and SPION@MSNs, (b) design of SPION@MSNs as an AMF heating-activated drug delivery platform, (c) synthesis of new fluorinated ferrofluids using SPION@SiO_2 nanoparticles for *in vivo* mechanosensing, (d) development of ultrasound-responsive SPION@MSNs for controllable drug and release monitoring, and (e) investigation of magnetic hyperthermia-induced cancer immunotherapy. In (a, Chapter 3) a sensitive detecting method utilizing fluorescence depolarization was reported to examine the local AMF-induced heating mechanism of novel luminescent SPIONs in both suspensions and in drug-delivery mesoporous silica nanoparticles for spatial control of therapeutics delivery and release. In (b, Chapter 4) a magnetically activated and enzyme-responsive SPION@MSNs with extra-large pores to deliver and release anticancer peptides on-demand, where the nanoparticles can shrink xenograft tumors in mice without harming the animals. In (c, Chapter 5) we introduced a novel and facile synthesis of ferrofluids in the fluorous phase. While the optimal goal of this study is using the fluorous magnetic droplets to optimize *in vivo* mechanical force measurements based on microdroplet deformation, we envision seeing more applications in theranostics and medical device coating. In (d, Chapter 6) we discussed the design of different MSNs-based or core/shell-based nanoplatforms that respond to the ultrasonic stimulation. We anticipate that the change of surrounding environment of SPIONs core can generate MRI contrast change for monitoring drug delivery and release and advancing precision medicine. In (e, Chapter 7) a predictive mathematical model was developed by integrating thermal-responsive heat shot protein synthesis and cell death to obtain the optimal temperature and exposure time for producing the desirable antitumor immune activation. Magnetic hyperthermia has been used in clinics to treat glioblastoma multiforme cancer, and we foresee the potential of such application in other disease treatments.

1.2 Abstracts of the Dissertation Chapters

1.2.1 Magnetism, Ultrasound, and Light-Stimulated Mesoporous Silica Nanocarriers for Theranostics and Beyond

Stimuli-responsive multifunctional mesoporous silica nanoparticles (MSNs) have been studied intensively during the past decade. A large variety of mesopore capping systems have been designed, initially to show that it could be done and later for biomedical applications such as drug delivery and imaging. On-command release of cargo molecules such as drugs from the pores can be activated by a variety of stimuli. This paper focuses on three noninvasive, biologically usable external stimuli: magnetism, ultrasound, and light. We survey the variety of MSNs that have been and are being used and assess capping designs and the advantages and drawbacks of the nanoplatforms' responses to the various stimuli. We discuss important recent advances, their basic mechanisms, and their requirements for stimulation. On the basis of our survey, we identify fundamental challenges and suggest future directions for research that will unleash the full potential of these fascinating nanosystems for clinical applications.

1.2.2 Probing the Local Nanoscale Heating Mechanism of a Magnetic Core in Mesoporous Silica Drug-Delivery Nanoparticles Using Fluorescence Depolarization

In the presence of an alternating magnetic field (AMF), a superparamagnetic iron oxide nanoparticle (SPION) generates heat. Understanding the local heating mechanism of a SPION in suspension and in a mesoporous silica nanoparticle (MSN) will advance the design of hyperthermia-based nanotheranostics and AMF-stimulated drug delivery in biomedical applications. The AMF-induced heating of single-domain SPION can be explained by the Néel relaxation (reorientation of the magnetization) or the Brownian relaxation (motion of the particle). The latter is investigated using fluorescence depolarization based on detecting the mobility-dependent polarization anisotropy (r) of two luminescence emission bands at different wavelengths corresponded to the europium-doped luminescent SPION (EuSPION) core and the silica-based intrinsically emitting shell of the core−shell MSN. The fluorescence depolarization experiments are carried out with both the free and the silica-encapsulated SPION nanoparticles with and without application of the AMF. The r value of a EuSPION core-mesoporous silica shell in the presence of the AMF does not change, indicating that no additional rotational motion of the core−shell nanoparticles is induced by the AMF, disproving the contribution of Brownian heating and thus supporting Néel relaxation as the dominant heating mechanism.

1.2.3 Self-Contained Nanocapsules Carrying Anticancer Peptides for Magnetically Activated and Enzyme-Cleaved Drug Delivery

A self-contained nanocapsule for nonspecific cytotoxic anticancer drugs delivery and release activated by an enzyme and an alternating magnetic field (AMF) is introduced. This specific prodrug-like drug delivery platform is based on an esterase, an oligomer-based separating barrier, and ester-linked anticancer peptides melittin encapsulated together in the enlarged pore spaces of the mesoporous silica nanoparticles. A superparamagnetic iron oxide nanoparticle core embedded in the center acts as a nanoheater to stimulate a cascade drug release. Each pore space was designed as a reaction nano-vial for the activation of the drug release when the solution inside of the nano-vial is heated. By employing a thermo-responsive separating barrier as a shield of the peptide drug as well as a separator between the ester-containing peptides and the esterase, the nonspecific cytotoxic effect of the drug and off-target drug release are avoided because the drugs remain inactive in the absence of AMF stimulation. When AMF heating actuates the removal of the separating barrier and exposes the peptide drugs to the enzymes, drugs release can be activated. In vivo antitumor experiments further revealed that the nanocapsules exhibited excellent biocompatibility and high tumor-targeting/inhibiting efficiency. The selected esterase, which is in close proximity to the ester-containing peptide drug, efficiently cleaves the ester bonds, thereby causing a catalytic release of peptide drugs and intensified anticancer efficacy.

1.2.4 A Facile Method to Synthesize Fluorinated Ferrofluids for Measuring Mechanics in Living Systems

Fluorinated ferrofluids were prepared through a biphasic ligand attachment method, where the covalent grafting of perfluoro ligands onto the colloidal SPION@SiO_2 nanoparticles enables phase transfer of colloids from an aqueous phase to a perfluorocarbons (PFCs) oil phase. Two different perfluoroalkyl silanes, perfluorodecyltriethoxysilane (PFDTES) and perfluoropolyether (PFPE), with molecular weight (MW) differ by more than 10 times were used as surfactants in this system. We explore chemistry-material relationships between the surfactants and nanoparticles and optimize the silanization process to achieve perfluoro-functionalized SPION@SiO_2 nanoparticles that are non-ionic and are highly soluble in the PFCs oil. It was found that the low-MW PFDTES pre-grafted on the SPION@SiO_2 nanoparticles can assist with the attachment of high-MW PFPE (MW= 4000-8000 g/mol) via silanol polymerization, resulting in a nanoparticle total silane attachment of more than 70 w%. This unique approach can be used for the attachment of a variety of high-MW silanes for extended applications in biomedical fields.

1.2.5 Drug Delivery by Ultrasound-Induced Binding Affinity Change

Superparamagnetic Iron oxide nanoparticles (SPIONs) have been intensely studied and used in biomedical applications. SPIONs are excellent T_2 contrast agents for magnetic resonance imaging (MRI), one of the leading imaging modalities in cancer diagnostics. Recent advances in MRI-guided high-intensity focused ultrasound (MRgHIFU) show promises in the drug delivery platforms where the release of drugs can be triggered by ultrasound (US) energy. In this study, we demonstrated that the anticancer drugs in mesopores of SPION@MSNs can be blocked via the binding between host and guest, where uncapping events occur in response to the US-induced lowering of binding affinity, leading to anticancer drug release.

1.2.6 Nano-Therapeutic Cancer Immunotherapy Using Hyperthermia-Induced Heat Shock Proteins: Insights from Mathematical Modeling.

Nano-therapeutic utilizing hyperthermia therapy in combination with chemotherapy, surgery, and radiation are known to treat various types of cancer. These cancer treatments normally focus on reducing tumor burden. Nevertheless, it is still challenging to confine adequate thermal energy in a tumor and obtain a complete tumor ablation to avoid recurrence and metastasis while leaving normal tissues unaffected. Consequently, it is critical to attaining an alternative tumor-killing mechanism to circumvent these challenges. Studies have demonstrated that extracellular heat shock proteins (HSPs) activate antitumor immunity during tumor cell necrosis. Such induced immunity was further shown to assist in regressing tumors and reducing recurrence and metastasis. However, only a narrow range of thermal doses is reported to be able to acquire the optimal antitumor immune outcome. Consequently, it is crucial to understand how extracellular HSPs are generated. In this work, a predictive model integrating HSP synthesis mechanism and cell death model is proposed to elucidate the HSP involvement in hyperthermia cancer immune therapy and its relation with dead tumor cells. This new model aims to provide insights into the thermally released extracellular HSPs by dead tumor cells for a more extensive set of conditions, including various temperatures and heating duration time. Our model is capable of predicting the optimal thermal parameters to generate maximum HSPs for stimulating antitumor immunity, promoting tumor regression, and reducing metastasis. The obtained nonlinear relation between extracellular HSP concentration and increased dead cell number, along with rising temperature, shows that only a narrow range of thermal dose is able to generate the optimal antitumor immune result. Our predictive model is capable of predicting the optimal temperature and exposure time to generate HSPs involved in the antitumor immune activation, with a goal to promote tumor regression and reduce metastasis.

1.3 References

(1) Estelrich, J.; Escribano, E.; Queralt, J.; Busquets, M. A. Iron Oxide Nanoparticles for Magnetically-Guided and Magnetically-Responsive Drug Delivery. *Int. J. Mol. Sci.* 2015, 16 (4), 8070–8101.

(2) Knežević, N. Ž.; Ruiz-Hernández, E.; Hennink, W. E.; Vallet-Regí, M. Magnetic Mesoporous Silica-Based Core/Shell Nanoparticles for Biomedical Applications. *RSC Adv.* 2013, 3 (25), 9584.

(3) Banobre-Lopez, M.; Teijeiro, A.; Rivas, J. Magnetic Nanoparticle-Based Hyperthermia for Cancer Treatment. *Reports Pract. Oncol. Radiother.* 2013, 18 (6), 397–400.

(4) Gordon, R. T.; Hines, J. R.; Gordon, D. Intracellular Hyperthermia - a Biophysical Approach to Cancer Treatment via Intracellular Temperature and Biophysical Alterations. *Med. Hypotheses* 1979, 5 (1), 83–102.

(5) Arruebo, M.; Fernández-pacheco, R.; Ibarra, M. R.; Santamaría, J. Magnetic Nanoparticles for Drug Delivery. *NanoToday* 2007, 2 (3), 22–32.

(6) Yanagisawa, T.; Shimizu, T.; Kuroda, K.; Kato, C. The Preparation of Alkyltrimethylammonium-Kanemite Complexes and Their Conversion to Microporous Materials. *Bulletin of the Chemical Society of Japan*. 1990, pp 988–992.

(7) Beck, Jeffrey, S.; Chu, Cynthia, T.-W.; Johnson, Ivy, D.; Kresge, Charles, T.; Leonowicz, Michael, E.; Roth, Wieslaw, J.; Vartuli, James, C. Synthetic Porous Crystalline Material: Its Synthesis and Use. WO/1991/011390, 1991.

(8) Chiola, V.; Rirsko, E. J.; Vanderpool, C. D. Process for Producing Low Bulk Density Silica. US Patent 3556725, 1971.

(9) Kembuan, C.; Saleh, M.; Rühle, B.; Resch-Genger, U.; Graf, C. Coating of Upconversion Nanoparticles with Silica Nanoshells of 5-250 Nm Thickness. Beilstein J. *Nanotechnol.* 2019, 10, 2410–2421.

Chapter 2 Magnetism, Ultrasound, and Light-Stimulated Mesoporous Silica Nanocarriers for Theranostics and Beyond

Chapter 2 is reproduced with permission from *J. Am. Chem. Soc.* 2021, 143, 16, 6025–6036. Copyright 2021 American Chemical Society. Co-author contributions: Lin, F. C., Xie, Y., Deng, T. and Zink, J. I. reviewed the literature and drafted the manuscript. Jeffrey I. Zink was the P.I.

Table of Content Figure

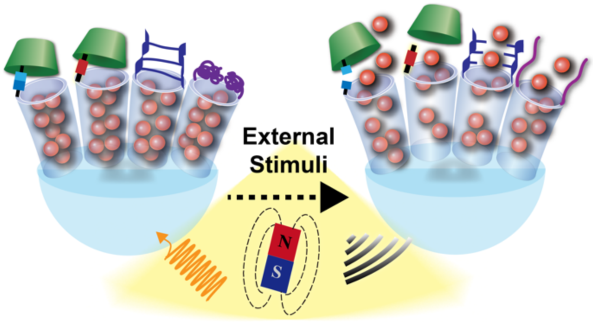

2.1 Introduction

Chemical and materials research involving mesoporous silica has developed rapidly in the past decade, driven initially by interest in this new type of structurally ordered nanomaterial and accelerated by the potential applications in catalysis and especially biomedical drug delivery. Most of the materials can be synthesized on the benchtop at moderate temperatures, and the resulting silica structures can be readily derivatized with a huge variety of organic, inorganic and biomolecules that have functions varying from supramolecular nanomachines to cancer cell targeting ligands. In this Perspective we focus primarily on mesoporous silica nanoparticles (MSNs), which are made by the sol-gel synthesis of silica and the self-assembling surfactant templating of the pores. The original materials were multi-sized aggregates, but further research ultimately led to controllable synthesis of spherical particles with primary sizes of less than 100 nm with mesopores between 2 – 10 nm in diameter **Figure 2.1a**).[1,2] The attractive features of MSNs, such as porous frameworks and surface functionality, allow various types of fabrication methods and have led to advanced applications of MSNs in multiple fields.[3–7] Various advanced architectures of MSNs such as large-pore MSNs (LPMSNs, **Figure 2.1b**), hollow MSNs (HMSNs, **Figure 2.1c**), or core-shell MSNs (**Figure 2.1d**) have also gained significant interest for multifunctional biomedical purposes.[1,8]

Over a decade ago during the initial excitement about all things nano, (popularized by the title of Feynman's lecture "There's Plenty of Room at the Bottom"),[9] there was great fascination and interest in supramolecular structures, especially in the synthesis and properties of molecules in molecules such as rotaxanes that could function as nanomachines.[10,11] Around the same time, self-assembled and templated porous nanostructures described above also became popular. It was a logical extension to try to put molecules in the pores and cap the pores with nanomachines. Early studies involved materials synthesis, emptying the self-assembled surfactants from the pores, and filling them with molecules from a solution. Examples include proteins,[12] hydrophobic drugs,[13] and fluorescent dyes.[14,15] Alternatively, the desired molecules could be dissolved in the initial sol used in the synthesis and become incorporated during the templating and gelation process.[16] Many early studies used macroscopic aggregates or thin films for luminescent molecules, polymers, or living cells encapsulation.[17–19]

The next challenge required not only filling the pores in the nanoparticles with molecules such as drugs but also trapping them in the pores with controllable nanomachine caps.[20–23] The pores essentially became tiny capped bottles in the particles; the challenge was to controllably cap the particles and uncap them at will. Today there are literally hundreds of types of caps designed to be specifically opened by a chosen stimulus.[22–24] For biomedical drug delivery applications, the stimuli must be biocompatible and feasible to control.[25] How can a particle deep in a tumor in the interior of an organism be controlled? Two classes of control have been developed: autonomous chemical stimulus that exists at the desired biological site (such as pH change in a tumor or cancer cell), and external stimuli that can non-invasively penetrate the body and tumor and open the cap.

The emphasis of this Perspective is on external control of nanoparticles potentially useful for medical therapy. We first discuss recent developments in trapping and releasing molecules from the pores using biocompatible external stimuli and some of the advanced capping systems of MSN carriers designed for the three types of stimuli — magnetism, ultrasound, and light (**Figure 2.2**). Light stimulation has the best spatial resolution but the poorest tissue penetration; magnetism has great tissue penetration but the poorest resolution. The major application of interest is drug delivery, but we will also discuss briefly diagnosis and targeting. The clinical relevance of these stimuli will also be highlighted. We then provide our insights on the future directions the field could take to advance biomedical applications and accelerate clinical translation of MSNs-based drug delivery platforms.

2.2 Alternating Magnetic Field Control of Nanocaps

Magnetic fields have the best penetration of tissue of the three external stimuli discussed in this Perspective. Superparamagnetic iron oxide nanoparticles (SPIONs) become heated in the presence of an alternating magnetic field (AMF). Thus, a material such a SPION in the core of a MSN (SPION@MSN, **Figure 2.1d**) can be stimulated by AMF to activate thermosensitive caps and release drugs. The SPION core is able to raise the local temperature in the vicinity of SPION, rendering rapid heat distribution on the SPION@MSN surface that activates a thermo-sensitive capping system without overheating the particles' surroundings. Magnetic heating of SPIONs is caused by Néel and Brownian relaxation; the former involves the internal orientation of the magnetic moment whereas the latter is related to the physical rotation of the particle as a whole.[26] Though the Néel and Brownian relaxation coexist, Neel relaxation is the dominant contributor to the heating.[27] SPIONs by themselves in AMF have shown great promise for site-selected hyperthermia treatment of tumors.[28] In this section, we will focus our discussion on the key advances in AMF-mediated uncapping of SPION@MSNs for selective and on-command drug release.

2.2.1 AMF-Stimulated Supramolecule-Based Nanocaps

In 2010, the first in vitro study of SPION@MSNs reported their capability of effectively actuating supramolecular nanovalves and releasing anticancer drugs upon exposure to an AMF (**Figure 2.3**).[29] The nanovalve consists two parts, an alkylammonium thread attached on the particle surface and a cucurbit(6)uril ring, where cucurbit(6)uril interacts with the thread via the formation of a pseudorotaxane stabilized by the hydrogen-bonding and London forces. Because the thread-ring binding decreases with increasing temperature, magnetic heating of the core caused release of the ring and triggered drug release from the pores. The feasibility of using this magnetically activated system to release chemotherapy drug doxorubicin (DOX) for inducing apoptosis in a breast cancer cell line demonstrated that AMF-responsive delivery systems hold significant promise for on-demand anti-cancer drug release. A recent AMF-activated nanoplatform was further designed to simultaneously deliver multiple drugs. AMF-responsive SPION@MSNs were co-assembled with LPMSNs loaded with the antimicrobial peptide melittin (MEL).[30] The localized heating from the SPION was responsible for the activation of the caps and release of the antibiotic ofloxacin (OFL) encapsulated in the mesopores of SPION@MSNs. This delivery platform was not only AMF-sensitive but also respond to pathogen cells, realizing co-releasing of multiple drugs (large-molecular-weight MEL and small-molecule-weight OFL) to treat multidrug resistance (MDR) of pathogens. In addition, the delivery platform can achieve high-efficiency targeting with pathogenic biofilms under the stimuli of AMF heating and pathogens. The dual drug-loaded co-assemblies were shown to have a strong capacity to thoroughly eradicate in vivo pathogenic biofilms from implants and efficiently prevented host tissue infection and inflammation.

Another example of an AMF-responsive nanocap is based on attaching a bulky adamantane-β-cyclodextrin (β-CD) moiety to the surface of SPION@MSN via a thermally reversible Diels-Alder reaction (**Figure 2.4**).[31] The dissociation of the bulky gatekeeper, followed by the unblocking of pores, was stimulated by a heat-triggered cycloreversion under an AMF. The test-tube experiments showed that a large amount of fluorescein was released upon local heating from 37 °C to 65 °C, whereas almost no leakage was observed at 37 °C. Another advance was to use an AMF trigger to tune drug dosage to realize temporal, and spatial control of therapeutics delivery.[32] In this study, an adamantane-β-CD complex was conjugated on the SPION@MSN via an aliphatic azo-containing compound. Cleavage of the azo bond under AMF heating triggered the release of cargo DOX. The cargo could be released in stepwise manner by applying multiple sequential exposures to AMF, and the viability decrease of pancreatic carcinoma cells (PANC-1) was well-correlated with increase of the AMF exposure, thereby suggesting their potential use for advancing precision medicine.

2.2.2 AMF-Stimulated Polymer-Based Nanocaps

The use of thermolabile azo bonds in the design of an AMF-responsive polymeric capping system was first established by incorporating the azo moieties into the backbone of the linear polymer polyethylene glycol (PEG).[33] Biocompatible and thermo-degradable azo-PEG was covalently conjugated to the surface of SPION@MSNs. The C-N bonds of the azo moieties were cleaved site-specifically upon AMF exposure, resulting in the release of N_2 gas, the generation of lower molecular weight fragments, and most importantly the release of the entrapped cargo. Neither the polymeric capping system nor the generated degradation products exhibited cytotoxicity on NIH 3T3 fibroblast cells, indicating the feasibility of using this polymer-based capping system for biomedical applications.

In addition to bond breaking of caps for drug delivery, thermo-responsive phase changing polymers have been used. Poly(N-isopropylacrylamide) (PINIPAM) can switch reversibly from a hydrophilic, linear state to a hydrophobic, globular state when heated above the lower critical solution temperature (LCST) of 32 ˚C. Taking advantage of this property, a thermo-responsive PINIPAM-based copolymer cap was designed to simultaneously administer several drugs for improving the treatment efficiency against MDR cancers.[34] The copolymer was made by cross-linking PINIPAM with branched polyethyleneimine (PEI) chains that retain negatively charged proteins by electrostatic or hydrogen bonding interactions. The attached protein on the hydrated polymer aids in blocking the release of small molecules trapped inside the pores. When the temperature is raised above LCST under AMF, the PINIPAM phase transition causes polarity inversion; the tridimensional polymeric network change was followed by the subsequent release of fluorescein from the mesopores, and the release of proteins attached into the polymer branches. Such dual release, accompanied by the synergic effect associated with hyperthermia, improves the efficacy of antitumor therapy. The next step was to generate PNIPAM-based nanocaps with a LCST that is suitable for in vivo drug delivery applications. Studies have shown that different phase-transition temperatures (38 – 44 ˚C) of the copolymer can be obtained by adjusting the amount of hydrophilic co-monomer, thus a more clinically feasible capping system can be achieved.[35]

2.2.3 AMF-Stimulated Biomolecule-Based Nanocaps

Given the importance of biocompatibility and high cellular uptake of nanoparticles for efficient intracellular drug release, many efforts have been made to develop biomolecule-based capping systems. Ideal candidates are biocompatible and biodegradable peptides that can self-assemble at physiological temperature to block the pore openings and disassemble at elevated temperature to open the pore entrance. Such self-assembling peptides were shown to successfully trap the anticancer drug DOX, and the temperature-sensitive disassembling process efficiently responded to AMF for controlled drug release, resulting in efficient killing of PANC-1 cells.[36]

DNA, which undergoes a sharp melting transition (dehybridization process) that can be tuned in the range of physiological temperature through changes in the surface density of the oligonucleotides on the nanoparticles and the chain length, is useful as a cap for drug delivery platforms.[37,38] Single-stranded DNA-modified magnetic silica particles' mesopores can be capped via the hybridization with magnetic crystals conjugated with complementary DNA sequence.[39] Owing to the presence of magnetic species, these MSNs were capable of heating the surrounding media to hyperthermia level (47 ˚C), inducing dehybridization, and releasing a model drugs fluorescein in an on and off sequence due to the reversible dehybridization/hybridization of the DNA. In another study, double-stranded DNA was employed to gate the pore entrance of SPION@MSN and to deliver the anticancer drug DOX.[38] In this study, In vitro experiments were conducted to show that the SPION@MSN-DNA complex could release DOX fast at 50 ˚C via the denaturation of DNA capping chains triggered by the AMF heat. The low cytotoxicity of the nanoparticle complex and the effective cell uptake of the particles in murine breast cancer 4T1 cells was also demonstrated, suggesting their potential in biomedical applications. Future work using oligonucleotide-based AMF-responsive capping systems should focus on tuning the critical release temperature, i.e. DNA melting temperature, by changing the length of single-stranded DNA oligonucleotides.[40]

While treatment by combining hyperthermia and controlled drug delivery was shown successfully in both in vitro and in vivo studies, to make such systems clinically applicable, careful operation is required to ensure that the desired temperature is reached, but not exceeded, and that healthy tissues injury is minimal. The safety limit for humans is that the product $(\mathrm{H} \times \mathrm{f})$ of magnetic field amplitude (H) and frequency (f) should not exceed the value $5 \times 10^9 \mathrm{Am}^{-1}\mathrm{s}^{-1}$. Therefore, it is necessary to mitigate the risks of tissue overheating that is associated with necrosis, where necrotic tissues release cellular contents into the extracellular space and promote tumor progression. To address these concerns and advance the design of hyperthermia-based nanotheranostics, a recent study implemented dual-luminescent SPION@MSN to investigate the local heating mechanism of a SPION in suspension and in a MSN and determined that the Néel relaxation was the dominant contributor to the heating of a SPION@MSN.[27] In another study, the MSN interior temperature was measured optically and was shown to have a much higher temperature than that of the bulk solution during AMF exposure.[41] These results all suggest high promise of AMF-stimulated drug delivery in biomedical applications, especially for selective and on-command drug release.

2.3 Ultrasound Control of Nanocaps

The tunable dual thermal and/or mechanical effects of ultrasound can be used to stimulate a wide variety of nanocap designs and produce highly versatile and advantageous methods for controlling MSN-based drug delivery systems. The heat produced by ultrasound can be applied to the thermo-sensitive capping systems discussed in the previous section, and the additional mechanical effects can be applied to uncap pores via other ultrasound responsive mechanisms such as bond breaking. Ultrasound can be carefully modulated by tuning frequency, power density, duty cycles, and exposure time.[42] The depth of penetration and potential cavitation can be tuned by changing the frequency. The intensity of the ultrasound plays a major role in not only the cavitation effects but also the thermal effects.[42] By focusing ultrasound waves into a small volume – the focal point – which is usually several cubic millimeters,[43] high intensity focused ultrasound (HIFU) with an intensity of ≥ 3 W/cm^2 and deep tissue penetration capability offers a noninvasive method for nanoparticle-enabled delivery of drugs. HIFU can locally trigger cargo release at a specific location with little or even no side effects because its intensity is strong only at the focal point. Current therapeutic applications utilize both the thermal effects of HIFU, which benefit from the rapid temperature rise at HIFU focal point to induce coagulative necrosis, and mechanical (cavitation) effects that break chemical bonds.[44] Combined with imaging methods such as low frequency ultrasound or magnetic resonance imaging (MRI), HIFU is able to ablate the tumor tissue precisely with minimal invasion and has been used to treat solid tumors such as prostate, rectal, pancreatic, breast, bladder, brain, and bone.[44,45] In addition, HIFU can temporarily disrupt the blood–brain barrier (BBB) and help the therapeutic agents into the brain.[46] In the following sections, we will discuss how ultrasound responsive capping systems control the pore entrance accessibility and advance the cargo delivery systems and the development of nanotheranostics.

2.3.1 Ultrasound-Stimulated Supramolecular-Based Nanocaps

Cavitation is one of the major mechanical effects produced by ultrasound. It depends on a broad variety of parameters such as ultrasound frequency and the presence of bubbles or cavitation nuclei.[42] It was demonstrated that MSNs can be drug carriers and inertial cavitation nuclei at the same time; the mechanical strain induced by the acoustic cavitation can help enhance and control the drug release.[47,48] For example, β-CD-capped MSNs with hydrophobic internal channels were designed for the delivery of the hydrophobic cancer drug paclitaxel (PTX), where the loaded hydrophobic PTX and the gas stored in the hydrophobic mesopores acted as an ultrasonic cavitation nuclei.[48] In addition to the excellent synergistic effect in vitro and the high biocompatibility in vivo, it was demonstrated that this delivery platform could significantly inhibit the 4T1 mammary tumor growth by more than 3-fold when compared with the MSNs without hydrophobic modification.

Thermal effects generated in biological tissues by ultrasound were also utilized by dibenzo-crown ether periphery nanovalves on SPION@MSNs for ultrasound-responsive drug delivery and tumor cell imaging. The mesopores were blocked by the interaction between cations (Na^+ or Cs^+) and the oxygen-rich, electronic donating crown ether's ethylene glycol chains.[49] The blocking agents dissociated from dibenzo-crown ethers by the energy gained from ultrasound, leading to 3-fold enhanced DOX release. The in vitro biological evaluation revealed that the nanoparticles are biocompatible and are taken up by L929 normal fibroblast cells. The embedded SPIONs caused the spin-spin T_2 relaxation time changes; the attained dark contrast on the MRI images further demonstrates their potential use as theranostic agents.

HIFU can be guided by an imaging technique such as MRI or low-frequency ultrasound imaging.[45,51] Due to this attractive feature, many multifunctional nanoparticles have been developed to realize both diagnostic and therapeutic outcomes. For example, a theranostic approach that can control and monitor drug release using magnetic resonance-guided high intensity focused ultrasound (MRgHIFU) was developed (**Figure 2.5**).[50] In this method, a SPION@MSN structure was used: the mesoporous silica shell provides large pore volume for cargo storage and delivery and the water access to the paramagnetic SPION core changes after drug release, leading to T_2 MRI contrast change. The HIFU-responsive cap containing an aliphatic azo-containing compound was attached to the nanoparticle surface and control drug release. Using this design, the image contrast changes can be used to measure cargo release and the therapeutic efficacy. The process was visualized in human pancreatic cancer cells. It brings possible applications of assessing the precision of HIFU-triggered drug release, and drug dose painting.

2.3.2 Ultrasound-Stimulated Polymer-Based Nanocaps

The cavitation caused by ultrasound can also be applied on MSNs coated with polymer-based capping systems. The synergy between MSNs and polymer was shown to enhance the ultrasonic susceptibility and reliability of ibuprofen drug release,[52] where the convection increase due to the effects of cavitation increased the diffusion rate of the drug and facilitated faster drug release. Additionally, high intensity ultrasound can cause irreversible biological changes such as cancer cell eradication and is capable of inducing chemical change for cargo release.[53] For example, the ultrasound stimulation can result in a change of polymer conformation and the subsequent release of DOX in LNCaP tumor cells (**Figure 2.6**). By further coating the polymer-grafted MSNs with a PEI layer, it can enhance nanoparticle internalization into Decidua Mesenchymal Stem Cells (DMSNs), where DMSNs acted as transporters to the tumor tissue.[54] Such engineered nanoparticles were shown to release Calcein-AM in vivo after 10 min of ultrasound application and the DOX-loaded PEI-coated nanoparticles could be retained in DMSNs for 6 days and exhibited high migratory capacity toward the tumor homogenate, leading to the effective uptake of DMSNs. The release of DOX, which only occurred when the platform is exposed to ultrasound, resulted in the reduction of N-Nitroso-N-methylurea cell viability. Future approaches of polymeric delivery systems should focus on the enhancing the efficiency of particle internalization into cells for better treatment efficacy and clinical applications.

HIFU is being used in the clinic. There are several designs of capping systems that are responsive to HIFU that demonstrate promising potential for applications. A reversible ultrasound-responsive hybrid nanocarrier based on alginate-coated MSN was designed to utilize mechano-responsive chemical bond breaking and reforming of the capping systems for realizing HIFU-controlled cargo release.[55] It was demonstrated that 100% of the cargo can be released after HIFU irradiation with low in vitro cytotoxicity. In another study, polydopamine (PDA) coated MSNs were shown to release DOX due to ultrasonic cavitation, where the pulsatile drug release could be controlled by switching the HIFU on and off.[56] PEG was also designed to cap the pore in a biofriendly MSN drug delivery platform for MRgHIFU.[57] The PEG-coated nanocarriers enabled the HIFU-triggered release of FDA approved gadolinium-based contrast agent, $Gd(DTPA)^{2-}$ without hyperthermia because cavitation induced by HIFU could lead to PEG cleavage and degradation. With MRgHIFU, real time spatial- and temporal-control of cargo release in three-dimensional space can be realized. The study further demonstrated that the dose of cargo release was correlated to HIFU stimulation times and power levels. The significance of this platform for future biomedical applications was supported by ex vivo results demonstrating that MRgHIFU achieved selective stimulation spatially in the presence of nanoparticles. This platform is promising for precise therapy that delivers drugs to a specific tissue in real time.

2.4 Light Control of Nanocaps

Light energy is an important stimulus for biomedical applications. An important advantage of light over magnetism and ultrasound is its high spatial resolution, but a limiting disadvantage is its low penetration depth into tissue. The most important growth area in current photo-stimulated drug delivery research involves the use of low energy light (red and near infrared (NIR)) because of its deeper penetration depth compared to that of visible and UV light. This topic will be discussed in more detail below. Important medical applications not involving drug release and thus not discussed here include photodynamic therapy via production of reactive oxygen species, [58] and photo-induced hyperthermia kill cells by heating.[59]

The six most important processes used to stimulate drug delivery using light are a) photochemical bond cleavage (photodissociation), b) supramolecular bond cleavage (mechanical bond cleavage), c) photoisomerization, d) photo-induced redox reactions, e) photoinduced acidity changes (photoacids) and f) photo-induced thermolysis. In most cases, a large molecule or polymer is held in place over MSN pore openings and the photon causes it to move away from the pore by cleaving a bond holding it in place, by changing the bonding constant holding a supramolecular structure together, by causing a structural change in the molecule itself, or by local heating. [94-100] (Purely photothermal effects are similar to those caused by magnetic and ultrasonic heating that were discussed in the previous two sections.) Photoexcitation of molecules that act as "transducers", such as photo reductants and photo acids, can in turn activate pore unblocking, for example by breaking disulfide bonds by reduction or pH-sensitive supramolecular bonds by acidification.

2.4.1 NIR Light-Responsive Nanocaps

UV and visible light can provide enough energy to break chemical bonds in molecules, but they suffer from poor penetration depth and may induce tissue injury. NIR light can minimize the scattering from the tissue and achieve centimeter penetration depth. The penetration of the laser beam is deepest when the wavelength of laser is between 700 – 1300 nm, which is called the biological window.[60,61] The penetration depth of the laser beam in the tissue also depends on the extinction coefficient of different components in the tissues. Although the penetration depth of

NIR light is higher than that of UV and visible light, the photon energy of NIR light is too low to stimulate the cleavage of most chemical bonds or excite photo-isomerization reactions.

Two methods of overcoming the energy limitation are currently being studied: coherent two-photon absorption, and sequential multiphoton upconversion. The former requires specific types of molecules with large two-photon absorption cross-sections,[62] and the latter requires designed combinations of IR-absorbing ions or molecules.[63] The result of the two-photon absorption process is excitation to an excited electronic state, with twice the energy of the individual photons, that can cause bond cleavage and photo-isomerization. The advantages of two-photon excitation are that it can penetrate deeper in tissue with low scattering losses, inflict lower damage on healthy cells, and have high spatial resolution. However, the efficiency of two-photon absorption is low and varies with the square of the light intensity; pulsed lasers with high power densities are necessary for this process.[64] Despite these physical constraints, examples of two-photon energy for stimulating cargo release caused by directly cleaving the bonds between nanoparticles and capping molecules have been reported using coumarin derivatives as the linkers.[65, 66] Additionally, molecules with high two-photon cross sections can act as "transducers" by transferring energy to another molecule that in turn causes cargo release. For example, a fluorophore can be activated by two-photon absorption and transfer energy by Förster resonance energy transfer (FRET) to an active component, functionalized azobenzene derivatives that are photo-regulators of mass transport in pores.[67] They were attached in the vicinity of two-photon responsive fluorophores with a high two-photon absorption cross sections. FRET caused photo-isomerization of azobenzene, leading to cargo release (**Figure 2.7**).[68]

A photo-redox-active molecule (one that becomes a strong reducing agent in an excited electronic state) can be excited by two-photon energy and reduce disulfide bonds in a linker holding a nearby capping molecule and thereby releasing it. A photoreduction system using a photo-transducer with high two-photon cross-section released electrons to reduce disulfide bonds holding cyclodextrin caps on MSNs when activated by two-photon absorption.[69] In this design, EDTA was used to inhibit the back electron transfer from the oxidized photo-transducer. After pulsed 800 nm laser excitation, the cleavage of disulfide bonds released Rhodamine B cargo. Another photo-redox example also involving photocleaving disulfide bonds for releasing anti-cancer drugs used nanogates on mesoporous organosilica nanoparticles loaded with DOX.[70] Disulfide nanogates were photocleaved by two-photon energy and DOX was released from the pores. In an in vitro study, 70% of MCF-7 breast cancer cells were killed after photoexcitation.

In addition to coherent two-photon absorption, sequential absorption of two NIR photons can stimulate upconverting nanoparticles (UCNP) that emit UV light. Absorption of the emitted light by appropriate linker molecules can dissociate the chemical bonds between a nanoparticle and a cap. For example, MSNs with rare earth cores in MSN shells were loaded with DOX and capped with β-CD bonded to the particles with photosensitive Pt(IV)-containing linkers. When excited with NIR light, the UCNPs emitted UV light that was absorbed by the linker and broke the linker bonds releasing both Pt(IV) pro-drugs and the DOX from the pores.[71] In vitro experiments showed that the double-drug release system induced cell death under NIR irradiation, and in vivo mouse studies showed that the nanoparticles had better efficacy under NIR light compared to that using UV light due to higher penetration depth of the NIR. Owing to their diverse and abundant mechanisms, utilization of light as an external stimulus has shown great potential for trigger-responsive drug delivery.

2.5 Outlook and Perspectives

Though considerable progress and advances have been made over the past decade towards externally controlled MSN-based drug delivery (and other innovative applications) by exploring different capping systems, challenges for their use in biomedical applications need to be addressed to achieve clinical translation. To summarize and look toward the future, we point out various research opportunities and practical consideration involved in preclinical development and clinical translation of external responsive MSN-based nanocarriers.

2.5.1 Research Opportunities Taking Advantage of Modern Clinically Available Medical Devices

External triggers discussed in this Perspective are attractive because the triggering events can be controlled remotely outside of human bodies. The high promise for external stimuli for various therapies has been evidenced by their progress in clinical trials and usages. HIFU was FDA approved and was first applied in the clinic in 2004 to treat uterine fibroids under the guidance of MRI.[72] SPION-AMF-based therapy in phase-I and phase-II clinical trials of glioblastoma and prostate cancer treatments showed promising results.[28] The patients are treated by the NanoActivator® (MagForce, Germany) device that generates the AMF. Our perspective is that AMF and HIFU are the two stimuli of the future that provide wide-open opportunities for taking advantage of newly available clinical instrumentation. Along with them, new stimuli-responsive drug delivery nanoparticles will be needed to exploit instruments that will become available in the future. For example, external electromagnetic stimuli such as radiofrequency (RF) waves (100 kHz to 300 GHz)[73–75] or microwaves (100 MHz to 3 GHz)[76] have been suggested as stimuli of drug release. The low-power RF field can transmit throughout the brain, resulting in improved drug penetration across the BBB for an efficient drug delivery to glioma cells. The magnetic cores of

Fe_3O_4@MSNs doped with ZnO have microwave-absorbing and thermal conversion properties and can generate local heat under microwave radiation, suggesting a new path toward thermo-stimulated drug delivery platforms.[76] Despite the promising results, further research is needed to confirm their exploitability in clinics.

Throughout this Perspective, examples of exceptional performances in vitro and in vivo of each type of stimulus have been demonstrated. It is important to note that all stimuli discussed in this Perspective produce heat. Although the heat can be controlled and can help trigger cargo release on-demand, it can be dangerous to human tissues if too much is produced. Stimuli with low power is generally safer but requires caps that respond sensitively. While stimuli with periodic or short pulses may provide a better control of the release profile, the attained treatment efficiency should be carefully compared with other conditions. Appropriate parameters for each stimulus must be carefully analyzed for its usage in vivo. Analysis on these external stimulations should be conducted to make sure that stimuli only aim at the desired groups (e.g., nanocaps) but not the other components (e.g., protective coating or targeting ligands) of nanocarriers because these components play a crucial role in enhancing their performance in living organisms, as will be discussed next.

2.5.2 Research Directions Based on Surface Engineering for Enhancing Targeting Efficacy

A key feature of a nanoplatform to combat a disease is its capability of specifically targeting the diseased cells without affecting the normal healthy tissues. To achieve the optimal treatment efficacy, the nanoparticles carrying the cargo need to be capable of reaching the location of interest and interact exclusively with the targeted cells. Active targeting via the specific interaction between ligands decorating the surface of the nanocarriers and the receptors overexpressed on the target cells has been used to enhance nanoparticle uptake.[77,78] MSN-based nanoplatforms offer an array of potential solutions for the development of receptor-based active targeting. For example, short-stranded DNA or RNA oligonucleotides with a specific sequence, the aptamer, could be developed to serve as not only the stimuli-responsive capping system but also the targeting ligands on the nanoparticle surface. As another example, a supramolecular cap discussed above can be functionalized with targeting agents such as folic acid to add targeting functionality and thus achieve the enhanced selective targeting of cancer cells.[48] Polymer coated MSNs can be further covered with an oppositely charged polymer with targeting functionality via electrostatic forces; for example, the interactions between the anionic PEI and cationic hyaluronic acid (HA).[79] Methods of introducing different functional groups to the surface of nanocarriers, such as polymers with various surface functionalities, are worth investigation in further prospective studies to append both targeting and capping agents to the particle surface for enhancing cell and tumor uptake as well as stimuli-responsive release of a drug.

Studies also showed that the interactions between cells and nanoparticles are highly sensitive to the nanoparticle surface chemistry. For example, by fusing zwitterionic lipid-based vesicles on MSNs – the so-called "protocells", individual cell targeting and delivery can be achieved.[80] Moreover, nanoparticles with zwitterionic surfaces have been shown to offer low nonspecific binding with the bioenvironment and high cell uptake,[81] suggesting that the nanoparticle surface charges (i.e. those of the charged functional groups of the capping systems) should be appropriately designed and optimized for in vivo targeting applications. The development of new approaches such as coating the MSN surfaces with biomolecule-based layers to mimic exosomes or cell membranes will also be an interesting field to focus on for a more direct targeting and enhanced treatment efficacy.[82] By building a protein corona shield on the MSNs functionalized with targeting agents, it was demonstrated that the interactions between MSNs and biological systems can be regulated, avoiding the clearance of MSNs by macrophages and retaining their targeting ability in vitro and in vivo.[83] Apart from surface modification of the MSN surface, the aspect ratios of the particles were shown to have impact on cellular uptake mechanism and different aspects of cellular function.[84] Such evidence suggests that the unique characteristic features of MSNs (e.g., both surface and structure) will play an important role in enhancing therapeutic efficacy.

2.5.3 Research Opportunities Using Core-Shell, Large-Pore and Hollow MSNs

Monitoring the dose in real time is another very challenging and important topic to pursue for the advancement of precision medicine. Discussed earlier in this Perspective, measuring and controlling the drug release from SPION@MSNs can be realized using MRgHIFU.[57] When using light as the stimulus, fluorescence quenching is a possible future direction to achieve real-time monitoring of drug release by capturing the change of emission intensity or wavelength before and after drug release. To further advance light-stimulated platforms and allow the observation of the light-based processes in deep tissue, shortwave infrared (SWIR) light appears promising. HMSNs that have mesopores that open into a large cavity has been used for optical imaging with SWIR via the assembly of SWIR-emissive J-aggregates in HMSNs.[85] This development resulted in a significant improvement in depth penetration, contrast, and sensitivity and is therefore worthwhile to be further explored for advancing therapeutic drug monitoring.

MSN-based platforms can also be designed for enhancing MRI contrast. While it is known that microbubbles can enhance ultrasound imaging and air-filled MSNs can serve as a HIFU-responsive ultrasound contrast agent,[86,87] air, which provides paramagnetic susceptibility when compared with the surrounding diamagnetic water, is also a source of contrast in MRI.[88] We anticipate that the future design of gas-encapsulated MSNs can be used as MRI contrast agents that can be triggered by the external stimuli that we discussed in this Perspective. In addition to improving MRI contrast via utilization of gas, a spotlight technique was developed to enhance MRI contrast specifically at the targeted tissue with ~1.5 mm^3 resolution.[89] This technique is based on periodic HIFU responsive MSNs modified with Gd(DTPA)^2 and PNIPAM. These MSNs can generate reversible MRI contrast changes. Spectral analysis extracts periodic signal changes, and a modulation enhancement map is reconstructed with a contrast enhancement of almost 100-fold at HIFU focal point compared to conventional MRI protocol. This spotlight technique can potentially be utilized to identify detailed tissue structure as well as enhance MRI contrast change with a wide variety of applications. Combined with the drug delivery features of MSNs, we envisioned that it would open more possibilities in the field of theranostics.

In addition to utilizing regular MSNs in the advancements of diagnosis, LPMSNs (**Figure 2.1b**) have great potential for the encapsulation of large biomolecules such as peptides and proteins that are increasingly important new therapeutic agents. The delivery of RNA or DNA to date mainly involved the outside surfaces of particles. Recently, LPMSNs are being investigated for gene therapy and to deliver relatively large biomolecules such as siRNA, IL-4 cytokines, and antigenic protein.[90] The pore tunability of MSNs was used to regulate antigen delivery efficacy and demonstrated the enhanced immune response intensity by using MSNs with large pores.[91] These strategies could lead to more advanced designs of MSN-based vaccines for cancer immunotherapy, which is a rapidly developing area. LPMSNs have been employed to encapsulate smaller functional nanoparticles to realize MR cancer diagnosis/imaging[92], bimodal MR/NIR imaging,[93] and biosensing.[94] They have also been used to immobilize enzymes without capping by utilizing physical adsorption.[95] Similar to the chemical amplifier where a nanogate controls the access to an encapsulated enzyme,[96] a more advanced design of mechanized particles that involves a catalyst-based production of amplified response when triggered can potentially increase detection sensitivity and be used as a controllable sensor to identify targeted signals from circulating cancer cells.[97]

The growing usage of the LPMSNs requires design and testing of large stimuli-responsive caps. Burst release of the encapsulated cargo sometimes occurs after the drug administration, resulting in a significant decrease in the number of cargo drugs that can reach the pharmacological target in the body. While it can be envisioned that suitable pore gatekeepers can minimize leakage and premature release of cargo, not many supramolecular-based nanocaps that can block the large pore openings have been reported.[96] We think the design and synthesis of stimuli-responsive capping systems for LPMSNs will open up new opportunities in both theranostic and biosensor applications.

It is interesting to note that HMSNs are underutilized in spite of their potentially large storge capacity. HMSNs have been used to trap a large quantity of nitric oxide (NO) donors that released NO in response to ultrasound, resulting in an excellent in vivo effect in inhibiting the Panc-1 tumor.[98] Because the internal cavity of a HMSN is connected to the particle surface through the mesoporous channels, these kinds of particles merit further applications.[99]

2.6 General Considerations

An obvious and extremely important component of the design of capping systems is that the material must function in relevant biofluids (e.g., blood, cytosol) at or near the physiological pH of 7.2. Nanomachines that function beautifully in distilled water may not operate at all in the presence of proteins (e.g., albumins) or other common biomolecules. Equally importantly, the particles must be dispersible (minimal aggregation) in the biofluids. Well known strategies for increasing dispersibility, for example by attaching PEG polymers to the particle’s surfaces, may decrease the number of capping molecules that can be attached and also interfere with their operation. Despite the successful utilization of MSNs in vitro and in vivo, full understanding of their biocompatibility in biological systems is needed before their translation to the clinic. A second and extremely important constraining consideration is the toxicity of the final nanoparticle. Spherical MSNs have been shown to be safe, but each new cap or attached molecule creates a new particle that must be tested for safety. This constraint means that when designing a new capping system, not only the cap and all other molecules attached must be nontoxic, but also all of the degradation products resulting from the response to stimulation must also be nontoxic. Other essential factors for the MSN-based carriers' uses in clinics include ensuring high purity and uniformity of nanoparticles, which sometimes may be challenging. It will be necessary to establish cost-effective and scalable methods to fabricate various kinds of well-dispersed high-quality MSNs with good reproducibility in order to receive approval from the FDA.

Ultimately, MSNs possessing capping systems that respond to one or more external stimuli hold great promise for biological applications such as diagnostics and therapeutics. Despite their promise, to advance and succeed in clinical trials, well-defined parameters for the stimuli should be established and more effort should be focused on addressing, identifying, and solving the potential toxicity of the designed nanosystems. The system should be kept as simple as possible through first utilizing its intrinsic properties to the fullest extent before incorporating any other component for improvement of treatment efficacy. The challenges that nanosystems face for use in various applications are multi-faceted. Successful clinical translation of nanoparticles depends on cooperation between physicochemical and biomedical sciences and interdisciplinary research in academic, industrial, and clinical settings to address the real clinical challenges.[82] Finally, to accurately compare preclinical results, to improve existing nanoparticles, and to design promising new nanosystems, more effort on the standardization of the laboratory practices and preclinical characterization, including physicochemical, in vitro, and in vivo characterization, is necessary. Such a standard can help future researchers recognize the critical healthcare needs when designing the nanoparticles and speed up the advancement of MSN-based nanosystems using past experiences. If all the challenges can be appropriately solved and requirements can be met, triggered MSN-based drug delivery nanocarriers that avoided deleterious off-target effects can strengthen the treatment efficacy and offer a very promising research field with high impact for therapeutic applications.

2.7 Figures

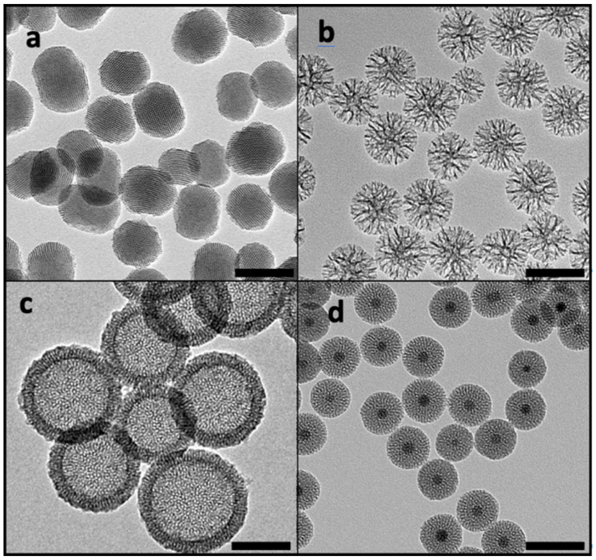

Figure 2.1 TEM images of the most common spherical mesoporous silica nanoparticles (MSNs) used for biomedical drug delivery. (a) Tubular pores ~2.5 nm in diameter in a two-dimensional hexagonal array. The pores are commonly templated with cetyltriammoniumammonium bromide (CTAB) surfactant. (b) "Large pore" MSNs with dendritic center-radial oriented pores ~ 4 nm in diameter. The pore size can be changed using "swelling" agents, larger molecular weight templating surfactants, or a hydrophilic and hydrophobic solvent mixture. (c) Hollow MSNs. The hollow center is frequently formed by condensing mesoporous silica around a spherical nanoparticle that is then dissolved and leaves behind a spherical void. (d) Core-shell MSNs with radial pores. This important example contains a superparamagnetic iron oxide (SPION) core. Scale bar: 100 nm

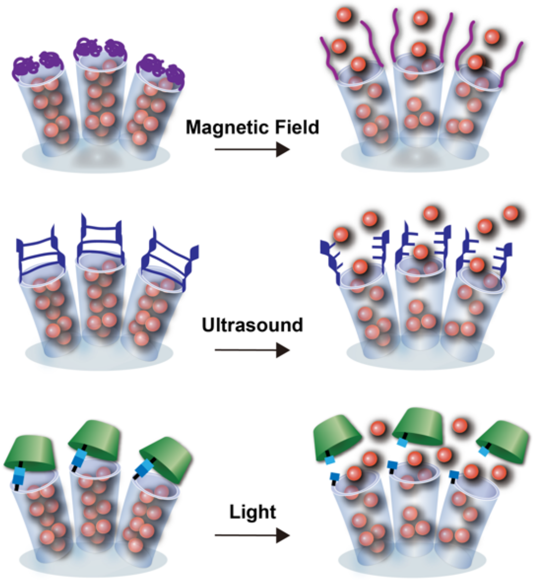

Figure 2.2 Schematic representations of capping systems over pores and their responses to external magnetic field, ultrasound, or light stimuli that cause cargo molecules trapped in the capped pores to be released. Top: the phase change of polymer caps on a SPION@MSN that is stimulated by heat from a superparamagnetic core in an alternating magnetic field (AMF). Middle: bond cleavage of linker-based caps that are triggered by ultrasound. Bottom: the dissembling of supramolecular caps that are activated by light. In all cases the trapped cargo molecules (orange spheres) diffuse out of the pores after the stimulation opens the cap. Note that the pores are not drawn to scale and that each illustration only shows a few of many pores in a nanoparticle.

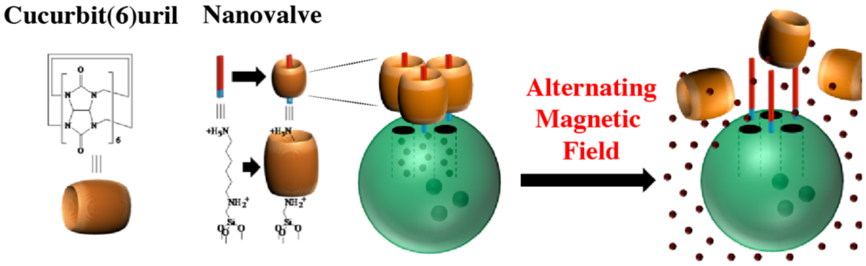

Figure 2.3 AMF activation of a nanovalve. The bulky cucurbit(6)uril caps trap cargo molecules in the pores of a SPION@MSN. Upon heating of the core by the AMF, the temperature-dependent binding constant of the cucurbit(6)uril to the diamine thread decreases, resulting in the disassembly of the nanovalve and subsequent release of cargo. Image adopted with permission from ref [29]. Copyright 2010 American Chemical Society.

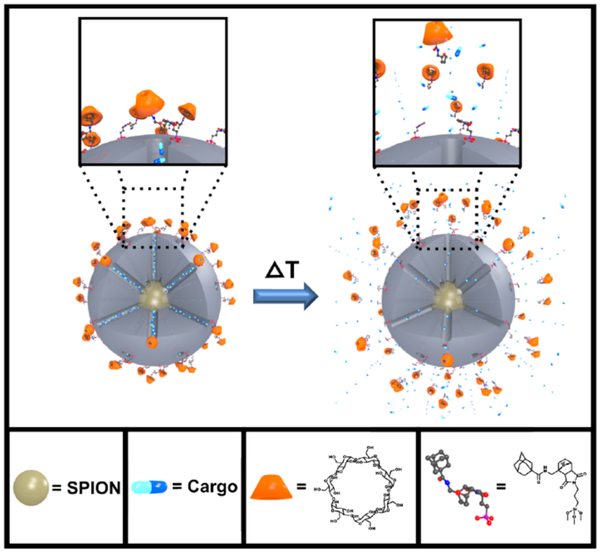

Figure 2.4 AMF-responsive bulky molecular caps are attached to pore openings by thermally reversible Diels-Alder reactions and trap the cargo inside the pores. When the temperature is raised by AMF heating of the core, a cyclo-reversion reaction is triggered, leading to dissociation of the bulky caps and allowing cargo molecules to diffuse out of the mesopores. Image adopted from ref [31] with permission from The Royal Society of Chemistry.

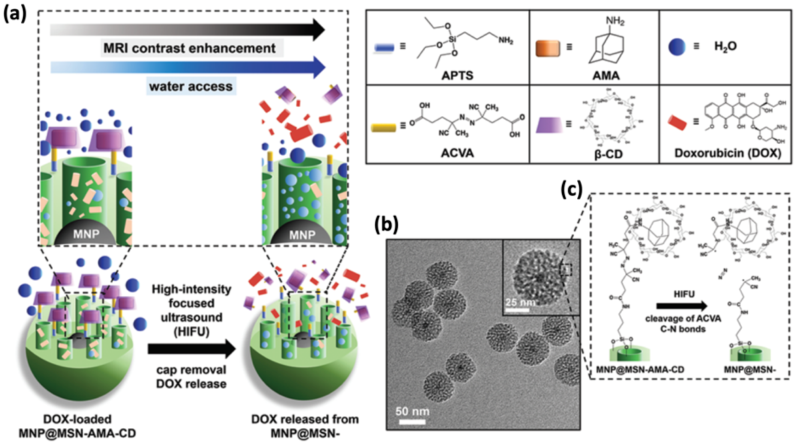

Figure 2.5 Capping system stimulated by high-intensity focused ultrasound (HIFU) to control drug release from MSNs. The release is imaged by magnetic resonance imaging (MRgHIFU). (a) On the left, doxorubicin (DOX) is trapped in the mesopores by β-CD caps that are held in place by thermo-sensitive azo bonds. On the right, after the HIFU stimulation is turned on, the thermo-sensitive bonds are cleaved by HIFU, the cap is opened and DOX is released. The increased water access to the superparamagnetic iron oxide core causes the T_2 MRI contrast to change. (b) TEM images of core-shell MSNs, and (c) the bond cleavage reaction stimulated by HIFU. Image adopted from ref [50] with permission from The Royal Society of Chemistry.

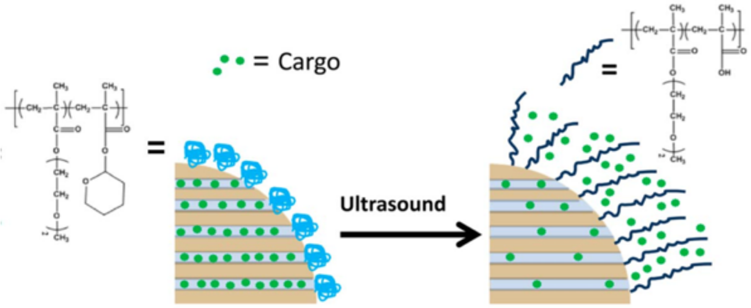

Figure 2.6 An ultrasound-responsive copolymer grafted on the surface of MSNs changes conformation in response to ultrasound irradiation. The cargo is retained in the pores when the polymer is coiled. Ultrasound irradiation induces the change in polymer conformation to extended coil-like, unblocking the pore openings and allowing the trapped cargo to be released. The image adopted from ref. [53] Copyright 2015 American Chemical Society.

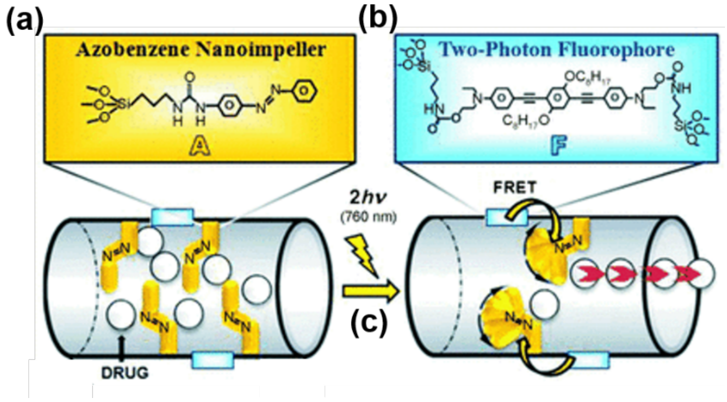

Figure 2.7 The mechanism of a two-photon infrared light-activated transducer for cargo release. (a) An azobenzene "nano-impeller" is in its trans configuration in its ground electronic state. (b) When excited with 760 nm two-photon energy, the fluorophore with a large two photon absorption cross-section transfers the energy to azobenzene via fluorescence resonance energy transfer (FRET). (c) The excited azobenzenes in the pores undergo reversible trans-cis isomerizations and act as nano-impellers; the large amplitude motions allow the cargo molecules to escape from the pores. Image adopted from ref [68] with permission from John Wiley and Sons.

2.8 References

(1) Kankala, R. K.; Han, Y. H.; Na, J.; Lee, C. H.; Sun, Z.; Wang, S. Bin; Kimura, T.; Ok, Y. S.; Yamauchi, Y.; Chen, A. Z.; Wu, K. C. W. Nanoarchitectured Structure and Surface Biofunctionality of Mesoporous Silica Nanoparticles. *Adv. Mater.* 2020, 32 (23), 1–27.

(2) Yanagisawa, T.; Shimizu, T.; Kuroda, K.; Kato, C. The Preparation of Alkyltrimethylammonium-Kanemite Complexes and Their Conversion to Microporous Materials. *Bulletin of the Chemical Society of Japan*. 1990, pp 988–992.

(3) Vivero-Escoto, J. L.; Huxford-Phillips, R. C.; Lin, W. Silica-Based Nanoprobes for Biomedical Imaging and Theranostic Applications. *Chem. Soc. Rev*. 2012, 41 (7), 2673–2685.

(4) Lee, J. E.; Lee, N.; Kim, T.; Kim, J.; Hyeon, T. Multifunctional Mesoporous Silica Nanocomposite Nanoparticles for Theranostic Applications. *Acc. Chem. Res.* 2011, 44 (10), 893–902.

(5) Ambrogio, M. W.; Thomas, C. R.; Zhao, Y. L.; Zink, J. I.; Stoddart, J. F. Mechanized Silica Nanoparticles: A New Frontier in Theranostic Nanomedicine. *Acc. Chem. Res.* 2011, 44 (10), 903–913.

(6) Argyo, C.; Weiss, V.; Bräuchle, C.; Bein, T. Multifunctional Mesoporous Silica Nanoparticles as a Universal Platform for Drug Delivery. *Chem. Mater*. 2014, 26 (1), 435–451.

(7) Biju, V. Chemical Modifications and Bioconjugate Reactions of Nanomaterials for Sensing, Imaging, Drug Delivery and Therapy. *Chem. Soc. Rev.* 2014, 43 (3), 744–764.

(8) Liong, M.; Lu, J.; Kovochich, M.; Xia, T.; Ruehm, S. G.; Nel, A. E.; Tamanoi, F.; Zink, J. I. Multifunctional Inorganic Nanoparticles for Imaging, Targeting, and Drug Delivery. *ACS Nano* 2008, 2 (5), 889–896.

(9) Feynman, R. P. There's Plenty of Room at the Bottom: An Invitation to Enter a New Field of Physics. *American Physical Society Lecture*, 1959, California Institute to Technology.

(10) Xue, M.; Yang, Y.; Chi, X.; Yan, X.; Huang, F. Development of Pseudorotaxanes and Rotaxanes: From Synthesis to Stimuli-Responsive Motions to Applications. *Chem. Rev.* 2015, 115 (15), 7398–7501.

(11) Schalley, C. A.; Beizai, K.; Vögtle, F. On the Way to Rotaxane-Based Molecular Motors: Studies in Molecular Mobility and Topological Chirality. *Acc. Chem. Res*. 2001, 34 (6), 465–476.

(12) Slowing, I. I.; Trewyn, B. G.; Lin, V. S. Y. Mesoporous Silica Nanoparticles for Intracellular Delivery of Membrane-Impermeable Proteins. *J. Am. Chem. Soc.* 2007, 129 (28), 8845–8849.

(13) Lu, J.; Liong, M.; Zink, J. I.; Tamanoi, F. Mesoporous Silica Nanoparticles as a Delivery System for Hydrophobic Anticancer Drug. *Small* 2007, 3 (8), 1341–1346.

(14) Manzano, M.; Vallet-Regí, M. Mesoporous Silica Nanoparticles for Drug Delivery. *Adv. Funct. Mater.* 2020, 30 (2), 3–5.

(15) Li, Z.; Barnes, J. C.; Bosoy, A.; Stoddart, J. F.; Zink, J. I. Mesoporous Silica Nanoparticles in Biomedical Applications. *Chem. Soc. Rev.* 2012, 41 (7), 2590–2605.

(16) Klichko, Y.; Khashab, N. M.; Yang, Y. W.; Angelos, S.; Stoddart, J. F.; Zink, J. I. Improving Pore Exposure in Mesoporous Silica Films for Mechanized Control of the Pores. *Microporous Mesoporous Mater.* 2010, 132 (3), 435–441.

(17) Hernandez, R.; Franville, A. C.; Minoofar, P.; Dunn, B.; Zink, J. I. Controlled Placement of Luminescent Molecules and Polymers in Mesostructured Sol-Gel Thin Films [10]. *J. Am. Chem. Soc.* 2001, 123 (6), 1248–1249.

(18) Lu, Y.; Ganguli, R.; Drewien, C. A.; Anderson, M. T.; Jeffrey Brinker, C.; Gong, W.; Guo, Y.; Soyez, H.; Dunn, B.; Huang, M. H.; Zink, J. I. Continuous Formation of Supported Cubic and Hexagonal Mesoporous Films by Sol-Gel Dip-Coating. *Nature* 1997, 389 (6649), 364–368.

(19) Chia, S.; Urano, J.; Tamanoi, F.; Dunn, B.; Zink, J. I. Patterned Hexagonal Arrays of Living Cells in Sol-Gel Silica Films [1]. *J. Am. Chem. Soc.* 2000, 122 (27), 6488–6489.

(20) Rühle, B.; Saint-Cricq, P.; Zink, J. I. Externally Controlled Nanomachines on Mesoporous Silica Nanoparticles for Biomedical Applications. *ChemPhysChem* 2016, 17, 1769–1779.

(21) Kumar, N.; Chen, W.; Cheng, C.; Deng, T.; Ruining, W.; Zink, J. I. Stimuli-Responsive Nanomachines and Caps for Drug Delivery. *Enzym.* 2018, 43, 31–65.

(22) Cheng, C. A.; Deng, T.; Lin, F. C.; Cai, Y.; Zink, J. I. Supramolecular Nanomachines as Stimuli-Responsive Gatekeepers on Mesoporous Silica Nanoparticles for Antibiotic and Cancer Drug Delivery, *Theronostics* 2019, 9.

(23) Chen, W.; Glackin, C. A.; Horwitz, M. A.; Zink, J. I. Nanomachines and Other Caps on Mesoporous Silica Nanoparticles for Drug Delivery. *Acc. Chem. Res.* 2019, 52 (6), 1531–1542.

(24) Aznar, E.; Oroval, M.; Pascual, L.; Murguía, J. R.; Martínez-Mánez, R.; Sancenón, F. Gated Materials for On-Command Release of Guest Molecules. *Chem. Rev.* 2016, 116 (2), 561–718.

(25) Croissant, J. G.; Butler, K. S.; Zink, J. I.; Brinker, C. J. Synthetic Amorphous Silica Nanoparticles : Toxicity and Biomedical and Environmental Implications. *Nat. Rev. Mater.* 2020, 5, 886–90.

(26) Rosensweig, R. E. Heating Magnetic Fluid with Alternating Magnetic Field. *J. Magn. Magn. Mater.* 2002, 252, 370–374.

(27) Lin, F.; Zink, I. Probing the Local Nanoscale Heating Mechanism of a Magnetic Core in Mesoporous Silica Drug-Delivery Nanoparticles Using Fluorescence Depolarization. *J. Am. Chem. Soc.* 2020, 142, 5212–5220.

(28) Liu, X.; Zhang, Y.; Wang, Y.; Zhu, W.; Li, G.; Ma, X.; Zhang, Y.; Chen, S.; Tiwari, S.; Shi, K.; Zhang, S.; Fan, H. M.; Zhao, Y. X.; Liang, X. J. Comprehensive Understanding of Magnetic Hyperthermia for Improving Antitumor Therapeutic Efficacy. *Theranostics* 2020, 10 (8), 3793–3815.

(29) Thomas, C. R.; Ferris, D. P.; Lee, J. H.; Choi, E.; Cho, M. H.; Kim, E. S.; Stoddart, J. F.; Shin, J. S.; Cheon, J.; Zink, J. I. Noninvasive Remote-Controlled Release of Drug Molecules in Vitro Using Magnetic Actuation of Mechanized Nanoparticles. *J. Am. Chem. Soc.* 2010, 132 (31), 10623–10625.

(30) Yu, Q.; Deng, T.; Lin, F. C.; Zhang, B.; Zink, J. I. Supramolecular Assemblies of Heterogeneous Mesoporous Silica Nanoparticles to Co-Deliver Antimicrobial Peptides and Antibiotics for Synergistic Eradication of Pathogenic Biofilms. *ACS Nano* 2020, 14 (5), 5926–5937.

(31) Rühle, B.; Datz, S.; Argyo, C.; Bein, T.; Zink, J. I. A Molecular Nanocap Activated by Superparamagnetic Heating for Externally Stimulated Cargo Release. *Chem. Commun.* 2016, 52 (9), 1843–1846.

(32) Chen, W.; Cheng, C. A.; Zink, J. I. Spatial, Temporal, and Dose Control of Drug Delivery Using Noninvasive Magnetic Stimulation. *ACS Nano* 2019, 13 (2), 1292–1308.

(33) Saint-Cricq, P.; Deshayes, S.; Zink, J. I.; Kasko, A. M. Magnetic Field Activated Drug Delivery Using Thermodegradable Azo-Functionalised PEG-Coated Core-Shell Mesoporous Silica Nanoparticles. *Nanoscale* 2015, 7 (31), 13168–13172.

(34) Baeza, A.; Guisasola, E.; Ruiz-Hernández, E.; Vallet-Regí, M. Magnetically Triggered Multidrug Release by Hybrid Mesoporous Silica Nanoparticles. *Chem. Mater.* 2012, 24 (3), 517–524.

(35) Guisasola, E.; Baeza, A.; Talelli, M.; Arcos, D.; Moros, M.; De La Fuente, J. M.; Vallet-Regí, M. Magnetic-Responsive Release Controlled by Hot Spot Effect. *Langmuir* 2015, 31 (46), 12777–12782.

(36) Ruan, L.; Chen, W.; Wang, R.; Lu, J.; Zink, J. I. Magnetically Stimulated Drug Release Using Nanoparticles Capped by Self-Assembling Peptides. *ACS Appl. Mater. Interfaces 2019, 11 (47), 43835–43842.*

(37) Jin, R.; Wu, G.; Li, Z.; Mirkin, C. A.; Schatz, G. C. What Controls the Melting Properties of DNA-Linked Gold Nanoparticle Assemblies? *J. Am. Chem. Soc.* 2003, 125 (6), 1643–1654.

(38) Zhu, Y.; Tao, C. DNA-Capped Fe3O4/SiO2 Magnetic Mesoporous Silica Nanoparticles for Potential Controlled Drug Release and Hyperthermia. *RSC Adv.* 2015, 5 (29), 22365–22372.

(39) Ruiz-Hernández, E.; Baeza, A.; Vallet-Regí, M. Smart Drug Delivery through DNA/Magnetic Nanoparticle Gates. *ACS Nano* 2011, 5 (2), 1259–1266.

(40) Yu, Z.; Li, N.; Zheng, P.; Pan, W.; Tang, B. Temperature-Responsive DNA-Gated Nanocarriers for Intracellular Controlled Release. *Chem. Commun*. 2014, 50 (26), 3494–3497.

(41) Dong, J.; Zink, J. I. Taking the Temperature of the Interiors of Magnetically Heated Nanoparticles. *ACS Nano* 2014, 8 (5), 5199–5207.

(42) Boissenot, T.; Bordat, A.; Fattal, E.; Tsapis, N. Ultrasound-Triggered Drug Delivery for Cancer Treatment Using Drug Delivery Systems: From Theoretical Considerations to Practical Applications. *J. Control. Release* 2016, 241, 144–163.

(43) Yildirim, A.; Blum, N. T.; Goodwin, A. P. Colloids, Nanoparticles, and Materials for Imaging, Delivery, Ablation, and Theranostics by Focused Ultrasound (FUS). *Theranostics* 2019, 9 (9), 2572–2594.

(44) Malietzis, G.; Monzon, L.; Hand, J.; Wasan, H.; Leen, E.; Abel, M.; Muhammad, A.; Price, P.; Abel, P. High-Intensity Focused Ultrasound: Advances in Technology and Experimental Trials Support Enhanced Utility of Focused Ultrasound Surgery in Oncology. Br. *J. Radiol.* 2013, 86 (1024).

(45) Chiara Zini Stephen Thomas, Alessandro Napoli, Carlo Catalano, Aytekin Oto, E. H. Ultrasound- and MR-Guided Focused Ultrasound Surgery for Prostate Cancer. *World J. Radiol.* 2012, 4 (6), 247.

(46) Timbie, K. F.; Mead, B. P.; Price, R. J. Drug and Gene Delivery across the Blood-Brain Barrier with Focused Ultrasound. *J. Control. Release* 2015, 219, 61–75.

(47) Paris, J. L.; Mannaris, C.; Cabañas, M. V.; Carlisle, R.; Manzano, M.; Vallet-Regí, M.; Coussios, C. C. Ultrasound-Mediated Cavitation-Enhanced Extravasation of Mesoporous Silica Nanoparticles for Controlled-Release Drug Delivery. *Chem. Eng. J.* 2018, 340 (December 2017), 2–8.

(48) Wang, J.; Jiao, Y.; Shao, Y. Mesoporous Silica Nanoparticles for Dual-Mode Chemo-Sonodynamic Therapy by Low-Energy Ultrasound. *Materials (Basel).* 2018, 11 (10).

(49) Lee, S. F.; Zhu, X. M.; Wang, Y. X. J.; Xuan, S. H.; You, Q.; Chan, W. H.; Wong, C. H.; Wang, F.; Yu, J. C.; Cheng, C. H. K.; Leung, K. C. F. Ultrasound, PH, and Magnetically Responsive Crown-Ether-Coated Core/Shell Nanoparticles as Drug Encapsulation and Release Systems. *ACS Appl. Mater. Interfaces* 2013, 5 (5), 1566–1574.

(50) Cheng, C.-A.; Chen, W.; Zhang, L.; Wu, H. H.; Zink, J. I. Magnetic Resonance Imaging of High-Intensity Focused Ultrasound-Stimulated Drug Release from a Self-Reporting Core@shell Nanoparticle Platform. *Chem. Commun.* 2020, 56, 10297.

(51) Niu, D.; Wang, X.; Li, Y.; Zheng, Y.; Li, F.; Chen, H.; Gu, J.; Zhao, W.; Shi, J. Facile Synthesis of Magnetite/Perfluorocarbon Co-Loaded Organic/Inorganic Hybrid Vesicles for Dual-Modality Ultrasound/Magnetic Resonance Imaging and Imaging-Guided High-Intensity Focused Ultrasound Ablation. *Adv. Mater.* 2013, 25 (19), 2686–2692.

(52) Kim, H. J.; Matsuda, H.; Zhou, H.; Honma, I. Ultrasound-Triggered Smart Drug Release from a Poly(Dimethylsiloxane)- Mesoporous Silica Composite. *Adv. Mater.* 2006, 18 (23), 3083–3088.

(53) Paris, J. L.; Cabanas, M. V.; Manzano, M.; Vallet-Regí, M. Polymer-Grafted Mesoporous Silica Nanoparticles as Ultrasound-Responsive Drug Carriers. *ACS Nano* 2015, 9 (11), 11023–11033.

(54) Paris, J. L.; De La Torre, P.; Victoria Cabañas, M.; Manzano, M.; Grau, M.; Flores, A. I.; Vallet-Regí, M. Vectorization of Ultrasound-Responsive Nanoparticles in Placental Mesenchymal Stem Cells for Cancer Therapy. Nanoscale 2017, 9 (17), 5528–5537.

(55) Li, X.; Wang, Z.; Xia, H. Ultrasound Reversible Response Nanocarrier Based on Sodium Alginate Modified Mesoporous Silica Nanoparticles. *Front. Chem.* 2019, 7.

(56) Li, X.; Xie, C.; Xia, H.; Wang, Z. PH and Ultrasound Dual-Responsive Polydopamine-Coated Mesoporous Silica Nanoparticles for Controlled Drug Delivery. *Langmuir* 2018, 34 (34), 9974–9981.

(57) Cheng, C. A.; Chen, W.; Zhang, L.; Wu, H. H.; Zink, J. I. A Responsive Mesoporous Silica Nanoparticle Platform for Magnetic Resonance Imaging-Guided High-Intensity Focused Ultrasound-Stimulated Cargo Delivery with Controllable Location, Time, and Dose. *J. Am. Chem. Soc.* 2019, 141 (44), 17670–17684.

(58) Baskaran, R.; Lee, J.; Yang, S.-G. Clinical Development of Photodynamic Agents and Therapeutic Applications. *Biomater. Res.* 2018, 22 (1), 25.

(59) Sharma, S. K.; Shrivastava, N.; Rossi, F.; Tung, L. D.; Thanh, N. T. K. Nanoparticles-Based Magnetic and Photo Induced Hyperthermia for Cancer Treatment. *Nano Today* 2019, 29.

(60) Ding, X.; Liow, C. H.; Zhang, M.; Huang, R.; Li, C.; Shen, H.; Liu, M.; Zou, Y.; Gao, N.; Zhang, Z.; Li, Y.; Wang, Q.; Li, S.; Jiang, J. Surface Plasmon Resonance Enhanced Light Absorption and Photothermal Therapy in the Second Near-Infrared Window. *J. Am. Chem. Soc.* 2014, 136 (44), 15684–15693.

(61) Qian, H. S.; Guo, H. C.; Ho, P. C.-L.; Mahendran, R.; Zhang, Y. Mesoporous-Silica-Coated Up-Conversion Fluorescent Nanoparticles for Photodynamic Therapy. *Small* 2009, 5 (20), 2285–2290.

(62) Pawlicki, M.; Collins, H. A.; Denning, R. G.; Anderson, H. L. Two-Photon Absorption and the Design of Two-Photon Dyes. *Angew. Chemie - Int. Ed.* 2009, 48 (18), 3244–3266.

(63) Wang, Y.; Kohane, D. S. External Triggering and Triggered Targeting Strategies for Drug Delivery. *Nat. Rev. Mater*. 2017, 2 (6), 17020.

(64) Rwei, A. Y.; Wang, W.; Kohane, D. S. Photoresponsive Nanoparticles for Drug Delivery. *Nano Today* 2015, 10 (4), 451–467.

(65) Guardado-Alvarez, T. M.; Sudha Devi, L.; Russell, M. M.; Schwartz, B. J.; Zink, J. I. Activation of Snap-Top Capped Mesoporous Silica Nanocontainers Using Two Near-Infrared Photons. *J. Am. Chem. Soc*. 2013, 135 (38), 14000–14003.

(66) Vuilleumier, J.; Gaulier, G.; De Matos, R.; Ortiz, D.; Menin, L.; Campargue, G.; Mas, C.; Constant, S.; Le Dantec, R.; Mugnier, Y.; Bonacina, L.; Gerber-Lemaire, S. Two-Photon-Triggered Photorelease of Caged Compounds from Multifunctional Harmonic Nanoparticles. *ACS Appl. Mater. Interfaces* 2019, 11 (30), 27443–27452.

(67) Liu, N.; Dunphy, D. R.; Atanassov, P.; Bunge, S. D.; Chen, Z.; López, G. P.; Boyle, T. J.; Jeffrey Brinker, C. Photoregulation of Mass Transport through a Photoresponsive Azobenzene-Modified Nanoporous Membrane. *Nano Lett.* 2004, 4 (4), 551–554.

(68) Croissant, J.; Maynadier, M.; Gallud, A.; Peindy N'Dongo, H.; Nyalosaso, J. L.; Derrien, G.; Charnay, C.; Durand, J.-O.; Raehm, L.; Serein-Spirau, F.; Cheminet, N.; Jarrosson, T.; Mongin, O.; Blanchard-Desce, M.; Gary-Bobo, M.; Garcia, M.; Lu, J.; Tamanoi, F.; Tarn, D.; Guardado-Alvarez, T. M.; Zink, J. I. Two-Photon-Triggered Drug Delivery in Cancer Cells Using Nanoimpellers. *Angew. Chemie Int. Ed.* 2013, 52 (51), 13813–13817.

(69) Guardado-Alvarez, T. M.; Devi, L. S.; Vabre, J.-M.; Pecorelli, T. A.; Schwartz, B. J.; Durand, J.-O.; Mongin, O.; Blanchard-Desce, M.; Zink, J. I. Photo-Redox Activated Drug Delivery Systems Operating under Two Photon Excitation in the near-IR. *Nanoscale* 2014, 6 (9), 4652–4658.

(70) Croissant, J. G.; Qi, C.; Mongin, O.; Hugues, V.; Blanchard-Desce, M.; Raehm, L.; Cattoën, X.; Wong Chi Man, M.; Maynadier, M.; Gary-Bobo, M.; Garcia, M.; Zink, J. I.; Durand, J.-

O. Disulfide-Gated Mesoporous Silica Nanoparticles Designed for Two-Photon-Triggered Drug Release and Imaging. *J. Mater. Chem. B* 2015, 3 (31), 6456–6461.

(71) Dai, Y.; Bi, H.; Deng, X.; Li, C.; He, F.; Ma, P.; Yang, P.; Lin, J. 808 Nm Near-Infrared Light Controlled Dual-Drug Release and Cancer Therapy in Vivo by Upconversion Mesoporous Silica Nanostructures. *J. Mater. Chem. B* 2017, 5 (11), 2086–2095.

(72) Fruehauf, J. H.; Back, W.; Eiermann, A.; Lang, M. C.; Pessel, M.; Marlinghaus, E.; Melchert, F.; Volz-Köster, S.; Volz, J. High-Intensity Focused Ultrasound for the Targeted Destruction of Uterine Tissues: Experiences from a Pilot Study Using a Mobile HIFU Unit. *Arch. Gynecol. Obstet.* 2008, 277 (2), 143–150.

(73) Turan, O.; Bielecki, P.; Perera, V.; Lorkowski, M.; Covarrubias, G.; Tong, K.; Yun, A.; Rahmy, A.; Ouyang, T.; Raghunathan, S.; Gopalakrishnan, R.; Griswold, M. A.; Ghaghada, K. B.; Peiris, P. M.; Karathanasis, E. Delivery of Drugs into Brain Tumors Using Multicomponent Silica Nanoparticles. *Nanoscale* 2019, 11 (24), 11910–11921.

(74) Šoltys, M.; Kovačík, P.; Lhotka, M.; Ulbrich, P.; Zadražil, A.; Štěpánek, F. Radiofrequency Controlled Release from Mesoporous Silica Nano-Carriers. Microporous Mesoporous *Mater.* 2016, 229, 14–21.

(75) Turan, O.; Bielecki, P. A.; Perera, V.; Lorkowski, M.; Covarrubias, G.; Tong, K.; Yun, A.; Loutrianakis, G.; Raghunathan, S.; Park, Y.; Moon, T.; Cooley, S.; Dixit, D.; Griswold, M. A.; Ghaghada, K. B.; Peiris, P. M.; Rich, J. N.; Karathanasis, E. Treatment of Glioblastoma Using Multicomponent Silica Nanoparticles. *Adv. Ther.* 2019, 2 (11), 1900118.

(76) Shi, Z.; Yang, C.; Li, R.; Ruan, L. Microwave Thermal-Triggered Drug Delivery Using Thermosensitive Peptide-Coated Core–Shell Mesoporous Silica Nanoparticles. *J. Mater. Sci.* 2020, 55 (14), 6118–6129.

(77) Bazak, R.; Houri, M.; El Achy, S.; Kamel, S.; Refaat, T. Cancer Active Targeting by Nanoparticles: A Comprehensive Review of Literature. *J. Cancer Res. Clin. Oncol.* 2015, 141 (5), 769–784.

(78) Attia, M. F.; Anton, N.; Wallyn, J.; Omran, Z.; Vandamme, T. F. An Overview of Active and Passive Targeting Strategies to Improve the Nanocarriers Efficiency to Tumour Sites. *J. Pharm. Pharmacol.* 2019, 71 (8), 1185–1198.

(79) Shahin, S. A.; Wang, R.; Simargi, S. I.; Contreras, A.; Parra Echavarria, L.; Qu, L.; Wen, W.; Dellinger, T.; Unternaehrer, J.; Tamanoi, F.; Zink, J. I.; Glackin, C. A. Hyaluronic Acid Conjugated Nanoparticle Delivery of SiRNA against TWIST Reduces Tumor Burden and Enhances Sensitivity to Cisplatin in Ovarian Cancer. *Nanomedicine Nanotechnology, Biol. Med.* 2018, 14 (4), 1381–1394.

(80) Durfee, P. N.; Lin, Y. S.; Dunphy, D. R.; Muñiz, A. J.; Butler, K. S.; Humphrey, K. R.; Lokke, A. J.; Agola, J. O.; Chou, S. S.; Chen, I. M.; Wharton, W.; Townson, J. L.; Willman,

C. L.; Brinker, C. J. Mesoporous Silica Nanoparticle-Supported Lipid Bilayers (Protocells) for Active Targeting and Delivery to Individual Leukemia Cells. *ACS Nano* 2016, 10 (9), 8325–8345.

(81) Chakraborty, A.; Dalal, C.; Jana, N. R. Colloidal Nanobioconjugate with Complementary Surface Chemistry for Cellular and Subcellular Targeting. *Langmuir* 2018, 34 (45), 13461–13471.

(82) Nel, A. E. Transformational Impact of Nanomedicine: Reconciling Outcome with Promise. *Nano Lett.* 2020, 20, 5601–5603.

(83) Oh, J. Y.; Kim, H. S.; Palanikumar, L.; Go, E. M.; Jana, B.; Park, S. A.; Kim, H. Y.; Kim, K.; Seo, J. K.; Kwak, S. K.; Kim, C.; Kang, S.; Ryu, J. H. Cloaking Nanoparticles with Protein Corona Shield for Targeted Drug Delivery. *Nat. Commun.* 2018, 9 (1), 1–9.

(84) Huang, X.; Teng, X.; Chen, D.; Tang, F.; He, J. The Effect of the Shape of Mesoporous Silica Nanoparticles on Cellular Uptake and Cell Function. *Biomaterials* 2010, 31 (3), 438–448.

(85) Chen, W.; Cheng, C. A.; Cosco, E. D.; Ramakrishnan, S.; Lingg, J. G. P.; Bruns, O. T.; Zink, J. I.; Sletten, E. M. Shortwave Infrared Imaging with J-Aggregates Stabilized in Hollow Mesoporous Silica Nanoparticles. *J. Am. Chem. Soc.* 2019, 141 (32), 12475–12480.

(86) Wang, X.; Chen, H.; Zhang, K.; Ma, M.; Li, F.; Zeng, D.; Zheng, S.; Chen, Y.; Jiang, L.; Xu, H.; Shi, J. An Intelligent Nanotheranostic Agent for Targeting, Redox-Responsive Ultrasound Imaging, and Imaging-Guided High-Intensity Focused Ultrasound Synergistic Therapy. *Small* 2014, 10 (7), 1403–1411.

(87) Yildirim, A.; Chattaraj, R.; Blum, N. T.; Goldscheitter, G. M.; Goodwin, A. P. Stable Encapsulation of Air in Mesoporous Silica Nanoparticles: Fluorocarbon-Free Nanoscale Ultrasound Contrast Agents. *Adv. Healthc. Mater.* 2016, 5 (11), 1290–1298.

(88) Lu, G. J.; Farhadi, A.; Szablowski, J. O.; Lee-Gosselin, A.; Barnes, S. R.; Lakshmanan, A.; Bourdeau, R. W.; Shapiro, M. G. Acoustically Modulated Magnetic Resonance Imaging of Gas-Filled Protein Nanostructures. *Nat. Mater.* 2018, 17 (5), 456–463.

(89) Deng, T.; Zhang, L.; Wu, H. H.; Zink, J. I. A Nanoparticle Enabled Focused Ultrasound-Stimulated Magnetic Resonance Imaging Spotlight. *Chem. Commun.* 2019, 55 (69), 10261–10264.

(90) Cha, B. G.; Jeong, J. H.; Kim, J. Extra-Large Pore Mesoporous Silica Nanoparticles Enabling Co-Delivery of High Amounts of Protein Antigen and Toll-like Receptor 9 Agonist for Enhanced Cancer Vaccine Efficacy. *ACS Cent. Sci.* 2018, 4 (4), 484–492.

(91) Hong, X.; Zhong, X.; Du, G.; Hou, Y.; Zhang, Y.; Zhang, Z.; Gong, T.; Zhang, L.; Sun, X. The Pore Size of Mesoporous Silica Nanoparticles Regulates Their Antigen Delivery Efficiency. *Sci. Adv.* 2020, 6 (25).

(92) Niu, D.; Liu, Z.; Li, Y.; Luo, X.; Zhang, J.; Gong, J.; Shi, J. Monodispersed and Ordered Large-Pore Mesoporous Silica Nanospheres with Tunable Pore Structure for Magnetic Functionalization and Gene Delivery. *Adv. Mater.* 2014, 26 (29), 4947–4953.

(93) Yang, F.; Skripka, A.; Tabatabaei, M. S.; Hong, S. H.; Ren, F.; Huang, Y.; Oh, J. K.; Martel, S.; Liu, X.; Vetrone, F.; Ma, D. Magnetic Photoluminescent Nanoplatform Built from Large-Pore Mesoporous Silica. *Chem. Mater.* 2019, 31 (9), 3201–3210.

(94) Li, M.; Lao, Y. H.; Mintz, R. L.; Chen, Z.; Shao, D.; Hu, H.; Wang, H. X.; Tao, Y.; Leong, K. W. A Multifunctional Mesoporous Silica-Gold Nanocluster Hybrid Platform for Selective Breast Cancer Cell Detection Using a Catalytic Amplification-Based Colorimetric Assay. *Nanoscale* 2019, 11 (6), 2631–2636.

(95) Liu, T.; Zhang, N.; Wang, Z.; Wu, M.; Chen, Y.; Ma, M.; Chen, H.; Shi, J. Endogenous Catalytic Generation of O2 Bubbles for in Situ Ultrasound-Guided High Intensity Focused Ultrasound Ablation. *ACS Nano* 2017, 11 (9), 9093–9102.

(96) Xue, M.; Zink, J. I. An Enzymatic Chemical Amplifier Based on Mechanized Nanoparticles. *J. Am. Chem. Soc.* 2013, 135 (47), 17659–17662.

(97) Gribko, A.; Künzel, J.; Wünsch, D.; Lu, Q.; Nagel, S.; Knauer, S.; Stauber, R. H.; Ding, G. Bin. Is Small Smarter? Nanomaterial-Based Detection and Elimination of Circulating Tumor Cells: Current Knowledge and Perspectives. *Int. J. Nanomedicine* 2019, 14, 4187–4209.

(98) Zhang, K.; Xu, H.; Jia, X.; Chen, Y.; Ma, M.; Sun, L.; Chen, H. Ultrasound-Triggered Nitric Oxide Release Platform Based on Energy Transformation for Targeted Inhibition of Pancreatic Tumor. *ACS Nano* 2016, 10 (12), 10816–10828.

(99) Du, L.; Liao, S.; Khatib, H. A.; Stoddart, J. F.; Zink, J. I. Controlled-Access Hollow Mechanized Silica Nanocontainers. *J. Am. Chem. Soc.* 2009, 131 (42), 15136–15142.

Chapter 3 Probing the Local Nanoscale Heating Mechanism of a Magnetic Core in Mesoporous Silica Drug-Delivery Nanoparticles Using Fluorescence Depolarization

This chapter of the dissertation was reproduced with permission from *J. Am. Chem. Soc.* 2020, 142, 5212−5220. Copyright 2020 American Chemical Society. Lin F.-C. designed and performed all the experiments. Jeffrey I. Zink was the P.I. In addition, detailed theory and synthesis of SPIONs was included in this chapter.

Table of Content Figure

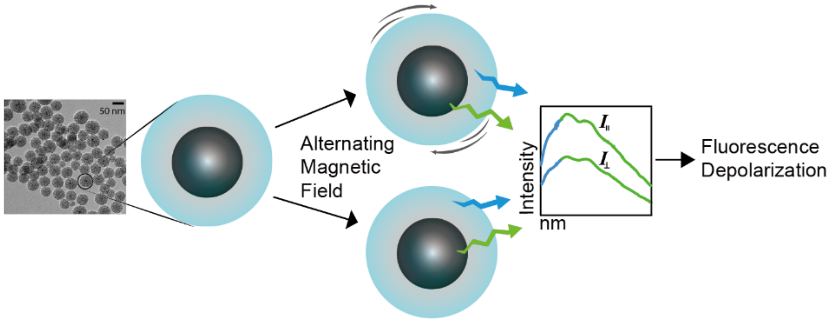

3.1 Introduction

Superparamagnetic iron oxide nanoparticles (SPION), possessing both therapeutic (hyperthermia) and imaging (MRI) features, are of importance in biomedical applications. The inherent T_2-weighted magnetic resonance imaging (MRI) contrast change caused by SPIONs has been extensively exploited in cancer diagnosis and treatment monitoring.[1,2] In addition, SPIONs have also been tailored for use as drug delivery agents for cancer therapeutics.[1,3,4] Noninvasive alternating magnetic fields (AMF) in conjunction with SPIONs makes possible on-command hyperthermia cancer treatment and immunotherapy.[5–7] Due to the heating ability of SPIONs that can be directly controlled by using AMF, they are widely developed for heat-activated drug release.[1,3,8]

Magnetic induction heating generated by SPIONs when subjected to an AMF depends on the relaxation time for reorientation of magnetic moments in the SPIONs resulted from the thermal fluctuations at a finite temperature.[9] The magnetization of each particle only starts to respond to the applied magnetic field when the temperature is above the so-called blocking temperature (T_B), where the thermal energy overcomes the anisotropy barrier and magnetic moments of each particle begin to fluctuate.[10] The magnetically-induced heating of single-domain SPIONs can be caused by two basic relaxation mechanisms, Néel relaxation and Brownian relaxation.[5,9] Néel relaxation involves the internal rotation of the magnetic moment with respect the crystalline axes, whereas the rotation of the particles as a whole was termed Brownian relaxation.[5,9,11]

The Néel-Brownian magnetization relaxation of SPIONs in an AMF has been studied from a theoretical point of view.[12] The calculations predict that the rotation of magnetic nanoparticles in a liquid as a whole occurs when the AMF amplitude is smaller than the particle anisotropy field.[12] However, when a large amplitude of AMF is applied, particles will only oscillate slightly, accompanied by sharp jumping of the magnetization vector from one magnetic potential well to another.[12] In another theoretical study, a trend of decreasing specific absorption rates with higher dispersion viscosity of magnetite nanoparticles due to the changes in free particle rotation was calculated, implying the presence of a Brownian relaxation heating component.[11] Previous discussion on magnetite particles with a range of particle sizes also pointed out that Brownian relaxation process tends to dominate when the particle size is larger than 8 nm.[9] Despite of the theoretical studies on various aspects of the magnetic nanoparticle behavior in a liquid, the relaxation contributions of SPION encapsulated in MSN (SPION@MSN) in AMF of moderate amplitude and frequency have not yet been investigated experimentally.

Mesoporous silica nanoparticles (MSNs) are mechanically, thermally and chemically stable silica matrices containing pores with large internal volume, and are suitable carriers of cargo molecules such as anticancer drugs that can be stimulated by heat to release the drugs.[13] Studies using MSN for the delivery and release of drugs at a selectively targeted site with AMF temporal control have been reported.[13–16] In these systems, the thermo-responsive gatekeepers on the surface of MSNs (tens of nanometers from the magnetic core) mediate the release of drugs through the localized nanoscale AMF heating of the core SPION. Given the importance of confining sufficient thermal energy at the suitable heating range and carrying out spatial control of therapeutics delivery and release while leaving particles' surroundings unaffected,[5] it is necessary to understand the local SPION heating mechanism for the development of a more selected and precise local heating upon AMF trigger. Studies have exploited biological[17,18] and chemical methods[19] to demonstrate that the temperature rise localized in the magnetic nanoparticles immediate surroundings. Evidence of a temperature gradient between the MSN and the bulk solution during AMF exposure was also established by the direct use of a nanothermeter.[20] The nanoparticles become much hotter than the surroundings; however, the dominant mechanism for generating this local heat is still unclear.

The goal of this study is to investigate the mechanism of the local heating processes on the nanoscale of the particle and help optimize hyperthermia-based drug release platforms with such understanding of the mechanism. Based on the reported theoretical results,[9,11,12,21] both Néel relaxation and Brownian relaxation could possibly occur when a big amplitude of the AMF as compared to the particle anisotropy field is applied on the SPIONs with average particle size larger than 10 nm, which were synthesized and used in this study. In this work, we adopted a sensitive detection method utilizing fluorescence depolarization technique[22–25] to examine if there is a change in the motion of SPION@MSNs stimulated by AMF. We also synthesized a novel dual-luminescent EuSPION@MSNs with two-separated emission peaks, one from the europium-doped luminescent superparamagnetic core (EuSPIONs) and another from MSN shell, to individually probe the rotating motion of the SPION core and MSN skeleton upon the AMF actuation. Based on the results collected by exposing EuSPION@MSNs to different experimental conditions, we conclude that no additional motion is caused by an AMF, thus contradicting the Brownian explanation and implicating that Néel relaxation dominates the nanoscale heating.

3.2 Theory of Magnetic Heating by SPIONs

The magnetic heating is accomplished by rotating the magnetic moment of each SPION against an energy barrier. The heating of magnetic fluids subjected to an alternating magnetic field (AMF) can be explained by the linear response theory (LRT),[26] which was developed based on the assumption that the heat generation is only due to the rotational relaxation of non-interacting single domain nanoparticles. The LRT model shows an expression of the power dissipation (P),

$$P = \mu_0 \pi \chi'' f H^2 \qquad (1)$$

, where μ_0 is the free space permeability, χ'' is the out-of-phase component of the complex ferrofluid susceptibility, f is the rotation frequency, and H is the magnetic field intensity. This expression agrees with our previous induced heating results which showed that, by varying experimental conditions such as magnetic field induction power and the exposure time to the magnetic field, different heating temperatures could be obtained.[27] Equation (1) can be rewrote as,

$$P = \pi \mu_0 \chi_0 H_0^2 f \frac{2\pi f \tau}{1 + (2\pi f \tau)^2} \qquad (2)$$

, where χ_0 is the actual susceptibility and τ is the effective relaxation time. This equation displays the high dependence of the power dissipation on the two relaxation processes involved in the heat generation, including the Brownian relaxation (characterized by the parameter τ_B) and Néel relaxation (characterized by the parameter τ_N), since the effective relaxation time ($\frac{1}{\tau} = \frac{1}{\tau_B} + \frac{1}{\tau_N}$) is dependent on the collective contributions of both relaxation processes. The particle that has undergone Brownian relaxation produces heat by friction (shear) between SPIONs and the surrounding fluid if conditions such that the rotation of the magnetic moment results in the rotation of the particle itself, that is, particles are free enough to rotate following the applied AMF.[28] The other process that involves the thermal energy dissipation through the rearrangement of atomic dipole moments within the SPIONs is known as Néel relaxation where the magnetic moment rotates following the main AMF while the particle itself remains fixed.[29] Due to the difficulty of confining sufficient thermal energy in a tumor while leaving healthy tissues unaffected, it is important to retrieve information, such as heating parameters, of SPIONs via for the optimization of treatments.

3.3 Synthesis of Lanthanide Ions (Ln)-Doped Luminescent SPIONs

A new class of Ln-doped luminescent SPIONs, possess both optical and magnetic properties associated with their f-block electronic configurations, is introduced. Three different dopants — uranium, terbium, and europium, were incorporated in SPIONs. The Ln-doped SPIONs were synthesized by a thermal decomposition of Fe-oleate in the presence of Ln-oleate (Tb-oleate or Eu-oleate) or uranyl acetate. This synthesis method aims to achieve three goals: (1) a new emission peak at a wavelength that is different from the intrinsic luminescence generated by the defect sites of silica skeleton, (2) spherical morphology of Ln-SPIONs for the easiness of silica coating, and (3) preserved superparamagnetic property of Ln-SPIONs for the magnetic heating under an AMF.

From the emission spectrum of SPIONs with different dopants, it can be seen that only the Eu-doped SPIONs generate an emission peak centered at a 550 nm that is different from that of the silica shell (**Figure 3.1**), whereas both U-doped and Tb-doped have an emission peak at around 450 nm that is overlapping with the emission peak of the silica shell. With the emission peak of Eu-SPIONs fall within the targeted wavelength range, the synthesis procedure of Eu-SPIONs was further optimized so that both morphology and superparamagnetic properties of SPIONs can be preserved after Eu ions doping. It can be seen that complex structure of the as-synthesized Fe oleate by changing washing procedures would influence the morphology of Eu-doped iron oxide nanoparticles.[30] The morphology of Eu-doped iron oxide nanoparticles changed from a spherical shape (**Figure 3.2C**) to cubic shape (**Figure 3.2B**) with an additional ethanol/acetone washing step. This can be explained by the presence/absence of oleic acid, in which oleic acid played an important role in controlling the crystal growth along the <100> or <111> direction of magnetite.[31] The magnetic properties of Eu-doped iron oxide nanoparticles can be improved from a paramagnetic state to a superparamagnetic state by carrying out the synthesis in trioctylamine or benzyl ether, respectively (**Figure 3.2A**). T_B of Eu-doped iron oxide nanoparticles synthesized under different conditions were also measured. T_B of Eu-SPIONs is below 200 K whereas paramagnetic Eu-doped iron oxide nanoparticles obtained T_B that are above 200K. After synthesis optimization, spherical Eu-SPIONs that exhibit luminescence at room temperature were prepared for extended analytical applications using optical methods

3.4 Results and Discussion

3.4.1 Possible Motions of the Core and the Shell caused by AMF

The Brownian heating mechanism of the magnetic core in MSNs could be proven if movement caused by the AMF of the embedded EuSPION and the silica shell were observed. The two possible motions in the presence of the AMF are shown in **Scheme 3.1**. In (a) neither the core nor the shell rotates additionally in response of the applied AMF and in (b) oscillation of embedded core in AMF drives silica shell to rotate with it due to the strong interaction between the hydrophobic ligands on the core and the silica framework. In the case of (a), Néel relaxation would be the dominant mechanism of the heat production. If the SPION core does not physically re-orientate in the AMF, the rearrangement of atomic dipole moments within the SPIONs must occur to generate the observable temperature increase. In the cases of (b), the friction caused by physical rotations of the magnetic core-shell nanoparticles heat up the surroundings, indicating that Brownian relaxation contributes to the nanoenvironment temperature change of the EuSPION@MSN.

3.4.2 Steady-State Degree of Polarization Measurements for AMF-Induced Motions

In this study, the possible motions of the embedded EuSPION and the silica shell caused by the AMF was measured through steady-state fluorescence depolarization spectroscopy using the instrument arrangement shown in **Figure 3.3**. The steady-state depolarization was primarily determined by the stationary orientational distribution of the luminescent molecules at equilibrium state.[32] Therefore, the molecule orientation was monitored by the steady-state degree of anisotropy, r, given by

$$\mathrm{r} = \frac{\mathrm{I}_{\parallel} - \mathrm{I}_{\perp}}{\mathrm{I}_{\parallel} + 2\mathrm{I}_{\perp}} \qquad (3)$$

where $\mathrm{I}_{\parallel}$ and $\mathrm{I}_{\perp}$ are the emission intensities parallel and perpendicular to the polarization direction of the exciting light, respectively. Upon the excitation of a molecule by a polarized continuous-wave light source, the molecules that are aligned with the oriented field vector of the laser beam absorb the light and emit at a later time depending on the fluorescence lifetime.[25] The r can take values between 0 and 0.4. When the laser-excited probe molecule can freely tumble and entirely randomize before emitting at a later time due to the rapid motion, r = 0. A maximum value of 0.4 indicates that the emitter cannot reorient freely. In the case when the rotational correlation time (τ_c) [33,34] of a particle is much longer than its fluorescence lifetime, where the particle rotates too slowly to cause depolarization during the fluorescence lifetime, the fluorescence is only partially depolarized leading to a residual anisotropy.[32] The residual anisotropy values ($0 < r < 0.4$) describe the average angular distribution of the fluorescent probe and thus serve as an index of the angular range of the probe molecules. Therefore, if Brownian relaxation occurs the degree of constraints of probe molecules will be altered in the presence of AMF. The additional orientation of the EuSPION core and intrinsically emitting silica shell of an EuSPION@MSN (> 50 nm) will further depolarize its emission with respect to the vector of excitation, resulting in a decrease of r. Accordingly, the obtained r results were used to analyze the rotating motion of the free cores and the core-shell nanoparticles. After applying AMF, r of the magnetic core and the shell of a core-shell nanoparticle decrease in the case of the Brownian relaxation. On the other hand, r values remain the same on condition that no physical rotation occurs which corresponds to the Néel relaxation shown in **Scheme 3.1**.

3.4.3 Synthesis and Properties of the Luminescent EuSPION

EuSPIONs with diameters of 12 nm (**Figure 3.4a**) were synthesized by a modified thermal decomposition method[35,36] and europium was used as a dopant to make the SPIONs luminescent. The dopant molar ratio (Eu: Fe) of 0.125 was measured by ICP-OES. The luminescence spectrum of the particles consists of a broad emission band between 450-700 nm centered at around 525 nm (**Figure 3.5a**, **Figure S 3.1a**). The excitation spectrum monitored at 550 nm consists of a broad band between 275-525 nm (**Figure S 3.1b**). A similar band was also observed by monitoring the emission at 600 nm (**Figure S 3.1b**). The origins of the emission are the 5d → 4f transitions of the divalent Eu ions in the host Fe_3O_4 crystals. The lowest energy excited state electronic configuration of Eu^{2+} is $4f^65d^1$ instead of $4f^6$ for Eu^{3+}. The outer 5d subshell, which is more sensitive to the surrounding crystal anions compared with the deep-lying 4f subshell, splits to several sublevels according to its crystal symmetry and results in a broad-band emission.[37,38] The occurrence of both divalent and trivalent Eu ions in the EuSPION was confirmed by the XPS (**Figure S 3.1c**). The high-resolution scan binding energy (BE) spectra of europium with an incompletely occupied 4f-subshell exhibits splitting into two separated signals at BE positions of 1135.3 eV and 1165.3 eV corresponding to $Eu^{3+}3d_{5/2}$ and $Eu^{3+}3d_{3/2}$, respectively (**Figure S 3.1c**).[39] Along with the Eu^{3+} ions, doublet positions at 1127.2 eV and 1156.2 eV are in agreement with literature values for Eu^{2+} ions.[39] The XPS data also contain peaks from the core levels of C_{1s}, O_{1s}, and Fe_{2p} (**Figure S 3.1c**). The peaks at 709.0 eV and 722.1 eV were assigned to $Fe_{2p3/2}$ and $Fe_{2p1/2}$, respectively (**Figure S 3.1c**). Note that to access a deeper penetration depth, Ar^+ ion sputtering was performed to strip away surface ligands (oleic acid); the intensities of the carbon and oxygen peaks decreased after the surface ablation process.

3.4.4 Magnetic Properties of Superparamagnetic Luminescent EuSPION

The doping of europium ions resulted in the decrease of the saturation magnetization (M_s) from ~56 emu g^{-1} for SPION to 32 emu g^{-1} for EuSPION (**Figure S 3.2a**), which agrees with the lowering of M_s reported in the literature.[40,41] The EuSPION still possessed superparamagnetic properties at room temperature. The M-H loop showed a zero coercivity at 300 K (**Figure 3.4b**) and the occurrence of hysteresis at a temperature of 5 K (**Figure 3.4b**, inset), which is below T_B = 98 K. T_B, which describes a transition from a magnetically blocked state to a superparamagnetic state, was determined by measuring the temperature dependence of the magnetization in zero-field-cooled (ZFC) and field-cooled (FC) states in an applied magnetic field of 50 Oe (**Figure**

3.4c). The presence of the magnetization difference between the ZFC and FC modes also indicates a superparamagnetic behavior of the synthesized EuSPION.[21] Studies have shown that the physiochemical properties of magnetic particles can be affected by the surface modification.[42,43] Therefore, the M-H loop (**Figure S 3.3a**) and M-T loop (**Figure S 3.3b**) of the magnetic core coated with the mesoporous silica shell were also measured. Although both M_s values of SPION@MSNs and EuSPION@MSNs decreased slightly when compared with M_s value of the respective magnetic core, field-dependent magnetization curves showed the magnetic properties of the EuSPIOs and SPIONs were preserved after the silica coating (Figure **S 3.3**).

The superparamagnetic EuSPIONs were heated by an AMF that was generated using an induction coil and oscillation frequency of 375 kHz. The final bulk temperature in ethanol after approximately 1.5 min of AMF exposure increased from 26 to 29 ^oC using the highest induction power for SPION@MSN and EuSPION@MSN measurements whereas the temperature rose less than 1^oC when low induction power was used. Note that the temperature localized in the core should be higher than the measured bulk temperature. The majority of our measurements were carried out at the temperature mentioned above except for one control experiment with a starting temperature of 50^oC. To characterize the heating of EuSPION under AMF exposure, specific loss power (SLP) was determined from the temperature-time profile of EuSPION in cyclohexane (**Figure S 3.2b**). The temperature of the cyclohexane solution containing EuSPION with a concentration of 4mg/mL achieved 45^oC after 6 min of AMF actuation. The SLP of the SPION was calculated to be 137.9 W/g with an AMF power of 5 kW. Using the measured T_B of EuSPION, the anisotropy constant (K_{eff} = 4.7 x10^3 J/m^3) and the anisotropy energy (H_K = 564 Oe) were calculated (See SI).

3.4.5 Fluorescence Anisotropy Measurements of Free EuSPION

Polarized emission spectra of EuSPION were measured from particles dispersed in organic solvents because the particles, with the hydrophobic end of the coated oleic acid facing outward, do not disperse well in polar solvent. The spectra and anisotropy results are shown in **Figure 3.5a**. The r values for the free EuSPION in hexane are 0.036 both with and without application of the AMF. An oscillation frequency of 375 kHz corresponds to the rotation of the magnetic vector of the AMF by one radian in 4.2×10^{-7} s. The rotational correlation time τ_c, defined as the average time for a molecule to rotate over one radian, is related to the rotational diffusion coefficient (D_{rot}) of the particles by the equation of $\tau_c = t/<\theta^2> = 1/(2D_{rot})$ (See SI). Using the hydrodynamic size of particles acquired by DLS (**Figure S 3.4a**) and the viscosity of dispersions, the calculated $\tau_c = 2.0\text{x}10^{-7}$ s of free EuSPION dispersed in hexane is smaller than the time AMF needed to rotate one radian. To be able to observe the possible motion triggered by the AMF (decrease of r) and examine the dependence of particle motion on solvent viscosity, we dispersed the EuSPIONs in cyclohexane (approximately 3 times more viscous than hexane at room temperature). Due to the increased viscosity, the calculated τ_c increased from $2.0\text{x}10^{-7}$ s to $6.5\text{x}10^{-7}$ s, which is longer than the time the AMF needs to rotate one radian. In other words, the rotational frequency of the AMF is higher than the Brownian diffusion rotation frequency of the EuSPIONs dispersed in cyclohexane. As expected, because r and τ_c are related to the bulk viscosity, r increased to 0.062 due to the slower rotational motion of the particles in cyclohexane (**Figure 3.5b**). The capability of our method to detect the small r variation between particles that are rotating relatively fast (small τ_c) but at different speeds also indicates that further orientation of particles induced by the AMF could be observed as well. Nevertheless, the value r = 0.062 was unchanged upon application of the AMF with different strengths, implying no further motion of the EuSPIONs is triggered. Even though Brownian relaxation is calculated to dominate for particles with diameters > 6 nm,[44] the results suggest that the local heating generated by the EuSPION is dominated by the Néel relaxation. The predominance of Néel relaxation as the origin of the local heating is possibly due to the moderate H_K of the EuSPION in comparison to the applied field H_0, where the magnetic mode, the magnetization oscillations, can be realized.[12]

Figure 3.5b shows that when EuSPIONs were measured in the solid form, the emission spectra of $I_{||}$ and $I_{\perp}$ are almost the same, indicating an isotropic depolarization (r = 0) possibly caused by energy transfer between closely packed Eu ions. The zero r value serves as a negative control for all the r measurements.

3.4.6 Luminescence of the MSN shell

Mesoporous silica has an intrinsic emission in UV-VIS range, peaking at around 450 nm as shown in **Figure 3.6b**. The surfaces of the MSNs in an ambient environment are typically covered by siloxane (Si-O-Si) and silanol groups (Si-OH). The origin of the blue-green photoluminescence from the mesoporous silica network has been assigned to two adjacent facing germinal silylene groups and to a silylene-dioxasilirane pair.[45,46]

3.4.7 Fluorescence Anisotropy Measurements of Core Shell EuSPION@MSN

EuSPION@MSN was made by synthesizing a mesoporous silica shell around the EuSPIONs (**Figure 3.4d**). The independent luminescences from the superparamagnetic core and the silica shell in the green (550 nm, (**Figure 3.6a**)) and blue (450 nm, (**Figure 3.6b**)) regions of the spectrum make it possible to measure simultaneously the effects of the AMF on the motions of the components. The emission spectrum of the core-shell EuSPION@MSN (**Figure 3.6c**) is the sum of the spectra of the individual components. These two bands were fit to the emission spectra of the EuSPION@MSN (Figure 3.6d), and the best fit showed that at 450 nm the spectrum from the silica contributed 75% to the total and the EuSPION core contributed 25%. To calculate the r values for each component, the parallel and perpendicular intensities were measured at 450 nm to maximize the contribution from the silica and at 550 nm to maximize that from the EuSPION (**Figure 3.7a**). The r value calculated from the 450 nm polarized emission spectra was r = 0.180 ± 0.003 and that from the 550 nm emission was r = 0.178 ± 0.004 (**Figure 3.7b**). The motions of the two components are the same within experimental error, implying that the core rotates at the same speed as the shell. These values also did not change in the presence of the magnetic field, i.e., no statistically significant decrease in r in the AMF is evidence of no Brownian component to the mechanism of AMF-induced heating. These results verify scenario (a) in **Scheme 3.1** and show that Néel relaxation is the dominant contributor to the interior temperature rise. Note the decrease in intensity of the fluorescence spectra with increasing AMF is possibly due to the temperature-dependent quantum yield of luminescence.

3.4.8 Fluorescence Anisotropy Measurements of Dye-Doped SPION@MSN-RITC

Further measurements and evaluation of the r measurements were conducted by attaching the fluorescent dye RITC to the core-shell particles (SPION@MSN-RITC) and simultaneously measuring the luminescence of the silica shell and the attached dye (**Figure 3.8a**). It was reported that τ_c of RITC molecules that move freely in solution is in the picosecond time scale while τ_c of dye molecules that are electrostatically bound to the nanoparticles is in the nanosecond time scale.[32] The silica luminescence of SPION@MSN-RITC has r =0.094, similar to that of the un-doped silica shell (**Figure S 3.5c**); whereas, the RITC dye attached to the silica skeleton gives much smaller r =0.023 (**Figure 3.8b**). There are two possible explanations for the small value of r. First, closely spaced RITC molecules attached to interior pore walls or on the outer surface may undergo energy transfer and thus randomize the polarization. Secondly, many of the dyes on the outer surface are still mobile as a result of the long APTES bond and thus depolarize the fluorescence. The observed r value is similar to that of free dye ($r < 0.05$) reported in the literature.[32] Upon AMF application, neither r values of the attached dyes nor the silica shell decreased, indicating no additional motion of the SPION@MSN-RITC is activated.

3.4.9 Fluorescence Anisotropy Measurements of Silica Nanoparticles without a Core

Polarized luminescence spectra of MSNs with a diameter similar to that of the EuSPION@MSNs discussed above were collected for r calculations. Without AMF, the MSNs have an r value ($r = 0.168$) that is almost the same as that of the EuSPION@MSN ($r = 0.178$). After applying AMF, r of the MSNs was not altered by AMF as expected due to the absence of the magnetic core. In the interest of obtaining a positive control for the depolarization experiments as well as further inspecting the slower motion and size effect of particles on r, we synthesized a bulkier and heavier PEI-MSN that is almost twice the size of the MSNs discussed above. The emission maximum of the PEI-MSN slightly shifted due to the attachment of the polymer (**Figure 3.9a**). Because r of the probe molecules depends on the degree of constraints, the obtained r of 0.262 was indeed much larger than the value collected using MSN and other nanoparticles with a smaller size (**Figure S 3.6**), and the results correspond well to the measured τ_c (**Table 3.1**).

The high r value of PEI-MSN has a larger range of variation and allowed measurement of the decrease of r with temperature due to the disrupted degree of orientational constraint. It was observed that r of PEI-MSN did not decrease significantly until a temperature of 60°C was reached (by bulk heating), which is far higher than the temperature reached during the depolarization measurements (**Figure S 3.7**). Because the highest bulk temperature rise caused by the AMF was 30°C, the thermal effect from Brownian rotational diffusion motion on the measured r was negligible. Consequently, the lowering of r, if any, will be due to the mechanic alternation by AMF.

For EuSPION@MSN (at a bulk temperature of ~25°C or 50°C), we did not observe the lowering of r resulted from the whole particle fluctuation along with the vector of AMF (**Figure 3.7**, Figure **S 3.8**). Even when measuring SPION@MSN with a larger core size of 19 nm (**Figure S 3.5c**, **Figure S 3.5f**) that can possibly generate interior heat with more contribution from Brownian relaxation, the rotating motion of the whole particle, i.e., the decrease of the shell r, was still not seen when it was subjected to the AMF (**Figure S 3.5e**). It can thus be concluded that the interior heating of the EuSPION@MSN is dominated by the Néel relaxation mechanism. An observed nonlinear temperature rise when exposed to low and high power actuation also reflects the higher sensitivity of Néel relaxation to the applied magnetic field strength,[47] which further reinforce our conclusion.

3.5 Conclusions

We have utilized fluorescence depolarization to investigate the possible AMF-induced rotational motions of a SPION in suspension and in the core of an MSN based on the residual anisotropy values obtained from the polarized luminescence intensities from the SPION core and intrinsically emitting silica shell. The emission peaks, which are separated by a wavelength of approximately 100 nm, were used to individually probe the motions of the magnetic core and shell under variable AMF induction powers when the particles were dispersed in solvents with different viscosities. The bulk temperature proportionally increased with the magnetic field induction power; however, we observed no additional rotational motion for either the free SPIONs or the silica encapsulated SPION nanoparticles in the presence of AMF. These results show the absence of a Brownian contribution to the heating and thus suggest that Néel relaxation is the dominant contributor to the local heating of the magnetic nanoparticle. To our knowledge, this is the first optical study of the nanoscale heating mechanism of the silica-encapsulated magnetic core. The unique dual-luminescence approach can also be employed to analyze relative core and shell motions of various kinds of nanoparticles used in hyperthermia-based nanotheranostics.

3.6 Experimental Section

3.6.1 Materials and Chemicals

Sodium hydroxide (NaOH) (Fisher), Hexadecyltrimethylammonium bromide (CTAB) (≥99%, Sigma), tetraethyl orthosilicate (TEOS) (≥99%, Sigma), ethyl acetate (≥99.5%, Sigma), L-Arginine (≥98%, Sigma-Aldrich), polyethyleneimine, branched, M.W. 1,800 (PEI) (99%, Alfa Aesar), 3-(Trihydroxysilyl)propyl methyl-phosphonate, monosodium salt, 42 wt% solution in water (HPMP) (Aldrich), aminopropyltriethoxysilane (APTES) (Sigma-Aldrich), rhodamine B isothiocyanate (RITC) (Sigma), iron(III) chloride hexahydrate ($FeCl_3 \cdot 6H_2O$) (≥98%, Aldrich), europium(III) chloride hexahydrate ($EuCl_3 \cdot 6H_2O$) (99.9%, Aldrich), Sodium oleate (99%, TGI), oleic acid (90%, Aldrich), hexane (≥98.5%, Fisher), cyclohexane (≥99%, Macron), chloroform (99.9%, EMD), benzyl ether (98%, Aldrich), ammonium nitrate (95%, Alfa Aesar) were used. All chemicals were reagent grade and used without further purification or modification.

3.6.2 Nanoparticles Synthesis

Synthesis of MSNs. Unfunctionalized MSNs were synthesized following a previously reported procedure with a slight modification.[48] In brief, 250 mg of CTAB was dissolved in 120 mL water, followed by the addition of 875 μL of NaOH solution (2.000M) under stirring. The solution was heated at 85°C for 30 min. After the temperature stabilized, 1200 μL of TEOS and 0.8 mL of ethyl acetate were added dropwise to the solution under vigorous stirring. The solution was kept at 85°C with stirring for another 2 h. After the solution was cooled to room temperature, the nanoparticles were collected by centrifugation (12 min at 7830 rpm), washed 2x with ethanol and then were dispersed in 50 mL of ethanol containing 1g of ammonium nitrate for surfactant removal.

The solution was refluxed at 60°C for 1 h under stirring. Afterward, the nanoparticles were washed 2x with water and 2x with ethanol. The removal procedure was repeated twice, and the nanoparticles were redispersed in 20 mL of ethanol.

Synthesis of PEI-MSNs. The attachment of PEI on the surface of MSN was performed according to a published procedure.[49] A similar experiment was carried out as that for MSN. Instead of adding ethyl acetate, the solution was heated at 85°C for another 30 min, followed by the addition of 250 μL of HPMP solution (diluted to 1.5 mL with water) under vigorous stirring. Stirring was continued for 1.5 h at 85°C, and the solution was allowed to cool to room temperature. The surfactant was extracted with the same removal procedure. Afterward, the nanoparticles were mixed with PEI (4:1) for 1 h twice, washed 2x with ethanol, and redispersed in ethanol for measurement.

Synthesis of SPIONs. SPIONs were synthesized by a modified thermal decomposition method.[35,36] Briefly, $FeCl_3 \cdot 6H_2O$ (2 mmol) and sodium oleate (0.2 mmol) were dissolved in a mixture of solvent (14 mL) composed of ethanol, Millipore water, and hexane with a ratio of 4:3:7. The resulting solution was refluxed at 70°C for 4 h. The solution was transferred to a separatory funnel, and the top organic layer containing the Fe-oleate was washed 3x with warm water (3x 5 mL). Afterward, hexane was allowed to evaporate at 70°C overnight. The Fe-oleate complex precursor was dispersed in 10 mL of benzyl ether containing 1.5 mmol of oleic acid. The mixture was degassed with N_2 under stirring for 30 min at room temperature. Then, the mixture was heated to 200°C at a heating rate of 3°C min^{-1}, kept at that temperature for 2h, and then heated to 300°C with the same heating rate. The mixture was allowed to reflux and age at this temperature for 1 h before cooling down to room temperature under N_2. After that, ethanol was added to precipitate the black product. The precipitate was collected by centrifugation, washed 3x with ethanol, and redispersed in hexane containing 50 µL of oleic acid.

Synthesis of EuSPIONs. A similar experiment was carried out to that for SPION to synthesize EuSPION. Besides the Fe-oleate complex, Eu-oleate complex was also prepared using 0.2 mmol of $EuCl_3 \cdot 6H_2O$. Two washed complexes were combined together and heated at 70°C overnight to evaporate hexane. All other procedures were the same.

Synthesis of SPION@MSN, EuSPION@MSN, and SPION@MSN-RITC. The synthesis of SPION@MSN started with transferring SPION from the organic layer to aqueous layer with the help of CTAB.[13,16] In brief, SPION were dissolved in chloroform at a concentration of 2.5 mg/mL. 140 mg of CTAB was dissolved at 45 mL of Millipore water at 37°C. Two milliliters of the SPION solution were added to the transparent CTAB solution, and the mixture was sonicated for 10 min and probe-sonicated (40% output) for another 5 min to generate an oil-in-water emulsion. The resulting emulsion was heated at 70°C for 15 min to evaporate chloroform. The clear colloidal SPION in aqueous solution was probe-sonicated for another 5 min before heated to 80°C. After solution temperature was stabilized, 20 mg of L-Arginine was added, followed by the dropwise addition of TEOS (225 µL). The solution was allowed to react under stirring at 80°C for 3 h, and the same surfactant removal procedure was carried out. EuSPION@MSN were synthesized following the same procedure except EuSPION were used instead of SPION. A similar synthesis procedure was carried out to that for SPION@MSN-RITC except RITC-APTES solution was added with the TEOS.[50]

3.6.3 Optical Measurements

In the static fluorescence anisotropy studies, the emission anisotropy was measured at a dilute concentration (< 1mg/mL) where the scattering of exciting and emitting light was minimized. The sample in a quartz cuvette was excited at 377 nm continuously by a vertically polarized Coherent CUBE diode laser with a polarization ratio of 100:1. Before transmitting through the sample solution, the laser spot was focused to about 100 μm, allowing for good spatial resolution. The luminescence of the sample was guided to a Glan-Thompson polarizer placed in front of the monochromator with a 300 groove/mm grating. The polarizer allowed only parallel or perpendicular emission components to pass through at a given time. To test the set-up of the optics, an isotropic light source was used, and the resulting intensity difference between parallel and perpendicular measurements was < 0.5%. A 435 nm cut-on filter was placed in front of the polarizer. A depolarizer (scrambler) was placed in front of the slit to reduce the polarization bias caused by the grating (Figure 3.3). The slit was wide-open (300 μm) to eliminate deflection effects when turning the polarizer. Luminescence data in image mode was also collected before measurements to make sure all the pixels containing luminescence signals fall within the defined ROI on the CCD chip. During the experiment, each polarization measurement was carried out with an exposure time of 5s. Emission spectra were recorded in the 435-700 nm range. For each experimental condition, the measurement was repeated five times. For collecting the emission of solid EuSPION, the laser beam was shined on the powder loaded in a capillary tube.

Fluorescence excitation spectra were measured with a Horiba Fluorometer PTI QM-400. Parameters were set as following: Slit= 5nm, step size= 1s, integration= 0.1s, bios=-0.25. Spectra were collected after automatic background correction. Data processing were conducted using MATLAB software. (1) Spectra De-noise: the ‘cmddenoise’ function from MATLAB wavelet toolbox was applied to all spectra. Wavelet ‘sym4’ was used. The level of the decimated wavelet transform was set 5 and the number of intervals was set 3. Default threshold rule was used. (2) Spectra Fitting: the ‘lsqcurvefit’ function was used to estimate the emission components of the

EuSPION@MSN spectra at different wavelengths. The emission peaks at 435-472 nm and 532-546 nm of EuSPION@MSN were fitted by multiplying the same wavelength ranges of MSN and EuSPION emission spectrum, respectively, with different ratio-factors using nonlinear least-squares solver.

3.6.4 AMF-Induced Superparamagnetic Heating

Magnetic heating was carried out using a Magnetic Hyperthermia System manufactured by MSI Automation, Inc. The five-turn copper coil diameter and height were 50 mm, the oscillation frequency was 375 kHz, and the induction power was set at 5 kW for the “high power” measurements and 2.5 kW for the “low power” measurements. The magnetic field strengths were 250 Oe and 125 Oe for the high and low power settings, respectively.

3.6.5 Characterization

Superconducting quantum interference device (SQUID) Quantum Design MPMS7 magnetometer was used to confirm the superparamagnetic behavior of the SPION and EuSPION. The field-dependent magnetization of SPION and EuSPION were measured at both 5K and 300K and the M vs. T in an applied magnetic field of 50 Oe. Measurement of Specific Loss Power (SLP) was carried out to investigate the heat-generation efficiency of EuSPION. The EuSPIONS were dispersed in cyclohexane (4 mg/mL) in a 2 mL vial. The temperature of the bulk was recorded as a function of AMF (5 kW) trigger time. The sample was well insulated from the coil and the minimum heat transfer from the coil to the solvent was subtracted from the data. The calculation of specific heat loss power of EuSPION is shown in Supporting Information.

Inductively coupled plasma optical emission spectroscopy (ICP-OES) using a Shimadzu ICPE-9000 instrument was carried out to determine the iron/europium ratio of EuSPION quantitatively. 5 mg of EuSPION powder was dissolved in 10 mL of the nitric acid solution for digestion and was diluted with 2.5% nitric acid for measurement. 0-20 ppm calibration curves for iron and europium were created. X-ray photoelectron spectroscopy (XPS) was carried out using a Thermo Scientific ESCALAB 252 Xi to confirm the presence of europium. For the high-resolution scans, 40 eV pass energy with 0.1 eV step size was used. The cleaning process was performed by bombarding the surface of a sample (2x2mm) for a few minutes using high kinetic energy Ar^+ ions. Carbon signal was set to 285 eV for energy calibration. Transmission electron microscopy (TEM) images were required on a Tecnai T12 Quick CryoEM and CryoET (FEI) with an operating voltage of 120 kV. A suspension (0.2mg/mL, 5 μL) of SPION or MSN nanoparticles in hexane or ethanol, respectively, was dropped on a 200-mesh carbon-coated copper grid, followed by solvent evaporation at room temperature. Zeta-potential analysis and dynamic light scattering (Zeta/DLS) were acquired on a ZetaSizer Nano (Malvern Instruments Ltd., Worcestershire, U.K.) in Millipore water and hexane for MSN and SPION, respectively. Zeta-potential values confirmed the successful attachment of PEI polymer on the surface of MSN. DLS gave the average diameter of particles at room temperature.

3.7 Acknowledgment

The authors thank Dr. Ignacio Martini, Dr. Bastian Ruehle, Dr. Chao-Hsiung Hsu, and Dr. Emily Cosco for technical assistance.

3.8 Schemes and Figures

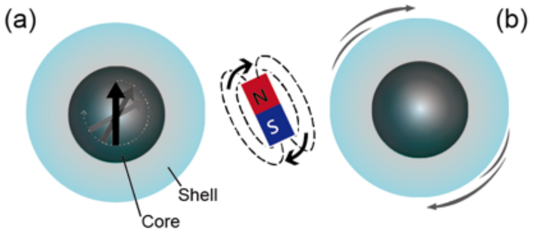

Scheme 3.1 Two possible scenarios of the nanoparticle rotational motion under AMF exposure. Scenario (a) shows that only the internal magnetization vector moves (Néel relaxation) whereas scenario (b) shows that the entire particle moves (Brownian relaxation).

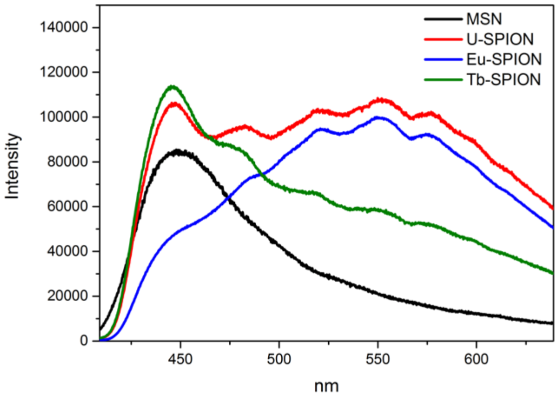

Figure 3.1 Emission spectra of Ln-doped SPIONs (Ex. 377 nm) in hexane, including U-SPIONs, Eu-SPIONs, and Tb-SPIONs.

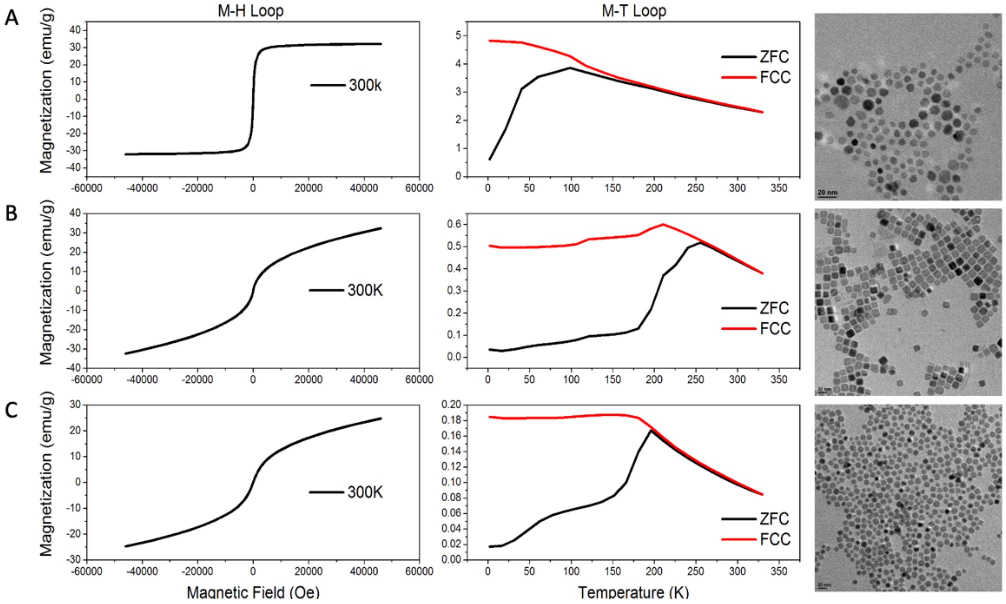

Figure 3.2 Field-dependent magnetization curves (M-H loop) at 300K, ZFC/FC modes of Temperature-dependent magnetization curves (M-T loop) under an applied magnetic field of 50 Oe, and TEM images of EuSPIONs synthesized under different experimental conditions.

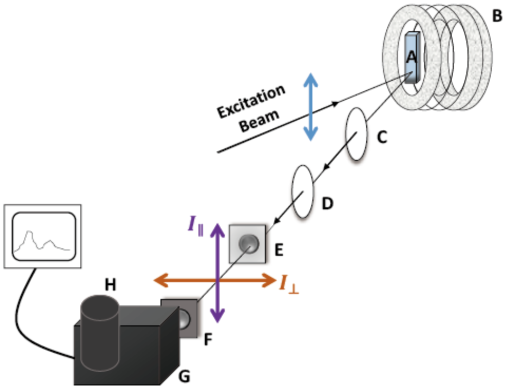

Figure 3.3 Experimental arrangement combining AMF with fluorescence spectroscopy. Components are as follows: (A) sample, (B) five-turn AMF coil, (C) collecting lens, (D) focusing lens, (E) polarizer, (F) depolarizer, (G) monochromator, (H) CCD detector. The sample was excited by a vertically polarized laser pulse with an excitation wavelength of 377 nm.

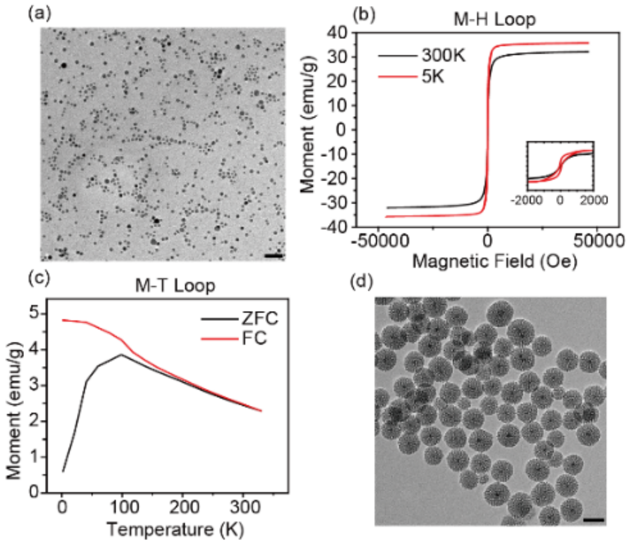

Figure 3.4 (a) TEM image of EuSPIONs. (Black bar scales 50 nm) (b) Field-dependent magnetization curves (M-H loop) of EuSPIONs at 300K and 5K (inset: magnification of M-H curves from -2000 to 2000 Oe at 300K and 5K). (c) ZFC/FC modes of Temperature-dependent magnetization curves (M-T loop) of EuSPIONs under an applied magnetic field of 50 Oe. Blocking temperature of EuSPIONs was determined to be 98K. (d) TEM image of EuSPION@MSNs.

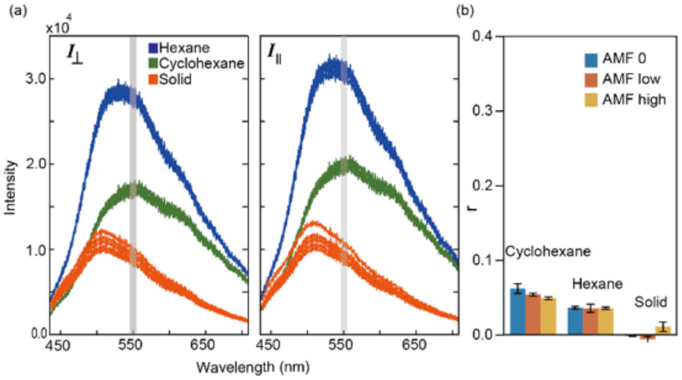

Figure 3.5 (a) Polarized emission spectra of EuSPIONs (Ex. 377 nm) in hexane, cyclohexane, and in solid form. (b) Corresponding r collected at 550±5 nm in different AMF strengths.

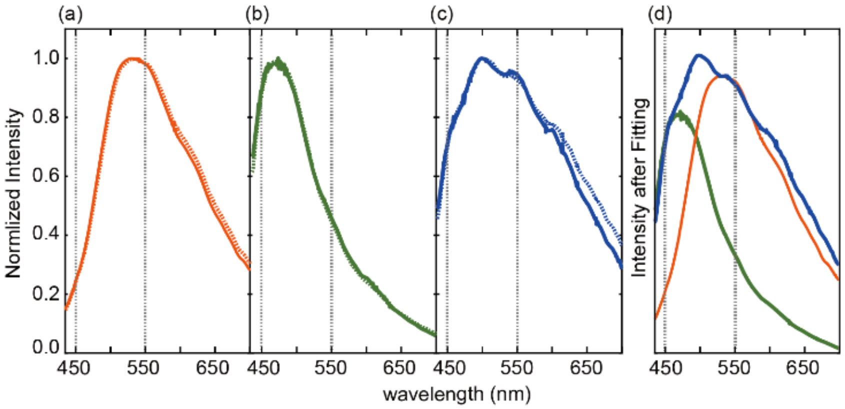

Figure 3.6 The normalized emission spectra for (a) EuSPIONs, (b) MSNs, and (c) EuSPION@MSNs (Solid line: $I_{\parallel}$ dots: $I_{\perp}$). (d) Fitting of EuSPIONs and MSNs emission peaks in emission spectra of EuSPION@MSNs. Silica shell and EuSPIONs contribute approximately 75% intensity to the emission of EuSPION@MSNs at 450nm and 550nm, respectively.

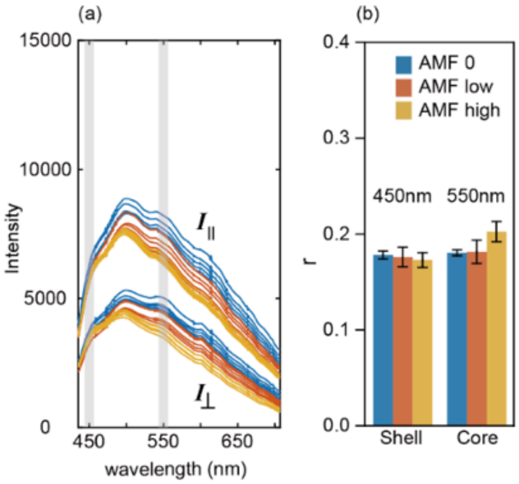

Figure 3.7 (a) Polarized ($I_{\parallel}$ and $I_{\perp}$) emission spectra of EuSPION@MSNs (Ex. 377 nm) in ethanol. (b) r of luminescent magnetic core and silica shell of EuSPION@MSNs in different AMF strength. (Luminescence of shell collected at 450±5 nm and core at 550±5 nm).

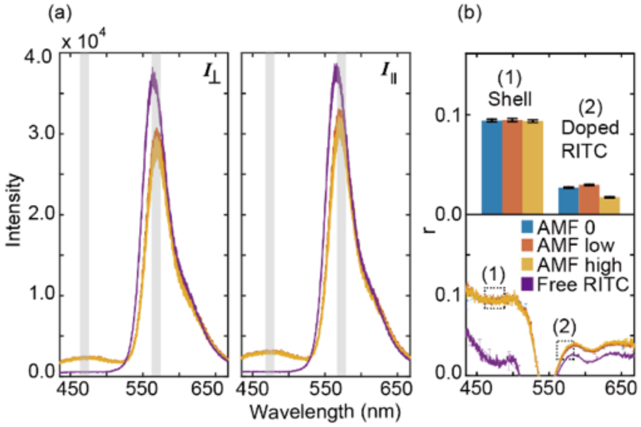

Figure 3.8 (a) Polarized emission spectra of SPION@MSNs-RITC and free RITC dye in ethanol (at the 570 nm emission maximum). The blue band that corresponds to the silica shell only appeared when SPION@MSNs-RITC was measured. (b) r of the silica shell and the doped RITC dye in different AMF strengths collected at 465±5 nm and 570±5 nm, respectively. (Ex: 377 nm)

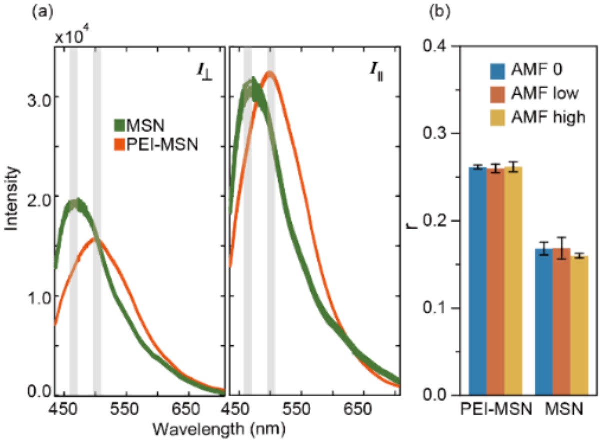

Figure 3.9 (a) Polarized emission spectra of MSNs and PEI-MSNs in ethanol (Ex. 377 nm). (b) r of various MSNs in different AMF strengths. The wavelength with maximum emission peak intensity (MSN=465±5 nm and PEI-MSN=500±5 nm) was used to calculate each r. For each experimental condition, the measurement was repeated five times.

3.9 Supporting Information

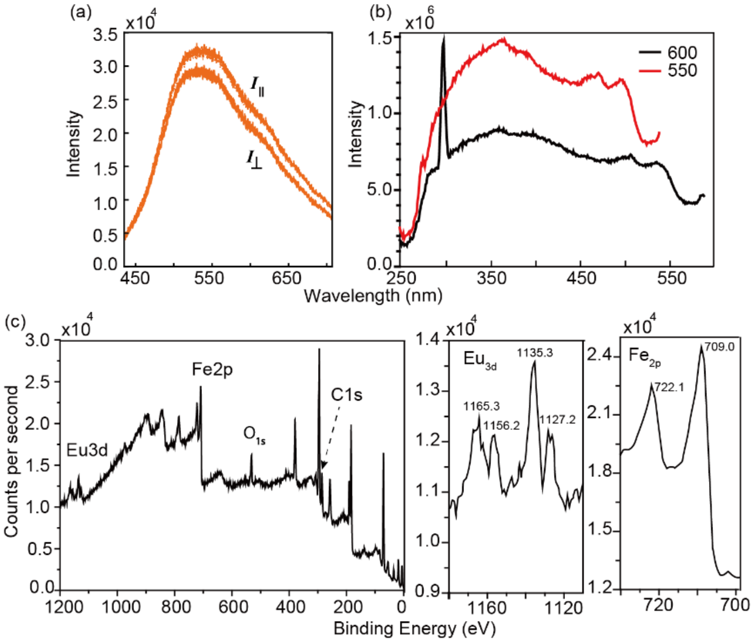

Figure S 3.1 (a) Polarized and depolarized emission spectra of EuSPIONs with an excitation wavelength of 377 nm. (b) Fluorescence excitation spectra of EuSPIONs monitored at 550 and 600 nm. EuSPIONs were dispersed in hexane for the optical measurements. (c) High-resolution XPS spectra of EuSPIONs and the enlarged Eu and Fe regions of EuSPIONs XPS spectra.

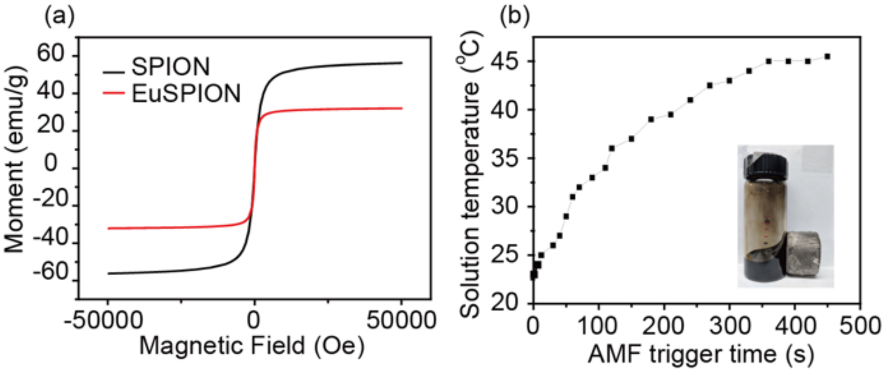

Figure S 3.2 (a) Field-dependent magnetization curves (M-H loop) of SPIONs and EuSPIONs at 300K. (b) Temperature-time profile of a cyclohexane solution (4mg/ml) containing EuSPIONs in AMF. (Image: EuSPIONs respond to an external magnetic field.)

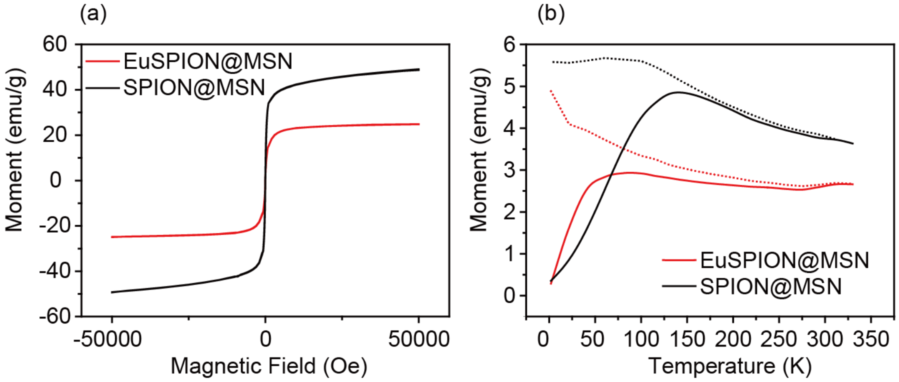

Figure S 3.3 (a) Field-dependent magnetization curves (M-H loop) of SPION@MSNs and EuSPION@MSNs at 300K. Both M_s values of SPION@MSNs (~46.5 emu/g) and EuSPION@MSNs (~24.4 emu/g) decreased when compared with the M_s value of the respective magnetic core. (b) ZFC/FC modes of Temperature-dependent magnetization curves (M-T loop) of SPION@MSNs and EuSPION@MSNs under an applied magnetic field of 50 Oe (Solid: ZFC, Dots: FC). Blocking temperatures were determined to be 143K and 90K for SPION@MSNs and EuSPION@MSNs, respectively.

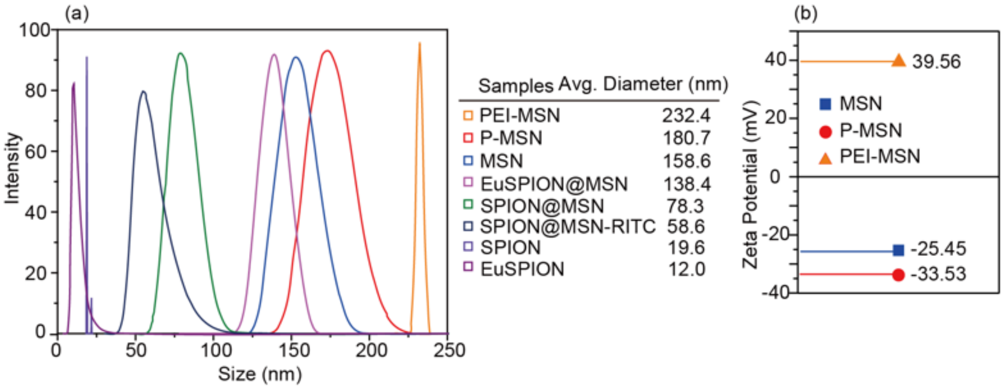

Figure S 3.4 (a) Characterization of the nanoparticles'sizes using DLS. (b) The positive zeta potential value shows the successful attachment of PEI-MSNs. The nanoparticles were dispersed in deionized water (pH=7).

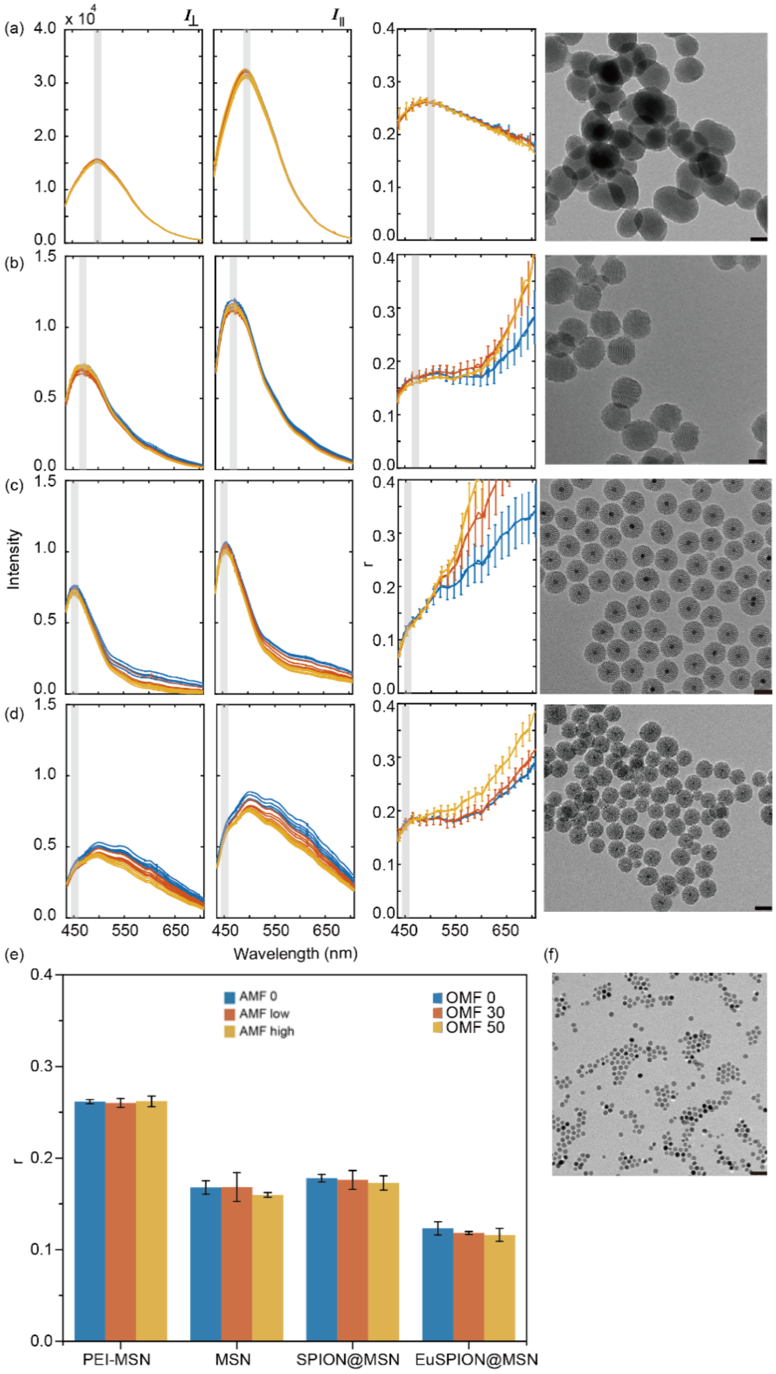

Figure S 3.5 Polarized emission spectra, r, and TEM images of (a) PEI-MSNs, (b) MSNs, (c) SPION@MSNs, and (d) EuSPION@MSNs in ethanol. (Scale bar: 50 nm) (e) r calculated from the silica shell photoluminescence of particles under different induction powers of AMF. (500±5 nm for PEI-MSNs and 450±5 nm for the others) (f) TEM images of SPIONs (Scale bar: 50 nm). Each bar is the average of five measurements. The induction power was set at 5 kW for the "high power" measurements and 2.5 kW for the "low power" measurements.

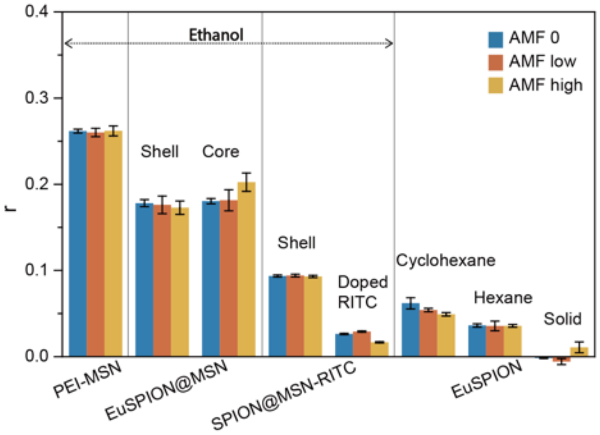

Figure S 3.6 Comparison of r calculated from the emission spectra of PEI-MSNs (500±5 nm), EuSPION@MSNs (shell: 450±5 nm blue band, core: 550±5 nm green band), SPION@MSNs-RITC (shell: 465±5 nm blue band, doped RITC on shell: 570±5 nm), EuSPIONs in cyclohexane, EuSPIONs in hexane, and dry EuSPION powder (550±5 nm) with different AMF induction powers (5 kW for the "high power" measurements and 2.5 kW for the "low power" measurements).

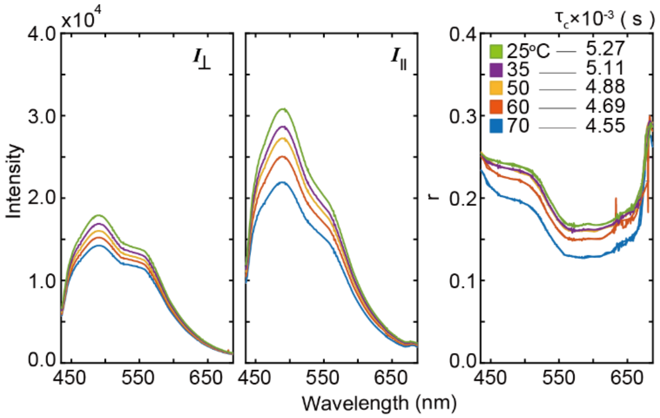

Figure S 3.7 (a) Polarized emission spectra and the r of PEI@MSNs in ethanol measured at temperatures of 25, 35, 50, 60, and 70^{o}C. (b) r started to decrease after reaching a threshold temperature (~ 60^{o}C). The decrease of emission intensity shown on the polarized emission spectra is due to the temperature-dependent quantum yield of luminescence.

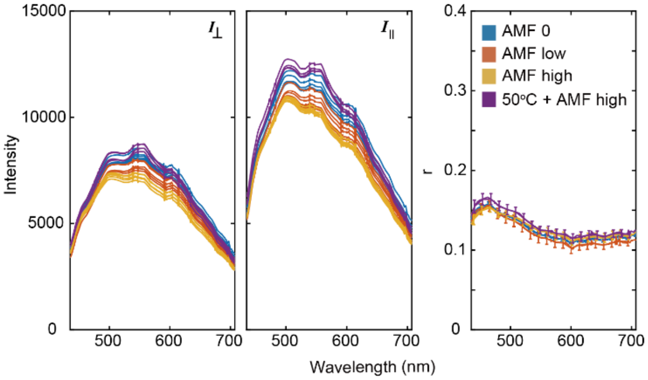

Figure S 3.8 (a) Polarized emission spectra and the r of EuSPION@MSNs in ethanol measured at ~25°C in the absence of AMF (AMF 0), in the presence of AMF (AMF low and AMF high), and at ~50°C of the pre-heated sample followed by AMF exposure using the high induction power. The difference of r values at different experimental conditions is minimal, indicating Néel relaxation is the only heating mechanism presents at a temperature range of 25°C-50°C. The induction power was set at 5 kW for the "high power" measurements and 2.5 kW for the "low power" measurements.

Calculation of specific loss power (SLP) , The anisotropy constant (K_{eff}), and the anisotropy field (H_K) of EuSPION:

SLP = $(CV_s/m)(dT/dt)$

where C is the volumetric heat capacity of the solution, V_s is the volume of solution, m is the mass of the particle, and dT/dt is the initial slope of the temperature rise vs. time curve for the particle heating. Therefore, SLP of EuSPION in cyclohexane:

$$\text{SLP} = \frac{2.75843\ \text{J mL}^{-1}\text{K}^{-1} \times 1\ \text{mL}}{4\times10^{-3}\text{g}} \times \frac{1\ \text{K}}{5\ \text{s}} = 137.9\ \text{Wg}^{-1}$$

The anisotropy constant (K_{eff}) of the EuSPION can be estimated by the measured T_B based on the following equation:

$T_B = K_{eff} V/(25K_B)$

where K_B is the Boltzman constant and V is the volume of the particle.

$$\mathrm{K_{eff}} = \frac{25 \times 98\mathrm{K} \times 1.38 \times 10^{-23} \times 3\ \mathrm{m^2 \cdot kg \cdot s^{-2} \cdot K^{-1}}}{4 \times \pi \times (12 \times 10^{-9})^3\ \mathrm{m^3}} = 4.671 \times 10^3\ \mathrm{J \cdot m^{-3}}$$

$$= 4.671 \times 10^4\ \mathrm{erg \cdot cm^{-3}}$$

The particle anisotropy field (H_K) can be estimeated using the calculated K_{eff}, as shown:

$H_K = 2\ K_{eff}/M_s$

where the saturation magnization (M_s) in units of emu/ cm^3 was obtained assuming that the density of EuSPION is similar to that of magnetite (ρ= 5.175 g/cm^3).

$$\mathrm{H_K} = \frac{2 \times 4.671 \times 10^4\ \mathrm{erg \cdot cm^{-3}}}{32\ \mathrm{emu \cdot g^{-1}} \times 5.175\ \mathrm{g \cdot cm^{-3}}} = 564.13\ \mathrm{erg \cdot emu^{-1}} \approx 0.5\mathrm{H_0}$$

where H_0 is the magnetic field strength.

Calculation of rotational diffusion coefficient of particles:

$D_{rot} = kT/f_{rot}$

where k is Boltzmann's constant, T is the temperature, and $f_{rot} = 6\eta V$ is defined as a friction coefficient where η is an effective microscopic viscosity and V is the hydrodynamic volume of a sphere. f_{rot} can be written with respect to the radius (R) of the particles,

$f_{rot}=6\eta V=8\eta\pi R^3$

The mean-square angular deviation of the angle θ by which a vector bound to a particle rotates about a single axis in time t is

$\langle\theta^2\rangle=2D_{rot}t$

The rotational correlation time (τ_c) is defined as the average time for a molecule to rotate over one radian, which gives

$\tau_c = 1/(2D_{rot})$

Note that in order to compare with the Brownian time constant of Brownian relaxation, the one-dimensional system was used for calculating τ_c of particles.

Sample	Emitter	τ_c	AMF 0	AMF low	AMF high
EuSPION	EuSPION	n/a	-0.002±0.001	-0.006±0.003	0.011±0.006
EuSPION $_{\text{hexane}}$	EuSPION	$2.0\text{x}10^{-7}$	0.036±0.002	0.036±0.006	0.036±0.002
EuSPION $_{\text{cyclohexane}}$	EuSPION	$6.5\text{x}10^{-7}$	0.061±0.007	0.054±0.002	0.049±0.002
EuSPION@MSN	MSN	$1.1\text{x}10^{-3}$	0.178±0.004	0.176±0.010	0.173±0.009
EuSPION@MSN	EuSPION	$1.1\text{x}10^{-3}$	0.180±0.003	0.182±0.012	0.202±0.011
Free RITC	RITC	n/a	0.023±0.001	n/a	
SPION@MSN-RITC	RITC	n/a	0.023±0.001	0.026±0.001	0.029±0.001
SPION@MSN-RITC	MSN	$8.4\text{x}10^{-5}$	0.094±0.001	0.094±0.002	0.093±0.001
SPION@MSN	MSN	$2.0\text{x}10^{-4}$	0.123±0.007	0.118±0.002	0.116±0.007
MSN	MSN	$1.7\text{x}10^{-3}$	0.168±0.007	0.168±0.012	0.160±0.003
PEI-MSN	MSN	$5.3\text{x}10^{-3}$	0.262±0.002	0.260±0.005	0.262±0.006

Table 3.1 r of all measurements in the absence/presence of the AMF. The τ_c of each nanoparticle in the absence of the AMF was calculated. The τ_c of each nanoparticle correlated well with the obtained r. Larger τ_c gives rise to larger r and vice versa. The magnetic vector of a AMF with an oscillation frequency of 375 kHz takes 4.24×10^{-7}s to rotate one radian.

3.10 References

(1) Revia, R. A.; Zhang, M. Magnetite Nanoparticles for Cancer Diagnosis, Treatment, and Treatment Monitoring: Recent Advances. *Mater. Today* 2016, 19, 157–168.

(2) Knežević, N.; Gadjanski, I.; Durand, J. O. Magnetic Nanoarchitectures for Cancer Sensing, Imaging and Therapy. *J. Mater. Chem. B* 2019, 7 (1), 9–23.

(3) Cardoso, V. F.; Francesko, A.; Ribeiro, C.; Bañobre-López, M.; Martins, P.; Lanceros-Mendez, S. Advances in Magnetic Nanoparticles for Biomedical Applications. Adv. Healthc. *Mater.* 2018, 7 (5), 1–35.

(4) Lee, J. H.; Kim, J. W.; Cheon, J. Magnetic Nanoparticles for Multi-Imaging and Drug Delivery. *Mol. Cells* 2013, 35 (4), 274–284.

(5) Chang, D.; Lim, M.; Goos, J. A. C. M.; Qiao, R.; Ng, Y. Y.; Mansfeld, F. M.; Jackson, M.; Davis, T. P.; Kavallaris, M. Biologically Targeted Magnetic Hyperthermia: Potential and Limitations. *Front. Pharmacol.* 2018, 9.

(6) Wu, W.; Wu, Z.; Yu, T.; Jiang, C.; Kim, W. S. Recent Progress on Magnetic Iron Oxide Nanoparticles: Synthesis, Surface Functional Strategies and Biomedical Applications. Sci. Technol. *Adv. Mater.* 2015, 16 (2).

(7) Lin, F. C.; Hsu, C. H.; Lin, Y. Y. Nano-Therapeutic Cancer Immunotherapy Using Hyperthermia-Induced Heat Shock Proteins: Insights from Mathematical Modeling. *Int. J. Nanomedicine* 2018, 13, 3529–3539.

(8) Norris, M. D.; Seidel, K.; Kirschning, A. Externally Induced Drug Release Systems with Magnetic Nanoparticle Carriers: An Emerging Field in Nanomedicine. *Adv. Ther.* 2019, 2.

(9) Rosensweig, R. E. Heating Magnetic Fluid with Alternating Magnetic Field. *J. Magn. Magn. Mater.* 2002, 252, 370–374.

(10) Daniela, C.; Gabriel, C.; Charles, J. O. Magnetic Properties of Variable-Sized Fe3O4 Nanoparticles Synthesized from Non-Aqueous Homogeneous Solutions of Polyols. *J. Phys. D. Appl. Phys.* 2007, 40 (19), 5801.

(11) Shah, R. R.; Davis, T. P.; Glover, A. L.; Nikles, D. E.; Brazel, C. S. Impact of Magnetic Field Parameters and Iron Oxide Nanoparticle Properties on Heat Generation for Use in Magnetic Hyperthermia. *J. Magn. Magn. Mater.* 2015, 387, 96–106.

(12) Usov, N. A. Dynamics of Magnetic Nanoparticle in a Viscous Liquid : Application to Magnetic Nanoparticle Hyperthermia Dynamics of Magnetic Nanoparticle in a Viscous Liquid : Application to Magnetic Nanoparticle Hyperthermia. *J. Appl. Phys.* 2012, 112 (023901).

(13) Rühle, B.; Datz, S.; Argyo, C.; Bein, T.; Zink, J. I. A Molecular Nanocap Activated by Superparamagnetic Heating for Externally Stimulated Cargo Release. *Chem. Commun.* 2016, 52, 1843–1846.

(14) Chen, W.; Cheng, C.-A.; Zink, J. I. Spatial, Temporal, and Dose Control of Drug Delivery Using Non-Invasive Magnetic Stimulation. *ACS Nano* 2019, 13, 2, 1292-1308.

(15) Saint-Cricq, P.; Deshayes, S.; Zink, J. I.; Kasko, A. M. Magnetic Field Activated Drug Delivery Using Thermodegradable Azo-Functionalised PEG-Coated Core-Shell Mesoporous Silica Nanoparticles. *Nanoscale* 2015, 7 (31), 13168–13172.

(16) Thomas, C. R.; Ferris, D. P.; Lee, J. H.; Choi, E.; Cho, M. H.; Kim, E. S.; Stoddart, J. F.; Shin, J. S.; Cheon, J.; Zink, J. I. Noninvasive Remote-Controlled Release of Drug Molecules in Vitro Using Magnetic Actuation of Mechanized Nanoparticles. *J. Am. Chem. Soc.* 2010, 132 (31), 10623–10625.

(17) Hamad-schifferli, K.; Schwartz, J. J.; Santos, A. T.; Zhang, S.; Jacobson, J. M. Remote Electronic Control of DNA Hybridization through Inductive Coupling to an Attached Metal Nanocrystal Antenna. *Nature* 2002, 415, 152–155.

(18) Stanley, S. A.; Gagner, J. E.; Damanpour, S.; Yoshida, M.; Dordick, J. S.; Friedman, J. M. Radio-Wave Heating of Iron Oxide Nanoparticles Can Regulate Plasma Glucose in Mice. *Science*. 2012, 336, 604–608.

(19) Chiu-lam, A.; Rinaldi, C.; Family, J. C. P. Nanoscale Thermal Phenomena in the Vicinity of Magnetic Nanoparticles in Alternating Magnetic Fields. *Adv Funct Mater.* 2016, 26 (22), 3933–3941.

(20) Dong, J.; Zink, J. I. Taking the Temperature of the Interiors of Magnetically Heated Nanoparticles. *ACS Nano* 2014, 8 (5), 5199–5207.

(21) Caruntu, D.; Caruntu, G.; O'Connor, C. J. Magnetic Properties of Variable-Sized Fe3O4 Nanoparticles Synthesized from Non-Aqueous Homogeneous Solutions of Polyols. *J. Phys. D. Appl. Phys.* 2007, 40 (19), 5801–5809.

(22) Mckieman, J. M.; Dunn, B.; Zink, J. I.; Hurd, A. J. In Situ Fluorescence Probing of the Chemical Changes during Sol-Gel. *J. Am. Ceram. Soc.* 1995, 78 (6), 1640–1648.

(23) Huang, M. H.; Soyez, H. M.; Dunn, B. S.; Zink, J. I. In Situ Fluorescence Probing of Molecular Mobility and Chemical Changes during Formation of Dip-Coated Sol - Gel Silica Thin Films. *Chem. Mater* 2000, 12, 231–235.

(24) Franville, A. C.; Dunn, B.; Zink, J. I. Molecular Motion and Environmental Rigidity in the Framework and Ionic Interface Regions of Mesostructured Silica Thin Films. *J. Phys. Chem. B* 2001, 105 (42), 10335–10339.

(25) Huang, M. H.; Soyez, H. M.; Dunn, B. S.; Zink, J. I.; Sellinger, A.; Brinker, C. J. In Situ Fluorescence Probing of the Chemical and Structural Changes during Formation of Hexagonal Phase Cetyltrimethylammonium Bromide and Lamellar Phase CTAB/Poly(Dodecylmethacrylate) Sol-Gel Silica Thin Films. *J. Sol-Gel Sci. Technol.* 2008, 47 (3), 300–310.

(26) Rosensweig, R. E. Heating Magnetic Fluid with Alternating Magnetic Field. *J. Magn. Magn. Mater.* 2002, 252, 370–374.

(27) Dong, J.; Zink, J. I. Taking the Temperature of the Interiors of Magnetically Heated Nanoparticles. *ACS Nano* 2014, 8 (5), 5199–5207.

(28) Rosales, A. M.; Aznar, E.; Coll, C.; Mendoza, R. A. G.; Bojorge, A. L. U.; González, N. F.; Martínez-Máñez, R.; Guerrero, F. del P.; Olmedo, J. J. S. Study of the Dependency of the Specific Power Absorption Rate on Several Characteristics of the Excitation Magnetic Signal When Irradiating a SPION-Containing Ferrofluid. *J. Magn.* 2016, 21 (3), 1–8.

(29) Deatsch, A. E.; Evans, B. A. Heating Efficiency in Magnetic Nanoparticle Hyperthermia. *J. Magn. Magn. Mater.* 2014, 354, 163–172.

(30) Bronstein, L. M.; Huang, X.; Retrum, J.; Schmucker, A.; Pink, M.; Stein, B. D.; Dragnea, B. Influence of Iron Oleate Complex Structure on Iron Oxide Nanoparticle Formation. *Chem. Mater.* 2007, 19 (15), 3624–3632.

(31) Yang, J.; Kou, Q.; Liu, Y.; Wang, D.; Lu, Z.; Chen, L.; Zhang, Y.; Wang, Y.; Zhang, Y.; Han, D.; Xing, S. G. Effects of Amount of Benzyl Ether and Reaction Time on the Shape and Magnetic Properties of Fe3O4 Nanocrystals. *Powder Technol.* 2017, 319, 53–59.

(32) Tleugabulova, D.; Duft, A. M.; Zhang, Z.; Chen, Y.; Brook, M. A.; Brennan, J. D. Evaluating Formation and Growth Mechanisms of Silica Particles Using Fluorescence Anisotropy Decay Analysis. *Langmuir* 2004, 20, 5924–5932.

(33) Mcnaughton, B. H.; Kinnunen, P.; Shlomi, M.; Cionca, C.; Pei, S. N.; Clarke, R.; Argyrakis, P.; Kopelman, R. Experimental System for One-Dimensional Rotational Brownian Motion. *J. Phys. Chem. B* 2011, 115, 5212–5218.

(34) Lavalette, D.; Tétreau, C.; Tourbez, M.; Blouquit, Y. Microscopic Viscosity and Rotational Diffusion of Proteins in a Macromolecular Environment. *Biophys. J.* 1999, 76 (5), 2744–2751.

(35) Xie, J.; Peng, S.; Brower, N.; Pourmand, N.; Wang, S. X.; Sun, S. One-Pot Synthesis of Monodisperse Iron Oxide Nanoparticles for Potential Biomedical Applications. *Pure Appl. Chem.* 2006, 78 (5), 1003–1014.

(36) Park, J.; An, K.; Hwang, Y.; Park, J.; Noh, J. I. N.; Kim, J. a E. Y.; Park, J.; Hwang, N. Ultra-Large Scale Syntheses of Monodisperse Nanocrystals via a Simple and Inexpensive Route. *Nature* 2004, 3 (12), 1–13.

(37) Silly, M.; Blanchandin, S.; Sirotti, F.; Lux, F.; Lemercier, G.; Charra, F.; Silly, M.; Blanchandin, S.; Sirotti, F.; Lux, F.; Chevreux, S.; Silly, M. G.; Lemercier, G.; Charra, F. Evidence of Mixed-Valence Hydrated Europium-Chloride Phase in Vacuum by Means of Optical and Electronic Spectroscopies To Cite This Version : HAL Id : Cea-01478836 Evidence of Mixed-Valence Hydrated Europium-Chloride Phase in Vacuum by Means of Optical An. *J.Phys.Chem. C* 2013, 117, 9766–9771.

(38) Kobayasi, T.; Mroczkowski, S.; Owen, J. F.; Brixner, L. H. Fluorescence Lifetime and Quantum Efficiency for 5D−4F Transitions in Eu2+ Doped Chloride and Fluoride-Crystals. *J. Lumin.* 1980, 21 (77), 247–257.

(39) Dhara, S.; Imakita, K.; Mizuhata, M.; Fujii, M. Europium Doping Induced Symmetry Deviation and Its Impact on the Second Harmonic Generation of Doped ZnO Nanowires. *Nanotechnology* 2014, 25.

(40) Jang, J. T.; Nah, H.; Lee, J. H.; Moon, S. H.; Kim, M. G.; Cheon, J. Critical Enhancements of MRI Contrast and Hyperthermic Effects by Dopant-Controlled Magnetic Nanoparticles. *Angew. Chemie - Int. Ed.* 2009, 48 (7), 1234–1238.

(41) Yang, L.; Zhou, Z.; Liu, H.; Wu, C.; Zhang, H.; Huang, G.; Ai, H.; Gao, J. Europium-Engineered Iron Oxide Nanocubes with High T1 and T2 Contrast Abilities for MRI in Living Subjects. *Nanoscale* 2015, 7, 6843–6850.

(42) Khramtsov, P.; Barkina, I.; Kropaneva, M.; Bochkova, M.; Timganova, V.; Nechaev, A.; Byzov, I.; Zamorina, S. Magnetic Nanoclusters Coated with Albumin , Casein , and Gelatin :

Size Tuning , Relaxivity , Stability , Protein Corona , and Application in Nuclear Magnetic Resonance Immunoassay. *Nanomaterials* 2019, 9 (1345).

(43) Park, J. C.; Lee, G. T.; Kim, H.; Sung, B.; Lee, Y.; Kim, M.; Chang, Y.; Seo, J. H. Surface Design of Eu-Doped Iron Oxide Nanoparticles for Tuning the Magnetic Relaxivity. A*CS Appl. Mater. Interfaces* 2018, 10, 25080−25089.

(44) Torres, T. E.; Jr, E. L.; Calatayud, M. P.; Sanz, B.; Ibarra, A.; Fernández-pac, R.; Mayoral, A.; Marquina, C.; Ibarra, M. R.; Goya, G. F. The Relevance of Brownian Relaxation as Power Absorption Mechanism in Magnetic Hyperthermia. *Sci. Rep.* 2019, 9, 3992.

(45) Carbonaro, C. M.; Corpino, R.; Ricci, P. C.; Chiriu, D. Sensitivity to Oxygen Environments of Mesoporous Silica Samples with Different Porosities. *J. Non. Cryst. Solids* 2014, 401, 60–65.

(46) Aboshi, A.; Kurumoto, N.; Yamada, T.; Uchino, T. Influence of Thermal Treatments on the Photoluminescence Characteristics of Nanometer-Sized Amorphous Silica Particles. *J. Phys. Chem.* C 2007, 111 (24), 8483–8488.

(47) Deissler, R. J.; Wu, Y.; Martens, M. A. Dependence of Brownian and Néel Relaxation Times on Magnetic Field Strength. *Med. Phys.* 2014, 41 (1).

(48) Ruehle, B.; Clemens, D. L.; Lee, B. Y.; Horwitz, M. A.; Zink, J. I. A Pathogen-Specific Cargo Delivery Platform Based on Mesoporous Silica Nanoparticles. *J. Am. Chem. Soc.* 2017, 139 (19), 6663–6668.

(49) Shahin, S. A.; Wang, R.; Simargi, S. I.; Contreras, A.; Parra Echavarria, L.; Qu, L.; Wen, W.; Dellinger, T.; Unternaehrer, J.; Tamanoi, F.; Zink, J. I.; Glackin, C. A. Hyaluronic Acid Conjugated Nanoparticle Delivery of SiRNA against TWIST Reduces Tumor Burden and Enhances Sensitivity to Cisplatin in Ovarian Cancer. *Nanomedicine Nanotechnology, Biol. Med.* 2018, 14 (4), 1381–1394.

(50) Kim, J.; Kim, H. S.; Lee, N.; Kim, T.; Kim, H.; Yu, T.; Song, I. C.; Moon, W. K.; Hyeon, T. Multifunctional Uniform Nanoparticles Composed of a Magnetite Nanocrystal Core and a Mesoporous Silica Shell for Magnetic Resonance and Fluorescence Imaging and for Drug Delivery **. *Angew. Chem. Int. Ed.* 2008, 47, 8438–8441.

Chapter 4 Self-Contained Nanocapsules Carrying Anticancer Peptides for Magnetically Activated and Enzyme-Cleaved Drug Delivery

This chapter of the dissertation is based on the collaborative work with Professor Qilin Yu at Nankai University when he was a visiting scholar in the Zink lab. Co-author contributions: Lin, F. C. and Yu, Q. designed and performed experiments. Yu, Q. conducted cell and animal experiments. Lin, F. C. and Yu, Q. drafted and reviewed the manuscript. Jeffrey I. Zink was the P.I.

Table of Content Figure

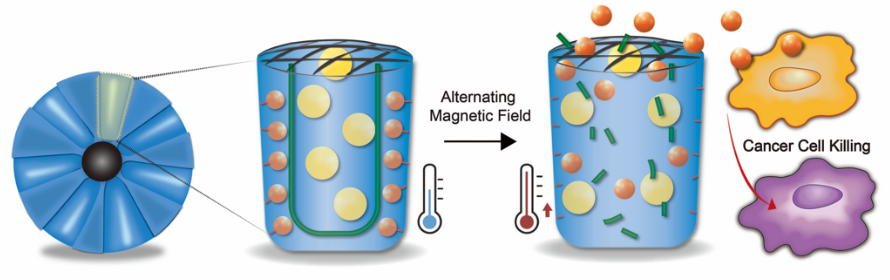

4.1 Introduction

Enzyme-activated prodrug delivery strategies are being increasingly investigated.[1–3] While several clinically successful prodrugs have been developed,[2,4] due to the ubiquity and heterogeneity of enzymes with defined specificity in biology,[1–3,5] elaborative design of the prodrug is still needed to overcome the limitations. First, the problem of unwanted side effects resulting from the distribution of human enzymes throughout the body has to be addressed. Although overexpression of cancer-related enzymes is mainly found in the areas of tumors, the wide tissue distribution of some prodrug-activating enzymes, such as aminopeptidase N, carboxylesterases, aldehyde oxidase, and glutathione S-Transferase, among others, can still cause untimely prodrug activation.[1,2] In addition, tumor heterogeneity leads to different enzyme expression patterns between tumors and various enzyme activities between patients, resulting in uncertain prodrug activation.[2,3] As a result, it is necessary to optimize substrate specificity and catalytic efficiency of enzymes for rapid, efficient, and selective cleavage of the prodrug at the targeted site. In order to address these problems and to meet the needs of medical applications, a prodrug-like nanocapsule that can activate the release of anticancer drugs contained itself in an efficient and controlled manner is presented in this study.

Melittin (MEL), a water-soluble cationic peptide comprised of 26 amino acids (GIGAVLKVLTTGLPALISWIKRKRQQ), is the principal toxin component of bee venom and plays an important role in host defense.[4,6] In China and many other Asian countries, melittin, together with other bee venom components, is widely used in the treatment of arthritis, rheumatism, erectile dysfunction, and skin disease, based on bee-sting therapy.[7,8] Moreover, this peptide has been demonstrated to have strong anticancer activities by disruption of membrane structures, induction of cancer-cell apoptosis, and suppression of angiogenesis through the VEGFR pathway.[9–12] However, its clinical application is frequently undesirable due to its non-specific cytotoxicity to normal cells, especially its activity of inducing hemolysis.[13,14] Therefore, it is necessary to develop MEL-delivery systems for their safe application in cancer therapy.[15,16] MEL was thus chosen as the model drug delivered in our nanocapsules.

Over the past years, nanoparticle-mediated drug delivery, which can protect cargos from premature degradation or release, has received considerable attention for cancer therapy. Studies have demonstrated internal cellular stimuli-responsive prodrug nanoparticles,[17–19] single external stimuli-activated [20] and multiple stimuli-responsive prodrug nanoparticles[21,22] that combine both external and internal stimuli for cancer therapy. External stimuli offer remote-control drug delivery in a spatial and temporal manner.[20–22] Noninvasive magnetically-induced heating stands out among the external stimuli being used in clinics, including heat, light, and ultrasound, due to its controllable localized heating and full penetration depth through tissue.[23,24] Magnetic fields in conjunction with superparamagnetic iron oxide nanoparticles (SPIONs) have attracted much attention for on-command hyperthermia treatment and immunotherapy.[25–27] Magnetic nanoparticle hyperthermia by using iron oxide nanoparticles (NanoTherm, MagForce Nanotechnologies), which is called "intratumoral thermotherapy", has culminated in clinical trials of such hyperthermia therapy on patients affected by glioblastoma multiforme and prostate tumors.[28–31]

Intrinsically biocompatible mesoporous silica nanoparticles (MSNs) are excellent candidates for the drug delivery platform[32–34] due to their cargo-carrying characteristics such as mesopores with a large internal volume and high surface area with easy surface functionalization capability.[35–37] Most importantly, the tunable pore structure and enlargeable pore size features of MSNs also enabled the delivery of large therapeutic biomolecules such as enzymes,[38] siRNA[39], cytokines,[40] and a protein antigen and toll-like receptor.[41] SPIONs embedded in MSNs (SPION@MSNs) possess the advantageous features of both the SPION core and the mesoporous silica shell, i.e., localized magnetic heating and a high loading capacity of various cargos, respectively.[42–44] Such a combination of both materials in a single core-shell nanostructure helps confine sufficient thermal energy at the suitable heating range, allowing spatio-temporal control of a therapeutic cargo release while leaving the particles' surroundings unaffected.

In this study, we used an extra-large-pore SPION@MSNs, denoted SPION@EXpMSNs, as the drug delivery vector for the design of the self-contained nanocapsules, where the pore structure of SPION@EXpMSNs provides ample space for multi-cargo delivery. The pore space of each SPION@EXpMSNs was visualized as a reaction nano-vial for the activation of the peptide drug release when the reacting solution inside of the nano-vial is heated to an elevated temperature. The concept of a heated nano-vial for a chemical reaction was based on the observation that the temperature inside a core-shell SPION@MSN under an AMF is much higher than the macroscopic bulk temperature.[45] The design principle is that drugs in the nano-vials remained "inactive" without application of the stimuli application and, before escaping from the pore, turned "active" through nanoscale heating of the nanoscopic volumes by means of an AMF, allowing triggered drug-release in a controllable manner.

4.2 Results and Discussion

4.2.1 Synthesis and Magnetic Properties of SPIONs and SPION@EXpMSNs

The design of the self-contained nanocapsules was carried out by encapsulating the peptide drug MEL, chitosan oligosaccharide (Cos), and pig liver esterase (PLE) together in the large pore space of SPION@EXpMSNs (**Scheme 4.1**), where the SPION acts as a heat source under AMF. MEL was first conjugated on the pore wall of the SPION@MSNs via an ester bond to avoid the premature drug release burst, and then the PLE was placed in the same interior pore space with MEL. The ester was separated from the esterase by introducing a barrier between them. Such a separating barrier, formed by Cos, was made thermoresponsive by incorporating azo bonds into the backbone. Cos was secured on top of the MEL via electrostatic attraction. Finally, biocompatible polyethylene glycol (PEG) bound over the pore openings blocked the pore entrances and kept the large PLE from escaping out of the pores. The successful securing of the cargo within the particle pores by PEG has been shown in our previous reports.[23,46]

To achieve heating under AMF, monodispersed SPIONs were prepared (**Figure 4.1a**).[47] SPIONs can be well suspended in organic solvents such as hexane and chloroform due to the coating of oleic acid with the outward-facing hydrophobic end. To achieve a controlled drug-delivery under AMF, SPIONs were encapsulated inside a mesoporous silica matrix with extra-large mesopores (**Figure 4.1b**). A superconducting quantum interference device (SQUID) was used to measure the magnetic properties of SPIONs and SPION@EXpMSNs. The saturation magnetization of SPIONs and SPION@EXpMSNs are 82 emu/g and 68 emu/g, respectively (**Figure 4.1c,d**). Although the saturation magnetization was reduced by the introduction of the mesoporous silica, possibly due to the surface spin disorder effects,[48,49] the SPION@EXpMSNs still possessed superparamagnetic properties. The field-dependent M-H loops showed that both SPIONs and SPION@EXpMSNs display zero hysteresis loops at 300 K and the occurrence of hysteresis at a temperature (5 K) below the blocking temperature, T_B (**Figure 4.1c,d**, insets). The blocking temperatures were estimated from the measurement of magnetization as a function of temperature using two standard states, the zero-field-cooled (ZFC) state and the field-cooled (FC) state. The reversible behavior of the ZFC-FC magnetization curve found for the temperature above the T_B also validated that both SPIONs and SPION@EXpMSNs are superparamagnetic non-interacting single-domain particles (**Figure 4.1e,f**).[49] The small difference in T_B between SPIONs and SPION@EXpMSNs is probably due to the surface-silica-coating effects[50] leading to the slightly decreased anisotropy constant (K_{eff}) for SPION@EXpMSNs.

To investigate the heat-generation efficiency of SPIONs under AMF, the specific loss power (SLP) was measured and calculated using eq 1, where C is the volumetric heat capacity of the solution, V_s is the volume of solution, m is the mass of the particle, and dT/dt is the initial slope of the temperature rise vs. time curve for the particle heating:

$$\mathrm{SLP} = \frac{C\,V_s}{m}\,\frac{dT}{dt} \qquad \text{eq 1}$$

AMF with a maximum induction power = 5 kW, magnetic field strength = 250 Oe, and oscillation frequency = 375 kHz was used. The SLP of the SPIONs was calculated to be 153.2 W/g (See SI) and the temperature of the cyclohexane solution containing the SPIONs with a concentration of 3 mg/mL leveled off at 45°C after 6 min magnetic actuation (**Figure S 4.1**). The SLP values of the SPIONs in different induction powers of AMF are also shown in SI. The temperature of the SPIONs' immediate surroundings is higher than the measured bulk temperature[45] and the effect of increase of the hydrodynamic volume on the interior heating efficacy of the SPIONs after the silica coating should be minimal since Néel relaxation was determined to be the dominant heating mechanism.[51] We envisioned that such heating performance of SPIONs made them a suitable heat source for the thermal-induced drug releasees without impairing the activity of esterase and the anticancer activity of the ester-linked MEL drugs.

4.2.2 Synthesis and Characterization of Peptide Drug-Loaded SPION@EXpMSNs

The 30±5 nm pore of SPION@EXpMSNs offered space for MEL conjugation and the other components. Transmission electron microscopy (TEM, **Figure 4.1b**) showed that the average particle size of the monodispersed SPION@EXpMSNs was 128±2 nm and the extra-large mesopores were well distributed over all particles. The pore walls of the mesoporous silica shell were functionalized with amine groups. To covalently bond the peptide drug MEL via an ester linker, SPION@EXpMSNs were first modified with β-CD, obtaining SPION@EXpMSN-CD, which exposes both abundant hydroxyl groups and β-CD cavities in the pores. The β-CD served two purposes: (1) to produce esters in the pore wall by heating the hydroxyl groups in the presence of alcohols and (2) to provide binding spots on the particle surface for the PEG via the adamantane-cyclodextrin inclusion. Such β-CD modification helped circumvent problems introduced by multi-step molecule attachments. The ester bond was formed by reacting the hydroxyl groups of β-CD with succinic anhydride, and a carboxyl group was exposed by the other end of the succinic acid. The generated carboxyl functionalized core-shell particle was denoted as SPION@EXpMSN-Suc. The SPION@EXpMSN-Suc was finally reacted with MEL by the EDC/NHS reaction, obtaining

SPION@EXpMSN-MEL (**Figure 4.2a**). TEM images revealed that both the SPION core and the pore structure remained in the final SPION@EXpMSN-MEL (**Figure 4.2b**). FT-IR spectra showed that SPION@EXpMSN-CD, SPION@EXpMSN-Suc, and SPION@EXpMSN-MEL had obvious adsorption peaks of -OH and -C-O-C-, -COOH and -COO-, -COOC- and -CO-NH- (**Figure 4.2c**). An increase in the size of the modified nanoparticles (with an average polydispersity of 0.140~0.157) as compared to the initial SPION@EXpMSNs (with an average polydispersity of 0.074) was observed in DLS analysis, indicating that slight aggregation of these nanoparticles occurred after the modifications (**Figure 4.2d**). ζ-potential analysis was also conducted to further validate the attachment after each step. The change of ζ-potential from a positive value to a negative value indicated the presence of carboxyl groups from the succinic acid, and the ζ-potential turned positive again after the drug attachment due to the positively-charged peptide drug MEL (**Figure 4.2e**). These results proved the successful modification of functional groups on the nanoparticles in each step.

4.2.3 Synthesis and Characterization of the Thermoresponsive Separating Barrier

The barrier introduced to the pore space not only prevented the MEL from being exposed to the normal cells but also served as a separator between the PLE and the ester bond-linker containing the MEL. The removal of the separating barrier resulting from the AMF-induced heating allows the direct contact of the trapped esterase with the ester bond, leading to the ester bond cleavage and the release of the conjugated drug. The heat-responsive separator was synthesized by forming an amide bond between the amine groups of chitosan and the carboxylate on 4,4'-azobis(4-cyanovaleric acid) (ACVA). The resulting products were designated as CosA. The excess of ACVA was present in the reacting solution to optimize the cross-linking. The successful chemical bond formation between Cos and ACVA was validated by FTIR (**Figure S**

4.2a) and ^{1}H-NMR (**Figure S 4.2b**). The absorptions at ν = 1656 cm^{-1} from amide I C=O bending and ν = 1079 cm^{-1} from C-O-C stretching were assigned to the amide bonds and C-O-C groups, respectively, in the backbone of Cos. Two bands at ν = 3400 and 3260 cm^{-1} in the IR spectrum due to N-H stretching vibrations indicated that some primary amines are still present in the backbone of CosA. The successful conjugation of ACVA to the primary amine of Cos through secondary-amide-bond formation was evidenced by a new characteristic absorption (amide II) at ν = 1550 cm^{-1}. Additionally, the appearance of absorption at ν = 2243 cm^{-1} (nitrile stretching) and absorption bands at ν = 2933 and 2966 cm^{-1} (C-H stretching) from ACVA suggested the successful conjugation of ACVA with Cos. Newly emerging absorption at ν = 1712 cm^{-1} (C=O stretching) also supports the presence of carboxylic group from ACVA. ^{1}H-NMR peaks stemming from the methyl groups of ACVA further confirmed the successful attachment of ACVA on Cos (**Figure S 4.2b**). By comparing the decrease of amine functional groups on glucosamine with the increase of methyl groups from ACVA, it was determined that approximately 44.4% of amines on the Cos were replaced by the ACVA (See SI).

4.2.4 PEG Screen on Particle Exterior Surfaces for Enzyme Trapping in Particle Pores

To achieve heat-responsive controlled release of MEL, SPION@EXpMSN-MEL was first covered by as-synthesized CosA through the electrostatic attraction between positively charged MEL and negatively charged ACVA grafted on CosA. The remaining pore spaces of SPION@EXpMSN-MEL+CosA were further loaded with PLE, followed by binding of Ada-modified PEG (PEGAda) on the particle surface via the host-guest interaction between β-CD and Ada to avoid the escape of PLE from the pores. The final particle, with PLE trapped inside the pores by the PEG porous screen, was termed SPION@EXpMSN-MEL+CosA+PLE+PEGAda. The successful binding of PEGAda was demonstrated by the improved colloidal stability shown in DLS analysis, where the decrease in size distribution was due to the prevention of aggregation by steric repulsion between the surface PEG (**Figure S 4.3a**). A reduction of ζ-potential value for the obtained PEGylated nanoparticles also indicated the binding of PEG on the particle surface (**Figure S 4.3b**). Enzymatic assays revealed that the PEG porous screen trapped most of the PLE in the pores, with only a small amount of PLE escape (<5%) from the nanoparticles (**Figure S 4.4**).

4.2.5 AMF-Triggered Enzyme Activation for Release of Drugs

To ensure the substrate specificity of the selected enzyme PLE, SPION@EXpMSN-MEL was first treated with free PLE, and then the MEL release resulting from the enzymatic activities was assessed by detection of fluorescence intensity of the FITC-MEL released to the supernatants. As expected, the addition of PLE induced the rapid release of MEL from SPION@EXpMSN-MEL. Without applying any external trigger, >75% of MEL was released 5 min after the PLE addition and >95% of MEL was released after 30 min (**Figure S 4.5**), showing that PLE effectively triggered MEL release from the mesopores of the particles owing to its catalytic effect to break down ester bonds between β-CD and succinic MEL.

The on-demand AMF-triggered drug release property of SPION@EXpMSN-MEL+CosA+PLE+PEGAda, with MEL drug well-shielded in the pore space by the thermo-responsive CosA, was then analyzed. Under no AMF stimulation, only a very low level of MEL (<5%) was released from the SPION@EXpMSN-MEL+CosA+PLE+PEGAda (**Figure 4.3a**). This result is similar to that of PLE-free nanoparticles, indicating that the separating barrier CosA on MEL prevented PLE from approaching the ester bonds (**Figure S 4.6**). In contrast, after exposure to AMF stimulation, MEL was released from SPION@EXpMSN-MEL+CosA+PLE+PEGAda in a time-dependent manner. The release efficiency of MEL achieved >50% after 30 min of AMF treatment and reached ~70% after 60 min due to the enzyme catalytic activity while the PLE-free nanoparticles remained at very low levels of MEL release (<5%) even after 60 min of AMF treatment (**Figure 4.3a**). These results indicated that AMF induced the cleavage of the C-N bond of the azo moieties on CosA and allowed direct contact between PLE and ester bonds for release of MEL from SPION@EXpMSN-MEL+CosA+PLE+PEGAda via catalytic hydrolysis. The results also further confirmed that CosA plays an essential role in this drug delivery system for realizing external-triggered ester bond cleavage and drug release. It is important to note that, during AMF treatment, the bulk temperature of the system only increased from 21 °C to 28 °C even after 60 min (**Figure 4.3a**), indicating that the system could avoid heating-related damage to normal tissues. The cleavage of the C-N bonds is resulted from the nanoscale heating internally from the SPION core.[24,44,45,51] Because the heat generated by the magnetic core and the heating efficiency of SPION is associated with the AMF amplitude,[52] the release efficiencies of FITC-MEL from SPION@EXpMSN-MEL+CosA+PLE+PEGAda under different AMF induction powers were also carefully analyzed. It can be seen that the higher the AMF induction power, the greater the release of MEL (**Figure 4.3b**).

AMF-triggered drug release was further investigated during co-incubation of the SPION@EXpMSN-MEL+CosA+PLE+PEGAda with the PANC-1 tumor cells. Under no AMF treatment, the FITC-tagged MEL (FITC-MEL)-containing nanocapsules adhered to the surface of the tumor cells; no colocalization of FITC-MEL with the intracellular lysosomes was observed (**Figure 4.3c**, top). Remarkably, after AMF treatment for 30 min, FITC-MEL entered into the cells and colocalized with lysosomes (**Figure 4.3c**, down). This result indicated that AMF could efficiently trigger MEL release from the nanocapsules, allowing diffusion of the released MEL into the intracellular lysosomes.

4.2.6 Cancer Cell Death by Induced AMF-Triggered Drug Release

To evaluate the cell-killing capacity of the peptide drug-loaded nanoparticles, we first tested the toxicity of SPION@EXpMSN-MEL to PANC-1 cancer cells in the presence of PLE (SPION@EXpMSN-MEL+PLE). Hoechst 33342/PI staining and fluorescence microscope analysis revealed that the addition of SPION@EXpMSN-MEL+PLE led to obvious diffusion of FITC-MEL into the cells and consequent extensive cell death (**Figure S 4.7a**), with the percent of dead cells reaching up to 90% (**Figure S 4.7b**). This result indicated that PLE-catalyzed MEL release was enough to kill most of the tumor cells.

Taking advantage of the heat-responsive CosA for the controlled release of MEL, the toxicity of SPION@EXpMSN-MEL+CosA+PLE+PEGAda to cancer cells can be regulated by AMF. As expected, without AMF treatment, there was no obvious cell death (<10%) observed for the SPION@EXpMSN-MEL+CosA+PLE+PEGAda, which is similar to the results obtained by the PLE-free nanoparticles (SPION@EXpMSN-MEL and SPION@EXpMSN-MEL+CosA). The negligible cell death can be explained by the observable extracellular distribution of FITC-MEL (**Figure 4.4a**), where such distribution indicated MEL remained in the pores of nanoparticles when no AMF was applied. Hence, these results demonstrated that SPION@EXpMSN-MEL+CosA+PLE+PEGAda is an excellent drug delivery vector for eliminating nonspecific cytotoxicity. At ambient temperature, CosA remained in contact with MEL and provided a strong inhibitory effect on the toxicity of MEL contained in the pore space. The low cell death level also indicated that SPION@EXpMSN-MEL+CosA+PLE+PEGAda offers a good degree of biocompatibility (**Figure 4.4b**).

To demonstrate the AMF-regulated cytotoxic effect of MEL, the cancer cells were treated with AMF for 30 min. It can be seen that, while the PLE-free nanoparticles only led to slight cell death (<20%), SPION@EXpMSN-MEL+CosA+PLE+PEGAda caused extensive cell death (>90%) after 30 min of AMF treatment, implying that the release of MEL was caused by the enzymatic activities of PLE (**Figure 4.4c, d**). Moreover, remarkable diffusion of FITC-MEL into the cancer cells after AMF treatment can be observed from the merged image of the fluorescence analysis, confirming the release of MEL from SPION@EXpMSN-MEL+CosA+PLE+PEGAda under AMF application (**Figure 4.4c**).

CCK-8 assay results showed that, without the AMF stimulation, there was no decrease of PANC-1 cell viability after 12 h of incubation with each type of MEL-containing SPION@EXpMSN (**Figure 4.5**). These results not only showed the good biocompatibility of SPION@EXpMSNs but also indicated that the use of SPION@EXpMSN-MEL+CosA+PLE to deliver MEL can efficiently reduce the nonspecific cytotoxic effects despite MEL being in close proximity to the trapped esterase. CCK-8 assays with the AMF actuation were also performed to evaluate the cell-killing capability of MEL released from the SPION@EXpMSN-MEL+CosA+PLE+PEGAda. Consistently, AMF caused the massive reduction (>80%) in the viability of the cells treated with the SPION@EXpMSN-MEL+CosA+PLE but had almost no impact on cell viability of the cells treated with PLE-free nanoparticles (**Figure 4.5**). These results further proved that non-specific cytotoxicity of MEL can be bypassed, and MEL released from SPION@EXpMSN-MEL+CosA+PLE in response to AMF can efficiently kill the tumor cells. The viability results of various composites were compared with that of PANC-1 cells treated by free MEL, which shows that there is no significant difference between the SPION@EXpMSNs group (**Figure 4.5**) and the free MEL group (**Figure S 4.8**). The released MEL, in fact partially modified by succinate, exhibited comparable cytotoxicity to an equivalent amount of the native pure MEL (**Figure S 4.8**, **Figure S 4.9**), indicating that the succinate modification in the released MEL had no impact on the cell-killing capacity of MEL. Together, these results revealed that active MEL was efficiently released from the nanocapsules triggered by AMF heating, leading to severe death of the tumor cells. The high efficiency of MEL release could be attributed to the close contact between the enzyme and its corresponding ester targets after AMF-triggered removal of CosA. Because the coexistence of the trapped enzymes and the enzyme-activated drug linkers offers continuous and close access of the enzymes toward the drug, leading to an enhanced catalytic effect, not only can a tailored release profile be achieved by utilizing this responsive drug delivery platform, but also a moderate AMF heating is enough for rapid and efficient activation of drug release and intensified killing of cancer cells. This operating system shields the normal cells from the nonspecific cytotoxicity of drugs, circumvents the off-target effects of a drug due to the ubiquity of esterase *in vivo*,[5,53] and realizes on-demand spatial and temporal drug release upon the application of AMF.

4.2.7 *In vivo* Antitumor Efficiency of the Nanocapsules under AMF Stimulus

For *in vivo* application of the SPION@EXpMSN-MEL+CosA+PLE+PEGAda, hemolysis assays were first performed to investigate their toxicity to blood cells. After 30 min of incubation, free MEL, similar to the positive control (Triton X-100 treatment), led to drastic hemolysis of the blood red cells. In contrast, the SPION@EXpMSN-MEL+CosA+PLE+PEGAda, similar to SPION@EXpMSN-MEL and SPION@EXpMSN-MEL+CosA, did not lead to obvious hemolysis after 30 min of co-incubation (Figure 6a). Therefore, hemolysis can be efficiently prevented by encapsulating MEL in the nanocapsules.

To evaluate the tumor-targeting efficiency of the SPION@EXpMSN-MEL+CosA+PLE+PEGAda, MEL was first tagged by Cy5, and then loaded into the nanocapsules. After 6 h of intravenous injection into the PANC-1 tumor-burden mice, the fluorescence of Cy5 in the mice was examined by an animal imaging system. Whole-body imaging showed that the SPION@EXpMSN-MEL+CosA+PLE+PEGAda were mainly accumulated at the tumor tissues, and partially distributed in the lung and liver (Figure 6b). Hence, the SPION@EXpMSN-MEL+CosA+PLE+PEGAda exhibited good tumor-targeting efficiency, which may be attributed to the enhanced permeability and retention (EPR) effect.

The antitumor capacity of the nanocapsules with the aid of AMF was further evaluated in the tumor-burden mice. On the 14th day after nanocapsule injection and AMF treatment, the tumors were sampled from the mouse for photographing and weighing (Figure 6c, 6d). While both SPION@EXpMSN-MEL, SPION@EXpMSN-MEL+CosA slightly reduced tumor sizes and weights, the SPION@EXpMSN-MEL+CosA+PLE+PEGAda had a severe impact on tumor growth, leading to a remarkable reduction of tumor weight (≈80%, Figure 6d). Histopathological observation further revealed that the tumor tissues treated by SPION@EXpMSN-MEL+CosA+PLE+PEGAda exhibited severely disrupted structures, while those treated by SPION@EXpMSN-MEL or SPION@EXpMSN-MEL+CosA had intact structures (Figure 6e), confirming severe tumor damage caused by SPION@EXpMSN-MEL+CosA+PLE+PEGAda. In addition, the treatment of the nanocapsules did not lead to an obvious change in mouse body weight and normal organ weight (Figure S10), nor caused obvious impact on the tissue structures of the tested organs (Figure 6f), suggesting good biosafety of the nanocapsules. Together, these results revealed that the nanocapsules had good biocompatibility and high tumor-targeting/inhibiting efficiency.

4.3 Conclusion

We designed and tested a self-contained nanocapsule for delivery of an enzyme-cleavable nonspecific cytotoxic anticancer peptide drug MEL, where the release of MEL was activated by

AMF. The successful encapsulation of esterase, the oligomer-based separating barrier, and ester-linked anticancer drug MEL together in the large pore space of the mesoporous silica nanoparticles was demonstrated. This drug delivery system is superior due to its capability of not only shielding the nonspecific cytotoxicity of the MEL but also realizing the co-delivery of ester-linked MEL and enzyme for realizing one-time, one-dose treatment. Most importantly, upon stimulation, the trapped esterase with selected substrate specificity can bypass the problem of differential hydrolysis of ester bonds in biological environments resulting from the *in vivo* heterogeneity of esterase activity and thus assure the spontaneous hydrolysis of the ester-containing peptide drug. In addition to preventing unwanted side effects caused by untimely drug release, these self-contained nanocapsules activate and release the drugs on-demand and in a highly efficient manner due to the high local concentration of specific enzymes near the ester-linked anticancer drug MEL. As a result, by using this nanocapsule, we demonstrated both *in vitro* and *in vivo* that the nanocapsules exhibited excellent biocompatibility and high tumor-targeting/inhibiting efficiency and, with just moderate AMF heating, an intensified anticancer efficacy could be achieved.

4.4 Experimental Section

4.4.1 Materials and Chemicals

Iron(III) chloride hexahydrate ($FeCl_3 \cdot 6H_2O$) (≥98%, Aldrich), sodium oleate (99%, TGI), oleic acid (90%, Aldrich), tri-n-octylamine (95%, Fisher), hexadecyltrimethylammonium bromide (CTAB) (≥99%, Sigma), tetraethyl orthosilicate (TEOS) (≥99%, Sigma), ethyl acetate (≥99.5%, Sigma), ammonia solution 28-30%, (3-aminopropyl)trimethoxysilane (97% APTMS) (Sigma-Aldrich), hexane (≥98.5%, Fisher), chloroform (99.9%, EMD), 4,4'-Azobis(4-cyanovaleric acid)(ACVA) (≥98%, Aldrich), chitosan oligosaccharides (Cos)(TGI), 4-(dimethylamino) pyridine (Sigma Aldrich), succinic anhydride (≥98%, Sigma Aldrich), 1-ethyl-3-(3-

dimethylaminopropyl) carbodiimide (EDC)(Sigma), N-hydroxysulfosuccinimide (NHS)(≥99%,CovaChem), PEG-NH_2 (MW ≈ 10,000)(Sigma), 1-adamantane ccarboxylic acid (ADACA)(Sigma). Melittin (MEL) and FITC-MEL were synthesized by GenScript and ChinaPeptides, respectively. Tosyl-β-CD was synthesized based on the method reported by Yang.[54]

4.4.2 Characterization

A superconducting quantum interference device (SQUID, Quantum Design MPMS7 magnetometer) was used to investigate the superparamagnetic properties of the SPION and SPION@EXpMSN. The field-dependent magnetization of SPION and SPION@EXpMSN were measured at both 5 K and 300 K in an applied magnetic field of 50 Oe. The blocking temperature of each sample was obtained by running a M vs T loop (from 2 K to 300 K) in an applied magnetic field of 50 Oe. Measurement of Specific Loss Power (SLP) was performed to investigate the heat-generation efficiency of SPION. The SPIONs were dispersed in cyclohexane (3 mg/mL) in a 2 mL vial. The temperature of the bulk was recorded as a function of AMF trigger time. The sample was well insulated from the coil, and the minimum heat transfer from the coil to the solvent was subtracted from the data. The temperature-increase profile of the cyclohexane solution and the calculation of specific heat loss power of SPION are shown in Supporting Information. Transmission electron microscopy (TEM) images were required on a Tecnai T12 Quick CryoEM and CryoET (FEI) with an operating voltage of 120 kV. The sample was prepared by dropping a suspension (0.2 mg/mL, 5 μL) of SPION or SPION@EXpMSN in hexane or ethanol, respectively, on a 200 mesh carbon coated copper grid, followed by solvent evaporation at room temperature. Zeta-potential analysis and dynamic light scattering (Zeta/DLS) were acquired on a ZetaSizer Nano (Malvern Instruments Ltd., Worcestershire, U.K.) in Millipore water and hexane for

SPION@EXpMSN and SPION, respectively. Zeta-potential values confirmed the successful functionalization in the pore space of SPION@EXpMSN after each step. DLS gave the average diameter of particles after each step at room temperature. Fourier-transform infrared spectroscopy (FTIR) analyses were performed on FTIR (JASCO FT/IR-420) spectrometer in the range of 4000−400 cm^{-1}.

AMF-Induced Superparamagnetic Heating

Magnetic heating was carried out using a Magnetic Hyperthermia System manufactured by MSI Automation, Inc. The five-turn copper coil diameter and height were both 50 mm. The samples were placed in the center of the coil with the help of a non-conducting holder to avoid direct contact with the coil. The induction power, magnetic field strength, and oscillation frequency were 5 Kw, 375 kHz, and 250 Oe, respectively.

Drug-Release Assays

To investigate release efficiency of the nanoparticles induced by PLE, 1 mg of SPION@EXpMSN-MEL was suspended in 1 mL of PBS (pH 7.4), and then 10 U of PLE were added into the suspension. After incubation at 37 °C for the indicated time, the suspensions were sampled and centrifuged, and the fluorescence intensity of the supernatants were measured by a fluorescence microplate reader (Perkin Elmer, USA). To evaluate AMF-responsive MEL release, 1 mg/mL of SPION@EXpMSN-MEL, SPION@EXpMSN-MEL+CosA, or SPION@EXpMSN-MEL+CosA+PLE+PEGAda was treated by AMF (5 kW, 375 kHz) for the indicated time, followed by measurement of fluorescence intensity of the supernatants. Release efficiency (% Release) of cleavable MEL is defined as the MEL contents released from the nanoparticles divided by the total MEL contents thoroughly released by PLE in the absence of CosA. The percent of PLE release was calculated by PLE activity in the nanoparticle-suspending solution divided by PLE activity in the nanoparticles ×100%.

Cell Viability Assays

To determine tumor cell-killing capacity of the nanoparticles, the human pancreatic cancer PANC-1 cells were cultured in DMEM medium supplemented with 10% fetal bovine serum (FBS) for 24 h. SPION@EXpMSN-MEL, SPION@EXpMSN-MEL+CosA, or SPION@EXpMSN-MEL+CosA+PLE (100 mg/L) were then added into the well cultures. After 12 h of incubation, the cells were then treated by AMF (5 kW, 375 kHz) for 30 min, followed by 24 h cell culturing. Cell viability was then evaluated by the Hoechst 33342/PI staining method and the CCK-8 assay kit.

Hemolysis Assays

To investigate the hemolysis effect of the nanocapsules, fresh mouse blood was sampled from healthy BALB/c nude female mice. Blood red cells were isolated from 1 mL of the mouse blood by centrifugation at 1, 500 rpm for 5 min, and then suspended in 5 mL of PBS buffer. The nanocapsules (100 mg/L), free MEL (6 μM), or Triton X-100 (0.5%, positive control) were added into the red cell suspensions. After incubated at 37 °C for 20 min, the suspensions were photographed for hemolysis evaluation.

In vivo Antitumor Model

To evaluate *in vivo* antitumor capacity of the nanocapsules, the BALB/c nude female mice were pre-inoculated at the hind leg sites by PANC-1 cells with 1×10^7 cells/mouse. After 5 days of culture, the nanocapsules were injected intravenously into the mice (200 mg/kg). After 2 h of nanocapsule circulation, the mice were treated by AMF (375 kHz, 5 kW) for 30 min. Four mice were used for each group. The mice were further fed for 14 days and killed. The tumors were sampled, photographed, and weighted. The animal experiments were approved by the Nankai Ethical Committee in compliance with the Chinese law on experimental animals.

Statistical Analysis

Each experiment was performed with three replicates. The results indicate the means ± SD. Difference between groups was compared by one-way analysis of variance (ANOVA) test ($P < 0.05$). Statistical tests were performed using the SPSS software package (version 20, IBM).

4.4.3 Nanoparticles Synthesis

Synthesis of SPIONs. A modified thermal decomposition method was used to synthesize SPIONs.[47] Briefly, 2.5 mmol of $FeCl_3 \cdot 6H_2O$ and 7.5 mmol sodium oleate were dissolved in a solvent mixture (14 mL) composed of ethanol, Millipore water, and hexane (4:3:7). After 4 h of refluxing at 70°C, the resulting solution was transferred to a separatory funnel, where the top organic layer containing the Fe-oleate was washed 3X with water and ethanol. Afterward, the resulting organic layer was transferred to a 3-neck round bottom flask and was kept at 70°C overnight to evaporate hexane. The Fe-oleate complex precursor along with 2-fold molar ratio of oleic acid were dispersed in 10 mL of tri-n-octylamine. Under stirring, the mixture was degassed with N_2 for 30 min at room temperature and then heated to 200 °C at a heating rate of 3 °C min^{-1}. After keeping at 200 °C for 2 h, the mixture was heated to 320 °C with the same heating rate and was allowed to reflux and age at this temperature for 1 h. Afterward, the mixture was cooled down to room temperature under N_2 and ethanol was added to precipitate the black product. The precipitate was collected by centrifugation, washed 3X with a mixture of ethanol and acetone, and redispersed in hexane containing 50 μL of oleic acid.

Synthesis of Amine-Functionalized SPION@EXpMSNs. SPION@EXpMSNs were synthesized based on a published approach with some modifications.[40,41] The synthesis of

SPION@EXpMSNs started with transferring SPIONs to an aqueous layer with the help of CTAB surfactant templates,[55] followed by the organic addictive-induced emulsion formed in the CTAB micelles that led to the enlarged pores.[40,41] The silica coating was then achieved by hydrolysis and condensation of TEOS in the presence of the surfactant micelles.[55] 6 mg of SPIONs stabilized with oleic acid were dispersed in 1.2 mL chloroform. In a glass vial, 200 mg CTAB was dissolved in 10 mL of Millipore water at 37ºC, followed by the addition of the prepared SPION solution. To transfer SPION from the organic layer to aqueous layer with the help of CTAB, the mixture was vortexed and sonicated for 10 min and probe-sonicated (40% output) for another 5 min to generate an oil-in-water emulsion. After evaporating chloroform at 75ºC for 10 min, the clear colloidal SPION in aqueous solution was obtained. After another 5 min of probe-sonication for confirming the absence of chloroform, the solution was cooled down to room temperature. Under stirring, the resulting solution was added to a mixture of solvent composed of 95 mL of Millipore water, 5 mL of methanol, and 20 mL of ethyl acetate. After mixing for 5 min, 3 mL of ammonia hydroxide was quickly added into the mixture, and then 300 μL of TEOS was added into the reaction solution. The solution was allowed to react for 15 h under stirring. The as-synthesized SPION@EXpMSN were collected by centrifugation, washed 2X with ethanol, and then were dispersed in 50 mL of ethanol containing 1 g of ammonia nitrate for CTAB surfactant removal. The solution was refluxed at 60ºC for 1.5 h under stirring, followed by 1X washing with water and washing twice with ethanol. The removal procedure was repeated twice, and the nanoparticles were dispersed in 20 mL of ethanol. For amine functional group modification, 90 mg of as-synthesized SPION@EXpMSN were dispersed in 40 mL of ethanol, and 30 μL of APTMS was added with stirring. After reacting under stirring for 15 h, amine-functionalized nanoparticles were washed three times with ethanol and redispersed in ethanol.

Synthesis of Peptide Drug-loaded SPION@EXpMSNs. To covalently conjugate the peptide drug MEL on the pore wall, 10 mg of SPION@EXpMSNs with amino groups exposed on their surfaces were first suspended in 20 mL of DMSO, and then 100 mg of Tosyl-CD was added into the suspensions. The mixture was magnetically stirred at room temperature for 24 h, obtaining SPION@EXpMSN-CD. The nanoparticles were then centrifuged, washed with DMSO and dH_2O, and dried by vacuum. Next, 10 mg of SPION@EXpMSN-CD were dissolved in 20 mL of DMF, and then 0.268 g LiCl was added into the solution. The mixture was heated to 85 °C under magnetic stirring, followed by addition of 0.15 g 4-(dimethylamino) pyridine, 9.6 μL of pyridine, and 0.1 g succinic anhydride under nitrogen. The mixture was kept at 85 °C for 18 h under magnetic stirring. After cooling down to room temperature, the nanoparticles were centrifuged, washed with deionized H_2O and ethanol. After vacuum drying, SPION@EXpMSN-Suc were obtained. 10 mg of SPION@EXpMSN-Suc were dissolved in 10 mL of 50 mM MES buffer (pH 6.0), and then 50 mg of EDC and 55 mg of NHS were added into the solution, followed by addition of 4 mg of MEL or FITC-MEL. The mixture was magnetically stirred at 4 °C for 24 h. The nanoparticles were centrifuged, washed by dH_2O, and dried, obtaining the final SPION@EXpMSN-MEL. The loading capacity of MEL by SPION@EXpMSN-Suc is 22.0% (w/w), which is calculated by the mass of MEL loaded into SPION@EXpMSN-Suc divided by the mass of SPION@EXpMSN-Suc used for loading×100%.

Synthesis of CosA. CosA was synthesized using carbodiimide crosslinker chemistry. The activation of the carboxylate groups was performed in MES buffer solution with an adjusted pH of 6.00. Briefly, 40 mg of ACVA were dissolved in 5 mL of MES buffer solution, followed by the addition of 60 mg of EDC and 30 mg of NHS, each in 1 mL of MES buffer solution. The solution was allowed to react for 45 min, then was added with 2 mL MES buffer solution containing 50 mg of Cos. After the molecules were crosslinked for 24 h, 30 mL of ethanol was added into the reaction solution to precipitate the final CosA product. The precipitate was re-dispersed with a minimal amount of water and washed with 20 mL of ethanol X2. The resulting product was lyophilized to remove the remaining water and stored at room temperature for further measurement.

Synthesis of PEGAda. To synthesize adamantane-modified PEG, 10 mg of 1-adamantane carboxylic acid were dissolved in 5 mL of NaOH (10 mM), and then were added into 50 mL of 50 mM MES buffer (pH 6.0). After addition of 20 mg of EDC and 22 mg of NHS, the solution was magnetically stirred at room temperature for 30 min. 50 mg of PEG-NH_2 (MW ≈ 10,000) were then added into and dissolved in the MES buffer (pH 6.0) containing the activated adamantane. The mixture was stirred for another 24 h, followed by dialysis using a dialysis bag (Cutoff MW = 4000) for 7 days. The final PEGAda was obtained by vacuum drying. To cap PLE in the nanoparticles, PEG-Ada (2 mg) was added into 1 mL of PBS (pH 7.4) containing 2 mg of SPION@EXpMSN-MEL or 2 mg of CosA and PLE-loaded SPION@EXpMSN-MEL (SPION@EXpMSN-MEL+CosA+PLE), followed by shaking at 4 °C for 24 h. The nanoparticles were centrifuged and washed by PBS, obtaining SPION@EXpMSN-MEL+PEGAda or SPION@EXpMSN-MEL+CosA+PLE+PEGAda.

4.5 Schemes and Figures

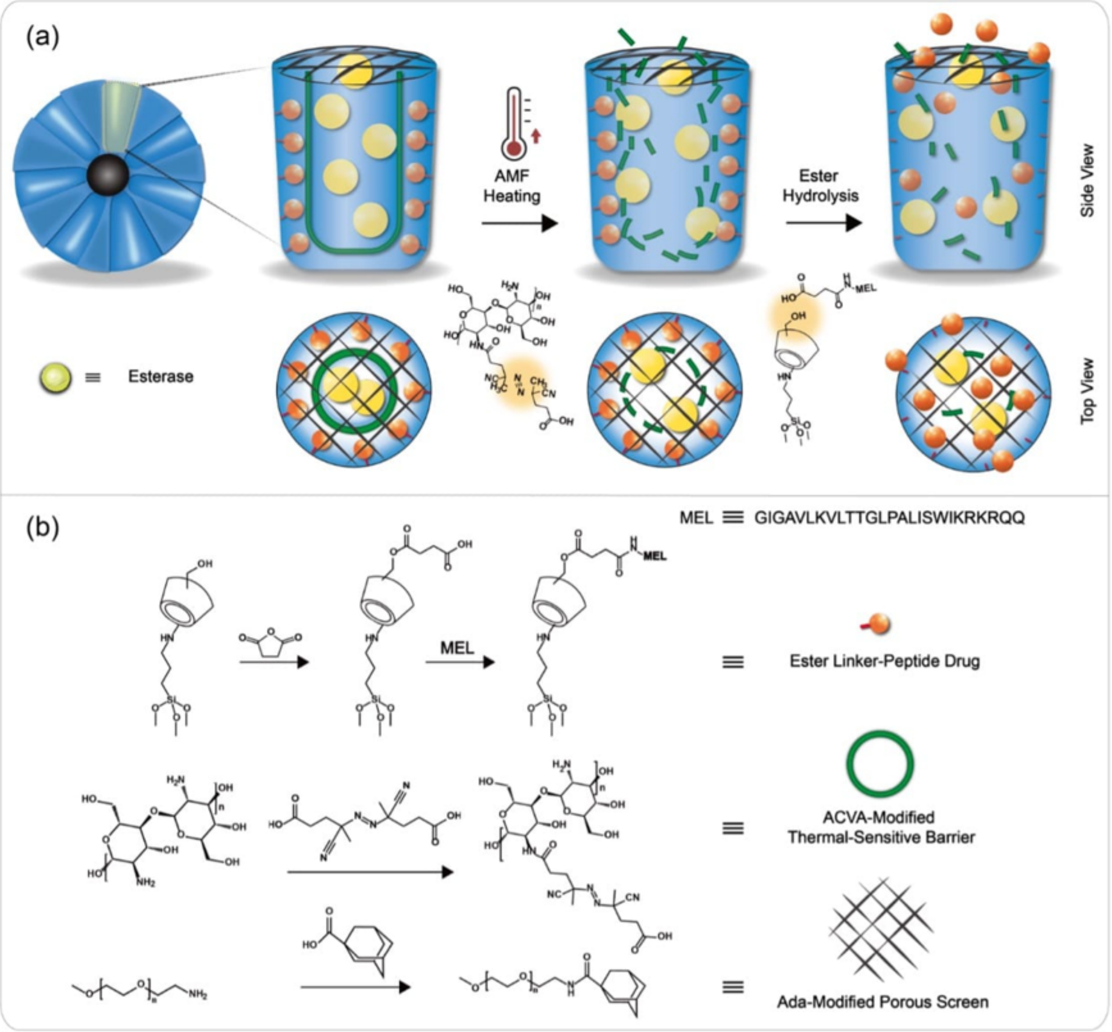

Scheme 4.1 (a) Schematic illustration of the encapsulation of peptide drugs and the AMF-triggered release of the peptide drugs from the pore of a core@shell large pore mesoporous silica nanoparticle (side view and top view). (b) Chemical synthesis steps of the ester linker-peptide drugs, the thermal-sensitive chitosan oligosaccharide barrier, and the PEG porous screen. The large pore in the nanoparticles provides ample space for containing the ester linker (red)-peptide drugs (orange), the thermal-sensitive separating barrier (green), and the enzymes (yellow). The enzymes were trapped by the PEG porous screen (black). The thermal-sensitive barrier is broken by AMF heating and pieces of it escape through the porous screen, allowing the enzymes to catalyze the cleavage of the ester bonds holding the drugs. The drugs are released and diffuse through the porous screen. (b) Systematic order of attachment of the components: red and orange → green → yellow → black.

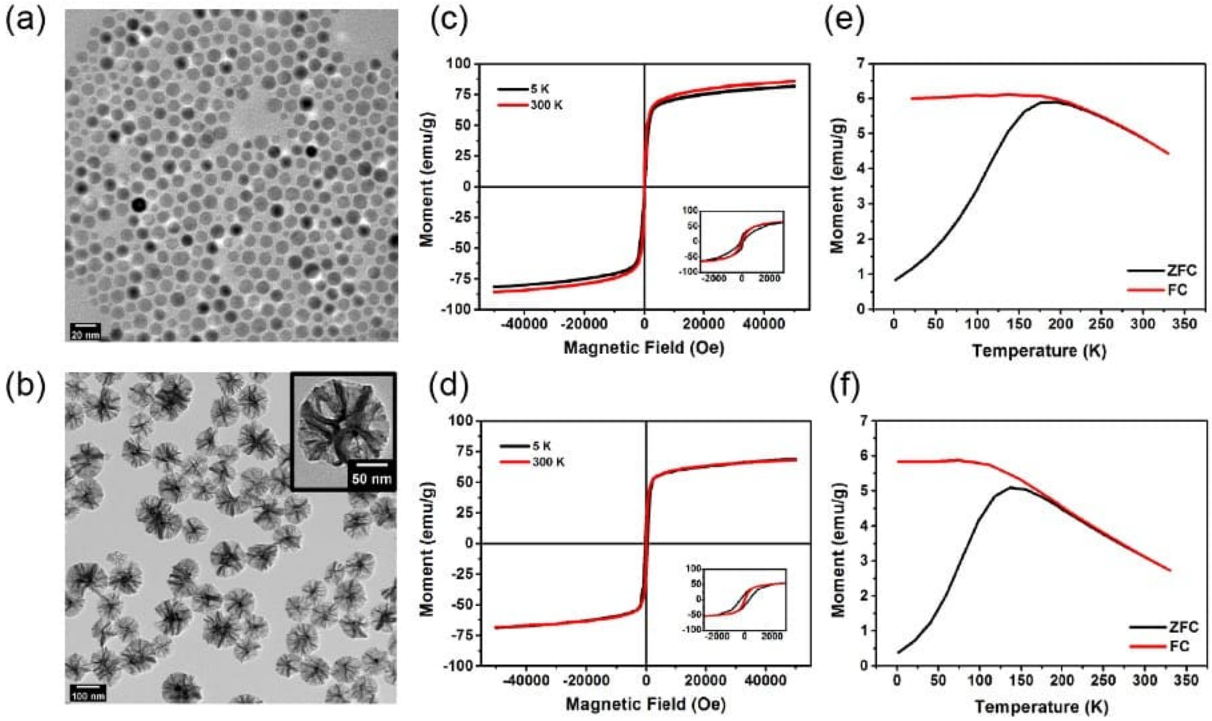

Figure 4.1 TEM images of (a) SPIONs and (b) SPION@EXpMSNs (inset: the enlarged SPION@EXpMSNs and a pore size of approximately 30 nm distributed over the particle). Field-dependent magnetization curves (M-H loops) of (c) SPIONs and (d) SPION@EXpMSNs at 300 K and 5 K (inset: magnification of M-H curves from −2500 to 2500 Oe). ZFC/FC modes of temperature-dependent magnetization curves (M-T loops) of (e) SPIONs and (f) SPION@EXpMSNs under an applied magnetic field of 50 Oe. Results from M-H and M-T loops showed that both the core and core@shell nanoparticles possess superparamagnetic characteristics.

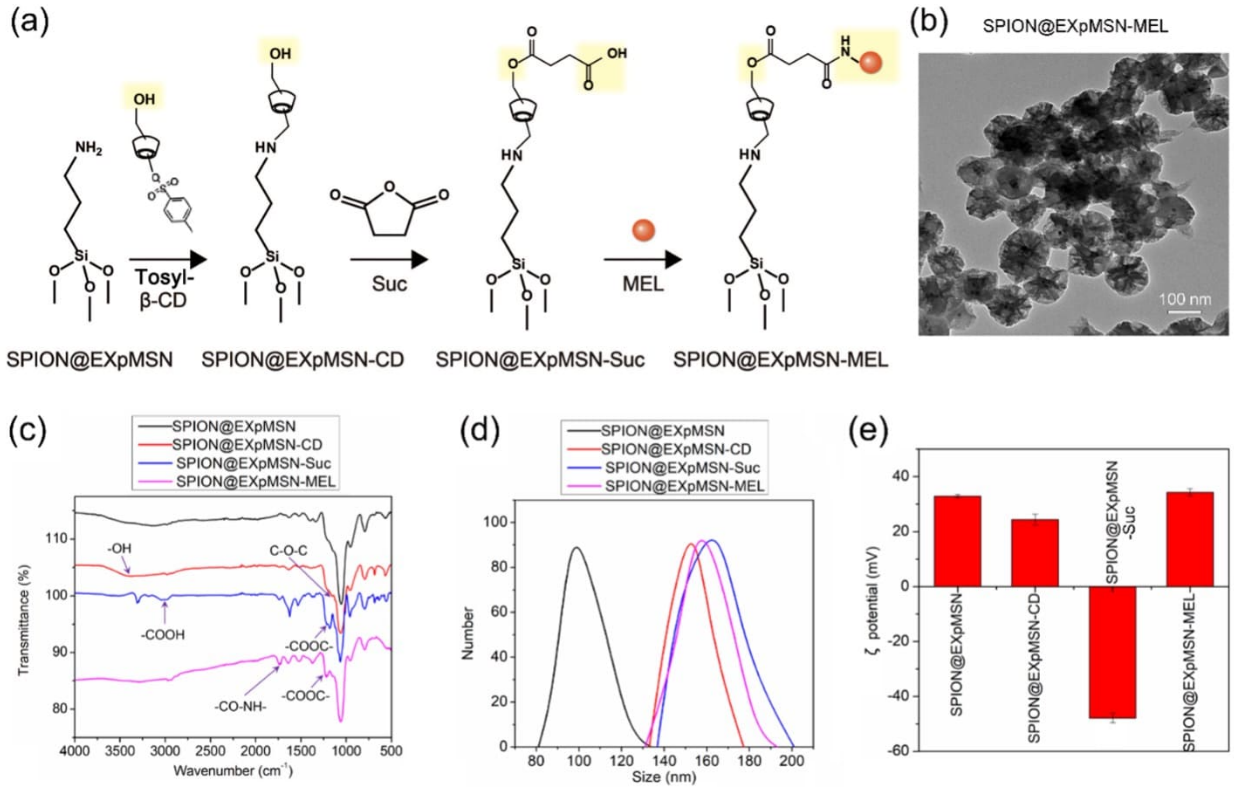

Figure 4.2 (a) Scheme of the step-by-step conjugation of the β-CD, succinic acid (Suc), and peptide drug melittin (MEL) on the pore wall of SPION@EXpMSNs to obtain SPION@EXpMSN-MEL. (b) TEM images of SPION@EXpMSN-MEL. (c) FT-IR spectra, (d) DLS size distribution, (e) ζ-potential values of SPION@EXpMSNs, SPION@EXpMSN-CD, SPION@EXpMSN-Suc, and SPION@EXpMSN-MEL, respectively.

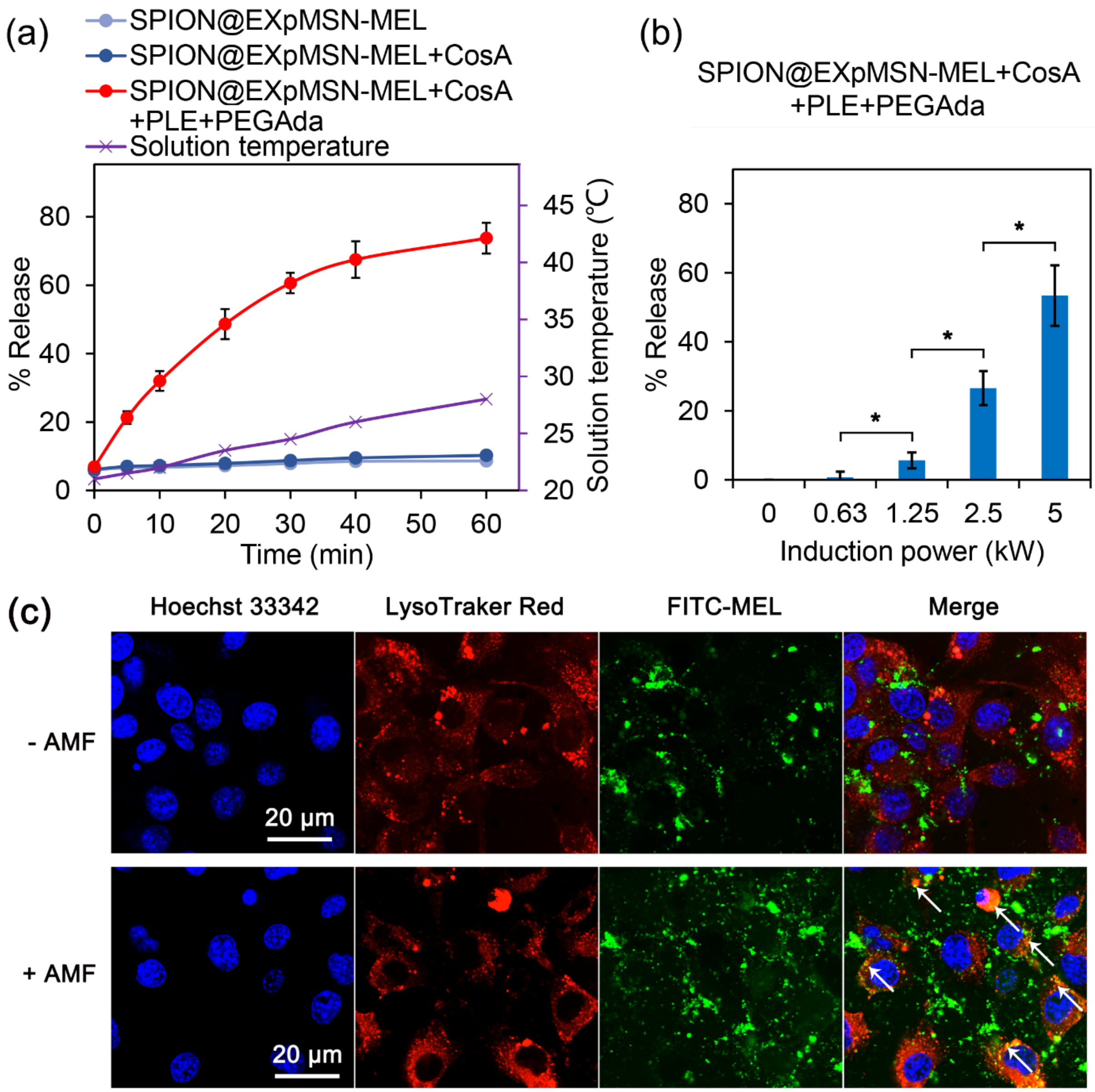

Figure 4.3 (a) Release profile of FITC-MEL from SPION@EXpMSN-MEL+CosA+PLE+PEGAda. (With or without PLE) and bulk temperature rise under different AMF exposure time (AMF was off at 0 min; AMF induction power = 5 kW). (b) Release of FITC-MEL from SPION@EXpMSN-MEL+CosA+PLE+PEGAda under AMF for 30 minutes with different induction power (0 ~5 kW) at an AMF frequency of 375 kHz. The samples were well-insulated from the coil to minimize the heat transfer from the coil. Asterisks (*) indicate significant difference between the SPION@EXpMSN-MEL+CosA+PLE group and other groups ($P<0.05$). (c) Confocal images of the PANC-1 tumor cells treated by the SPION@EXpMSN-MEL+CosA+PLE with no AMF stimulation (**- AMF**) or with AMF stimulation for 30 minutes (**+ AMF)**. The blue-emitting nuclei and red-emitting lysosomes of PANC-1 cells were stained by Hoechst 33342 and LysoTraker Red, respectively. The white arrows show the internalization of FITC- MEL to the lysosomes, indicating that MEL can be triggered and released by an external AMF.

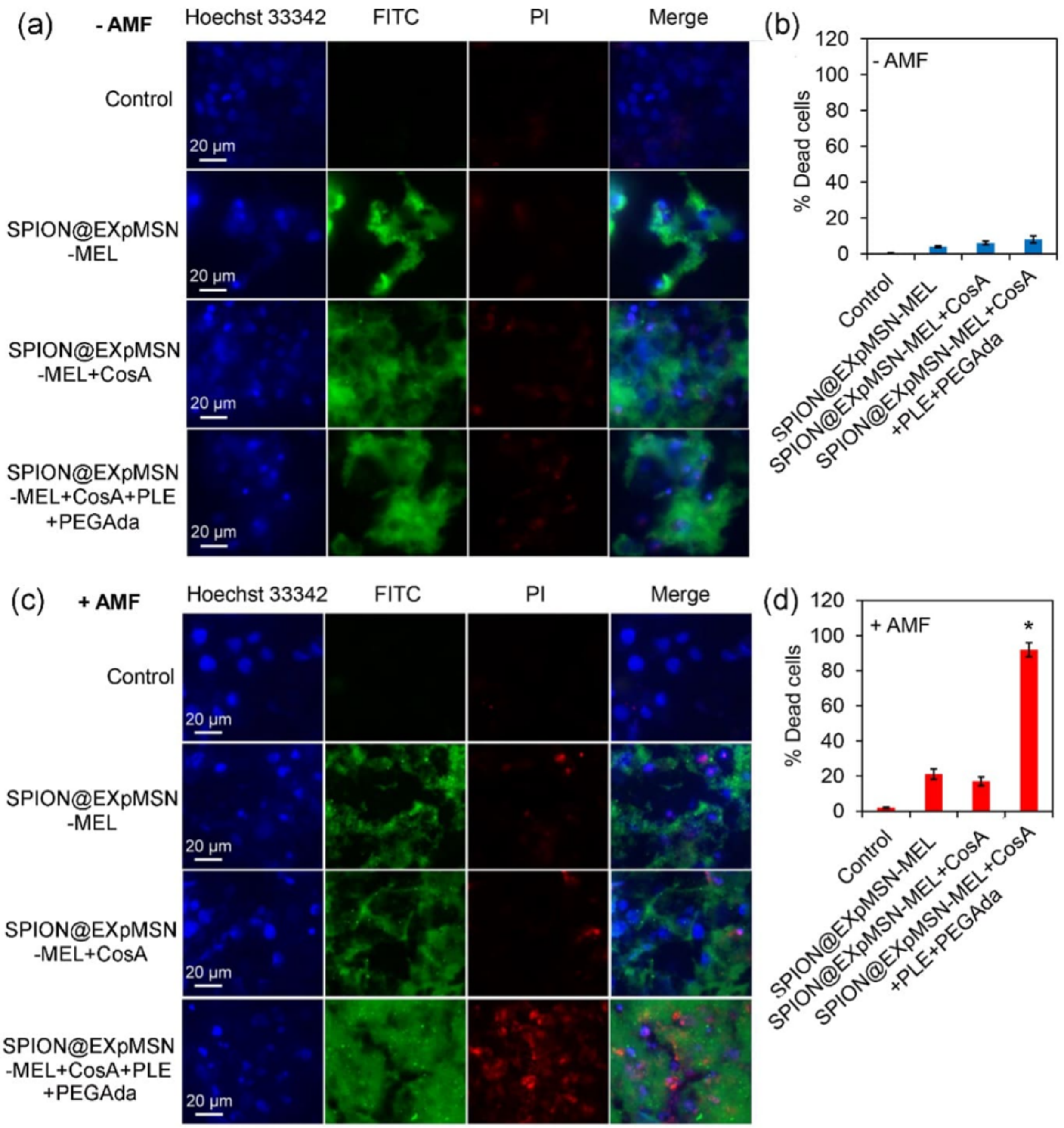

Figure 4.4 Cell death induced by SPION@EXpMSN-MEL, SPION@EXpMSN-MEL+CosA, or SPION@EXpMSN-MEL+CosA+PLE with no AMF stimulation (**- AMF** (a) and (b)) or with AMF stimulation for 30 minutes (**+ AMF**, (c) and (d)). (a,c) Fluorescence images of the treated PANC-1 cells with the blue-emitting nucleus and red-emitting dead cells stained by Hoechst 33342 and PI, respectively. (b,d) Statistical analysis of dead tumor cells. FITC indicates the distribution of FITC-MEL. The merged image shows that AMF heating initiated the triggered release of FITC-MEL, which then diffused into the cancer cells and caused significant killing of cancer cells. Asterisk (*) indicates significant difference between the SPION@EXpMSN-MEL+CosA+PLE group and other groups (*P*<0.05). The control group is cells without nanoparticle treatment.

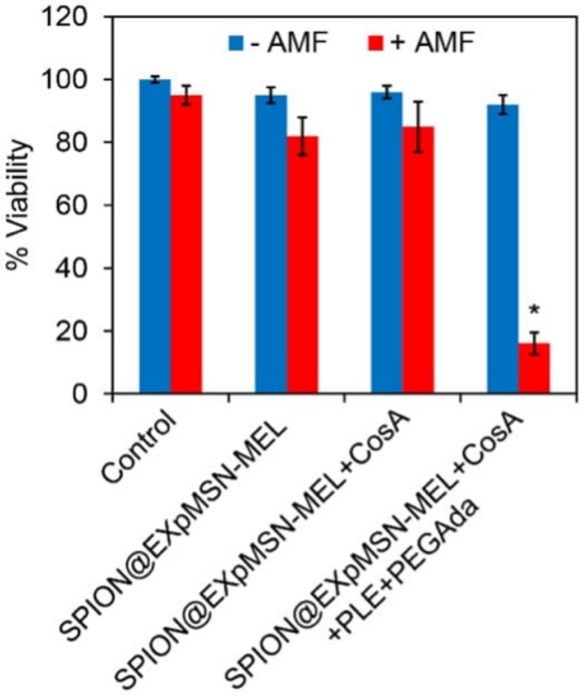

Figure 4.5 CCK-8 assays of PANC-1 cells treated by SPION@EXpMSN-MEL, SPION@EXpMSN-MEL+CosA, SPION@EXpMSN-MEL+CosA+PLE+PEGAda, and free MEL with the same initial concentration (6 μM). Cell viability treated with different MEL-contained core@shell nanoparticles under (a) no AMF treatment and (b) under AMF treatment. Asterisk (*) indicates significant difference between the SPION@EXpMSN-MEL+CosA+PLE+PEGAda group and other groups (P<0.05). The control group is cells without nanoparticle treatment.

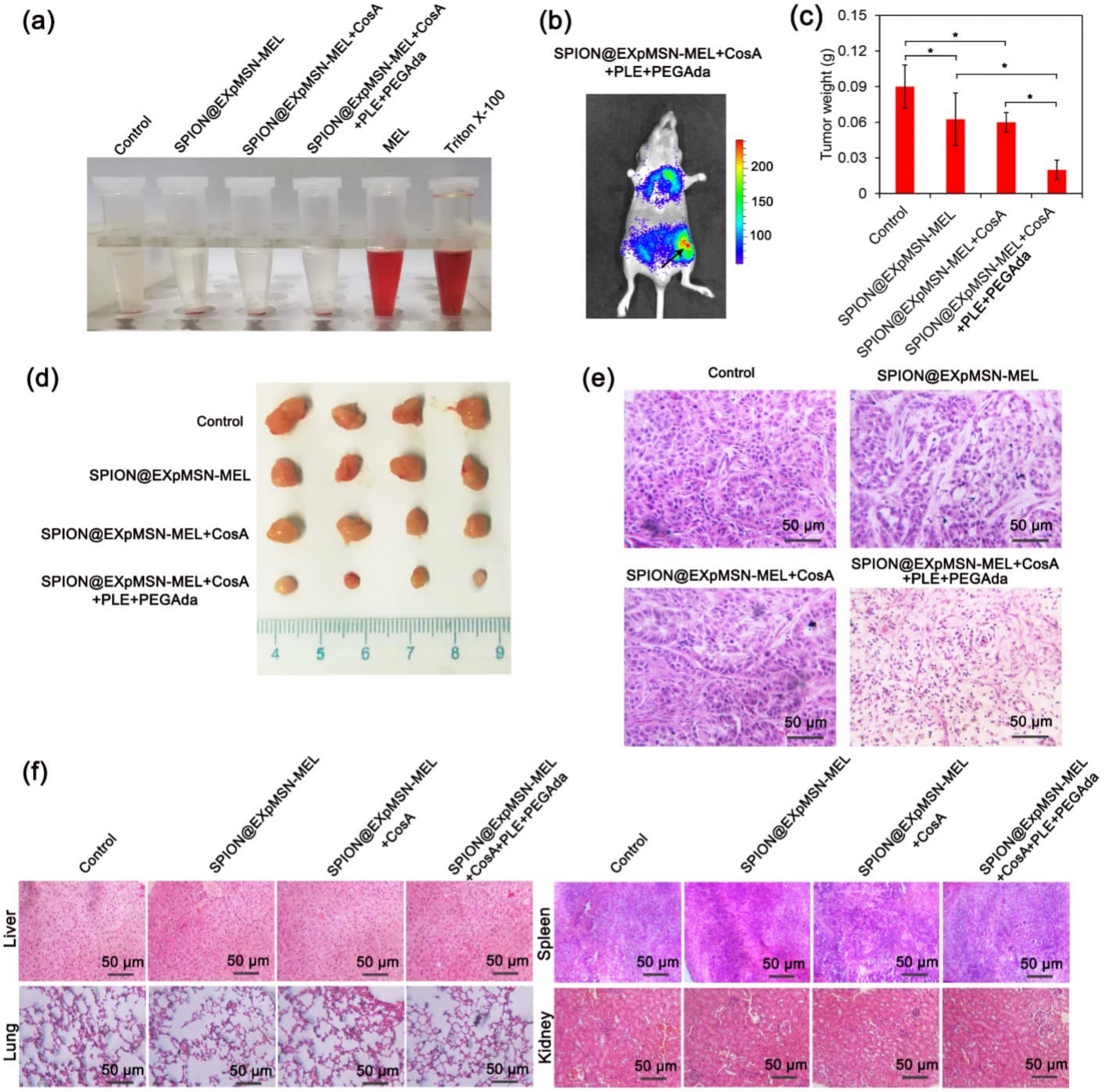

Figure 4.6 *In vivo* antitumor efficiency of the nanocapsules under AMF treatment. (a) Hemolysis assays of free MEL and the nanocapsules (three different groups: SPION@EXpMSN-MEL, SPION@EXpMSN-MEL+CosA, and the SPION@EXpMSN-MEL+CosA+PLE+PEGAda). The nanocapsules (100 mg/L) or free MEL (6 µM) were added into red cell suspension in PBS. The mixtures were incubated at 37 °C and photographed. The control group is cells without nanocapsules treatment. (b) Distribution of the SPION@EXpMSN-MEL+CosA+PLE+PEGAda nanoparticles in the PANC-1 tumor-burden mouse after 6 h of injection (50 mg/kg). The black arrow indicates the tumor site. Note that the nanocapsules accumulated mainly in the tumor tissues. (c) Tumor weights, (d) tumor volumes, (e) histopathological images of the tumor tissues, and (f) histopathological images of the organ tissues of the three different groups after 14 days of intravenous injection of nanocapsules and AMF treatment (30 min, 375 kHz, 5 Kw). Asterisks (*) indicate significant difference between the groups ($P<0.05$).

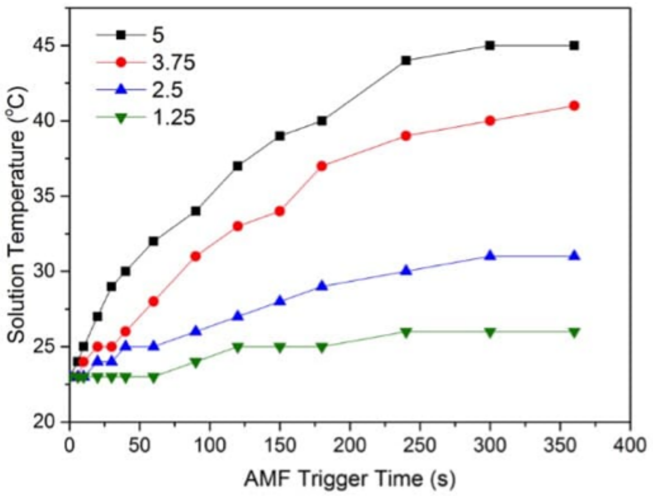

Figure S 4.1 Temperature-time profile of a cyclohexane solution (3 mg/mL) containing SPION in AMF with a power of 5, 3.75, 2.5, and 1.25 kW. The initial slope (dT/dt) of the profile was used to calculate the specific loss power (SLP) of SPION by equation 1, as shown:

$$\mathrm{SLP}_{5\ \mathrm{kW}} = \frac{\mathrm{C} \times \mathrm{V_s}}{\mathrm{m}}\frac{\mathrm{dT}}{\mathrm{dt}} = \frac{2.76\ \mathrm{J}\cdot\mathrm{mL}^{-1}\mathrm{K}^{-1} \times \mathrm{V_s}}{3 \times 10^{-3}\mathrm{g}} \times \frac{1\ \mathrm{K}}{6\ \mathrm{s}} = 153.3\ \mathrm{W}\cdot\mathrm{g}^{-1}$$

where C is the volumetric heat capacity of the solution, $\mathrm{V_s}$ is the volume of solution, and m is the mass of the particle. $\mathrm{SLP}_{3.75\ \mathrm{kW}}$, $\mathrm{SLP}_{2.5\ \mathrm{kW}}$, and $\mathrm{SLP}_{1.25\ \mathrm{kW}}$ are 92.0, 46.0, and 9.9 Wg^{-1}, respectively.

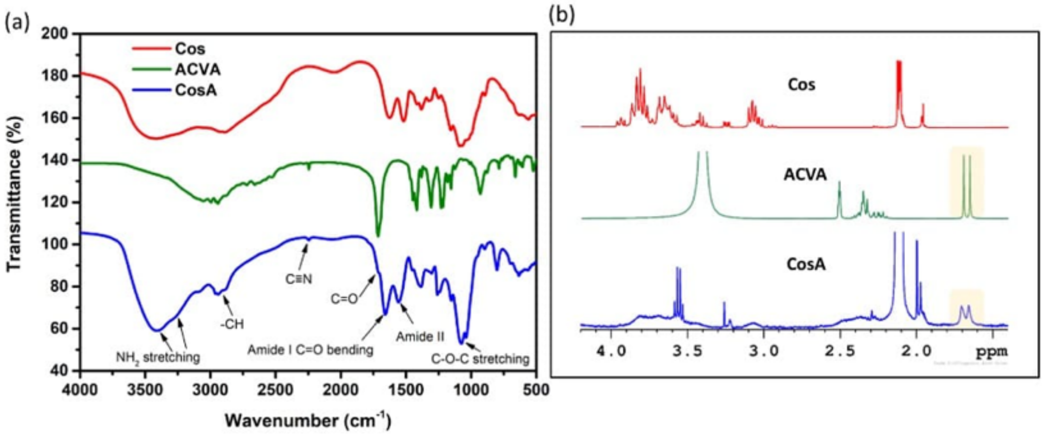

Figure S 4.2 Characterizations of CosA. (a) FTIR analysis, and (b) ^{1}H-NMR of CosA. The integrated ^{1}H-NMR spectrum was used to calculate the ACVA attachment on Cos.

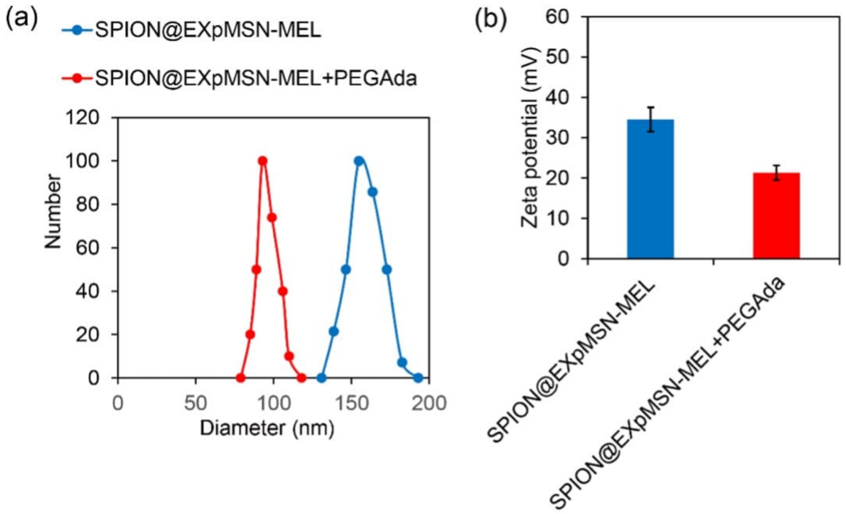

Figure S 4.3 (a) DLS size distribution and (b) Zeta potential of SPION@EXpMSN-MEL (before PEGAda addition) and SPION@EXpMSN-MEL+PEGAda (after PEGAda addition).

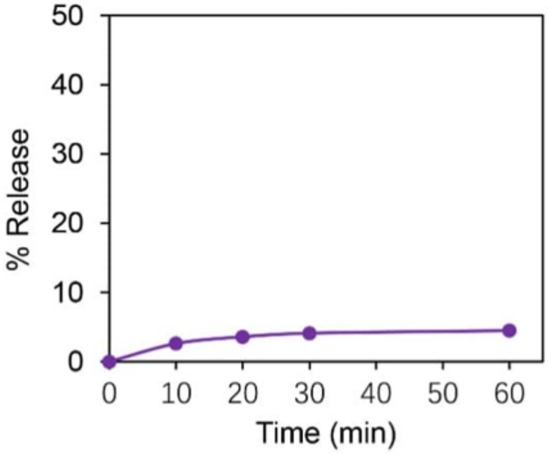

Figure S 4.4 Release of PLE from the SPION@EXpMSN-MEL+CosA+PLE+PEGAda nanoparticles, which are capped by PEGAda. The percent of PLE release was calculated by PLE activity in the nanoparticle-suspending solution divided by PLE activity in the nanoparticles ×100%. PLE activity was evaluated by DCFDA hydrolysis assays.

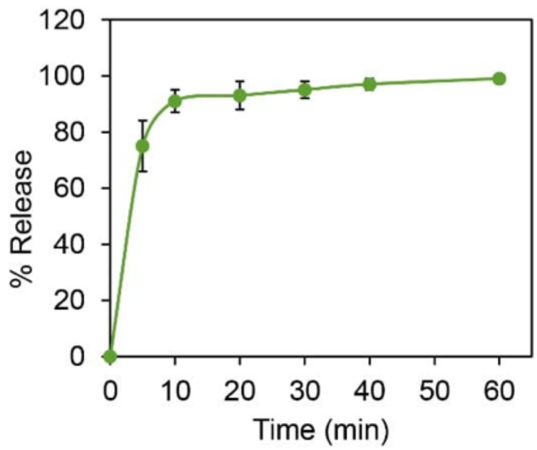

Figure S 4.5 Time-dependent release profile of FITC-MEL from SPION@EXpMSN-MEL triggered by free PLE via the catalytic effect. % Release = release efficiency of cleavable MEL.

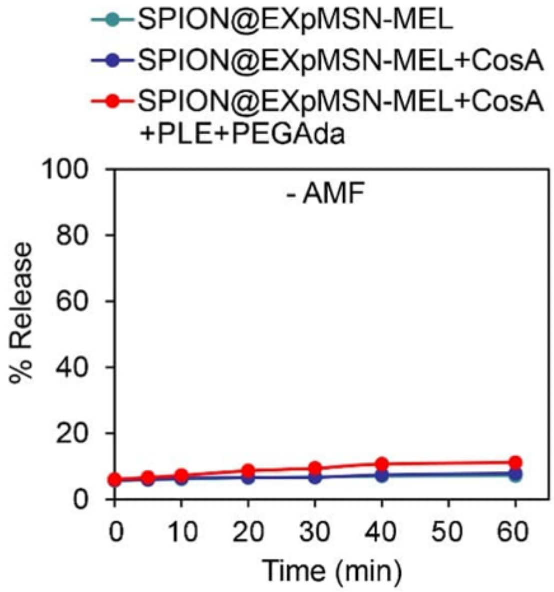

Figure S 4.6 Time-dependent release profile of MEL from SPION@EXpMSN-MEL+CosA+PLE+PEGAda with no AMF stimulation. CosA has a strong inhibitory effect on the toxicity of PLE-contained nanoparticles, leading to the minimized nonspecific cytotoxicity of the SPION@EXpMSN-MEL+CosA+PLE+PEGAda.

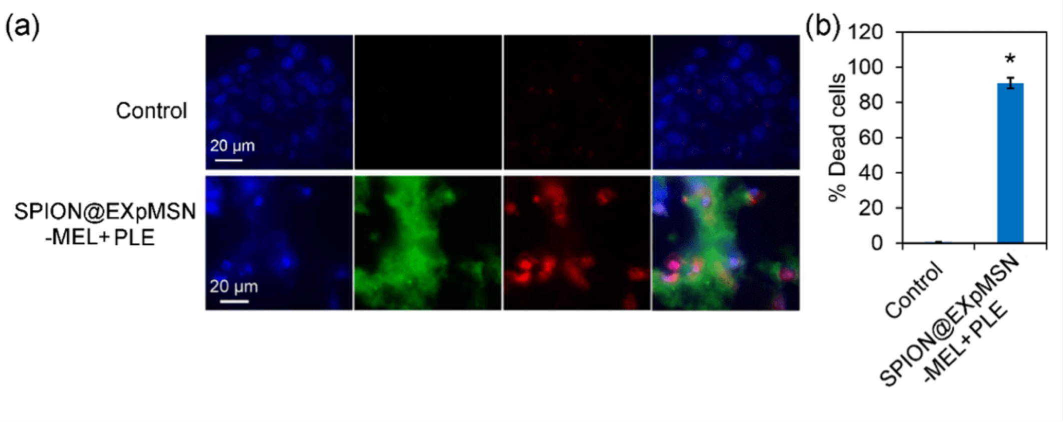

Figure S 4.7 Cell death of PANC-1 cells treated by SPION@EXpMSN-MEL+PLE (no PEGAda). (a) Fluorescence microscopy images of the cells. (b) Statistical analysis of dead cells. Panels from left to right: PANC-A cells with the blue-emitting nucleus stained by Hoechst 33342, green emission from FITC-MEL, red-emitting dead cells stained by PI, and the merged images. * indicates significant difference between the groups ($P<0.05$). The control group is cells without nanoparticle treatment.

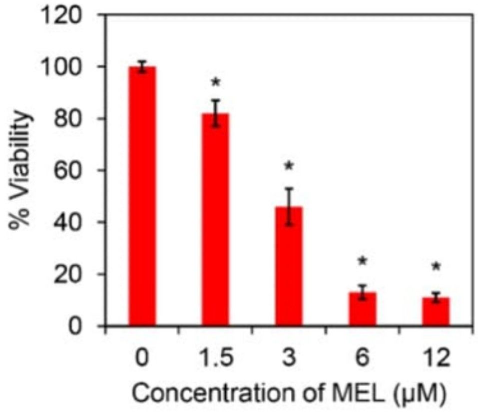

Figure S 4.8 Impact of native MEL doses on viability of tumor cell viability. * indicates significant difference between the groups ($P<0.05$). Note that the remaining cell viability at high MEL concentration (6 μM and 12 μM) is due to the limitation of the assay (resulting from background luminescence), which was based on detecting fluorescence. PI staining results showed the complete cell killing at an equivalent MEL concentration (6 μM).

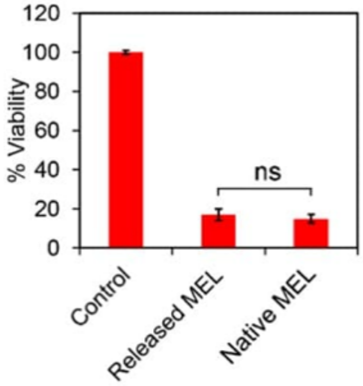

Figure S 4.9 Viability of the PANC-1 tumor cells treated by released MEL from the nanocapsules (100 mg/L) triggered by AMF (30 min) and native MEL (6 µM, same as the concentration of released MEL from the nanocapsules). Both the nanocapsule-released MEL and the native MEL caused comparable decrease in cell viability, indicating that the remaining succinate group at MEL has no impact on the cell-killing efficiency of MEL. Note that there is no significant difference between the released MEL group and the initial MEL group ($P < 0.05$).

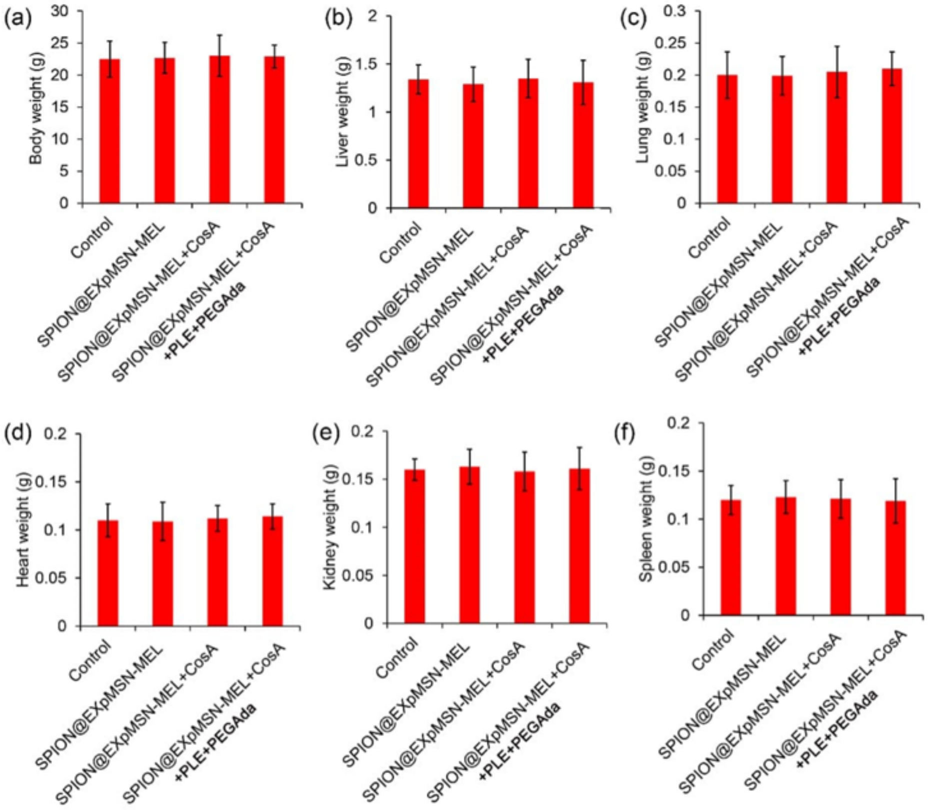

Figure S 4.10 Body and organ weights in the mice treated by the nanocapsules. Note that the nanocapsules have no obvious impact on the weights of both the bodies and the tested organs, including the liver, the lung, the heart, the kidney, and the spleen ($P<0.05$).

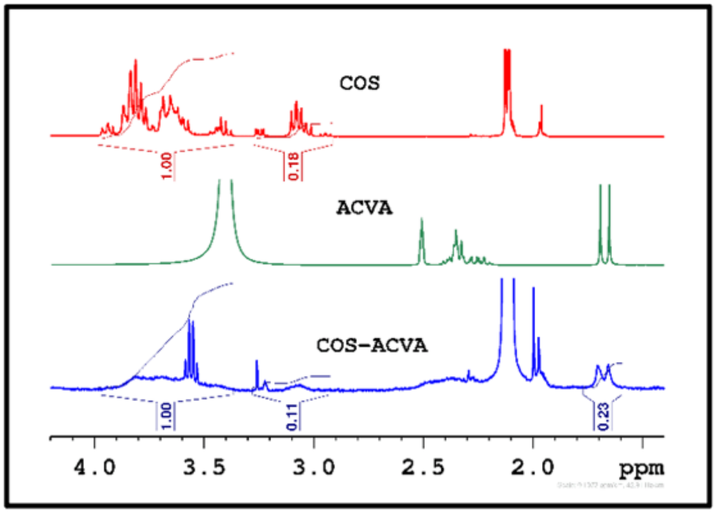

Note1: Calculation of ACVA attachment on Cos by the integrated ^{1}H-NMR spectrum.

COS-ACVA ^{1}H-NMR (400 MHz; 1% v/v CD_3COOD/D_2O): δ_H(ppm) = 1.5-2.0 (6H, H_3C-C(CN)), 3.0-3.4 (2H, GlcN(H-2)), 3.4-4.1 (11H, GlcN(H-3, H-4, H-5, H-6) + GlcNAc (H-2, H-3, H-4, H-5, H-6)).
COS ^{1}H-NMR (400 MHz; 1% v/v CD_3COOD/D_2O): δ_H(ppm) = 2.1 (3H, methyl protons of the acetylated glucosamine residues), 3.0-3.4 (2H, GlcN(H-2)), 3.4-4.1 (11H, GlcN(H-3, H-4, H-5, H-6) + GlcNAc (H-2, H-3, H-4, H-5, H-6), pyranose rings).
ACVA ^{1}H-NMR (400 MHz; $(CD_3)_2S$=O): δ_H(ppm) = 1.5-2.0 (6H, H_3C-C(CN)), 2.0-2.5 (8H, 2xCH_2CH_2COO).

3.4-4.1 ppm: GlcN(H-3, H-4, H-5, H-6) + GlcNAc (H-2, H-3, H-4, H-5, H-6) = 11 H
3.0-3.4 ppm: GlcN(H-2) = 2 H
1.00/0.18 = 5.6 ≈ 11 H/2 H = 5.5

0.18 → 0.11 = 9 NH_2 - 5 NH_2 = 4 NH_2 (4 NH_2 of glucosamine being replaced)
ACVA methyl group = 6 H
Therefore, 6 H × 4 = 24 H, which matches the integral of the region at 1.6-1.8 ppm.

As a result, approximately 4/9 NH_2 (= 44.4%) was replaced by ACVA.

4.6 References

(1) Sun, I. C.; Yoon, H. Y.; Lim, D. K.; Kim, K. Recent Trends in In Situ Enzyme-Activatable Prodrugs for Targeted Cancer Therapy. *Bioconjug. Chem.* 2020, 31 (4), 1012–1024.

(2) Rooseboom, M.; Commandeur, J. N. M.; Vermeulen, N. P. E. Enzyme-Catalyzed Activation of Anticancer Prodrugs. *Pharmacol. Rev.* 2004, 56 (1), 53–102.

(3) Prabha, M. Hydrolytic Enzymes Targeting to Prodrug / Drug Metabolism for Translational Application in Cancer. *J. Clin. Sci. Transl. Med.* 2018, 1 (1).

(4) Mayandi, V.; Xi, Q.; Goh, E. T. L.; Koh, S. K.; Jie Toh, T. Y.; Barathi, V. A.; Fazil, M. H. U. T.; S. Chalasani, M. L.; Varadarajan, J.; Ting, D. S. J.; Beuerman, R. W.; Chan, L. W.; Agrawal, R.; Barkham, T.; Zhou, L.; Verma, N. K.; Lakshminarayanan, R. Rational Substitution of ε-Lysine for α-Lysine Enhances the Cell and Membrane Selectivity of Pore-Forming Melittin. *J. Med. Chem.* 2020, 63, 3522−3537.

(5) Lavis, L. D. Ester Bonds in Prodrugs. *ACS Chem. Biol.* 2008, 3 (4), 203–206.

(6) Britt, H. M.; Mosely, J. A.; Sanderson, J. M. The Influence of Cholesterol on Melittin Lipidation in Neutral Membranes. *Phys. Chem. Chem. Phys.* 2019, 21 (2), 631–640.

(7) Lim, S. M.; Lee, S. H. Effectiveness of Bee Venom Acupuncture in Alleviating Post-Stroke Shoulder Pain: A Systematic Review and Meta-Analysis. *J. Integr. Med.* 2015, 13 (4), 241–247.

(8) Lyu, C.; Fang, F.; Li, B. Anti-Tumor Effects of Melittin and Its Potential Applications in Clinic. *Curr. Protein Pept. Sci.* 2018, 20 (3), 240–250.

(9) Qiao, H.; Fang, D.; Zhang, L.; Gu, X.; Lu, Y.; Sun, M.; Sun, C.; Ping, Q.; Li, J.; Chen, Z.; Chen, J.; Hu, L.; Di, L. Nanostructured Peptidotoxins as Natural Pro-Oxidants Induced Cancer Cell Death via Amplification of Oxidative Stress. *ACS Appl. Mater. Interfaces* 2018, 10 (5), 4569–4581.

(10) Liu, H.; Hu, Y.; Sun, Y.; Wan, C.; Zhang, Z.; Dai, X.; Lin, Z.; He, Q.; Yang, Z.; Huang, P.; Xiong, Y.; Cao, J.; Chen, X.; Chen, Q.; Lovell, J. F.; Xu, Z.; Jin, H.; Yang, K. Co-Delivery of Bee Venom Melittin and a Photosensitizer with an Organic-Inorganic Hybrid Nanocarrier for Photodynamic Therapy and Immunotherapy. *ACS Nano* 2019, 13 (11), 12638–12652.

(11) Oršolić, N. Bee Venom in Cancer Therapy. *Cancer Metastasis Rev.* 2012, 31 (1–2), 173–194.

(12) Li, Y.; Xu, N.; Zhu, W.; Wang, L.; Liu, B.; Zhang, J.; Xie, Z.; Liu, W. Nanoscale Melittin@Zeolitic Imidazolate Frameworks for Enhanced Anticancer Activity and Mechanism Analysis. *ACS Appl. Mater. Interfaces* 2018, 10 (27), 22974–22984.

(13) Juvvadi, P.; Vunnam, S.; Merrifield, R. B. Synthetic Melittin, Its Enantio, Retro, and Retroenantio Isomers, and Selected Chimeric Analogs: Their Antibacterial, Hemolytic, and Lipid Bilayer Action. *J. Am. Chem. Soc.* 1996, 118 (38), 8989–8997.

(14) Asthana, N.; Yadav, S. P.; Ghosh, J. K. Dissection of Antibacterial and Toxic Activity of Melittin: A Leucine Zipper Motif Plays a Crucial Role in Determining Its Hemolytic Activity but Not Antibacterial Activity. *J. Biol. Chem.* 2004, 279 (53), 55042–55050.

(15) Yu, X.; Dai, Y.; Zhao, Y.; Qi, S.; Liu, L.; Lu, L.; Luo, Q.; Zhang, Z. Melittin-Lipid Nanoparticles Target to Lymph Nodes and Elicit a Systemic Anti-Tumor Immune Response. *Nat. Commun.* 2020, 11 (1).

(16) Jin, H.; Zhao, G.; Hu, J.; Ren, Q.; Yang, K.; Wan, C.; Huang, A.; Li, P.; Feng, J. P.; Chen, J.; Zou, Z. Melittin-Containing Hybrid Peptide Hydrogels for Enhanced Photothermal Therapy of Glioblastoma. *ACS Appl. Mater. Interfaces* 2017, 9 (31), 25755–25766.

(17) Höcherl, A.; Jäger, E.; Jäger, A.; Hrubý, M.; Konefał, R.; Janoušková, O.; Spěváček, J.; Jiang, Y.; Schmidt, P. W.; Lodge, T. P.; Štěpánek, P. One-Pot Synthesis of Reactive Oxygen Species (ROS)-Self-Immolative Polyoxalate Prodrug Nanoparticles for Hormone Dependent Cancer Therapy with Minimized Side Effects. *Polym. Chem.* 2017, 8 (13), 1999–2004.

(18) Wang, L.; Yuan, Y.; Lin, S.; Cheng, D.; Wang, X.; Jiang, Q.; Shuai, X. Co-Delivery of 5-Fluorocytosine and Cytosine Deaminase into Glioma Cells Mediated by an Intracellular Environment-Responsive Nanovesicle. *Polym. Chem.* 2014, 5 (15), 4542–4552.

(19) Ling, X.; Tu, J.; Wang, J.; Shajii, A.; Kong, N.; Feng, C.; Zhang, Y.; Yu, M.; Xie, T.; Bharwani, Z.; Aljaeid, B. M.; Shi, B.; Tao, W.; Farokhzad, O. C. Glutathione-Responsive Prodrug Nanoparticles for Effective Drug Delivery and Cancer Therapy. *ACS Nano* 2019, 13 (1), 357–370.

(20) Chen, J.; Li, G.; Liu, Q.; Liang, Y.; Liu, M.; Wu, H.; Gao, W. A Photocleavable Amphiphilic Prodrug Self-Assembled Nanoparticles with Effective Anticancer Activity in Vitro. *Nanomaterials* 2019, 9 (6).

(21) Hou, B.; Zhou, L.; Wang, H.; Saeed, M.; Wang, D.; Xu, Z.; Li, Y.; Yu, H. Engineering Stimuli-Activatable Boolean Logic Prodrug Nanoparticles for Combination Cancer Immunotherapy. *Adv. Mater.* 2020, 1907210, 1–11.

(22) Wu, M.; Li, J.; Lin, X.; Wei, Z.; Zhang, D.; Zhao, B.; Liu, X.; Liu, J. Reduction/Photo Dual-Responsive Polymeric Prodrug Nanoparticles for Programmed SiRNA and Doxorubicin Delivery. *Biomater. Sci.* 2018, 6 (6), 1457–1468.

(23) Saint-Cricq, P.; Deshayes, S.; Zink, J. I.; Kasko, A. M. Magnetic Field Activated Drug Delivery Using Thermodegradable Azo-Functionalised PEG-Coated Core-Shell Mesoporous Silica Nanoparticles. *Nanoscale* 2015, 7 (31), 13168–13172.

(24) Chen, W.; Cheng, C. A.; Zink, J. I. Spatial, Temporal, and Dose Control of Drug Delivery Using Noninvasive Magnetic Stimulation. *ACS Nano* 2019, 13 (2), 1292–1308.

(25) Cazares-Cortes, E.; Cabana, S.; Boitard, C.; Nehlig, E.; Griffete, N.; Fresnais, J.; Wilhelm, C.; Abou-Hassan, A.; Ménager, C. Recent Insights in Magnetic Hyperthermia: From the "Hot-Spot" Effect for Local Delivery to Combined Magneto-Photo-Thermia Using Magneto-Plasmonic Hybrids. *Adv. Drug Deliv. Rev*. 2019, 138, 233–246.

(26) Pan, J.; Hu, P.; Guo, Y.; Hao, J.; Ni, D.; Xu, Y.; Bao, Q.; Yao, H.; Wei, C.; Wu, Q.; Shi, J. Combined Magnetic Hyperthermia and Immune Therapy for Primary and Metastatic Tumor Treatments. *ACS Nano* 2020, 14 (1), 1033–1044.

(27) Lin, F. C.; Hsu, C. H.; Lin, Y. Y. Nano-Therapeutic Cancer Immunotherapy Using Hyperthermia-Induced Heat Shock Proteins: Insights from Mathematical Modeling. *Int. J. Nanomedicine* 2018, 13, 3529–3539.

(28) Johannsen, M.; Gneveckow, U.; Eckelt, L.; Feussner, A.; Waldöfner, N.; Scholz, R.; Deger, S.; Wust, P.; Loening, S. A.; Jordan, A. Clinical Hyperthermia of Prostate Cancer Using Magnetic Nanoparticles: Presentation of a New Interstitial Technique. *Int. J. Hyperth.* 2005, 21 (7), 637–647.

(29) Johannsen, M.; Thiesen, B.; Wust, P.; Jordan, A. Magnetic Nanoparticle Hyperthermia for Prostate Cancer. *Int. J. Hyperth.* 2010, 26 (8), 790–795.

(30) Maier-Hauff, K.; Ulrich, F.; Nestler, D.; Niehoff, H.; Wust, P.; Thiesen, B.; Orawa, H.; Budach, V.; Jordan, A. Efficacy and Safety of Intratumoral Thermotherapy Using Magnetic Iron-Oxide Nanoparticles Combined with External Beam Radiotherapy on Patients with Recurrent Glioblastoma Multiforme. *J. Neurooncol.* 2011, 103 (2), 317–324.

(31) Liu, X.; Zhang, Y.; Wang, Y.; Zhu, W.; Li, G.; Ma, X.; Zhang, Y.; Chen, S.; Tiwari, S.; Shi, K.; Zhang, S.; Fan, H. M.; Zhao, Y. X.; Liang, X. J. Comprehensive Understanding of Magnetic Hyperthermia for Improving Antitumor Therapeutic Efficacy. *Theranostics* 2020, 10 (8), 3793–3815.

(32) Cheng, C. A.; Deng, T.; Lin, F. C.; Cai, Y.; Zink, J. I. Supramolecular Nanomachines as Stimuli-Responsive Gatekeepers on Mesoporous Silica Nanoparticles for Antibiotic and Cancer Drug Delivery, *Theranostics*, 2019, 9.

(33) Li, Z.; Barnes, J. C.; Bosoy, A.; Stoddart, J. F.; Zink, J. I. Mesoporous Silica Nanoparticles in Biomedical Applications. *Chem. Soc. Rev.* 2012, 41 (7), 2590–2605.

(34) Chen, W.; Glackin, C. A.; Horwitz, M. A.; Zink, J. I. Nanomachines and Other Caps on Mesoporous Silica Nanoparticles for Drug Delivery. *Acc. Chem. Res.* 2019, 52 (6), 1531–1542.

(35) Chen, W.; Cheng, C. A.; Lee, B. Y.; Clemens, D. L.; Huang, W. Y.; Horwitz, M. A.; Zink, J. I. Facile Strategy Enabling Both High Loading and High Release Amounts of the Water-Insoluble Drug Clofazimine Using Mesoporous Silica Nanoparticles. *ACS Appl. Mater. Interfaces* 2018, 10 (38), 31870–31881.

(36) Wu, S. H.; Lin, H. P. Synthesis of Mesoporous Silica Nanoparticles. *Chem. Soc. Rev.* 2013, 42 (9), 3862–3875.

(37) Tarn, D.; Ashley, C. E.; Xue, M.; Carnes, E. C.; Zink, J. I.; Brinker, C. J. Mesoporous Silica Nanoparticle Nanocarriers: Biofunctionality and Biocompatibility. *Acc. Chem. Res.* 2013, 46 (3), 792–801.

(38) Xue, M.; Zink, J. I. An Enzymatic Amplifier Based on Mechanized Nanoparticles Table of Contents. *J. Am. Chem. Soc.* 2013, 135, 17659–17662.

(39) Na, H. K.; Kim, M. H.; Park, K.; Ryoo, S. R.; Lee, K. E.; Jeon, H.; Ryoo, R.; Hyeon, C.; Min, D. H. Efficient Functional Delivery of SiRNA Using Mesoporous Silica Nanoparticles with Ultralarge Pores. *Small* 2012, 8 (11), 1752–1761.

(40) Kwon, D.; Cha, B. G.; Cho, Y.; Min, J.; Park, E.; Kang, S.; Kim, J. Extra-Large Pore Mesoporous Silica Nanoparticles for Directing in Vivo M2 Macrophage Polarization by Delivering IL - 4. *Nano Lett.* 2017, 17, 2747–2756.

(41) Cha, B. G.; Jeong, J. H.; Kim, J. Extra-Large Pore Mesoporous Silica Nanoparticles Enabling Co-Delivery of High Amounts of Protein Antigen and Toll-like Receptor 9 Agonist for Enhanced Cancer Vaccine Efficacy. *ACS Cent. Sci* 2018, 4, 484–492.

(42) Ruhle, B.; Datz, S.; Argyo, C.; Bein, T.; Zink, J. I. A Molecular Nanocap Activated by Superparamagnetic Heating for Externally Stimulated Cargo Release †. *Chem. Commun.* 2016, 52, 1843–1846.

(43) Yu, Q.; Deng, T.; Lin, F. C.; Zhang, B.; Zink, J. I. Supramolecular Assemblies of Heterogeneous Mesoporous Silica Nanoparticles to Co-Deliver Antimicrobial Peptides and Antibiotics for Synergistic Eradication of Pathogenic Biofilms. *ACS Nano* 2020, 14 (5), 5926–5937.

(44) Lin, F.-C.; Xie, Y.; Deng, T.; Zink, J. I. Magnetism, Ultrasound, and Light-Stimulated Mesoporous Silica Nanocarriers for Theranostics and Beyond. *J. Am. Chem. Soc.* 2021, 143, 6025–6036.

(45) Dong, J.; Zink, J. I. Taking the Temperature of the Interiors of Magnetically Heated Nanoparticles. *ACS Nano* 2014, 8 (5), 5199–5207.

(46) Cheng, C. A.; Chen, W.; Zhang, L.; Wu, H. H.; Zink, J. I. A Responsive Mesoporous Silica Nanoparticle Platform for Magnetic Resonance Imaging-Guided High-Intensity Focused Ultrasound-Stimulated Cargo Delivery with Controllable Location, Time, and Dose. *J. Am. Chem. Soc.* 2019, 141 (44), 17670–17684.

(47) Park, J.; An, K.; Hwang, Y.; Park, J. E. G.; Noh, H. J.; Kim, J. Y.; Park, J. H.; Hwang, N. M.; Hyeon, T. Ultra-Large-Scale Syntheses of Monodisperse Nanocrystals. *Nat. Mater.* 2004, 3 (12), 891–895.

(48) Larumbe, S.; G´omez-Polo, C.; P´erez-Landaz´abal, J. I.; Pastor, J. M. Effect of a SiO2 Coating on the Magnetic Properties of Fe3O4 Nanoparticles. *J. Phys. Condens. Matter* 2012, 24.

(49) Issa, B.; Obaidat, I. M.; Albiss, B. A.; Haik, Y. Magnetic Nanoparticles : Surface Effects and Properties Related to Biomedicine Applications. *Int. J. Mol. Sci.* 2013, 14.

(50) Ma, D.; Veres, T.; Clime, L.; Guan, J.; Kingston, D.; Simard, B. Superparamagnetic Fe x O y @ SiO 2 Core - Shell Nanostructures : Controlled Synthesis and Magnetic Characterization. *J. Phys. Chem. C* 2007, 111, 1999–2007.

(51) Lin, F.; Zink, I. Probing the Local Nanoscale Heating Mechanism of a Magnetic Core in Mesoporous Silica Drug-Delivery Nanoparticles Using Fluorescence Depolarization. *J. Am. Chem. Soc.* 2020, 142, 5212–5220.

(52) Rosensweig, R. E. Heating Magnetic Fluid with Alternating Magnetic Field. *J. Magn. Magn. Mater*. 2002, 252, 370–374.

(53) Dong, H.; Pang, L.; Cong, H.; Shen, Y.; Yu, B. Application and Design of Esterase-Responsive Nanoparticles for Cancer Therapy. *Drug Deliv.* 2019, 26 (1), 416–432.

(54) Yang, Y.; Zhang, Y. M.; Chen, Y.; Chen, J. T.; Liu, Y. Targeted Polysaccharide Nanoparticle for Adamplatin Prodrug Delivery. *J. Med. Chem.* 2013, 56 (23), 9725–9736.

(55) Liong, M.; Lu, J.; Kovochich, M.; Xia, T.; Ruehm, S. G.; Nel, A. E.; Tamanoi, F.; Zink, J. I. Multifunctional Inorganic Nanoparticles for Imaging, Targeting, and Drug Delivery. *ACS Nano* 2008, 2 (5), 889–896.

Chapter 5 A Facile Method to Synthesize Non-Ionic Fluorinated Ferrofluids for Measuring Mechanics in Living Systems

This chapter is based on collaborative work with Professor Ellen Sletten's group at UCLA and Professor Otger Campàs's group at UCSB. The study aims to optimize *in vivo* mechanical force measurements (*in vivo* mechanosensing) based on microdroplet deformation by the fluorinated ferrofluids that are encapsulated in the microdroplet under the application of external magnetic fields. Lin, F. C. designed and performed all the experiments. Jeffrey I. Zink was the P.I.

Table of Content Figure

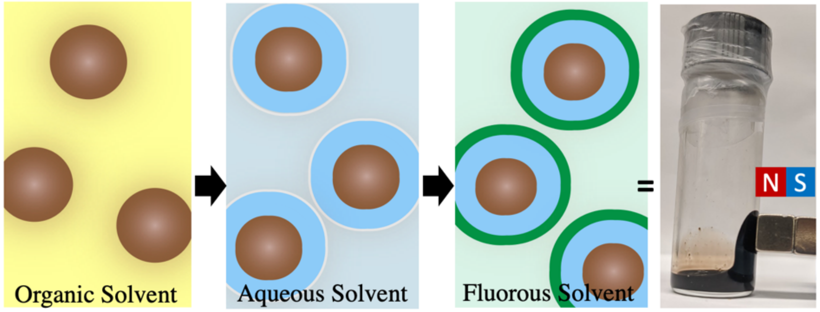

5.1 Introduction

Ferrofluids, possessing both magnetic properties and liquid behaviors, consist of single-domain magnetic nanoparticles, so-called superparamagnetic iron oxide nanoparticles (SPIONs), in a carrier liquid. The biorthogonal perfluorocarbons (PFCs) oils are of interest in this work because of their unique properties such as phase separation from organic and aqueous solutions. PFCs have been utilized as PFC nanoemulsions for therapeutic applications, such as, blood substitutes,[1] photosensitizer carriers,[2] gene delivery systems,[3] and for diagnostic purposes, such as, ^{19}F-MRI[4–6] and ultrasound[7,8] contrast agents.[9] PFCs have also been used to form cell-sized oil microdroplets for the measurements of cellular forces within developing three-dimensional (3D) tissues *in vivo*.[10,11] By encapsulating ferrofluids in PFC oil microdroplets, the magnetically responsive microdroplet technique enables both direct measurements of local material properties of the cellular microenvironment and local application of mechanical forces within developing tissues.[12] The formation and stabilization of both PFC nanoemulsions and microdroplets depend highly on their surface chemistries that are controlled by surfactants.[10,13] The presence of chemical contaminants, e.g., ionic surfactants, in the commercially available fluorinated ferrofluids can disrupt the interfacial tension between the liquid-liquid interface and affect the stability of the droplets. To expand the applications of fluorinated ferrofluids, it is essential to control the chemical functionalization of SPIONs with appropriate surface chemistry.

Stable PFCs oil-based ferrofluids have been difficult to synthesize. The stability of ferrofluids depends highly on the surfactants attached, where these surfactants have two major functions: (1) assure a distance between the magnetic particles to overcome the forces of attraction caused by van der Waals forces and magnetic attraction in order to prevent agglomeration of magnetic nanoparticles and (2) serve as the outer layer of the magnetic particle that is compatible with the liquid carrier.[14] Ionic surfactants are normally introduced into commercially-available PFCs oil-based ferrofluids to stabilize the ferrofluids, restricting them from applications that can only function well in the absence of ionic surfactants. The conventional strategy to synthesize fluorinated magnetic nanocrystals is to exchange ligands on the crystal surface with fluorinated ones.[15,16] For this ligand-exchange approach, ligands are non-covalently bonded and therefore the presence of free ionic surfactant cannot be fully avoided. Also, the magnetic nanocrystals tend to agglomerate and aggregate under high magnetic field gradients and separate out from the liquid carrier. Such ionic contaminants due to the loosely attached surfactants can be bypassed by introducing a thin layer of silica of which the surface comprises abundant hydrophilic silanol groups that can form chemical Si-O-Si bonds with silanes such as fluoroalkyl silane.[17,18] Here, we introduce new fluorinated ferrofluids by chemically grafting fluoroalkyl silanes on the surface of SPION@SiO$_2$ nanoparticles via silanization, where the ionic contaminants can be avoided and excellent chemical stability of fluorinated ferrofluids is achieved. We demonstrate that larger-sized fluoroalkyl silanes with molecular weights (MW) of 4000-8000 g/mol can be grafted on SPION@SiO$_2$ nanoparticles with the assistance of low-MW fluoroalkyl silanes. This opens a new and facile method for attaching both short and long silanes on the surface of magnetic nanocrystals to synthesize non-ionic fluorinated ferrofluids for extended applications.

5.2 Results and Discussion

SPION@SiO$_2$ nanoparticles were prepared by using a reverse microemulsion method (**Figure 5.1a**),[19] and monodispersed SPIONs with diameters of 20 ± 5 nm were synthesized by a modified thermal decomposition method (**Figure 5.1b**). SPIONs are stabilized by oleic acid and therefore can be suspended in low-MW non-polar hydrocarbon oils such as hexane. After silica coating, SPION@SiO$_2$ nanoparticles can be suspended in polar solvents such as ethanol. A dense silica shell was chosen to coat SPIONs due to its feasibility of reducing the shell thickness to < 5 nm by tuning the amount of TEOS and ammonia so that the magnetic ratio of the core/shell nanoparticles can be maximized (**Figure 5.1c**, **Figure S 5.1**).[19] Note that the water phase generated by the ammonia should be adjusted to provide a more confined space for the silica shell forming process so that surface roughness of SPION@SiO$_2$ nanoparticles can be reduced (**Figure S 5.1**). Two perfluoroalkyl silanes, perfluorodecyltriethoxysilane (PFDTES), **1**, and perfluoropolyether (PFPE), **2**, with MW differing by more than 10 times were used as surfactants to coat the surface of SPION@SiO$_2$ nanoparticles via chemical Si-O-Si bonds.

5.2.1 Synthesis of SPION@SiO_2-1 Using Biphasic Approach

To monitor the attachments of perfluoroalkyl silanes on SPION@SiO_2 nanoparticles and prevent self-condensation of silanes, a biphasic approach was implemented where the ethanol solution of SPION@SiO_2 nanoparticles and the PFCs solvent containing excess perfluoroalkyl silanes form a two-phase system (**Figure 5.2a**). An aliquot of water was added to the ethanol phase to promote the hydrolysis of perfluoroalkyl silanes. **Scheme 5.1** shows an illustration of silanization and phase transfer processes. When two phases are mixed, ethanol-soluble **1** diffuse through both phases, become hydrolyzed due to the presence of water in the ethanol phase, and undergo condensation with the abundant silanol groups on the SPION@SiO_2 nanoparticles to form Si-O-Si bonds. When SPION@SiO_2 nanoparticles are functionalized with a sufficient amount of perfluoroalkyl silanes, they become soluble in the PFCs phase. The attained non-ionic fluorinated ferrofluids (SPION@SiO_2-**1**) are highly soluble in HFE7700 PFCs oil and respond to an applied external field without agglomeration or coagulation (**Figure S 5.2**).

5.2.2 Attaching of Silane 2 via Direct-Coating Approach

To improve the solubility of fluorinated SPION@SiO_2 nanoparticles in PFCs oil, **2** that has a linear silane length that is approximately 5 times longer than **1** is used to functionalize SPION@SiO_2 nanoparticles. Different experimental conditions for the biphasic approach were applied to attach **2** on the nanoparticles surface (listed in **Table 5.1**); however, none of them facilitates the silianization and the phase transfer of nanoparticles (**Figure 5.2a**). This is due to the insolubility of **2** in the ethanol phase which restricts **2** from having contact with silanol sites on SPION@SiO_2 nanoparticles. Utilizing solubility of **2** in PFCs oil, a direct coating approach was implemented to attach **2** on SPION@SiO_2 nanoparticles. In this approach, SPION@SiO_2 nanoparticles were dispersed in PFCs oil containing an excess amount of **2**. Silanization occurred quickly due to the high reactivity between methyl silanes and the silanol groups, such a fast silanization process was also compared with that of the **1**, which is an ethyl silane. As shown in the TGA measurement, 28.9% and 9.8% of **2** and **1** were attached to the SPION@SiO$_2$ nanoparticles through the direct coating approach, respectively (**Figure S 5.3**). SPION@SiO$_2$-**2** or SPION@SiO$_2$-**1** was sequentially added with **1** or **2**, respectively, in which the increase of 24.7% was observed in the case of SPION@SiO$_2$-**1-2** (**Figure S 5.3**). This weight% increase indicates the poor surface coverage of SPION@SiO$_2$ nanoparticles by **1** via the direct coating due to the slower silanization process of ethyl silanes; the remaining unreactive silanol groups on the SPION@SiO$_2$-**1** surface allow the sequential attachment of **2**. In addition, TGA results show that the total silane attachment of SPION@SiO$_2$-**1-2** is almost 10% more than that of SPION@SiO$_2$-**2-1**, suggesting the use of low-MW surfactants to enhance the attachment of larger-sized surfactants. Such attachment of **2** can be attributed to the polymerization of silanols of **1** and **2**, as shown by the schematic illustration in **Figure 5.2c**. Note that although fluorinated ferrofluids were attained by using the direct coating approach, aggregation was observed, leading to challenges in obtaining reliable Dynamic Light Scattering (DLS) result. In addition, after drying in air, fluorinated ferrofluids synthesized by using a direct coating approach solidified and could not redisperse back to the PFCs oil, indicating the chemical instability of this ferrofluid system.[14]

5.2.3 Synthesis of SPION@SiO$_2$-1-2 Using a Combination of Biphasic and Direct-Coating Approach

DLS measurement shows SPION@SiO$_2$-**1** synthesized by the biphasic method attain an average size of 57.7 nm and a polydispersity index (PDI) of 0.148, indicating the absence of nanoparticle aggregation (**Figure 5.3a**). Accompanied by the positive initial confirmation of rapid silanization between **2** and SPION@SiO$_2$ nanoparticles in a PFCs oil via the direct-coating approach, fluorinated ferrofluids containing both **1** and **2** were prepared via a two-step procedure: biphasic and then direct coating. After SPION@SiO$_2$-**1** were phase-transferred to the PFCs oil via the biphasic approach, the washed SPION@SiO$_2$-**1** were re-dispersed in PFCs oil and were introduced with **2** to generate SPION@SiO$_2$-**1**-**2**. The successful attachment of **2** was confirmed by the TGA results, which show a 10% increase after the attachment of **2** via the polymerization of silanols (**Figure 5.2b**). DLS shows an average SPION@SiO$_2$-**1**-**2** nanoparticle size of 117.5 nm with a PDI of 0.161, demonstrating the successful preparation of monodispersed nanoparticles. TGA results show the comparison of weight% loss between the direct coating approach (24.7%) and the biphasic approach (10%), where less of **2** attachments using the biphasic approach is possible due to the fewer number of unreactive silanol sites on the surface of SPION@SiO$_2$-**1**.

5.2.4 Synthesis of SPION@SiO$_2$-[1+2] with 70% Total Silane Attachment Using Biphasic Approach

The previous results indicated that **2** can be attached on nanoparticle surfaces via polymerization with the silanols of the pre-grafted silanes and via formation of Si-O-Si bonds with the silanol sites on the exposed surface of SPION@SiO$_2$ nanoparticles. To further optimize the attachment of **2** as well as the total silane attachment, co-addition of **1** and **2** were performed via the biphasic approach to generate SPION@SiO$_2$-**[1+2]**. In this approach, both silanes **1** and **2** are introduced initially in the PFCs phase, where attachments of **2** on nanoparticles occur immediately after SPION@SiO$_2$ nanoparticles are able to access the PFCs phase once a sufficient amount of **1** are attached on the surface of the nanoparticles. This co-addition approach accelerates the phase transfer (ethanol to PFCs) process (**Figure 5.2a**) and maximizes the chance of **2** to attach on the remaining silanol sites on the surface of the nanoparticles and on the silanol sites of attached **1** before these silanol sites are fully reacted with free **1** present in the reaction. As a result, silane **1** not only brings SPION@SiO_2 nanoparticles and the absorbed water residues to the PFCs phase but also creates additional silanol sites for **2** to attach via polymerization, as shown in the schematic illustration (**Figure 5.2c**). In addition, smaller-size **1** are able to access the free spaces in the outermost layer formed by fluoroalkyl silanes, facilitating more silane attachments via the Si-O-Si polymerization. The enhanced attachment of **2** was confirmed by the TGA measurement (**Figure 5.2b**), where the weight% increased from 41.0% to 57.0% when both **1** and **2** are present in the biphasic system. Noted that with the same experimental condition mentioned above for the biphasic approach, but in the absence of **1**, SPION@SiO_2 nanoparticles remained in the ethanol phase, where such of result also demonstrates that silane **1** plays an essential role in the attachment of **2**. The grafting **2** on SPION@SiO_2 nanoparticles with the assistance of **1** was further confirmed by increasing the amount of **1** in the co-addition biphasic approach, where the TGA result shows that 69.3% of total attached silane can be achieved (**Figure 5.2b**).

The resulting fluoroalkyl silanes functionalized SPION@SiO_2 nanoparticles were further characterized by TEM, DLS, and FTIR. TEM image shows that the SPION@SiO_2-**[1+2]** are monodispersed (**Figure S 5.4**) and the DLS results show that SPION@SiO_2-**[1+2]** with volumetric ratio (**1**:**2**) of 4 and 2 obtained a larger average nanoparticle size of 130.5 nm (PDI=0.254) and 99.4 nm (PDI=0.226), respectively (**Figure 5.3a**), resulted from the increase in hydrodynamic diameter due to the addition of the outermost fluoroalkyl silane layer. In the FTIR spectrum (**Figure 5.3b**), the two peaks at ν = 802 and 1101 cm^{-1} arise from the Si-O-Si symmetric and asymmetric stretching, respectively, in the unfunctionalized SPION@SiO_2 nanoparticles and the peak at ν = 950 cm^{-1} corresponds to the Si-OH groups. After grafting of fluoroalkyl silanes, the appearance of two bands in the FTIR spectrum due to C-F stretching at ν = 1149 and 1207 cm^{-1}

shows the presence of C-F bonds attached to the surface of SPION@SiO_2 nanoparticles (**Figure 5.3b**).

To further validate that both **1** and **2** are both chemically grafted on the surface of the nanoparticles, the attachment of negative control silane **3** to the surface of SPION@SiO_2 nanoparticles was also performed by using the same biphasic approach. It was previously observed that attachment of **3** is sensitive to ultrasonication, where SPION@SiO_2 nanoparticles-**3** suspended in PFCs phase would transfer back to ethanol phase under ultrasonication (**Figure S 5.5a**), suggesting the unstable attachment of **3** on nanoparticles. From the TGA measurement, it can be seen that while loosely-attached **3** decomposed at a temperature of 150 °C, **1** and **2** attached on the SPION@SiO_2 nanoparticles started to decompose when a temperature of > 300 °C is reached, indicating the chemical stability of the attached **1** and **2** via the formation of the Si-O-Si bonds (**Figure S 5.5b**). Interestingly, when co-addition of **1** and **3** was performed via the biphasic approach, the resulting SPION@SiO_2 nanoparticles-**[1+3]** remained in the PFCs phase under ultrasonication (**Figure S 5.5a**). The improved stability of the **3** attached on the SPION@SiO_2 nanoparticles via co-addition was further confirmed by the TGA measurement, where no decomposition occurs at 150 °C (**Figure S 5.5b**). This interesting result further verifies the co-addition of low-MW surfactant with high-MW surfactants facilities the attachment of high-MW surfactants **2** and generates stable and non-ionic fluorinated ferrofluids with a total silane attachment of almost 70%.

5.3 Conclusion

In this study, new fluorinated ferrofluids were prepared through a biphasic ligand attachment method, where the magnetic nanoparticles were first coated with a thin silica layer, allowing perfluoroalkyl silanes to covalently graft to nanoparticles surface to eliminate the presence of ionic contaminants. It was demonstrated that high-molecular-weight surfactants can be grafted on the surface of SPION@SiO_2 nanoparticles in the presence of/with the assistance of low-molecular-weight surfactants, achieving a total silane attachment of 70 %. The mechanism of silane attachment was proposed and discussed. These new non-ionic fluorinated ferrofluids with enhanced fluoroalkyl silane attachment offer extended applications in biomedical fields.

5.4 Experimental Section

5.4.1 Materials and Chemicals

Chemicals. Iron(III) chloride hexahydrate (FeCl3·6H2O) (≥98%, Aldrich) , sodium oleate (99%, TGI), oleic acid (90%, Aldrich), Igepal CO-520 (Sigma), oleic acid (Sigma), tri-n-octylamine (95%, Fisher), tetraethyl orthosilicate (TEOS) (≥99%, Sigma), 1H,1H,2H,2H-Perfluorodecyltriethoxysilane (PFDTES, **1**, 97%, Sigma), 1H,1H,2H,2H-Perfluorodecyltrimethoxysilane (PFPE, **2**, 20% in fluorinated hydrocarbon, MW = 4000-8000 g/mol, 22-46 repeat units, Gelest), silane PFPE (**3**, MW = 989 g/mol, Surfactis Technologies), ammonia solution 28-30%, hexane (≥98.5%, Fisher), cyclohexane, chloroform (99.9%, EMD). HFE7700, HFE7200, HFE7100, perfluorohexane, and perfluoroctane.

5.4.2 Characterization

Transmission electron microscopy (TEM) images were required on a Tecnai T12 Quick CryoEM and CryoET (FEI) with an operating voltage of 120 kV. The sample was prepared by dropping a suspension (0.2 mg/mL, 5 μL) of nanoparticles in hexane, ethanol, or HFE7100 on a 200-mesh carbon coated copper grid, followed by solvent evaporation at room temperature. Dynamic light scattering (DLS) measurements were acquired on a ZetaSizer Nano (Malvern Instruments Ltd., Worcestershire, U.K.) in ethanol and HFE7700 for SPION@ SiO_2 and Fluoro- SPION@ SiO_2, respectively. Fourier-transform infrared spectroscopy (FTIR) analyses were performed on FTIR

(JASCO FT/IR-420) spectrometer in the range of 4000−400 cm^{-1}. TGA was performed on a PerkinElmer Pyris Diamond TG/DTA machine under air flow. Sample was loaded in aluminum pans, and the data were recorded from 50 to 100 °C at a scan rate of 20 °C/min, stayed at 100 °C for 30 min to remove water residuals, 100 to 600 °C at a scan rate of 15 °C/min, and finally stayed at 600 °C for 1 h. An empty aluminum pan was used as the reference.

5.4.3 Nanoparticles Synthesis

Synthesis of SPION@SiO$_2$ Nanoparticles. SPION@SiO$_2$ were synthesized based on a published reverse-microemulsion approach with some modifications.[19] In a typical synthesis of SPION@SiO$_2$ nanoparticles, 0.6 g Igepal CO-520 was dispersed in cyclohexane (19.4 mL) and sonicated for 20 min in a 50 mL three-necked flask. Then oleic-acid capped SPIONs dispersed in cyclohexane (9 mL) were added into the cyclohexane/Igepal mixture. After 15 min of sonicating and 4 h of magnetic stirring, 140 μL of ammonia was added into the mixture, and the system was sealed and stirred for another 3 h. 160 μL was injected into the mixture dropwise, and the system was kept under magnetic stirring for 36 h at room temperature before adding 5 mL of methanol to disrupt the emulsions. The precipitate was collected and washed with ethanol twice, and the as-obtained nanoparticles were dispersed in ethanol for further uses. Shell thickness of SPION@SiO$_2$ can be reduced by decreasing/tuning the TEOs and ammonia.

Synthesis of Perfluoro SPION@SiO$_2$-1. Biphasic exchange method was implemented for the PFDTES attachment. In an Eppendorf tube, various amounts 500 μL of perfluoro solvent PFH and 1mL ethanol of SPION@SiO$_2$ nanoparticles suspension (4mg/mL) forms two-phase system. **1** was added directly into the two-phase system, followed by the addition of an aliquot of water (volume ratio of Ethanol: **1**: water = 20: 1: 0.5 and 40: 1: 0.5 for 1st and 2nd addition, respectively.) The suspension was allowed to rotate for 2 days to bring the SPION@SiO$_2$-**1** nanoparticles down to the perfluoro phase. SPION@SiO$_2$-**1** nanoparticles were washed with solvent mixture (ethanol: HFE7200 = 5:1) two times before re-suspended in HFE7700.

Synthesis of SPION@SiO$_2$-1 or SPION@SiO$_2$-2 Nanoparticles by Direct Coating. Solvent exchange (centrifugation/redispersion) was first performed to transfer SPION@SiO$_2$ nanoparticles from ethanol to HFE7100 because **1** is not soluble in ethanol. 50 μL of **1** was added directly to SPION@SiO$_2$ nanoparticles suspension (20 mg/mL). The suspension was sonicated for 1h, followed by overnight rotation to make sure nanoparticle surface are covered by **1**. The SPION@SiO$_2$-**1** nanoparticles were washed with solvent mixture (ethanol: HFE7200 = 5:1) for two times before re-suspended in HFE7700. Same procedure was performed for synthesizing SPION@SiO$_2$-**2** nanoparticles except that 50 μL of **2** was added to nanoparticles suspension.

Synthesis of SPION@SiO$_2$-1-2 or SPION@SiO$_2$-2-1 Nanoparticles by Direct Coating. The washed SPION@SiO$_2$-**2** or SPION@SiO$_2$-**1** nanoparticles were re-suspended in HFE7100 containing 50 μL of **1** or **2**, respectively. The suspension was placed in sonication bath for 1 h and allowed to undergo silanization overnight at room temperature.

Synthesis of SPION@SiO$_2$-1-2 Nanoparticles (Biphasic + Direct Coating). SPION@SiO$_2$ nanoparticles were first transferred to the perfluoro phase with the same procedure as that of SPION@SiO$_2$-**1** nanoparticles. The washed SPION@SiO$_2$-**1** nanoparticles were re-dispersed in 200 μL of HFE7100. The remaining procedures for **2** attachments are the same as that of SPION@SiO$_2$-**2** nanoparticles. The final SPION@SiO$_2$-**1-2** Nanoparticles were re-suspended in HFE7700.

Synthesis of SPION@SiO$_2$-[1+2] Nanoparticles. Biphasic exchange method was implemented for co-attachment of **1** and **2**. In an Eppendorf tube, 500 μL of PFH (containing 200 and 50 μL of **1** and **2**) and 1mL ethanol of SPION@SiO$_2$ nanoparticles suspension (4mg/mL) forms two-phase system, followed by the addition of aliquot of water (volume ratio of Ethanol: **1**: water = 20: 1: 0.5 or 20: 1: 0.5 for 1st addition and 40: 1: 0.5 for 1st and 2nd addition. The two additions were separated by 1 day. The suspension was allowed to rotate for 2 days to bring the **1** and **2**-functionalized nanoparticles down to the perfluoro phase. SPION@SiO$_2$-**[1+2]** nanoparticles were rotated for an additional 5 days, allowing complete surface coverage, and finally washed with solvent mixture (ethanol: HFE7200 = 5:1) two times before re-suspended in HFE7700. Synthesis of SPION@SiO$_2$-**3** and SPION@SiO$_2$-**[1+3]** nanoparticles are similar to that of SPION@SiO$_2$-**1** and SPION@SiO$_2$-**[1+2]** nanoparticles.

5.5 Acknowledgements

The authors thank Professor Ellen Sletten, Professor Otger Campàs, Dr. Heidi L. van de Wouw and Dr. Antoine Via for the helpful discussion and suggestions and Daniel Estabrook, Carlos Gomez, and Yucen Liu for technical assistance. HFE perfluoro solvents were provided by both the Sletten and Campàs labs.

5.6 Figures, Scheme, and Table

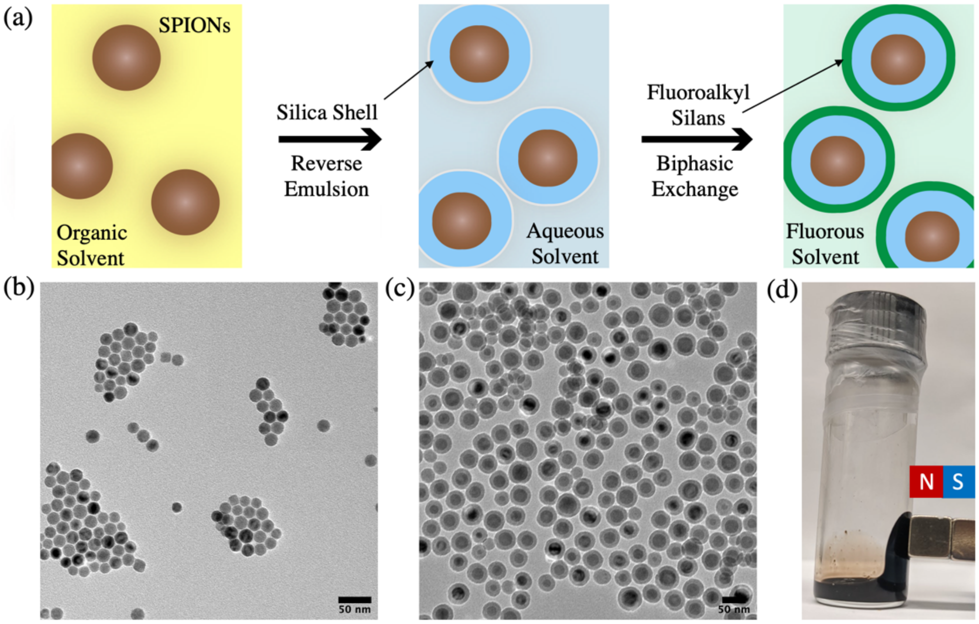

Figure 5.1 (a) Schematic illustration of fluorinated ferrofluids. SPIONs were first coated with a thin layer of silica for attachment of fluoroalkyl silanes. TEM images of (b) SPIONs and (c) SPION@SiO$_2$, and photo of (c) fluorinated ferrofluids under an application of external magnetic field. Organic solvent = hexane, aqueous solvent = ethanol, and fluorous solvent = HFE7700.

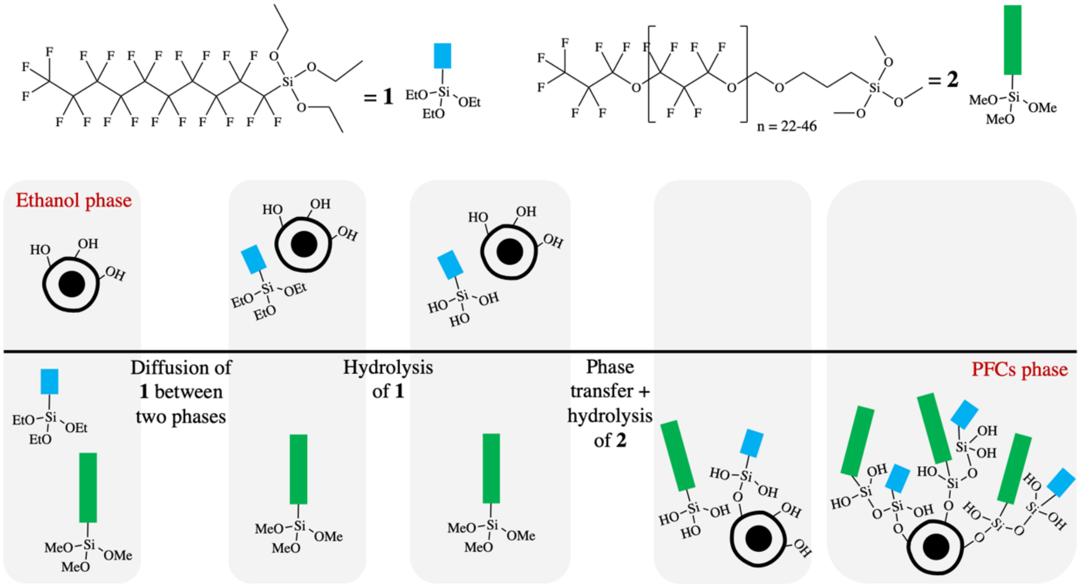

Scheme 5.1 Proposed mechanism of fluoroalkyl silane attachment and phase transfer of SPION@SiO$_2$ nanoparticles.

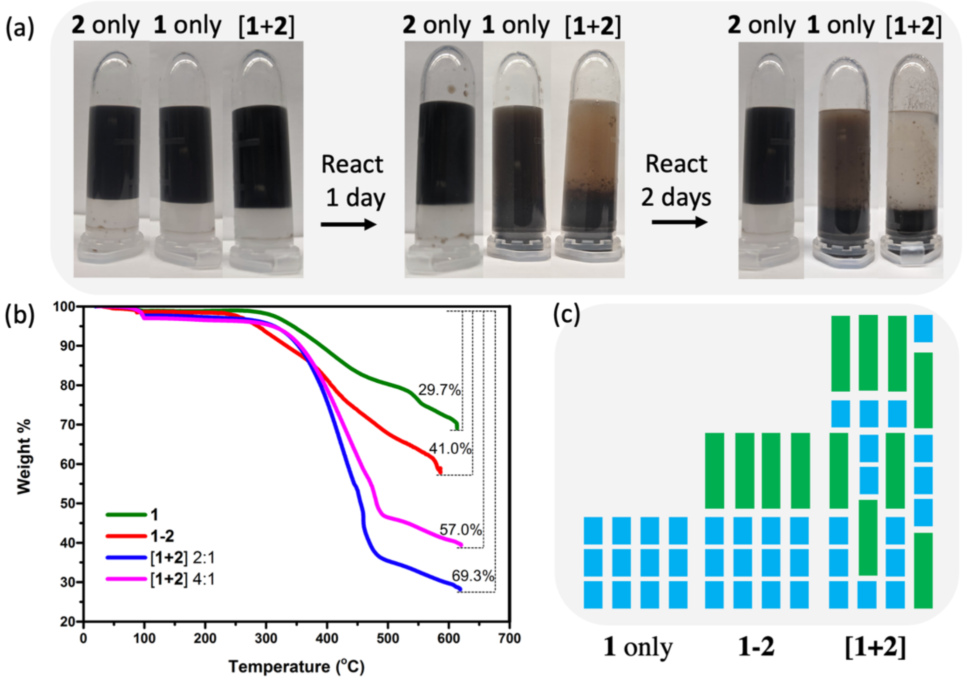

Figure 5.2 (a) Photos of the results of using the biphasic approach for attachment of **1** only, **2** only, or **1**+**2**. Co-addition of **1** and **2** accelerates the phase transfer of SPION@SiO$_2$ nanoparticles whereas no phase transfer was observed in the absence of **1**. (b) TGA results of silane attachments by using biphasic approach, biphasic + direct coating approach, and biphasic co-addition approach. (c) Schematic illustration of the enhanced total silane attachment via both the silanization between **2** and silanol sites on exposed SPION@SiO$_2$ nanoparticles surface and the polymerization between silanols of **1** and **2**.

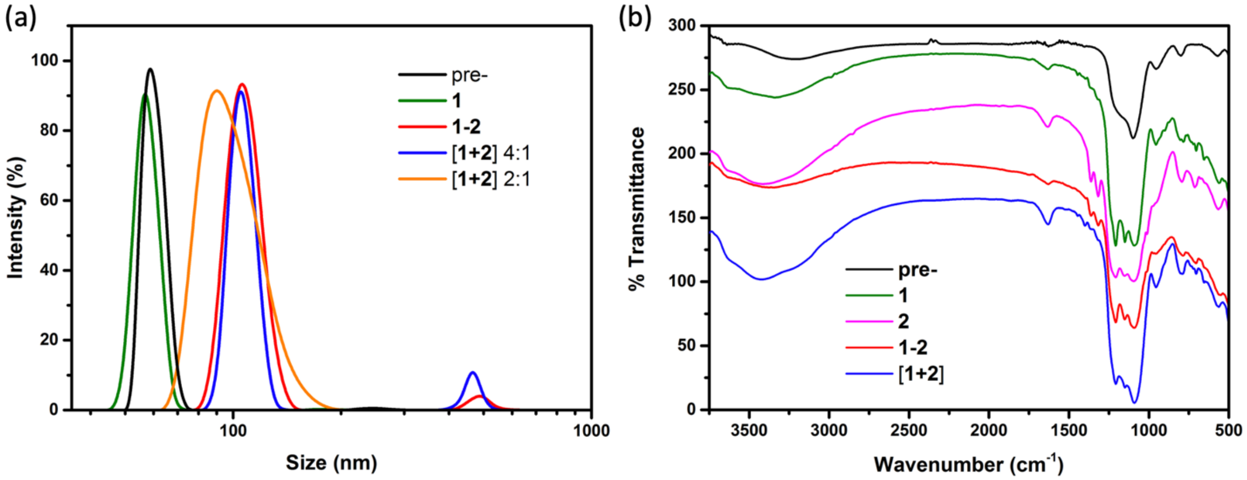

Figure 5.3 (a) DLS and (b) FTIR of comparison between the unfunctionalized SPION@SiO$_2$ nanoparticles (pre) with fluoroalkyl silanes-functionalized by using biphasic approach, biphasic + direct coating approach, and biphasic co-addition approach.

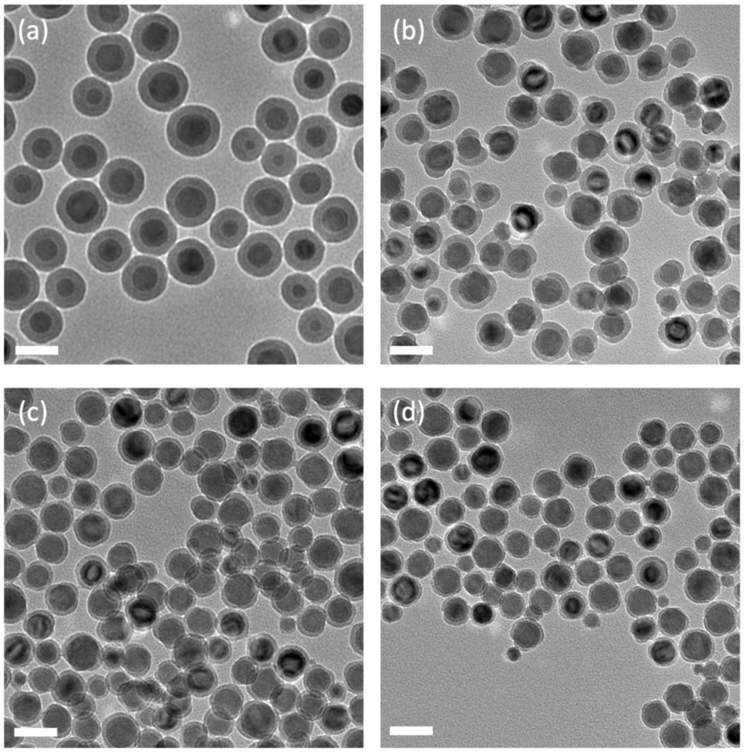

Figure S 5.1 TEM images of SPION@SiO$_2$ nanoparticles with (a) 15 nm silica shell thickness, (b) rough silica surface when only TEOS was reduced, and (c) 5 nm and (d) 3 nm silica shell thickness when both TEOS and ammonia were adjusted.

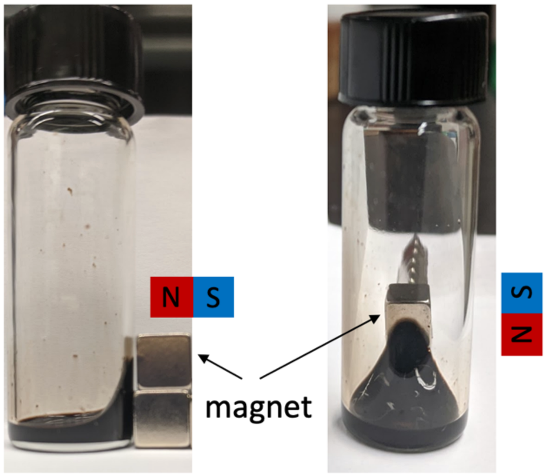

Figure S 5.2 Photos of the ferrofluid attraction to a magnet. SPION@SiO$_2$-**1** fluorinated ferrofluids were synthesized by using the biphasic approach.

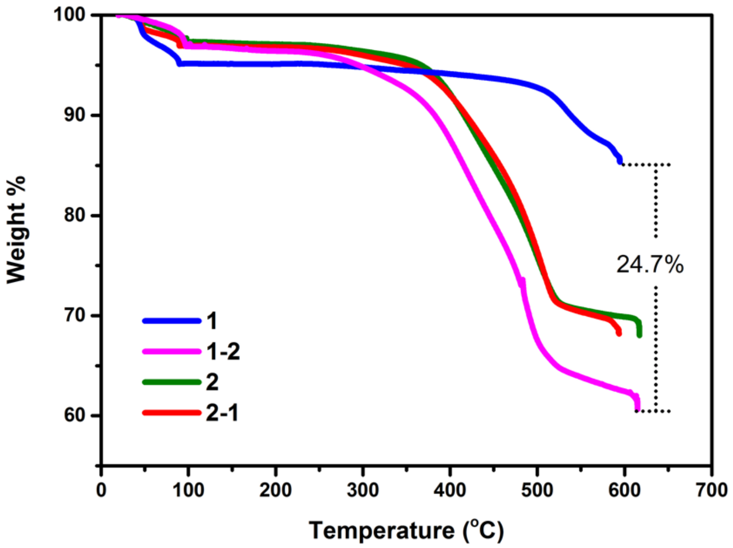

Figure S 5.3 TGA results of silane attachment via direct coating approach.

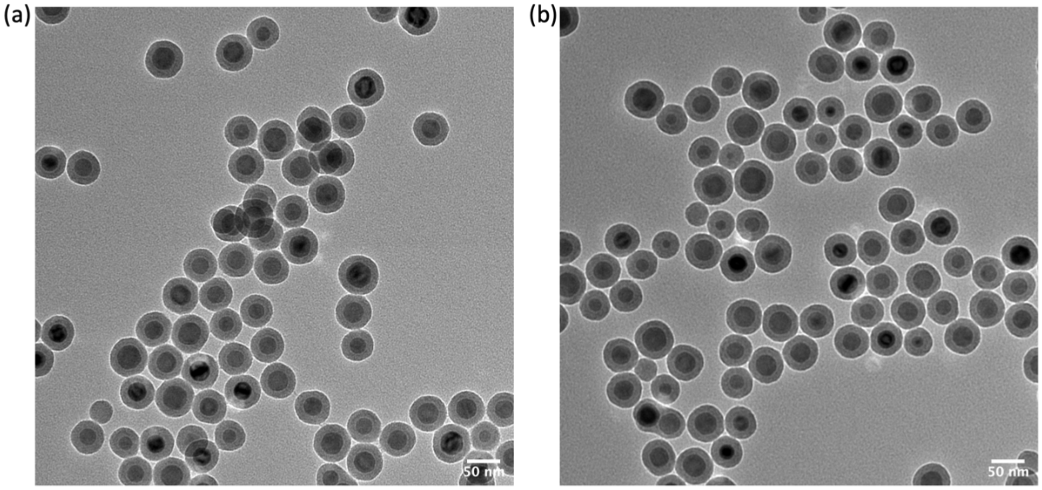

Figure S 5.4 TEM images of (a) unfunctionalized SPION@SiO$_2$ nanoparticles and (b) fluoroalkyl silanes-functionalized SPION@SiO$_2$ nanoparticles (SPION@SiO$_2$-**[1+2]**) via biphasic approach.

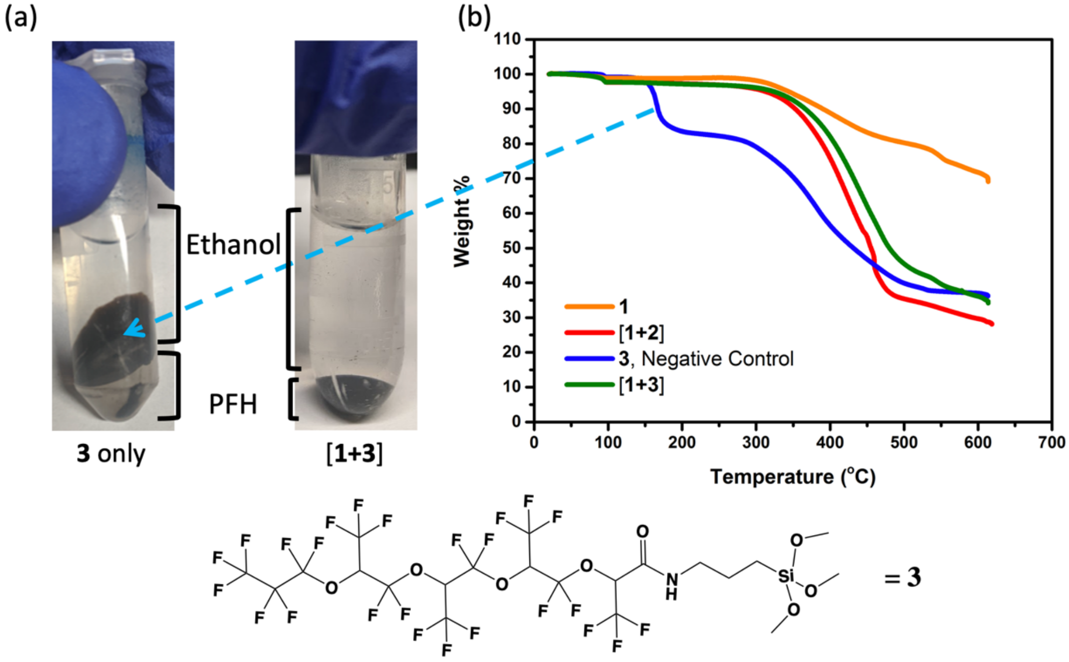

Figure S 5.5 (a) SPION@SiO_2-**3** in PFCs phase returned to the ethanol phase after 5 min of ultrasonication, indicating the loosely absorbed silanes. SPION@SiO_2-**[1+3]** remained in PFCs phase after sonication, suggesting the improved stability of attached **3** on nanoparticles with the assistance of **1**. (b) TGA of comparison between non-chemically bonded/absorbed silanes (negative control) with chemically bonded silane. The unstable silane layer generates a degradation peak at a temperature of 150°C.

Upper phase solvent	Ethanol									
Weight of nanoparticles (mg)	6	6	2	6	6	6	3	3	3	6
Lower phase perfluoro solvent	PFH								PFO	PFH
Perfluoro solvent amount (uL)	200						500	200	500	200
Amount of **2** (uL)	20	50	50	100	50	100	100	100	100	100
Water (uL)	100	100	0	0	200	200	100	300	300	100

Table 5.1 Different biphasic conditions tested to graft **2** on SPION@SiO_2 nanoparticles. Upper phase contains 1 mL of solvent. Solvent mixture of 3:1: 1: 0.1 Ethanol/ HFE7100/PFH/H_2O or 3:1: 1: 0.1 Ethanol/ HFE7100/H_2O was also tested. The reactions were allowed to be rotated for 1 week. The silanization of **2** with SPION@SiO_2 nanoparticles was monitored by the phase transfer of SPION@SiO_2 nanoparticles, where SPION@SiO_2 nanoparticles remained in the upper phase even with prolonged reaction time (>1week).

5.7 References

(1) Riess, J. G.; Riess, J. G. Oxygen Carriers (“blood Substitutes”) - Raison d’etre, Chemistry, and Some Physiology. *Chem. Rev.* 2001, 101 (9), 2797–2919.

(2) Day, R. A.; Estabrook, D. A.; Logan, J. K.; Sletten, E. M. Fluorous Photosensitizers Enhance Photodynamic Therapy with Perfluorocarbon Nanoemulsions. *Chem. Commun.* 2017, 53 (97), 13043–13046.

(3) Estabrook, D. A.; Day, R. A.; Sletten, E. M. Redox-responsive Gene Delivery from Perfluorocarbon Nanoemulsions through Cleavable Poly(2-oxazoline) Surfactants. *Angew. Chemie Int. Ed.* 2021, No. 10.1002/anie.202102413.

(4) Janjic, J. M.; Ahrens, E. T. Fluorine-Containing Nanoemulsions for MRI Cell Tracking. *Wiley Interdiscip. Rev. Nanomedicine Nanobiotechnology* 2009, 1 (5), 492–501.

(5) Tirotta, I.; Dichiarante, V.; Pigliacelli, C.; Cavallo, G.; Terraneo, G.; Bombelli, F. B.; Metrangolo, P.; Resnati, G. 19F Magnetic Resonance Imaging (MRI): From Design of Materials to Clinical Applications. *Chem. Rev.* 2015, 115 (2), 1106–1129.

(6) Tran, T. D.; Caruthers, S. D.; Hughes, M.; Marsh, J. N.; Cyrus, T.; Winter, P. M.; Neubauer, A. M.; Wickline, S. A.; Lanza, G. M. Clinical Applications of Perfluorocarbon Nanoparticles for Molecular Imaging and Targeted Therapeutics. *Int. J. Nanomedicine* 2007, 2 (4), 515–526.

(7) Rapoport, N.; Nam, K. H.; Gupta, R.; Gao, Z.; Mohan, P.; Payne, A.; Todd, N.; Liu, X.; Kim, T.; Shea, J.; Scaife, C.; Parker, D. L.; Jeong, E. K.; Kennedy, A. M. Ultrasound-Mediated Tumor Imaging and Nanotherapy Using Drug Loaded, Block Copolymer Stabilized Perfluorocarbon Nanoemulsions. *J. Control. Release* 2011, 153 (1), 4–15.

(8) Zimny, K.; Mascaro, B.; Brunet, T.; Poncelet, O.; Aristégui, C.; Leng, J.; Sandre, O.; Mondain-Monval, O. Design of a Fluorinated Magneto-Responsive Material with Tuneable Ultrasound Scattering Properties. *J. Mater. Chem. B* 2014, 2 (10), 1285–1297.

(9) Krafft, M. P.; Riess, J. G. Perfluorocarbons: Life Sciences and Biomedical Uses. *J. Polym. Sci. Part A Polym. Chem.* 2007, 46, 1185–1198.

(10) Campàs, O.; Mammoto, T.; Hasso, S.; Sperling, R. A.; O’connell, D.; Bischof, A. G.; Maas, R.; Weitz, D. A.; Mahadevan, L.; Ingber, D. E. Quantifying Cell-Generated Mechanical Forces within Living Embryonic Tissues. *Nat. Methods* 2014, 11 (2), 183–189.

(11) Lucio, A. A.; Mongera, A.; Shelton, E.; Chen, R.; Doyle, A. M.; Campàs, O. Spatiotemporal Variation of Endogenous Cell-Generated Stresses within 3D Multicellular Spheroids. *Sci. Rep.* 2017, 7 (1), 1–11.

(12) Serwane, F.; Mongera, A.; Rowghanian, P.; Kealhofer, D. A.; Lucio, A. A.; Hockenbery, Z. M.; Campàs, O. In Vivo Quantification of Spatially Varying Mechanical Properties in Developing Tissues. *Nat. Methods* 2017, 14 (2), 181–186.

(13) Estabrook, D. A.; Ennis, A. F.; Day, R. A.; Sletten, E. M. Controlling Nanoemulsion Surface Chemistry with Poly(2-Oxazoline) Amphiphiles. *Chem. Sci.* 2019, 10 (14), 3994–4003.

(14) Borduz, L.; Tsuda, S.; Hirota, Y. Ferrofluid Composition and Process. United States Pat. US 6,277,298 B1 2001.

(15) Kim, Y.; Lee, S.; Kim, S. Preparation of Fluorous Solvent-Dispersed Fe3O4 Nanocrystals: Role of Oxygen in Ligand Exchange. *Langmuir* 2016, 32 (14), 3348–3353.

(16) Dong, A.; Ye, X.; Chen, J.; Kang, Y.; Gordon, T.; Kikkawa, J. M.; Murray, C. B. A Generalized Ligand-Exchange Strategy Enabling Sequential Surface Functionalization of Colloidal Nanocrystals. *J. Am. Chem. Soc.* 2011, 133 (4), 998–1006.

(17) Brassard, J. D.; Sarkar, D. K.; Perron, J. Synthesis of Monodisperse Fluorinated Silica Nanoparticles and Their Superhydrophobic Thin Films. *ACS Appl. Mater. Interfaces* 2011, 3 (9), 3583–3588.

(18) Yildirim, A.; Budunoglu, H.; Daglar, B.; Deniz, H.; Bayindir, M. One-Pot Preparation of Fluorinated Mesoporous Silica Nanoparticles for Liquid Marble Formation and Superhydrophobic Surfaces. *ACS Appl. Mater. Interfaces* 2011, 3 (6), 1804–1808.

(19) Ding, H. L.; Zhang, Y. X.; Wang, S.; Xu, J. M.; Xu, S. C.; Li, G. H. Fe3O4@SiO2 Core/Shell Nanoparticles: The Silica Coating Regulations with a Single Core for Different Core Sizes and Shell Thicknesses. *Chem. Mater.* 2012, 24 (23), 4572–4580.

Chapter 6 Drug Delivery by Ultrasound-Induced Binding Affinity Change

This chapter of the dissertation is based on the collaborative work with Professor Holden Wu's group at UCLA Radiology. The goal of this study is to design and develop a core/shell drug delivery platform where the drug release can be triggered by high-intensity focused ultrasound (HIFU) and the release process can be monitored by magnetic resonance imaging that is coupled with the HIFU. Lin, F. C. designed and performed all the experiments. Jeffrey I. Zink was the P.I.

6.1 Introduction

Magnetic resonance imaging (MRI) offers noninvasive deep tissue penetration and attains 3D capabilities to imaging soft tissue, vessel, and lesion with high spatial and temporal resolutions. With the application of contrast agents such as SPIONs, the large magnetization can generate local magnetic field inhomogeneity, leading to enhanced MRI contrast change. Although the inherent MRI contrast of SPIONs allows one to monitor the particle localization and concentration and detect tumors, it is often difficult to distinguish the dark signal generated by the SPIONs from the other dark signals due to local field inhomogeneity and the artifacts resulted from the tissue interface and background noise. The demand for methods to monitor the injected drug delivery platform as well as drug release in real-time remains. Recent advances in non-invasive high-intensity focused ultrasound (HIFU) with mm-sized energy-focusing ability that can be guided by MRI or low-frequency ultrasound (US) imaging can offer switchable contrast changes for monitoring drug release via the change of SPIONs' surrounding environment.[1,2] This advanced technique also shows the high promise of US-responsive nano-platforms for controllable cargo delivery.[3]

US-responsive nanocaps for controllable drug delivery have been extensively studied in the field. The uncapping occurs due to US-induced bond breaking, pH change, polymer morphology change, etc., leading to the release of cargos on demand.[3] This work focuses on the design of capping systems based on host-guest inclusion complexes where β-cyclodextrins (β-CDs) can interact with diverse guest molecules. The association constant (K_a) for the guest-β-CD inclusion complexes depends on a variety of factors, including the size or orientation of guest molecules, substituent groups in the benzene ring on the guest molecule, pH and temperature, etc.[4–8] The interaction between host and guest, indicated by the K_a, decreases when bulk temperature increases.[4] The combination of mechanical and thermal effects of US is anticipated to lower the binding affinity between host and guest, allowing drug release.

6.2 Results and Discussion

6.2.1 US-Induced Lowering of Binding Affinity between Host and Guest

The drug delivery systems are designed based on surface modification of nanoparticles with phenol groups (guest), and after drug loading, the mesopores can be capped by introducing host β-cyclodextrin which forms an inclusion complex with the guest. **Scheme 6.1** shows that three guests were studied, including the naphthyl group (Nap), N-phenylaminopropyltrimethoxysilane (PhAPTES), and N-phenylaminomethyltriethoxysilane (PhAMTES). Based on the molecule size and number of phenyl rings, the K_a of PhAPTES and PhAMTES is estimated to be one order magnitude lower than K_a of Nap, which is approximately 2000 M^{-1}. PhAPTES and PhAMTES with different hydrocarbon lengths were compared to optimize the drug loading efficiency, where PhAPTES with shorter length was expected to reduce the chance of drugs to diffuse out. In addition, different hosts such as β-CDs and α-CDs with six and seven glucopyranose units, respectively, are also studied to minimize the pre-leakage of drugs before US stimulation.

To attach Nap, the surface of MSNs was functionalized with amine groups by hydrolysis and condensation of APTES, and Nap can form thiourea with amines via isothiocyanate-amine coupling (**Figure 6.1a**). The successful attachment of Nap on the surface of MSNs was confirmed by ζ-potential measurements, FTIR (**Figure 6.1c**), and UV-Vis (**Figure 6.1d**). ζ-potential values of MSN-NH_2 and MSN-Nap are +37.03 and +39.19, respectively. The appearance of two bands in the IR spectrum of MSN-Nap due to amide absorption (amide II) at $\nu = 1550\ cm^{-1}$ and thiocarbonyl at $\nu = 1100\ cm^{-1}$ supports the successful conjugation of Nap on MSNs. The UV-Vis peak intensity corresponds to Nap also becomes stronger as the concentration of MSN-Nap increases which further confirms the presence of Nap on MSNs. TEM image shows that the average diameter of MSN-Nap is 110 nm ± 5 nm (**Figure 6.1b**). From the dynamic light scattering (DLS) the average diameter is 91.8 nm at room temperature with a polydispersity index (PDI) below 0.2, showing that MSN-Nap are monodispersed in water.

For drug release testing, MSN-Nap dispersed in water were loaded with doxorubicin (DOX) for 24 h and capped with β-CDs in excess for 24 h. The uptake efficiency and capacity were found to be 7.75% and 18.5% when a DOX loading concentration of 3 μM was used. Different triggering conditions were tested, including 10 min probe sonication (40% amplitude), 30 min heating at 50 °C, 1h heating at 80 °C, and 5 or 10 min HIFU stimulation (20%, 30%, 40%, and 50% amplitude). None of the conditions can trigger the DOX release, indicating the inclusion complex formed by Nap and β-CD is too strong to separate. As a result, nanocarriers that have inclusion complexes with lower K_a were synthesized. In this case, MSN-PhAPTES and MSN-PhAMTES were synthesized based on the procedures reported previously[9,10] and were loaded with DOX, followed by capping with β-CDs and α-CDs. It was found that for MSNs with inclusion complexes of PhAPTES-α-CD, PhAPTES-β-CD, PhAMTES-α-CD, and PhAMTES-β-CD, the loading efficiencies are 8.40%, 9.74%, 13.79%, and 20.13%, and loading capacities are 21.1%, 24.5%, 34.7%, and 50.7%. The results indicate that more DOX can be encapsulated in the mesopores when a shorter silane length of guest and the bulkier host is used. Triggered drug release by the US was then performed on these nanoparticles. It can be seen that both US and bulk solution heating can alter the binding affinity of host-guest and release DOX in a controllable manner (**Figure 6.2a**). While a previous study showed that MSN-PhAPTES-β-CD can only release cargos at a pH < 5.0,[9] it can be seen that, with the assistance of US, 7.05% and 12.96% of DOX can be released at a pHs 6 and pH 7, respectively (**Figure 6.2b**). Future studies will focus on enhancing the drug release by using HIFU which offers both mechanical and thermal forces.

6.2.2 US-Induced Contrast Change Due to Bubble Generation and Phase Change of SPIONs' Surrounding Environment

In light of T_2 contrast change due to the exchange of the released drugs and the incoming water molecules in the pores of MSNs embedded with a superparamagnetic iron oxide nanoparticle core (SPION@MSNs),[2] extra-large-pore SPION core-shell nanoparticles (SPION@EXpMSNs) were synthesized for the encapsulation of perfluorocarbons (PFCs). The heat generated by the US can cause the continuous gasification and bubbling of liquid PFCs and thus promote the signal enhancement of ultrasound imaging.[11] In this case, PFCs are perfluorohexane, which has a boiling point of 56 °C. The surface of SPION@EXpMSNs was modified with biocompatible polyethylene glycol (PEG) to improve particle stability. To realize PEG modification via EDC/NHS reaction, amine-functionalized MSNs were first prepared, The successful attachment of APTMS and PEG on the surface of MSNs was confirmed by ζ-potential measurements and DLS, where DLS shows a decrease of average particle size and ζ-potential changes from +20 to -32 after PEG modification (**Figure 6.3a**). In addition, average particle size increases after encapsulation of PFCs and decreases upon gasification of PFCs by heat (**Figure 6.3a**). The prepared SPION@EXpMSN-PFH-PEG were used to test the T_2 contrast change induced by the US due to the change of the surrounding environment of the magnetic core.

Air bubbles, due to their positive susceptibility compared with diamagnetic water, are also a source of T_2 contrast in MRI.[12] It is hypothesized that the release of temperature-sensitive PFCs from the pore space of the SPION@EXpMSNs under the US trigger could generate multiple-stage changes in MR T_2 contrast (**Figure 6.3b**). Stage-1 T_2 contrast change is a result of the PFCs bubbles generated at a higher temperature upon the US trigger. The generated PFCs bubbles obtain a magnetic susceptibility that differs from that of water and thus produces nanoscale magnetic field gradients. Such gradients cause faster dephasing of the surrounding proton nuclear spins on water molecules, leading to T_2 contrast change. Variable temperature (VT) experiments using 14T NMR were performed to obtain T_2 values at room temperature and at an elevated temperature of 65 °C. T_2 % change was calculated to analyze T_2 contrast change induced by the PFCs bubbles, where a > 30% T_2 % change was observed (**Figure 6.3b**). T_2 % change decreased gradually with respect to time because fewer of PFCs were left in the nanoparticle pores for PFCs bubbles generation. The VT experiments were conducted 1 day or 1 week after PFCs encapsulation, suggesting that PFCs can be stably kept in the pore spaces at room temperature. It was observed that a stage-2 T_2 contrast change can be generated when the immediate surroundings of the SPIONs undergoes a phase change (hydrophobic PFCs to liquid water) (**Figure 6.3b**). The gasification of PFCs emptied out pore spaces of the SPION@EXpMSNs, allowing water molecules to enter. Such increase of water access of SPIONs improves the T_2 effect on the encountering proton spins, leading to another contrast change. Future work will focus on how the T_2-%-change differs with respect to temperature and particle concentration.

6.3 Conclusion

This study represents a proof of concept for the US-induced binding affinity change of an inclusion complex-based nanocap for the release of anticancer drugs. We also demonstrated that the change of the surrounding environment of the SPIONs core from a PFCs oil phase to an aqueous phase, accompanied by the generation of bubbles due to the gasification of PFCs, can generate multi-step T_2 contrast change. Future work will combine these two modalities for the development and design of new theranostic platforms that can be applied to a clinically available instrument such as MRI-guided HIFU.

6.4 Experimental Section

6.4.1 Materials and Chemicals

Iron(III) chloride hexahydrate (FeCl3·6H2O) (≥98%, Aldrich), sodium oleate (99%, TGI), oleic acid (90%, Aldrich), tri-n-octylamine (95%, Fisher), hexadecyltrimethylammonium bromide (CTAB) (≥99%, Sigma), tetraethyl orthosilicate (TEOS) (≥99%, Sigma), ethyl acetate (EA, ≥99.5%, Sigma), (3-aminopropyl)triethoxysilane (97% APTES) (Sigma-Aldrich), (3-aminopropyl)trimethoxysilane (97% APTMS) (Sigma-Aldrich), 1-naphthyl isothiocyanate, N-phenylaminopropyltrimethoxysilane (PhAPTMS), and N-phenylaminomethyltriethoxysilane (PhAMTES), hexane (≥98.5%, Fisher), chloroform (99.9%, EMD), 1-ethyl-3-(3-dimethylaminopropyl) carbodiimide (EDC)(Sigma), N-hydroxysulfosuccinimide (NHS)(≥99%,CovaChem), COOH-PEG-COOHCOOH ((M_p = 1983, 6568, and 24695 Da).

6.4.2 Characterization

Transmission electron microscopy (TEM) images were acquired on a Tecnai T12 Quick CryoEM and CryoET (FEI) with an operating voltage of 120 kV. Zeta-potential analysis and dynamic light scattering (Zeta/DLS) were acquired on a ZetaSizer Nano (Malvern Instruments Ltd., Worcestershire, U.K.). Fourier-transform infrared spectroscopy (FTIR) analyses were performed on FTIR (JASCO FT/IR-420) spectrometer in the range of 4000−400 cm^{-1}.

6.4.3 Nanoparticles Synthesis

Synthesis of MSNs. MSNs were synthesized using a sol-gel reaction in the presence of cationic surfactant templates. Briefly, 0.25 g CTAB was dissolved in a 120 mL of deionized water containing 875 μL of NaOH solution (2 M). Under vigorous stirring, the solution was heated to 85 °C in an oil bath and kept at this temperature for 30 min. 1.2 mL of TEOs was added dropwise into the solution followed by the addition of 0.79 mL EA. The reaction was stirred for another 2 h before cooling to room temperature. The final product was washed with ethanol three times to remove unreacted precursors and free surfactants.

Synthesis of MSN-Nap. APTES was first functionalized on MSNs for the attachment of Nap. Briefly, 150 mg MSNs were dispersed in 60 mL anhydrous toluene in an oven-dried round bottom flask. The whole solution was further dried under vacuum before heating up the solution to 90 °C. Under N_2 environment, 100 μL APTES was added and then the reaction mixture was heated to 130 °C and refluxed overnight. APTES-modified MSNs (MSN-APTES) were washed twice with ethanol. To remove CTAB template, MSNs-APTES were dispersed in a NH_4NO_3 ethanol solution (2 g/100 mL). The reaction mixture was heated to 60 °C and refluxed for 1 h. The surfactant removal process by extraction was repeated twice. After the extraction, MSN-APTES were centrifuged and further washed with deionized H_2O and ethanol twice. 140 mg of MSN-APTES and 100 w% of 1-naphthyl isothiocyanate were stirred and reacted in 40 mL ethanol overnight to obtain the final MSN-Nap. The final product was washed with ethanol twice to make that sure unattached 1-naphthyl isothiocyanate are washed away.

Synthesis of MSN-PhAMTES and MSN-PhAPTES. The synthesis of both MSN-PhAMTES and MSN-PhAPTES is similar to that of MSN-APTES. Under N_2 environment, 50 μL PhAMTES or PhAPTES was added to 100 mg MSNs in ethanol and then the reaction mixture was refluxed overnight in 20 mL anhydrous toluene.

Synthesis of SPIONs. A modified thermal decomposition method was used to synthesize SPIONs.[13] Briefly, 2.5 mmol of $FeCl_3 \cdot 6H_2O$ and 7.5 mmol sodium oleate were dissolved in a solvent mixture (14 mL) composed of ethanol, Millipore water, and hexane (4:3:7). After 4 h of refluxing at 70 °C, the resulting solution was transferred to a separatory funnel, where the top organic layer containing the Fe-oleate was washed 3X with water and ethanol. Afterward, the resulting organic layer was transferred to a 3-neck round bottom flask and was kept at 70 °C overnight to evaporate hexane. The Fe-oleate complex precursor along with 2-fold molar ratio of oleic acid were dispersed in 10 mL of tri-n-octylamine. Under stirring, the mixture was degassed with N_2 for 30 min at room temperature and then heated to 200 °C at a heating rate of 3 °C min^{-1}. After keeping at 200 °C for 2 h, the mixture was heated to 320 °C with the same heating rate and was allowed to reflux and age at this temperature for 1 h. Afterward, the mixture was cooled to room temperature under N_2 and ethanol was added to precipitate the black product. The precipitate was collected by centrifugation, washed 3X with a mixture of ethanol and acetone, and redispersed in hexane containing 50 μL of oleic acid.

Synthesis of Amine-Functionalized SPION@EXpMSN. SPION@EXpMSNs were synthesized based on a published approach with some modifications.[14,15] The synthesis of SPION@EXpMSN started with transferring SPIONs to an aqueous layer with the help of CTAB surfactant templates,[16] followed by the organic addictive-induced emulsion formed in the CTAB micelles that led to the enlarged pores.[14,15] The silica coating was then achieved by hydrolysis and condensation of TEOS in the presence of the surfactant micelles.[16] 6 mg of SPIONs stabilized with oleic acid were dispersed in 1.2 mL chloroform. In a glass vial, 200 mg CTAB was dissolved in 10 mL of Millipore water at 37 °C, followed by the addition of the prepared SPION solution. To transfer SPION from the organic layer to aqueous layer with the help of CTAB, the mixture was vortexed and sonicated for 10 min and probe-sonicated (40% output) for another 5 min to generate an oil-in-water emulsion. After evaporating chloroform at 75 °C for 10 min, the clear colloidal SPION in aqueous solution was obtained. After another 5 min of probe-sonication for confirming the absence of chloroform, the solution was cooled to room temperature. Under stirring, the resulting solution was added to a mixture of solvent composed of 95 mL of Millipore water, 5 mL of methanol, and 20 mL of ethyl acetate. After mixing for 5 min, 3 mL of ammonia hydroxide was quickly added into the mixture, and then 300 μL of TEOS was added into the reaction solution. The solution was allowed to react for 15 h under stirring. The as-synthesized SPION@EXpMSN were collected by centrifugation, washed 2X with ethanol, and then were dispersed in 50 mL of ethanol containing 1 g of ammonia nitrate for CTAB surfactant removal. The solution was refluxed at 60 °C for 1.5 h under stirring, followed by 1X washing with water and washing twice with ethanol. The removal procedure was repeated twice, and the nanoparticles were dispersed in 20 mL of ethanol. For amine functional group modification, 90 mg of as-synthesized SPION@EXpMSN were dispersed in 40 mL of ethanol, and 30 μL of APTMS was added with stirring. After reacting under stirring for 15 h, amine-functionalized nanoparticles were washed three times with ethanol and redispersed in ethanol.

Synthesis of SPION@EXpMSN-PHF-PEG. SPION@EXpMSNs were synthesized based on a published approach with some modifications.[14,15] Activation of COOH on PEG was first carried out using EDC/NHS carbodiimide reaction. Briefly, 3mg of COOH-PEG-COOHCOOH was dispersed in 600 μL of MES buffer (pH 6.5), which was followed by addition of 400 μL MES buffer containing 4 mg of EDC and 2 mg of NHS. The mixture was stirred for 1.5 h to allow the activation of COOH group. Amine-functionalized SPION@EXpMSNs powder from lyophilization (2 mg x 3 tubes) was vacuum sealed in 2 ml Eppendorf tubes, and then PFH (100 μL) was injected into each tube. The powder was immersed in PFH, followed by 5 min sonication in ice bath. After evaporation of PFH, 100 μL of water was added into the PHF-filled SPION@EXpMSN. The PHF-filled SPION@EXpMSN suspension was then added into the activated PEG solution, and then stirred for 5 h for the formation of carbodiimide bond. The nanoparticles were washed with cool water and dispersed in water (0.07 mg/mL) for NMR measurements.

6.5 Figures and Tables

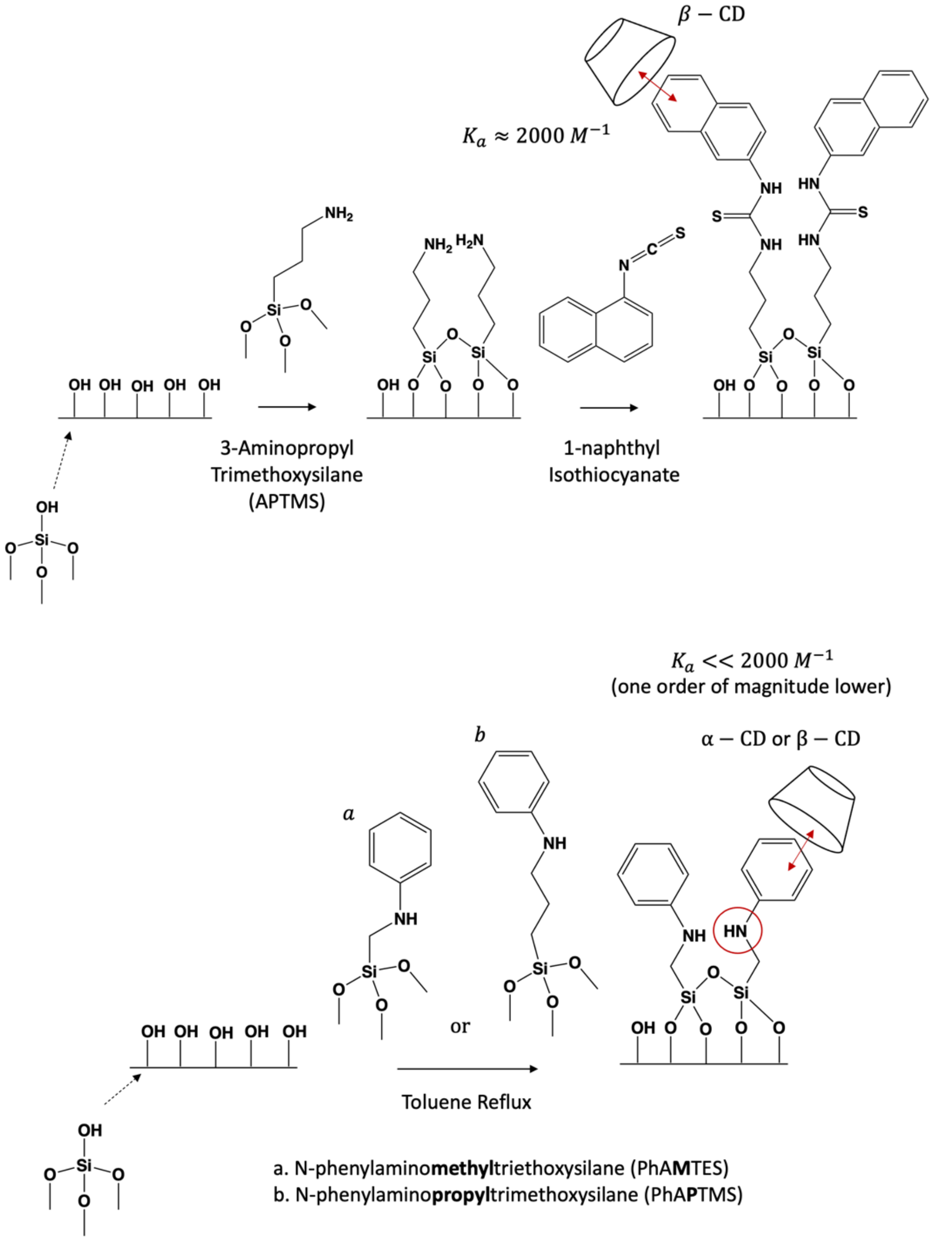

Scheme 6.1 Design of capping systems based on a host-guest inclusion complex with different association constant (K_a).

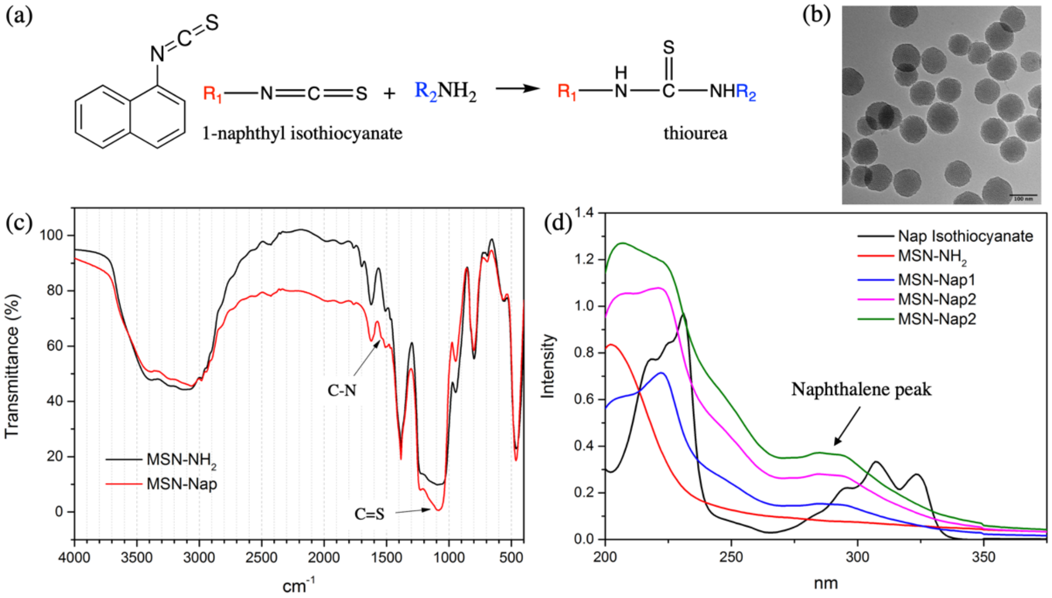

$R_1-N=C=S + R_2NH_2 \rightarrow R_1-NH-C(=S)-NHR_2$

Figure 6.1 Synthesis of naphthyl (Nap) group-functionalized MSNs. (a) Thiourea formed by the coupling between the amine and isothiocyanate group. (b) TEM image of MSN-Nap. (c) FTIR characterization of MSN-Nap. (d) UV-Vis spectrum of MSN-Nap.

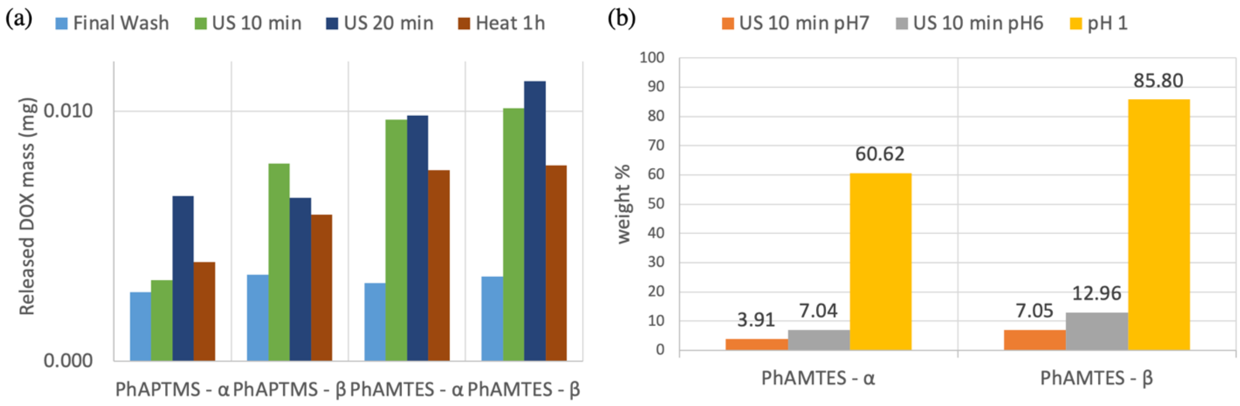

Figure 6.2 (a) DOX release by US-induced change of binding affinity. Probe sonication with a 40% amplitude was used. (b) DOX can be released at a physiological pH (pH 6 and pH 7) by US triggering.

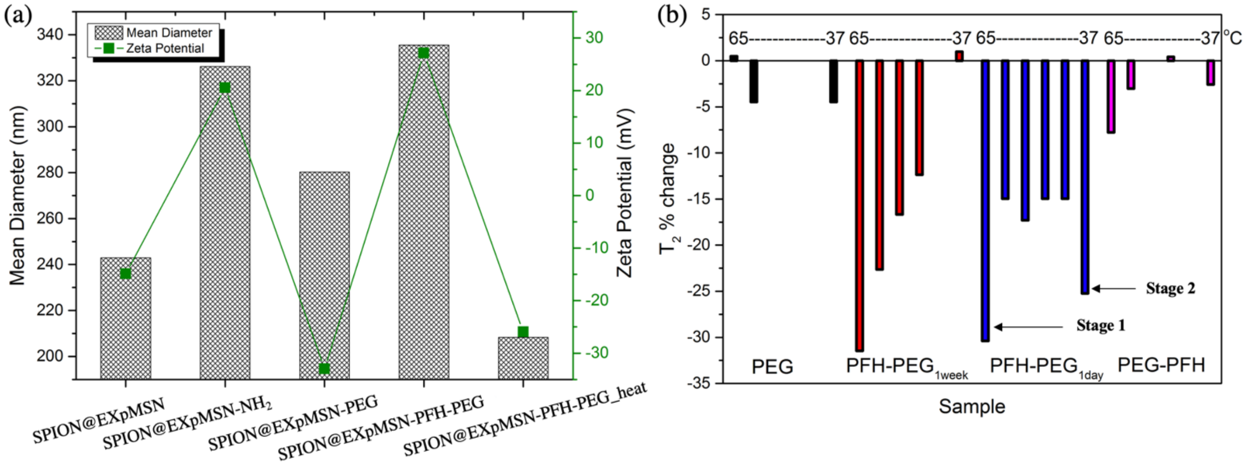

Figure 6.3 (a) Characterization by DLS size and Zeta potential showed the successful encapsulation of perfluorohexane (PFH) and attachment of PEG. (b) T_2 measurements by 14T NMR. T_2-%-change of SPION@EXpMSN-PHF-PEG (calculated with respect to the T_2 measured at 37 °C) shows that the gasification of the encapsulated PFH at a temperature of 65 °C generates the two-stage T_2 contrast change.

6.6 References

(1) Cheng, C. A.; Chen, W.; Zhang, L.; Wu, H. H.; Zink, J. I. A Responsive Mesoporous Silica Nanoparticle Platform for Magnetic Resonance Imaging-Guided High-Intensity Focused Ultrasound-Stimulated Cargo Delivery with Controllable Location, Time, and Dose. *J. Am. Chem. Soc.* 2019, 141 (44), 17670–17684.

(2) Cheng, C.-A.; Chen, W.; Zhang, L.; Wu, H. H.; Zink, J. I. Magnetic Resonance Imaging of High-Intensity Focused Ultrasound-Stimulated Drug Release from a Self-Reporting Core@shell Nanoparticle Platform. *Chem. Commun.* 2020, 56, 10297.

(3) Lin, F.-C.; Xie, Y.; Deng, T.; Zink, J. I. Magnetism, Ultrasound, and Light-Stimulated Mesoporous Silica Nanocarriers for Theranostics and Beyond. *J. Am. Chem. Soc.* 2021, 143, 6025–6036.

(4) Saha, S.; Roy, A.; Roy, K.; Roy, M. N. Study to Explore the Mechanism to Form Inclusion Complexes of β-Cyclodextrin with Vitamin Molecules. *Sci. Rep.* 2016, 6, 1–12.

(5) Li, Z.; Liu, H.; Qi, C.; Yang, A.; Deng, S. Preparation, Characterization and Molecular Modelling of Inclusion Complex between α-Naphthylacetic Acid with Ethylenediamine-β-Cyclodextrin. *J. Incl. Phenom. Macrocycl. Chem.* 2019, 93 (3–4), 289–299.

(6) Liu, B.; Zeng, J.; Chen, C.; Liu, Y.; Ma, H.; Mo, H.; Liang, G. Interaction of Cinnamic Acid Derivatives with β-Cyclodextrin in Water: Experimental and Molecular Modeling Studies. *Food Chem.* 2016, 194, 1156–1163.

(7) Kfoury, M.; Landy, D.; Auezova, L.; Greige-Gerges, H.; Fourmentin, S. Effect of Cyclodextrin Complexation on Phenylpropanoids' Solubility and Antioxidant Activity. Beilstein J. *Org. Chem.* 2014, 10, 2322–2331.

(8) Granadero, D.; Bordello, J.; Pérez-Alvite, M. J.; Novo, M.; Al-Soufi, W. Host-Guest Complexation Studied by Fluorescence Correlation Spectroscopy: Adamantane-Cyclodextrin Inclusion. *Int. J. Mol. Sci*. 2010, 11 (1), 173–188.

(9) Meng, H.; Xue, M.; Xia, T.; Zhao, Y.; Tamanoi, F. Autonomous in Vitro Anticancer Drug Release from Mesoporous Silica Nanoparticles by PH-Sensitive Nanovalves. *J. Am. Chem. Soc.* 2010, 132, 12690–12697.

(10) Du, L.; Liao, S.; Khatib, H. A.; Stoddart, J. F.; Zink, J. I. Controlled-Access Hollow Mechanized Silica Nanocontainers. *J. Am. Chem. Soc.* 2009, 131 (42), 15136–15142.

(11) Wang, X.; Chen, H.; Chen, Y.; Ma, M.; Zhang, K.; Li, F.; Zheng, Y. Perfluorohexane-Encapsulated Mesoporous Silica Nanocapsules as Enhancement Agents for Highly Efficient High Intensity Focused Ultrasound (HIFU). *Adv. Mater.* 2012, 24, 785–791.

(12) Lu, G. J.; Farhadi, A.; Szablowski, J. O.; Lee-Gosselin, A.; Barnes, S. R.; Lakshmanan, A.; Bourdeau, R. W.; Shapiro, M. G. Acoustically Modulated Magnetic Resonance Imaging of Gas-Filled Protein Nanostructures. *Nat. Mater.* 2018, 17 (5), 456–463.

(13) Park, J.; An, K.; Hwang, Y.; Park, J. E. G.; Noh, H. J.; Kim, J. Y.; Park, J. H.; Hwang, N. M.; Hyeon, T. Ultra-Large-Scale Syntheses of Monodisperse Nanocrystals. *Nat. Mater.* 2004, 3 (12), 891–895.

(14) Cha, B. G.; Jeong, J. H.; Kim, J. Extra-Large Pore Mesoporous Silica Nanoparticles Enabling Co-Delivery of High Amounts of Protein Antigen and Toll-like Receptor 9 Agonist for Enhanced Cancer Vaccine Efficacy. *ACS Cent. Sci* 2018, 4, 484–492.

(15) Kwon, D.; Cha, B. G.; Cho, Y.; Min, J.; Park, E.; Kang, S.; Kim, J. Extra-Large Pore Mesoporous Silica Nanoparticles for Directing in Vivo M2 Macrophage Polarization by Delivering IL - 4. *Nano Lett.* 2017, 17, 2747–2756.

(16) Liong, M.; Lu, J.; Kovochich, M.; Xia, T.; Ruehm, S. G.; Nel, A. E.; Tamanoi, F.; Zink, J. I. Multifunctional Inorganic Nanoparticles for Imaging, Targeting, and Drug Delivery. *ACS Nano* 2008, 2 (5), 889–896.

Chapter 7 Nano-Therapeutic Cancer Immunotherapy Using Hyperthermia-Induced Heat Shock Proteins: Insights from Mathematical Modeling

This chapter of the dissertation was adapted and reprinted with permission from Fang-Chu Lin, Chao-Hsiung Hsu, and Yung-Ya Lin. *Int J Nanomedicine*. 2018, 13, 3529-3539. This work is published and licensed by Dove Medical Press Limited. Lin, F.C. proposed and designed the study. Lin, F.C. and Hsu, Chao-Hsiung designed and generated the mathematical model. Jeffrey I. Zink and Yung-Ya Lin were co-P.I.s.

7.1 Introduction

The combination of nanomedicine and hyperthermia for cancer treatment is receiving increased attention. For example, it was shown that, by utilizing gold nanorods and laser irradiation as an external heating source, hyperthermia in combination with chemotherapy led to more than 90% of cell inviability.[1] Alternating magnetic-field hyperthermia for cancer treatment has also been shown to play an effective therapeutic role due to its ability to selectively target the cells of interest and induce local heating while minimizing secondary effects in surrounding healthy tissues.[2] Drug delivery systems incorporated with magnetic nanoparticles can also take advantage of induced heating under alternating magnetic fields to perform desired drug release.[2] A much improved tumor ablation after alternating magnetic-field hyperthermia was shown to be achieved when intravenous injection of magnetic nanoparticles was administrated.[3] Also, methotrexate-coupled magnetic nanoparticles in combined treatment with hyperthermia was employed, aiming to bypass severe side effects in non-target organs resulting from the heterogeneous tumor cell responses.[4] These hyperthermia studies mainly focused on directly killing tumor cells. Operating accurate tumor ablation to achieve complete tumor elimination and thus avoid metastasis, however, is still problematic. Consequently, to circumvent these challenges, attaining an alternative tumor-killing mechanism, such us hyperthermia-therapies-activated immunomodulation, is critical in cancer treatment.[5]

There is a rapidly growing interest in the combination of immunotherapy with hyperthermia for cancer treatment. Primary tumors treated with hyperthermia have led to spontaneous regression of untreated, distant metastases due to the heat-induced anti-tumor immune response.[5] It was demonstrated that local hyperthermia treatment, applied to identified tumors in inducing anti-tumor immune responses activated by extracellular heat shock proteins (HSPs), potentially reduces the risk of recurrence and metastasis.[6] Also, the level of HSPs in the sera of patients has been shown to be significantly higher after alternating magnetic field hyperthermia, where the increased serum levels of HSPs resulted in a better survival rate.[7]

HSPs are a family of proteins that are produced by cells in response to exposure to stressful conditions, including exposure to heat, cold, and UV light. HSPs are named according to their molecular weight. For example, the 70 kilodalton HSPs (HSP70s) are a family of conserved ubiquitously expressed HSPs, existing in virtually all living organisms. The Hsp70s are an important part of the cell's machinery for protein folding and help to protect cells from stress. In this study, we will focus on HSP70 due to its immunogenic properties in the extracellular environment[8] and develop a model for interpreting he reported experimental data.[9] (Note: we will denote HSP70 simply by HSP from now on.) Studies have shown that hyperthermia-induced necrotic cell death correlated with HSP release.[10] HSPs secreted into the extracellular space during cell necrosis act as danger signals and trigger an adaptive anti-tumor immune mechanism. Tumors undergoing heat stress by hyperthermia were followed by the release of tumor antigens which would be chaperoned by extracellular HSPs released from necrotic tumor cells. The HSP tumor-antigen complexes facilitate the presentation of tumor antigens, induce anti-tumor immunity, and activate immune cells.[11] Many of HSP-antigen complexes bind to and activate antigen-presenting cells (APCs).[12] Once APCs phagocytose HSP-antigen complex, APCs can present the antigens to cytotoxic T cells and initiate adaptive immune responses.[13] The interaction of HSP with APCs has driven the development of HSP-containing vaccines. Vaccines designed to deliver antigens directly to dentritic cells have been shown to generate impressive immune responses and protection from tumor challenge.[14] HSP-containing nanovaccines based on superparamagnetic iron oxide nanoparticles have demonstrated superior improvement in tumor targeting due to overexpression of HSP receptors on glioma and boost-up of anti-tumor responses.[15,16] As a result, HSP can aid in tumor targeting and anti-tumor immune activation.

It is crucial to understand how temperature influences the immune system. Heat-induced cell necrosis is often mediated by externally-applied thermal stress, which also elicits an up-regulation of HSPs to protect cancer cells undergoing heat stress.[17,18] Moderate hyperthermia with temperature ≤43°C was reported to promote thermotolerance, the ability possessed by intracellular HSPs to tolerate future hyperthermia treatments, by inducing HSP expression in cells.[19] As a result, the applicability of the hyperthermia treatment may be initially limited due to thermotolerance resulted from the up-regulation of intracellular HSP,[20] which also assists in inhibiting apoptosis by protecting against cell injury.[5] Study showed that HSP release starts at 41°C, reaches a maximum at 43°C, and is completely diminished at 45°C .[9] Hyperthermia at a temperature above 43°C triggers protein denaturation which leads to cellular death.[21] Also, it was observed that when primary tumors were heated to 45°C instead of 43°C, the resistance against secondary tumors was not established.[13] On account of these results, we expect to see an increase in HSP synthesis when an elevated temperature at around $41\,°\mathrm{C}$ is applied. Such increase is mainly contributed by the intracellular HSP induction. HSP amount will then achieve a maximum at around $43°\mathrm{C}$ due to the release of extracellular HSPs and then decrease when the temperature is raised further. Regarding heating exposure time, studies showed that irreversible cell damage only occurs after prolonged heat exposure when cell lines or tissues are exposed to temperatures of around $40 - 50°\mathrm{C}$.[5] Heating cells or tissues to temperatures $\geq 42°\mathrm{C}$ for one or more hours could result in significant cell killing.[22] This result can serve as a predicted approximate exposure time associated with the optimal temperature to achieve maximum extracellular HSP generation. Moreover, HSPs are thought to secrete into the extracellular space during cell necrosis, whereas it was observed that the secretion still takes place in the absence of cell death.[23] For this reason, the existence of a secretory pathway was proposed.[23]

This study investigated the secretion and synthesis of extracellular HSPs that are involved in anti-tumor immunological processes and its relationship with necrotic cells. Because only extracellular HSPs participate in immune activation, the study focused on the extracellular HSPs released from the necrotic cells after the cytotoxic temperature is achieved. Along these lines, we propose a new model which is capable of considering the amount of extracellular HSPs by incorporating HSP synthesis with cell death. Moreover, it has been reported that there seems to be a narrow range of optimal temperature for the heated tumor to induce adaptive immune responses.[13] Such temperature dependence indicates that different temperatures provide a different levels of impacts on the induced immune responses and highlights the need to understand temperature effects across a relatively narrow range of thermal dose. Thus, the proposed model will provide an informative analysis on thermal parameters for addressing the issue of temperature sensitivity in stimulating anti-tumor immunity. The model parameters will be analyzed to find the heating temperature and the exposure time that optimize the release of extracellular HSPs, which are correlated with cell death under thermal stress and bring out the greatest anti-tumor immune outcome.

7.2 Materials and Methods

7.2.1 Induction and Generation of HSPs

It is essential to consider the effect on the cellular responses, such as the upregulation of HSPs that occurs under heat stress due to thermotolerance effect, with a dynamic analysis. To account for such HSP-induced thermotolerance, which is triggered by the heat-shock response (HSR), a mathematical model of HSP-based HSR mechanism is introduced.[13,24,25] It can be seen from the mathematical model that HSP is the main component of this hyperthermia-involved mechanism. The model depicts the induced dynamical HSP synthesis by an external temperature stimulus and its interactions with key intracellular components in the HSR mechanism. In this work, the model used to calculate HSP synthesis induced at elevated temperatures is constituted by twelve reactions, where one of the rate constants shows the temperature dependence of the whole model.[24,25] The temperature-dependent rate constant describes the fraction of protein denaturation (native proteins $\xrightarrow{k_{11}^{T}}$ denatured proteins) as a function of temperature and is written as

$$k_{11}^{T} \approx m_{11} \times \left(1 - \frac{0.4}{e^{T-37}}\right) \times 1.4^{T-37}\ \text{min}^{-1} \qquad T \epsilon [37,45]℃ \qquad (1)$$

, where m_{11} is a time-scale dependent multiplier -- a variable used to fit the experimental data in the right units. k_{11}^{T} was approximated from the experimental data of differential scanning calorimetry[26,27] and is proportional to the function which describes the response of the substrate (i.e., the denatured protein) to the temperature.

7.2.2 HSP Synthesis and Cell Death Model Integration

It was suggested that HSP induction and the initiation of thermotolerance are due to the HSP's protective tendency when they are exposed to stressors[8] as well as the significant injury or dysfunction of some targeted tissues.[28,29] Also, the improved thermotolerance of the feeblest organ and cell systems further gives rise to the thermotolerance development.[30] Studies showed that heat stress that correlates with widespread cellular injury is relevant to the cell necrosis, while cell surface HSPs or those that are released from necrotic cells into extracellular environment participate in cellular anti-tumor immune activation.[11,30] Therefore, to take the number of free extracellular HSPs as the index of the anti-tumor immune activation, the previously discussed HSR mechanism model is proposed to be integrated with a cell death model. This integration is based on an assumption that the number of antigens is in excess such that all extracellular HSPs can form complexes with tumor antigens. In this work we only look at the immunomodulatory activities exerted by the free HSP at extracellular localization that are released from the heat-induced dead cells without considering the activation of immune cells due to the membrane HSP expression.[31]

In this study, a three-state cell death model proposed by O'Neill[32] was used to approximately determine the number of dead tumor cells in terms of heating temperature and exposure time. This model was chosen over Arrhenius-based models because it deals with continuous dynamic temperatures instead of a discrete, single-temperature heating that would create a marked discontinuity at temperatures around 43℃. The model contains three compartments: fully alive (A), fully dead (D), and vulnerable (V) compartments. These three compartments are related to each other by

$$\mathrm{A} \overset{\mathrm{k_f}}{\underset{\mathrm{k_b}}{\rightleftarrows}} \mathrm{V} \overset{\mathrm{k_f}}{\rightarrow} \mathrm{D} \qquad (2)$$

The transition from fully alive (A) to vulnerable (V), i.e., an injured state, is represented by a forward rate constant, $\mathrm{k_f}$, while a backward rate constant, $\mathrm{k_b}$, represents a self-healing process from vulnerable (V) to fully alive (A) state. The simplification made in the three-state cell death model, where the transition from vulnerable (V) to fully dead (D) possesses the same forward rate constant, $\mathrm{k_f}$, is based on an assumption that there is just a single damage process which accounts for all physiological damages, thus both transitions lead to the same result. The forward rate constant in this cell death model is defined as,[32]

$$\mathrm{k_f} = \overline{\mathrm{k_f}}\, \mathrm{e}^{\frac{\mathrm{T}}{\mathrm{T_k}}} (1 - \mathrm{A}) \qquad (3)$$

, where $\overline{\mathrm{k_f}}$ is a scaling constant and $\mathrm{T_k}$ (°C) sets to let the rate of the exponential increase with temperature. The exponential curve accounts for the insignificant thermal damage at body temperature and the fact that the already-damaged tissue is more prone to further damage.[32] Also, the inclusion of (1-A) considers the nonlinear influence from the damaged state of surrounding cells on the reaction dynamics. Therefore, the three-state cell death model allows the fitting of data over a wider thermotherapeutic temperature range than single-state models, including the beginning phase when cells are first exposed to the heat shock.

Heating duration time, τ, and the temperature, T, are the two experimental parameters that are often applied in the basic experimental practices. The free extracellular HSP concentration generation rate, $\mathrm{S}(\tau, \mathrm{T})$, is the product of the HSP concentration and the number of dead cells per unit of time:

$$\mathrm{S}(\tau, \mathrm{T}) = [\mathrm{HSP}](\tau, \mathrm{T}) \times \frac{\mathrm{dD}(\tau, \mathrm{T})}{\mathrm{d}\tau} \qquad (4)$$

Here $[\mathrm{HSP}](\tau, \mathrm{T})$ is the HSPs produced from HSR mechanism and $\mathrm{D}(\tau, \mathrm{T})$ is the fraction of cells in the dead state from three-state cell death model. Both $[\mathrm{HSP}](\tau, \mathrm{T})$ and $\mathrm{D}(\tau, \mathrm{T})$ depend on heating temperature and duration time in a nonlinear manner. The total free extracellular HSP concentration ($[HSP]_T$) can be calculated by taking the integral of $S(\tau, T)$ over the heating period respective to each temperature from 37 - 45℃. This equation is expected to help examine the relation between thermally induced HSP expression and cell death and qualitatively predict $[HSP]_T$ at each temperature and with different exposure times. The incorporation of cell death model into HSR mechanism model provides a macro aspect of how heat-generated dead tumor cells are related to HSPs produced from HSR mechanism, while such mechanism provides a micro description of how HSP increases due to the presence of denatured/misfolded proteins.

7.3 Results and Discussion

7.3.1 Analysis of Rate Constants

In the proposed mathematical model, besides the temperature setting, rate constants are also adjustable for the model analysis. Changing rate constants produces an increase or decrease in the fraction of cells in a compartment and alters the HSP synthesis under different degrees of heat stress. Due to the integration of the HSR mechanism and three-state death cell model, as shown by Eq. (4), the forward rate constant, k_f, which corresponds to the dead-cell fraction shown in Eq. (2), should relate to the denatured/misfolded protein, which is governed by the rate constant, k_{11}^T, in the HRS mechanism to some extent. Consequently, the total HSP synthesis, which is hypothetically correlated with the dead-cell number, should vary when different k_f values are used. As shown in **Figure 7.1A**, four $\overline{k_f}$ values, 0.10, 0.16, 0.20, and 0.30 min^{-1} were chosen to demonstrate how changing k_f value influences the total HSP production. Although a larger k_f value ought to correlate with a larger dead cell fraction compared with when a smaller k_f value is used, dramatic increase of HSP synthesis was observed when $\overline{k_f}$ = 0.16 min^{-1} was used, while $\overline{k_f}$ = 0.20 or 0.30 min^{-1} showed nearly unchanged [HSP] under a more enhanced heat stress, indicating that severe cell death at higher temperature does not necessarily give the most HSP synthesis. This phenomenon might be a result of the fact that the increase of HSPs in response to heat stress takes time to develop, and cells do not have sufficient time to express developed HSP under rapid necrosis.[33]

The backward rate constant, k_b, in the three-state cell death model[32] was determined from the experimental results, where each experiment was conducted with a fixed heating time and temperature and was assumed to be invariant with temperature. However, k_b describes the biological healing process, as shown in Eq. (2), and therefore is relevant with the thermotolerance effect of HSP. For this reason, k_b must have a coupling relation with the HSR mechanism, which includes a temperature-dependent k_{11}^{T}, as shown in Eq. (1). Such coupling relation can be achieved by employing Eq. (4), and upon the integration, k_b will no longer be temperature independent. **Figure 7.1B** shows the results of HSP synthesis at different temperatures with increasing k_b values 0.12, 0.23, 0.47, and 0.61 min^{-1}, respectively. Although a larger k_b value results in a decrease in the dead cell fraction, k_b = 0.47 min^{-1} gives a significantly higher production of HSP compared with the other chosen values, which, whether is larger or smaller than k_b = 0.47 min^{-1}, shows a slow decrease in $[HSP]_T$ when heating temperature is increased from 37°C to 45°C, as can been seen in **Figure 7.1B**. Owing to the coupled reactions in the HSR mechanism model, constants k_f, k_b, and k_{11}^{T} are all related with each other, making all parameters in the proposed [HSP]-cell death model temperature-dependent.

The fact that the cell undergoes a harsh thermal variation might have an inverse effect on the activation of adaptive immune responses. It is possible that HSP expression increases when tumor cells struggle to survive under milder heating conditions.[33] Although HSP can be increased by heat to generate anti-tumor immune responses that retarded tumor growth, it required some time to develop the immune response.[33] Rate constant analysis in **Figure 7.1** shows that with a specific chosen k_f or k_b value, synthesis of HSP responds to a gradual increase in temperature, achieving a maximum at a specific temperature, and decreases when the temperature is further raised. Such observation indicates that heating exposure time, τ, plays an important role in generating HSP and implies that there is an optimal heating temperature, T, corresponding to the exposure time, τ, to give an optimal HSP synthesis.

7.3.2 Analysis of Optimal HSP Synthesis

To achieve the release of extracellular HSP for immune activation, a critical temperature needs to be exceeded, where it was reported that cytotoxic temperatures for tumor cells are those over 42.5°C.[34] Studies of HSP in the mouse melanoma cell line[9] showed that the onset of HSP release was at 41°C, achieves maximum at 43°C, and the release is completely diminished at 45°C. Also, it was shown that heating primary tumors at 43°C activated anti-tumor immunity and induced resistance against rechallenge.[13] With respect to these in vitro results, the proposed [HSP]-cell death model was analyzed to see if the simulated results agree with the experimental data. **Figure 7.2** shows that, by adjusting either $\overline{k_f}$ to 0.15 min^{-1} or k_b to 0.62 min^{-1}, maximum HSP synthesis can be achieved at 43°C. The initiation of HSP synthesis was under milder thermal stress (< 43°C), which resulted from the thermotolerance effect present in the weakest cell systems due to intracellular HSPs. These intracellular HSPs do not contribute to the activated anti-tumor immunity because the temperature for tumor cell cytotoxicity is not yet reached. HSPs heated at a temperature above 42.5°C will be released from the dead tumor cells, travel to and enter the extracellular milieu, recognize the antigens released from the cytotoxic tumor cells, and activate the anti-tumor immunity. It can be seen in **Figure 7.2** that a maximum HSP synthesis is achieved at the cytotoxic temperature of 43°C, followed by a gradual decrease when the temperature continuously increases. This result again suggests that extracellular HSP synthesis does not respond linearly to the increase of temperature. It agrees with our previous argument that a milder cytotoxic heating temperature could be more stimulatory than a higher one. A milder temperature that is sufficient to cause tumor cell necrosis can help prevent overheating the surrounding tissues if an accurate prediction of the tissue response can be achieved. It has to be noted that, in combination with a more focusing and localized hyperthermia treatment, an even more milder temperature (≤42.5°C) could potentially achieve the same efficiency of anti-tumor immunity.[35] Note that this model focuses on immune activation at cytotoxic temperatures rather than the immunomodulatory activities under fever-like hyperthermia exposure such as lymphocyte function;[36] as a result, it is more suitable to use this model to analyze the parameters for that of localized hyperthermia treatment than that of a whole-body hyperthermia.

7.3.3 Effect of Heating Duration Time on HSP Synthesis

The results in **Figure 7.1** and **Figure 7.2** pointed out the importance of heating duration time, τ, in synthesizing HSP. Duration of heating might induce clustering in the plasma membrane and changes in membrane fluidity, which could affect the induced immunity.[37] Studies have shown that heating tumors at 43°C for 30 min expressed the largest amount of HSP, activated anti-tumor immunity, and led to a reduction in metastases.[9,13] Consequently, to achieve the optimal anti-tumor immune activation, heating duration time is a crucial parameter to analyze. Table 1 shows the optimized parameter values, while in **Figure 7.3A** the optimized results are shown in terms of HSP generation rate and accumulated HSP against heating duration time. Using either the optimized $\overline{\mathrm{k_f}}$ or $\mathrm{k_b}$ value, a maximum HSP synthesis at 43°C was achieved. Nevertheless, despite using the optimized $\overline{\mathrm{k_f}}$ value, dead cell fraction still increases when temperature is raised from 38°C to 45°C (**Figure 7.4**), indicating the production of HSP is not linearly related with dead cells number. This observation also implies that it might not be necessary to completely diminish the tumor cells to activate HSP-induced anti-tumor immunity. Although HSPs were synthesized at a slightly faster rate when a higher temperature (44℃ or 45℃) was applied, as shown in **Figure 7.3A**, a higher [HSP] was generated after heating at 43℃ for approximately 100 min. Comparably, assuming under the same condition, HSPs were generated at a much slower rate (and also less amount were obtained) when using heating temperatures that are close to body temperature. **Figure 7.3B** shows the optimized k_b result in terms of accumulated HSP against heating time. HSP accumulation at temperatures 44℃ and 45℃, although accumulating faster when the initial heating is applied, leveled out before HSP synthesis at temperatures 43℃ and achieved its maximum (slightly $>$ 100 min), with a lower final [HSP]. A similar result was obtained when using the optimized k_f value (**Figure 7.5**). The heating duration is defined as the time required for each specific temperature to reach its final accumulated [HSP]. It can be seen that, even though the difference of heating duration between the cytotoxic temperatures, 43℃, 44℃, and 45℃, is small, the final HSP accumulation at 43℃ is significantly higher than the other two temperatures. It shows that a relatively milder cytotoxic temperature can achieve a much-desired HSP production. By comparing with the HSP synthesis performed at 43℃, a lower temperature (38℃) only produces approximately 4-fold less amount of $[HSP]_T$ with a much longer heating duration (about 6-fold longer), as can be seen in **Figure 7.3B**.

Figure 7.6 shows the optimal HSP synthesis with respect to duration time, τ, and heating temperature, T, ranged from 37℃ to 45℃. It can be seen that, to achieve a maximum HSP synthesis at 43℃, it requires approximately 100 mins of duration time. Such an increase in HSP synthesis is not visible for other heating temperatures, even if a longer duration time is applied. The calculated optimal heating duration time (100 min) is longer compared to that in the previous in vitro studies.[9,13] It is crucial to include the biological factors that might modify the response because in vitro studies may not accurately reflect the cellular response in a physiologically relevant in vivo environment.[29] In vitro experiments are not able to include all the real-time regulation of HSP synthesis, whereas the HSR mechanism model used in this study consists of a system of twelve nonlinear ODEs describing the evolution of the key variables in the HSP synthesis regulation with respect to temperature. Sensitivity to hyperthermia varies among different kinds of cancer cells,[4] and the heating efficiency also depends on how temperature is administered to the cells.[29] Moreover, HSPs might secrete into extracellular space through a possible pathway.[23] As a result, it is necessary to put factors such as parameter dependency upon different cell lines, cell incubation times, and heat administrating methods, into consideration to achieve an optimal extracellular HSP synthesis.

7.4 Conclusion

Traditional cancer treatments normally focus on reducing tumor burden while stimulation of systemic self-defense against metastatic tumors has not been taken into much consideration.[6] Due to intracellular HSP's role of cell-protective chaperons, previous studies often focus on minimizing HSP expression in the targeted tumor region,[11] while maximized extracellular HSP expression could induce anti-tumor immunity. In our previous work, we developed magnetic resonance nano-theranostic hyperthermia using nontoxic, biocompatible magnetic nanoparticles to target and accumulate at the lesions to generate enhanced contrast for early lesion detection and generate heat to kill lesion cells directly through hyperthermia or indirectly through thermal activation and control releasing of drugs.[38–43] In this study, instead of focusing on producing a direct cell-killing effect, hyperthermia treatment serves to induce the anti-tumor immune system activated by the extracellular HSPs released from the heat-treated necrotic tumor cells. Such immunity is expected to detect and attack all metastases. We incorporate cell death model with extracellular HSP expression to investigate HSP synthesis under various temperatures and exposure times.

The model produced a maximum extracellular HSP synthesis at 43℃ with an approximate exposure time of 100 min, which is in agreement with the significant cell death obtained when cells or tissues are heated up to temperatures $\geq$ 42℃ for one or more hours. Discordant results of exposure time required to achieve a maximum extracellular HSP synthesis at 43℃ between the proposed model and in vitro data may be due to the possible effects of different cell lines[4,32] or a possible secretory pathway into extracellular space for HSPs.[23] The maximum amount achieved at 43℃ was then followed by a decrease in HSP synthesis when the temperature is further raised, suggesting that extracellular HSP synthesis does not respond linearly to the increase in temperature. Such outcome confirms that a milder cytotoxic heating temperature could be more stimulatory than a higher one. In conclusion, our model is capable of predicting the optimal temperature and exposure time to generate HSPs involved in the anti-tumor immune activation, with a goal to promote tumor regression and reduce metastasis.

7.5 Figures and Tables

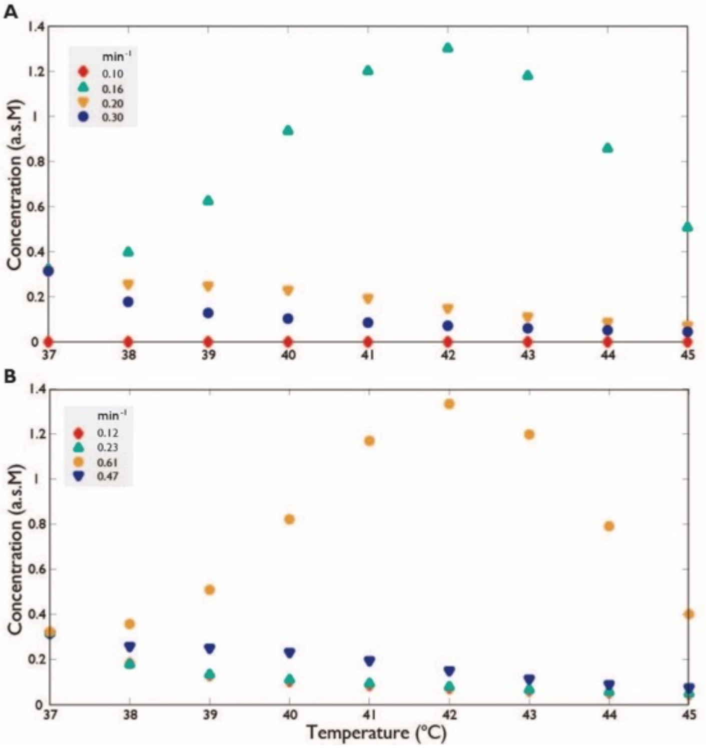

Figure 7.1 Total HSP generated at each temperature, in a.s.M (arbitrary scale molarity). (A) When $\overline{k}_f$ values are adjusted to 0.10, 0.16, 0.20, and 0.30 min^{-1}, respectively. (B) When k_b values are adjusted to 0.12, 0.23, 0.47, and 0.61 min^{-1}, respectively. A higher heating temperature, a larger $\overline{k}_f$, or a smaller k_b do not necessarily give the maximum HSP synthesis, indicating both heating temperature, T, and heating duration time, τ, are crucial parameters to achieve optimal immune activation.

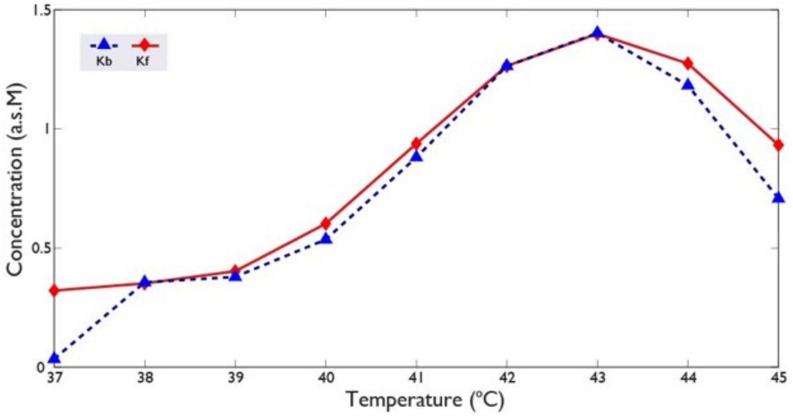

Figure 7.2 Total HSP generated at each temperature. Comparison between the chosen k_f and k_b values. After each rate constant adjustment, a maximum HSP synthesis at 43°C can be achieved and HSP amount decreases, if the temperature is further raised. $\overline{k}_f = 0.15$ and $k_b = 0.62$ min^{-1}. a.s.M (arbitrary scale molarity).

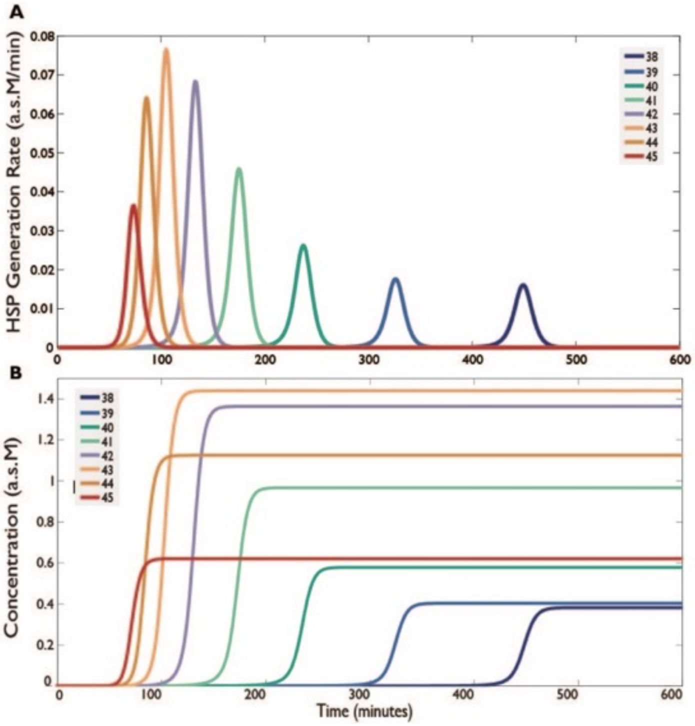

Figure 7.3 Maximum HSP synthesis is achieved at 43℃ by using either the optimized k_f or k_b. Results for cytotoxic temperatures (≥43°C) are significantly different from those that are around the body temperature. (A) HSP generation rate, $S(\tau, T)$, for different heating temperatures using the optimized k_b value. a.s.M/min. (B) Heating duration time and the accumulated HSP at different temperatures using the optimized k_b value

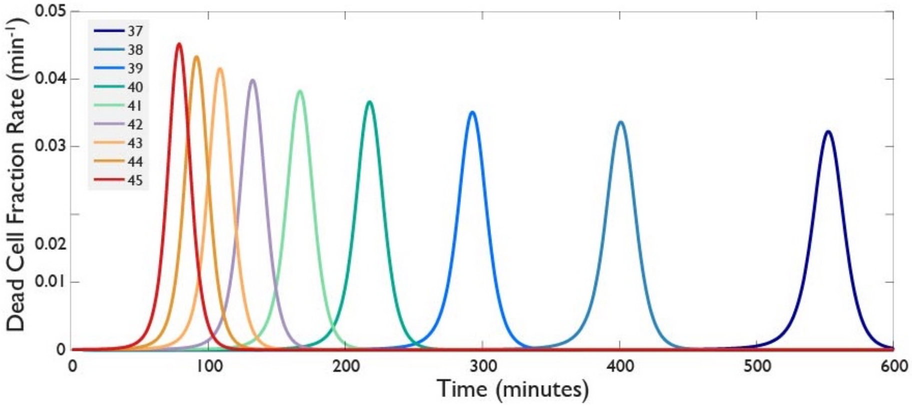

Figure 7.4 Dead cell fraction rate, $\frac{dD(\tau,T)}{d\tau}$, generated by cell death model using the optimized $\overline{k_f}$ value. Even though maximum HSP was obtained at 43℃, when heating temperature is raised, cells still die at a faster rate and the final dead cell fraction increases along with the applied temperatures.

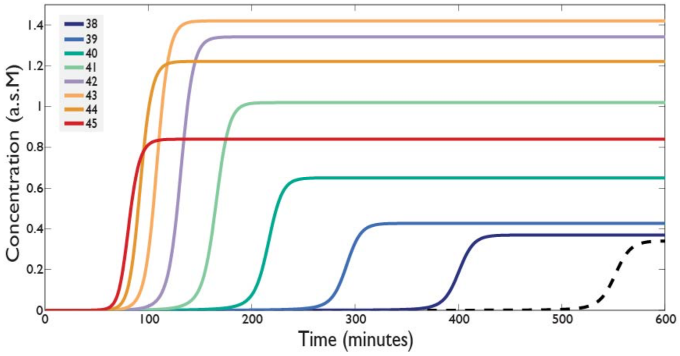

Figure 7.5 Heating duration time, τ, and the accumulated HSP at different temperatures, T, using the optimized $\overline{k_f}$ value. A maximum final accumulated HSP was achieved at 43℃ despite an enhanced HSP generation at higher temperatures when heat is applied initially. a.s.M (arbitrary scale molarity). The dashed line is for the result obtained at body temperature 37℃, as a reference.

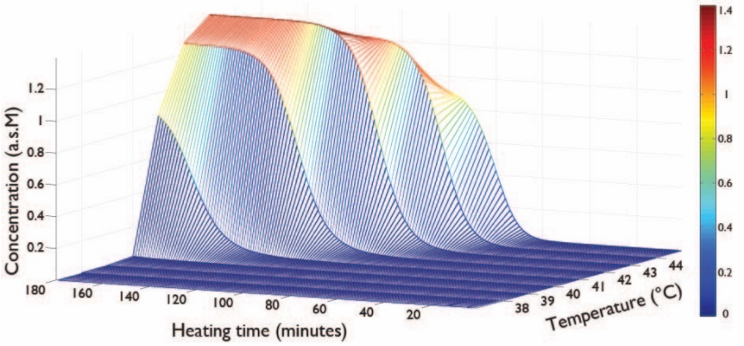

Figure 7.6 Maximum HSP synthesis with respect to heating temperature, T, and duration time, τ, using the optimized $\overline{k_f}$ value. Duration time is approximately 100 mins to achieve maximum HSP synthesis at 43℃. Maximum amount of HSP generated at the other temperatures is smaller than the amount achieved at 43℃, even a longer heating time is applied.

Parameter	**Optimized value**
$\overline{\mathbf{k_f}}$	0.15 min^{-1}
$\mathbf{k_b}$	0.62 min^{-1}
$\mathbf{m_{11}}$	0.015
$\mathbf{T_k}$	40.5 ℃

Table 7.1 List of [HSP]-cell death parameters and values for optimized results.

7.6 References

(1) Huang H-C, Yang Y, Nanda A, Koria P, Rege K. Synergistic administration of photothermal therapy and chemotherapy to cancer cells using polypeptide-based degradable plasmonic matrices. *Nanomedicine (Lond).* 2011, 6 (3), 459-473.

(2) Banobre-Lopez M, Teijeiro A, Rivas J. Magnetic nanoparticle-based hyperthermia for cancer treatment. *Reports Pract Oncol Radiother.* 2013, 18 (6), 397-400.

(3) Huang HS, Hainfeld JF. Intravenous magnetic nanoparticle cancer hyperthermia. *Int J Nanomedicine.* 2013, 8, 2521-2532.

(4) Stapf M, Pömpner N, Teichgräber U, Hilger I. Heterogeneous response of different tumor cell lines to methotrexate-coupled nanoparticles in presence of hyperthermia. *Int J Nanomedicine*. 2016, 11, 485-500.

(5) Chu KF, Dupuy DE. Thermal ablation of tumours : biological mechanisms and advances in therapy. *Nat Rev Cancer.* 2014, 14 (3), 199-208.

(6) Zhu J, Zhang Y, Zhang A, He K, Liu P, Lisa XX. Cryo-thermal therapy elicits potent anti-tumor immunity by inducing extracellular Hsp70-dependent MDSC differentiation. *Sci Rep.* 2016, 6 (1), 27136.

(7) Haen SP, Gouttefangeas C, Schmidt D, Boss A, Clasen S, Herbay AV, et al. Elevated serum levels of heat shock protein 70 can be detected after radiofrequency ablation. *Cell Stress Chaperones.* 2011, 16, 495-504.

(8) Seigneuric R, Mjahed H, Gobbo J, Joly AL, Berthenet K, Shirley S, et al. Heat Shock Proteins as Danger Signals for Cancer Detection. *Front Oncol*. 2011 ,1, 1-10.

(9) Ito A, Fujioka M, Tanaka K, Kobayashi T, Honda H. Screening of cytokines to enhance vaccine effects of heat shock protein 70-rich tumor cell lysate. *J Biosci Bioeng.* 2005, 100 (1), 36-42.

(10) Tanaka K, Ito A, Kobayashi T, Kawamura T, Shimada S, Matsumoto K, et al. Intratumoral injection of immature dendritic cells enhances antitumor effect of hyperthermia using magnetic nanoparticles. *Int J Cancer.* 2005,116 (4), 624-633.

(11) Frey B, Weiss E-M, Rubner Y, Wunderlich R, Ott OJ, Sauer R, et al. Old and new facts about hyperthermia-induced modulations of the immune system. *Int J Hyperth*. 2012, 28 (6), 528-542.

(12) Todryk S, Melcher AA, Hardwick N, Linardakis E, Bateman A, Colombo M, et al. Heat shock protein 70 induced during tumor cell killing induces Th1 cytokines and targets immature dendritic cell precursors to enhance antigen uptake. *J Immunol.* 1999, 163 (3), 1398-1408.

(13) Toraya-brown S, Sheen MR, Zhang P, Chen L, Baird JR, Demidenko E, et al. local

hyperthermia treatment of tumors induces CD8+T cell-meduated resistance against distal and secondary tumors. *Nanomedicine.* 2014, 10 (6), 1273-1285.

(14) Mcnulty S, Colaco CA, Blandford LE, Bailey CR, Baschieri S, Todryk S. Heat-shock proteins as dendritic cell-targeting vaccines - getting warmer. *Immunology*. 2013, 139 (4), 407-415.

(15) Shevtsov MA, Yakovleva LY, Nikolaev BP, Marchenko YY, Dobrodumov AV, Onokhin KV, et al. Tumor targeting using magnetic nanoparticle Hsp70 conjugate in a model of C6 glioma. *Neuro Oncol.* 2014, 16 (1), 38-49.

(16) Shevtsov MA, Nikolaev BP, Yakovleva LY, Parr MA, Marchenko YY, Eliseev I, et al. 70-kDa heat shock protein coated magnetic nanocarriers as a nanovaccine for induction of anti-tumor immune response in experimental glioma. *J Control Release*. 2015, 220, 329-340.

(17) Rylander MN, Diller KR, Wang S, Aggarwal SJ. Correlation of HSP70 expression and cell viability following thermal stimulation of bovine aortic endothelial cells. *J Biomech Eng.* 2005, 127 (5), 751-757.

(18) Rylander MN, Feng Y, Bass J, Diller KR. Thermally induced injury and heat-shock protein expression in cells and tissues. *Ann N Y Acad Sci*. 2005, 1066, 222-242.

(19) Samali A, Holmberg CI, Sistonen L, Orrenius S. Thermotolerance and cell death are distinct cellular responses to stress: Dependence on heat shock proteins. *FEBS Lett.* 1999, 461 (3), 306-310.

(20) Hildebrandt B, Wust P, Ahlers O, Dieing A, Sreenivasa G, Kerner T, et al. The cellular and molecular basis of hyperthermia. *Crit Rev Oncol Hematol.* 2002, 43 (1), 33-56.

(21) Lepock JR. Cellular effects of hyperthermia: Relevance to the minimum dose for thermal damage. *Int J Hyperth*. 2003, 19 (3), 252-266.

(22) Dewhirst MW, Vujaskovic Z, Jones E, Thrall D. Re-setting the biologic rationale for thermal therapy. *Int J Hyperth*. 2005, 21 (8), 779-790.

(23) Vega VL, Rodriguez-Silva M, Frey T, Gehrmann M, Diaz JC, Steinem C, et al. Hsp70 Translocates into the Plasma Membrane after Stress and Is Released into the Extracellular Environment in a Membrane-Associated Form that Activates Macrophages. *J Immunol.* 2008, 180 (6), 4299-4307.

(24) Rybi M, Szyma Z, Lasota S, Gambin A. Modelling the efficacy of hyperthermia treatment. *J Roy Soci Inter*. 2013, 10 (88)

(25) Szymańska Z, Zylicz M. Mathematical modeling of heat shock protein synthesis in response to temperature change. *J Theor Biol*. 2009, 259 (3), 562-569.

(26) Peper A, Grimbergen CA, Spaan JA, Souren JE, van Wijk R. A mathematical model of the hsp70 regulation in the cell. *Int J Hyperthermia*. 1998, 14 (1), 97-124.

(27) Lepock JR, Frey HE, Ritchie KP. Protein denaturation in intact hepatocytes and isolated cellular organelles during heat shock. *J Cell Biol.* 1993, 122 (6), 1267-1276.

(28) Hall DM, Oberley TD, Moseley PM, Buettner GR, Oberley LW, Weindruch R, et al. Caloric restriction improves thermotolerance and reduces hyperthermia-induced cellular damage in old rats. *FASEB J.* 2000, 14 (1), 78-86..

(29) Song AS, Najjar AM, Diller KR. Thermally Induced Apoptosis, Necrosis, and Heat Shock Protein Expression in 3D Culture. *J Biomech Eng.* 2014, 136 (7), 71006.

(30) Kregel KC, Sieck GC. Heat shock proteins: modifying factors in physiological stress responses and acquired thermotolerance. *J Appl Physiol.* 2002, 92 (5), 2177-2186.

(31) Shevtsov M, Huile G, Multhoff G. Membrane heat shock protein 70: a theranostic target for cancer therapy. *Philos Trans R Soc Lond B Biol Sci.* 2018, 373 (1738).

(32) O'Neill DP, Peng T, Stiegler P, Mayrhauser U, Koestenbauer S, Tscheliessnigg K, et al. A three-state mathematical model of hyperthermic cell death. *Ann Biomed Eng.* 2011, 39 (1), 570-579.

(33) Toraya-Brown S, Fiering S. Local tumour hyperthermia as immunotherapy for metastatic cancer. *Int J Hyperth*. 2014, 30 (8), 531-539.

(34) Dewey WC, Hopwood LE, Sapareto SA, Gerweck LE. Cellular responses to combinations of hyperthermia and radiation. *Radiology.* 1977, 123 (2), 463-474.

(35) Tsang Y-W, Huang C-C, Yang K-L, Chi M-S, Chiang H-C, Wang Y-S, et al. Improving immunological tumor microenvironment using electro-hyperthermia followed by dendritic cell immunotherapy. *BMC Cancer.* 2015, 15 (1), 1-11.

(36) Di Y-P, Repasky EA, Subjeck JR. Distribution of HSP70, protein kinase C, and spectrin is altered in lymphocytes during a fever-like hyperthermia exposure. *J Cell Physiol.* 1997, 172 (1), 44-54.

(37) Mace TA, Zhong L, Kilpatrick C, Zynda E, Lee C-T, Capitano M, et al. Differentiation of CD8 + T cells into effector cells is enhanced by physiological range hyperthermia. *J Leukoc Biol.* 2011, 90 (5), 951-962.

(38) Chen KJ, Wolahan SM, Wang H, et al. A small MRI contrast agent library of Gadolinium(III)-encapsulated supramolecular nanoparticles for improved relaxivity and sensitivity. *Biomaterials.* 2011, 32 (8), 2160–2165.

(39) Ho LC, Hsu CH, Ou CM, et al. Unibody core-shell smart polymer as a theranostic nanoparticle for drug delivery and MR imaging. *Biomaterials.* 2015, 37, 436–446.

(40) Li Z, Hsu CH, Dimitrov N, et al. Sensitive imaging of magnetic nanoparticles for cancer detection by active feedback magnetic resonance. *Magn Reson Med.* 2015, 74 (1), 33–41.

(41) Yao J, Hsu CH, Li Z, et al. Magnetic resonance nano-theranostics for Glioblastoma Multiforme. *Curr Pharm Des.* 2015, 21 (36), 5256–5266.

(42) Wang C, Li Z, Lin YY. Optimizing magnetic nanoparticle hyperthermia effect in MR nanomedicine. *Chinese Journal of Magnetic Resonance.* 2015, 32 (2), 248–260.

(43) Wang C, Hsu CH, Li Z, et al. Effective heating of magnetic nanoparticle aggregates for in vivo nano-theranostic hyperthermia. *Int J Nanomedicine.* 2017, 12, 6273–6287.